School of Mathematics, Computer Science and Engineering

Techno-Economic Assessment of a Solar Dish Micro Gas Turbine System

Davide Iaria

Supervisor: Prof. A. I. Sayma

Acknowledgements

Foremost I would like to thank my supervisor, Professor Abdulnaser Sayma, for his teachings, his regular advices and recommendations. Most of all I would like to thank him for encouraging and supporting me in every initiative I have taken during these years, which have enabled me to pull put the maximum from this experience.

I would also like to thank the university and the George Daniel's Foundation for contributing and supporting me to both complete my studies whilst attending a number of international conferences and placements. I would also like to thank my colleagues, and fellow PhD students, whose technical and non-technical support often provided a priceless support. An affectionate thanks goes to Jafar, Mohsen, Mahmoud, Bahareh and Izu.

A distinct thanks goes to Stavanger University and specifically to Dr. Hommam Nipkey and Prof. Mohsen Hassadi for their cooperation in this research. The work done together was central in the validation of the model presented in section 4 and the development of the neural network in section 5.3. Further thanks goes to Zhejiang University for hosting me and to Prof. Gang Xiao and Xin Zhou for their contribution on this thesis and their cooperation in this research. The work done together was essential in the development of the model presented in section 6.

Last but not least, special thanks go to my family and friends, and in particular to Giulia for standing by my side at all times, no matter what it takes.

Abstract

In this thesis a thermo-economic assessment of a stand-alone solar dish MGT power plant is presented. The study aims to develop a fundamental understanding of the impact of the main cycle parameters on plant performances and costs and to evaluate the possibility to incorporate hybridisation and thermal storage, considering technical limitations and economic aspects.

Objective have been achieved developing a flexible and modular tool for design and off-design performance evaluation of micro-turbine based solar power plants. This can then be adopted for different layouts and operational strategies. The model was validated against experimental data demonstrating the applicability and accuracy of the model for thermo-economic optimisation purposes. To guarantee modularity and flexibility an object-oriented programming approach, using the software C++, is adopted. Each component is represented using a class made of functions that perform a one-dimensional physical design for both design point and off-design performance in addition to a cost function.

Results in output from the above-mentioned tool were used to train machine learning algorithms, which were used to perform plant's optimisations considering dissimilar layouts, locations and operational strategies. A multi objective genetic algorithm was adopted as optimisation tool. The objective of the optimisation was

to minimise the levelised cost of energy of the plant while maximising the annual power output. Both environmental impact and plant dispachability were considered. As a final outcome of the optimisation, for each considered layout and operational strategy, a candidate point was selected and analysed. Parametric study on possible technological improvements of plants' components was also performed. The proposed optimum plant configurations are shown to be advantageous in term of levelised cost of energy, more dispatchable and with a reduced environmental impact.

Table of Contents

1. Introduction 17
1.1. Project Scope & Objectives 23
1.2. Thesis Structure 24
2. Literature Review 25
2.1. Solar Resource 25
2.2. CSP dish 28
2.2.1. Dish Stirling systems 29
2.2.2. Solar Dish Micro Gas Turbine 33
2.3. Solar Dish Power Cycles & equipment 34
2.3.1. Power Cycles and Engines 34
2.3.2. Solar Receiver 38
2.4. Hybridisation 39
2.5. Thermal Storage 42
2.6. Modelling Solar Dish MGT Power Plant 45
2.7. Thermo-economic Assessment of a Solar dish MGT Power Plant 46
2.8. Conclusions 48
3. Plant Modelling 51
3.1. Software Logic 52
3.2. Fluid Properties 53
3.3. Compressor 54
3.3.1. Centrifugal Compressor Thermodynamic 54

3.3.2. Compressor Design 56
3.3.3. Compressor Off-design 64
3.3.4. Compressor model validation 64
3.4. Recuperator 67
3.4.1. Recuperator geometrical characteristics 67
3.4.2. Heat transfer and Pressure Losses 68
3.4.3. Design and Off-Design Procedure 71
3.4.4. Recuperator Model Validation 72
3.5. Receiver and Dish Model 74
3.5.1. Receiver and Dish Design 77
3.5.2. Receiver model Validation 78
3.6. Turbine Model 79
3.6.1. Radial In-Flow Turbine Design and Off-Design 81
3.6.2. Turbine model validation 86
3.7. Shaft, High Speed Generator and Power Electronics 89
3.7.1. Rotor dynamics considerations 89
3.7.2. HSG and Power Electronics 91
3.8. Economic Model 92
3.9. Conclusions 95
4. Pure Solar System 97
4.1. Plant Design 98
4.1.1. Design Results 99
4.1.2. Components Maps 102
4.1.3. IPSEpro simulation set-up 105
4.2. Off-Design results 105
4.2.1. Operational strategies 107
4.2.2. Cost Analysis 108
4.3. Plant Optimisation 110
4.3.1. Plant Size Optimisation 110
4.3.2. Plant Design Optimisation 112

4.4. Plant Parametric Analysis 121
4.5. Conclusions 123
5. Hybrid System 125
5.1. Combustion Chamber Model 125
5.1.1.1. Combustion Chamber Design and Off-design 126
5.1.1.2. Combustion Chamber Cost 128
5.1.1.3. Emissions 129
5.2. Plant Design and Off-Design Performances 129
5.2.1. Cost Analysis 133
5.3. Plant Operational Strategies 135
5.3.1. Optimum operational strategy 137
5.4. Plant Optimisation: T_{rec}=cost 147
5.5. Plant Optimisation: P=cost 154
5.6. Parametric analysis 160
5.1. Conclusions 162
6. Integrated Thermal Storage 165
6.1. Thermal energy storage model 166
6.1.1. Modelling Laminar boundary layer 167
6.1.2. Honeycomb TES model 171
6.1.2.1. Material Selection 174
6.1.3. Heat Transfer coefficient and friction factor 176
6.1.3.1. Conjugate Heat Transfer Results 181
6.1.3.2. Regression results 185
6.1.4. One-dimensional model validation 187
6.2. Solar Dish MGT with Integrated Thermal Storage. 190
6.2.1. Case Studies 193
6.2.1.1. Design of a Thermal Energy Storage System 193
6.2.1.2. Day 1 194
6.2.1.1. Day 2 198
6.2.1.2. Influence of the storage size 200

6.3. Cost and LCOE analysis 201
6.4. Conclusions 203
7. Conclusions 205
7.1. Future Researches 208
7.2. Dissemination of the research 209

List of Figures

Figure 1: Global Levelised cost of electricity for existing renewable plants and auctions outcomes for plants to be commissioned. Source: IRENA database [2]. ... 17
Figure 2 Development of the cumulative installed CSP capacity by region, 2006-2016. Source IRENA database [2] ... 18
Figure 3. OMSoP project dish CSP system. Source: https://etn.global/ ... 19
Figure 4. Energy access in developing countries. Source: World alliance for decentralised energy 2018. ... 20
Figure 5: MGT's schematic. Source: CAPSTONE Turbine Corporation. ... 22
Figure 6. Distribution of the direct normal irradiation across the globe. © 2017 The World Bank, Solar resource data: Solargis. ... 26
Figure 7. Distribution of the global horizontal irradiation across the globe. © 2017 The World Bank, Solar resource data: Solargis ... 26
Figure 8. Solar radiation absorbed through the atmosphere. Source: [1]. ... 27
Figure 9. Left: Example of daily variation of DNI. Source [8] Right: Example of annual variation of DNI frequencies. Source: Heloclim, © 2014-2018 MINES ParisTech / Transvalor ... 28
Figure 10. Schematic of solar dish system. Source: [1]. ... 29
Figure 11. Vanguard system by ADVANCO. Source: [1] ... 30
Figure 12. Membrane dish built in Riyadh, Saudi Arabia. Source: [1] ... 30
Figure 13. Cummins Power Generation concentrator. Source: [1] ... 31
Figure 14. ANU SG4 dish. Source: [13]. ... 32
Figure 15. La Jet plant, California. Source: [1]. ... 33
Figure 16. Maricopa Solar Project, Arizona. Source: Tessera Solar. ... 33
Figure 17. OMSoP solar dish at Casaccia, Rome. ... 34
Figure 18. Stirling Cycle power cycle. ... 35
Figure 19. Working principle of Stirling engine. Source: [1] ... 36
Figure 20. T-s chart of a Brayton-Joule cycle. ... 36
Figure 21. Micro gas turbine breakthrough (Without recuperator). Source: OMSoP.eu ... 37

Figure 22. Stirling Engines solar receivers: (a) DIR, (b) Heat pipes receiver. Source: [1] 38
Figure 23. Air Cavity solar receiver: (a) Air Tubes, (b) Volumetric. Source: [15]. .39
Figure 24. Hybrid dish Stirling system developed by RIPASSO. Source: [17].....40
Figure 25. Breakthrough of the Heat pipe hybrid receiver and Stirling engine conceptualised by Moreno. Source: [18]. 41
Figure 26. Hybrid heat pipe receiver developed by DLR. Source: [21]. 41
Figure 27. SNL Dish-Stirling with integrated thermal storage. 44
Figure 28. ANU ammonia synthesis system. Source: [25]. 44
Figure 29. Pure solar system plant scheme. Source: https://omsop.serverdata.net.51
Figure 30. Program logic flow chart.....52
Figure 31. Centrifugal compressor meridional view. 55
Figure 32.Compressor inlet design flow chart. 59
Figure 33. Compressor outlet design flow chart.....59
Figure 34. Impeller geometries considered for the validation (not in scale). 64
Figure 35. Compressor validation: Characteristic maps for Eckardt impeller O. (a) Total to static isentropic efficiency versus mass flow rate. (b) Pressure ratio versus mass flow rate 65
Figure 36. Compressor validation: Characteristic maps for Eckardt impeller A. (a) Total to static isentropic efficiency versus mass flow rate. (b) Pressure ratio versus mass flow rate 66
Figure 37. Compressor validation: Characteristic maps for KIMM impeller. 66
Figure 38. Schematic of a plate-fin heat exchanger with offset strip fin. Source: [45]. 67
Figure 39. Fin geometries considered for the recuperator model validation. 73
Figure 40. Comparison between experimental and analytical data. Colburn factor (cyan) and friction factor (blue). Fin geometry *1/10-27.03* (a). Fin geometry *1/8-16.00(D)* (b). 73
Figure 41. Breakthrough of the adopted cavity receiver. 74
Figure 42. Receiver design flow chart 77
Figure 43. Results from receiver validation. 79
Figure 44. Radial turbine schematic 79
Figure 45. Results of the model validation. 87
Figure 46. Comparison between analytical and experimental data. (a) Total to Static Isentropic efficiency. (b) Total to Total isentropic efficiency 88
Figure 47. Efficiency of the HSG and power electronics, modelled as a single component, as a function of the rotational speed and power.....92
Figure 48. Schematic of a solar microturbine. 98
Figure 49. DNI frequencies in Rome for the period between 2004 and 2005 and the moving average of DNI (red line). 99

Figure 50 . Compressor characteristic maps. (a) Pressure ratio as a function of the corrected flow rate for different rotational speed. (a) Total to static isentropic efficiency as a function of the corrected flow rate for different rotational speed... 102
Figure 51. (a) Pressure drop across the recuperator as a function of the mass flow rate for both cold and hot side. (b) Recuperator effectiveness as function of the mass flow rate..... 103
Figure 52. Receiver characteristic maps: variation of outlet temperature (a), efficiency (b) and outlet pressure (c) with air corrected mass flow rate 104
Figure 53. Turbine Characteristic maps: corrected mass flow rate and efficiency for different rotational speeds 104
Figure 54. Plant Off-Design Performance charts: variation of TIT (a), output power (b), efficiency (c) and rotational speed (d) with DNI. 106
Figure 55. Control Maps of the plant. Variation of TIT (a), Power output (b) and efficiency (c) with DNI. 107
Figure 56. Cost breakdown of the plant..... 108
Figure 57. Annual energy produced at each DNI level..... 110
Figure 58. Plant size optimisation results. Left: Levelised cost of energy as function of the mass flow rate in design condition. Right: Energy produced along the year as function of the LCOE (pressure ratio = 3) 111
Figure 59. Specific annual power output for each DNI considering three different design mass flow rates. 112
Figure 60. Flow chart of the optimisation technique. 113
Figure 61. Goodness of fit of the response surfaces. 116
Figure 62. Response Surface: (a) LCOE as function of design PR and mass flow rate. (b) Annual energy generated as function of design PR and mass flow rate..... 118
Figure 63. History of the optimisation variables 119
Figure 64. Pareto front of the optimisation..... 119
Figure 65. Plant Off-Design Performance charts: variation of TIT, output power, efficiency and rotational speed with DNI. 120
Figure 66. Results of the parametric analysis, LCOE versus recuperator effectiveness for different locations and TITs..... 122
Figure 67. Total annual energy produced versus levelised cost of energy. Comparison between different locations and TITs. 123
Figure 68. (a) Breakthrough of a reverse flow combustor. (b) Breakthrough of a can combustor. Source: [73]..... 126
Figure 69. Plant performances during hybrid operation with constant power output and TIT. (a) Rotational speed and power output as a function of DNI. (b) Cycle efficiency as a function of DNI. (c) Receiver outlet temperature as a function of DNI. (d) Fuel flow rate as a function of DNI. (e) CO_2 emissions as a function of DNI. (f) NO_X emissions as a function of DNI. 132
Figure 70. Overall energy produced along the year for each DNI. 133

Figure 71. Cost breakthrough of the hybrid plant. 134
Figure 72. Performance parameters of the plant under variable DNI and rotational speed. (a) Power output as a function of DNI. (b) Cycle efficiency as a function of DNI. (c) Receiver outlet temperature as a function of DNI. (d) CO2 emissions as a function of DNI. (e) NOX emissions as a function of DNI. 136
Figure 73. Schematic of a MLP network [74] 138
Figure 74. ANN model structure 139
Figure 75. Comparison between the desired and predicted: (a) Power Output. (b) CO_2 emissions. (c) Electrical Efficiency. (d) Fuel Cost 141
Figure 76. Pareto front of the optimizations at different DNIs. 143
Figure 77. Daily variation of control parameters with constant output power. 144
Figure 78. Daily variation of output parameters with constant power output 144
Figure 79. Daily variation of control parameters with constant fuel cost. 146
Figure 80. Daily variation of output parameters with constant fuel cost. 146
Figure 81. Goodness of fit of the response surface. 149
Figure 82. Response surface: LCOE as a function of the design mass flow rate and pressure ratio 150
Figure 83. Response surface: Total annual energy produced along the year as a function of the design pressure ratio and mass flow rate. 150
Figure 84. Response surface: Annual CO_2 emission as a function of the design pressure ratio and mass flow rate 151
Figure 85. Response surface: Annual NO_X emission as a function of the design pressure ratio and mass flow rate 152
Figure 86. Hystory of the output parameters convergence. (a) LCOE. (b) E_{TOT}. . 152
Figure 87. Pareto front of the optimisation: E_{TOT} versus LCOE. 153
Figure 88. Goodness of fit of the response surface for each output parameter. 155
Figure 89. Response surface of the optimisation: LCOE as a function of power output and pressure ratio 156
Figure 90. Response surface of the optimisation: E_{TOT} as a function of design power output and pressure ratio. 157
Figure 91. Response surface of the optimisation: annual CO_2 emissions as function of the design power output and pressure ratio. 158
Figure 92. Pareto front of the optimisation LCOE vs E_{TOT}. 159
Figure 93. Performance parameters of the candidate point under variable DNI. .. 160
Figure 94. Results of the parametric analysis, LCOE versus recuperator effectiveness for different locations and TITs. Total annual energy produced versus levelised cost of energy. Comparison between different locations and TITs 161
Figure 95. Schematic of the thermal energy storage system 172
Figure 96. Results of storage media material selection. Source: CES selector software. 174
Figure 97. Results of insulator material selection 175

Figure 98. Detail of the fluid domain mesh 178
Figure 99. Results of the conjugate transfer model validation: heat transfer coefficient (left). Friction coefficient (right). 179
Figure 100. Comparison between TEXTAN and the present model for velocity profiles at different x^*. 180
Figure 101. Results of the conjugate heat transfer analysis, velocity profiles at different locations. (a) x=0.005. (b) x= 0.05. (c) x=0.1. (d) x=0.2. 182
Figure 102. Results of the conjugate heat transfer analysis, temperature profiles at different locations. (a) x=0.005. (b) x= 0.05. (c) x=0.1. (d) x=0.2. 183
Figure 103. Results of the conjugate heat transfer analysis Pressure profiles at different locations. 184
Figure 104. Comparison between conjugate heat transfer analysis (dots) and regression equation (lines) under variable diameter and Reynolds number. Nusselt number (a); Friction factor (b) 187
Figure 105. Results of one-dimensional model validation. Comparison between different Nusselt relationships and conjugate heat transfer analysis. Storage temperature at different locations: (a) x=0 m, (b) x=0.05 m, (c) x=0.1 m, (d) x=0.15 m and (e) x=0.2 m. Outlet fluid temperature (f). 189
Figure 106. Plant layout with closed circuit 192
Figure 107. Plant layout with open circuit 192
Figure 108. Daily variation of DNI (Blue) and output power (Yellow) during day 1. 194
Figure 109. Performances of the plant during Day 1. (a) Power Output. (b) Efficiency. (c) TIT (dashed line) and Storage temperature (Continue line). 197
Figure 110. Daily variation of DNI (Blue) and output power (Yellow) during day 2. 198
Figure 111. Performances of the plant during day 2. (a) Power Output. (b) Efficiency. (c) TIT (dashed line) and storage temperature (continue line). 199
Figure 112. Output power produced along the day. Comparison between no storage, 4h storage and 8h storage. 201
Figure 113. Cost Breakdown of the plant 203

List of Tables

Table 1. Compressor Design Procedure Input parameters 58
Table 2. Recuperator Design Input Parameters 72
Table 3. Receiver design input parameters. 78
Table 4. Radial In-Flow Turbine Design Input Parameters 81
Table 5. Turbine geometrical specifications 86
Table 6: Main design requirements 98
Table 7. The design parameters for the 7 kWe plant 100
Table 8. Detailed results of the components design for the compressor, receiver, dish, recuperator and the turbine 101
Table 9. Design space of the optimisation 116
Table 10. Statistical analysis of the response surface 117
Table 11. Candidate points in output from the optimisation. 120
Table 12: Main design requirements 130
Table 13. The design parameters for the 7 kWe plant 130
Table 14: Range of input parameters 140
Table 15: Training settings 140
Table 16: Prediction errors of output parameters 142
Table 17. Design space of the optimisation 147
Table 18. Statistical analysis of the response surface 148
Table 19. Candidate points in output from the optimisation. 153
Table 20. Design space of the optimisation 154
Table 21. Statistical analysis of the response surface 155
Table 22. Candidates from the optimisation. 159
Table 23. Infinite-series-solution functions for the circular tube; constant surface temperature; thermal-entry length [93]. 168
Table 24. Solid material properties. 175
Table 25. Mesh Independence study results. 177
Table 26. LCOE preliminary analysis. 203

Nomenclature

Abbreviations

CAGR = Cumulative Annual Growth Rate
CEPCI = Chemical Engineering Plant Cost Index
CHP = Combined Heat and Power
CPV = Concentrated Photo Voltaic
CSP = Concentrated Solar Power
DNI = Direct Normal Irradiation
GHI = Global Horizontal Irradiation
LCOE = Levelised Cost of Energy
MGT = Micro Gas Turbine
O&M = Operations and Maintenance
PCM = Phase Change Material
PV = Photo Voltaic
TES = Thermal Energy Storage

Subscripts and Superscripts

a = Axial component
amb = Ambient
app = apparent
c = Compressor
cav = Receiver cavity
f = Recuperator fin; fluid
fd = fully developed flow
g = Gas
h = Hub

i = *Compressor/ Turbine Impeller;*

in = *Inlet*

off = *Off-Design conditions*

out = *Outlet*

p = *Recuperator Primary Zone; Receiver pipe; Polytrophic*

r = *Radial velocity component*

rcv = *Receiver*

rec = *Recuperator*

s = *Isentropic; solid*

t = *Tip*

TS = *Total to Static*

TT = *Total to Total*

w = *Wall*

0 = *Total thermodynamic condition*

1 = *Compressor impeller inlet; Turbine Nozzle Inlet; Recuperator Cold Side*

2 = *Compressor impeller outlet; Recuperator hot side; Turbine impeller inelt*

3 = *Compressor diffuser exit; Turbine impeller outlet*

Greek Symbols

α = *Absolute flow angle; Absorptivity; Capital recovery factor; Thermal diffusivity*

β = *Relative flow angle;*

Υ = *Specific heat ratio*

δ_i = *Receiver pipe Thickness*

δ_w = *Recuperator plate thickness*

ε = *Clearance Gap; Recuperator Effectiveness; Emissivity*

η = *Efficiency*

θ = *Turbine rotational speed coefficient*

λ = *Recuperator fin off-set*

λ_n = *Eigen values*

μ = *Mass fraction; Dynamic viscosity; Correct flow rate*

ν = *Cinematic viscosity*

ξ = *Axial velocity ratio*

ρ = *Density*

σ = *Slip Factor; Recuperator porosity; Boltzman Constant*

τ_W = *Wall shear stresses*

φ = *Flow Coefficient*

χ = *Heat capacity ratio*

χ_1 = *Compressor inlet tip to inlet hub radius ratio*

χ_2 = *Compressor inlet tip to outlet tip radius ratio*

ψ = *Power input factor*

ω = *Angular velocity*

Symbols

a = *TES single element side length*

A = *Area*

A_K = *Langen Coefficient #1*

B_K = *Langen Coefficient #2*

C = *Absolute velocity; Heat capacity; Cost*

C_P = *Specific heat at constant pressure*

d = *TES duct diameter*

D = *Diameter*

D_{eq} = *TES Equivalent Diameter*

D_f = *Diffusion Factor*

D_h = *Hydraulic Diameter*

De = *Dean Number*

f = *Friction factor*

G = *Volumetric flow rate*

G_n = *Eigen Coefficient*

Gr = *Grashoff Number*

Gz = *Graetz Number*

h = *Enthalpy; Heat transfer coefficient*

i = *Interest rate*

j = *Colburn number*

k = *Thermal conductivity*

$K(x)$ = *Incremental pressure drop coefficient*

K_C *Recuperator contraction coefficient*

K_e = *Recuperator expansion coefficient*

L = *Recuperator length; TES length*

L_a = *Compressor/ Turbine axial length*

L_H = *Hydraulic length*

$\dot{m}$ = *Mass flow rate*

m = *polytrophic exponent; Recuperator fin parameter*

n = *Rotational speed*

N_P = *Recuperator number of passages*

N_S = *Specific Speed*

N_T = *TES number of ducts*

Nu = *Nusselt number*

p = *Pressure*

P_f = *Fin Length*

Pr = *Prandtl number*

Q = *Heat Flux*

R = *Radius; Thermal resistance*

Re = *Reynolds number*

R_W = *Non-dimensional thermal resistance*

T = *Temperature*

U = *Tangential velocity; Overall heat transfer coefficient*

x^* = *TES Non-dimensional axial direction*

W = *Relative velocity*

Z = *Compressor/ Turbine blade number*

1. Introduction

The growth of the world population along with the expansion of the industrial sector has led to an increasing demand for electrical power. This growth, in addition to the problem of decreasing greenhouse gas emissions, has driven the research to a significant boost of the development of "clean" power generation technologies [1].

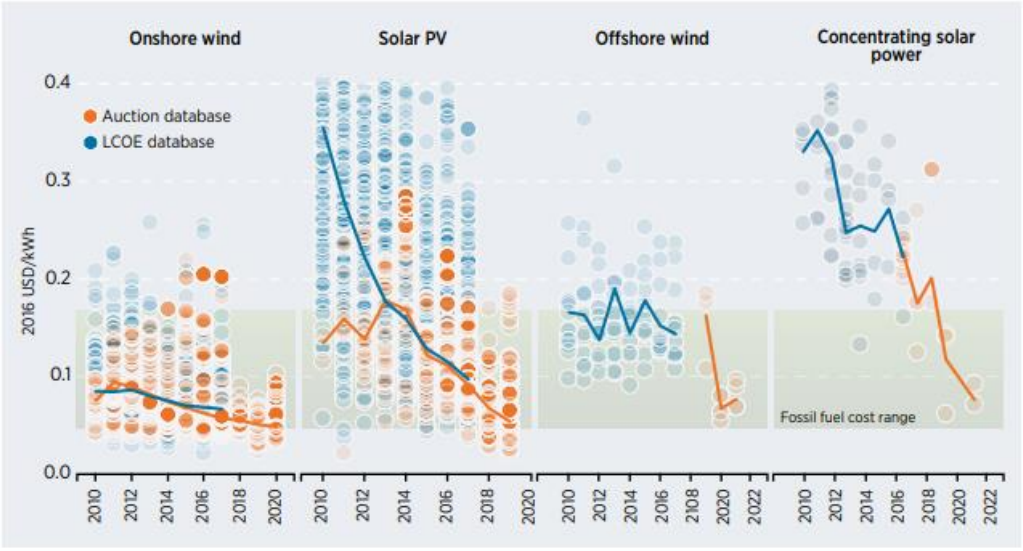

Figure 1: Global Levelised cost of electricity for existing renewable plants and auctions outcomes for plants to be commissioned. Source: IRENA database [2].

After years of steady cost decay, renewable power generation technologies are becoming a competitive way to meet power demand. According to IRENA [2], the results of new renewable power auctions, for new plants to be commissioned in the future, confirm that cost reductions are forecasted to continue till 2020 and beyond. As shown by Figure 1, electricity from renewables will soon be cheaper than fossil

fuels. In Figure 1, the circles represent a single existing plant or a commissioned plant, the lines are the global weighted average levelised cost of energy. The band represents the fossil fuel-fired power generation cost range.

In this context, there has been a renaissance of concentrated solar power (CSP) development, which demonstrate one of the highest energy cost reduction. CSP systems use mirrors to concentrate the direct normal component of solar radiation to generate forms of useful energy like heat or electricity. CSP plants do not absorb diffused or scattered radiation but only the direct normal irradiance (DNI), which is the flux density of direct light, measured on a flat plane perpendicular to the sun's rays [1]. The research is actively developing all types of CSP technologies: parabolic trough, central receiver tower, linear Fresnel, Fresnel lenses, paraboloid dishes. Al these systems are currently used commercially, and each technology can be suitable for specific market segments.

In the last years new plants have been built and commissioned for the future and new markets, such as India, South Africa, Morocco, the UAE, Australia, Chile and China, are emerging.

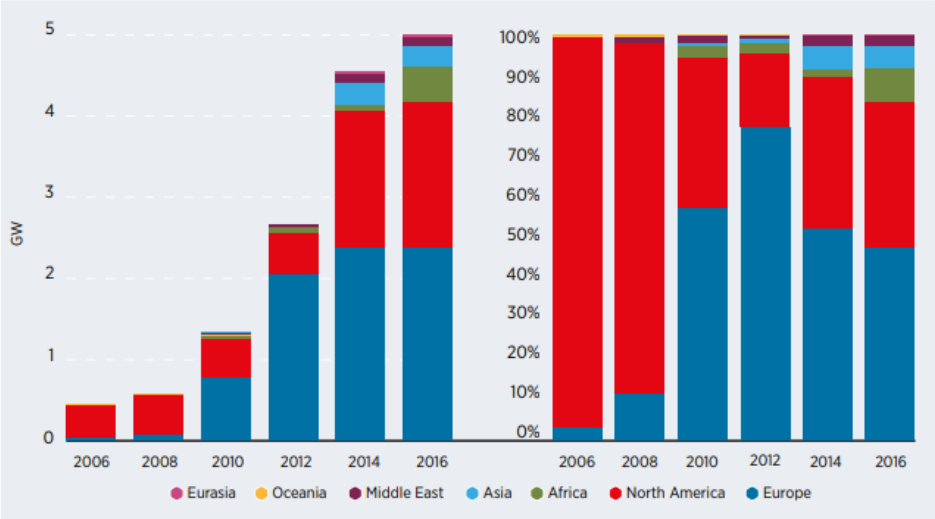

Figure 2 Development of the cumulative installed CSP capacity by region, 2006-2016. Source IRENA database [2].

Around 5 GW of cumulative installed capacity are present nowadays. Moreover, at the end of 2016, an estimated 4 GW of CSP projects were under construction or under development. This development was mainly driven by national policy support and incentives, cost reduction due to large scale production and technology improvements [2]. According to Markets&Markets [3] the CSP market was estimated at USD 4.02 Billion in 2015 and expected to grow at a compound annual cost rate (CAGR) of 10.3% from 2016 to 2021.

One of the most promising technologies is dish CSP. Dish CSP systems (Figure 3) are composed of a reflective paraboloidal surface. The paraboloid mirror reflects incident sunrays to a solar receiver, where the sunbeams are focused in a small region called the focal spot. The receiver is usually not so different from a heat exchanger and absorbs the irradiated energy, transferring it to the plant's working fluid. The working fluid then transfers its energy to a prime mover or engine. A sun tracking system is usually adopted to trail the sun in each direction and maximise the annual solar share.

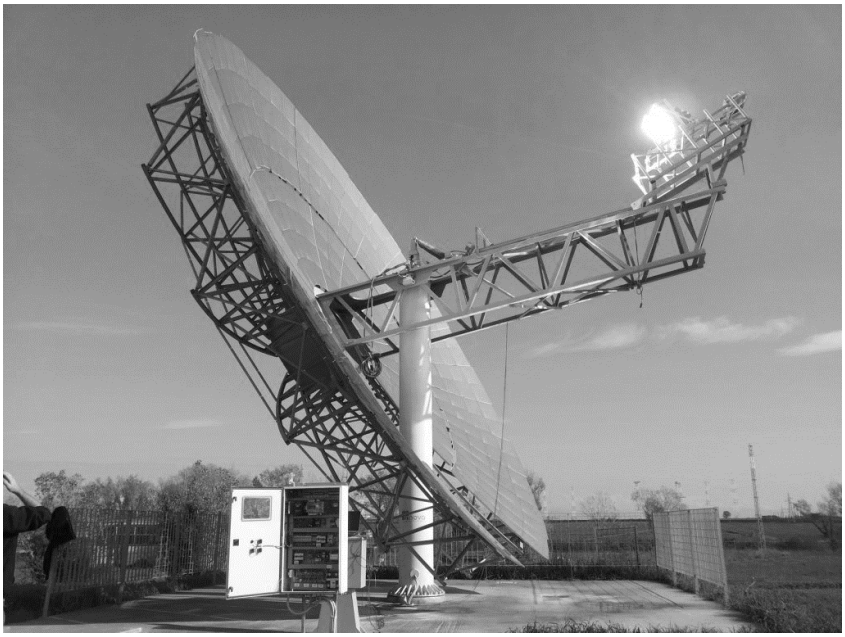

Figure 3. OMSoP project dish CSP system. Source: https://etn.global/

Solar dish can be stacked into larger plants in a similar fashion to photovoltaics (PV) or can be used as a stand-alone system for off-grid application. This characteristic, coupled with the possibility to produce combined heat and power (CHP), makes the system particularly suitable for isolated areas which lack connection to the national grid.

As shown by Figure 4, currently all around the world, over 1 billion people remain without access to electricity; most of them are in Africa, India and China, countries characterised by high level of direct solar irradiation. Fossil fuel generators (typically diesel-engines) and solar PV are the two technologies typically adopted for such application. Diesel engines are attractive for their capability to meet the power demand and their low capital cost. However, growing fuel costs, combined with the propensity for plants to be operated at part-load conditions, where efficiencies are low, results in high operations and maintenance (O&M) cost and levelised cost of energy (LCOE), typically 0.55 up to 3.33 USD/kWh for countries without highly subsidized oil supplies. Moreover, additional use of diesel power aggravates CO_2 and particulate emissions.

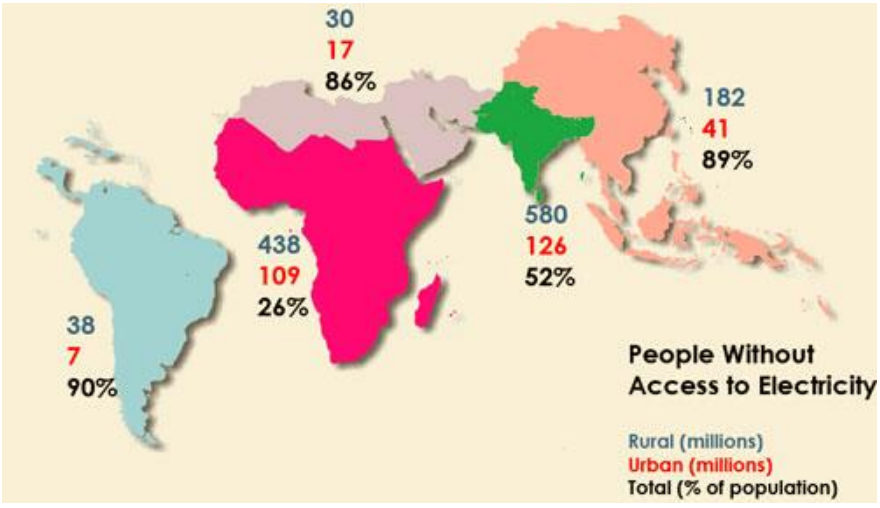

Figure 4. Energy access in developing countries. Source: World alliance for decentralised energy 2018.

PV panels on the other side, alleviate the pollution concerns and have negligible O&M costs but necessitate a considerable capital investment and are susceptible to solar fluctuation, which makes them not particularly reliable. To supply electricity 24/7 is then necessary to oversize the plant and incorporate storage systems, such as batteries, which cause a sharp increase of the capital cost [4].

Solar dish CSP systems seems to be an attractive alternative to these systems for isolated area power supply. The possibility to integrate a cost-effective thermal storage and the possibility to hybridise the system with a fuel back up makes the system particularly suitable for this application, combining all the advantages of PV and diesel engines. Nevertheless, the technology is still in an early stage of development and further progresses are needed to achieve a competitive cost of electricity as well as the technology readiness level required for commercialisation.

This system has been developed mainly using Stirling engines. The relatively high efficiency of the power cycle makes Stirling engines suitable for this application. A Stirling engine is a reciprocating, externally heated engine that works by cyclic compression and expansion of the working fluid, converting thermal energy in mechanical. Nevertheless, some technological issues make this arrangement expensive. For this application usually, the power cycle working fluid is either helium or hydrogen, due to their good heat-transfer characteristics. The design of the engine should then reduce leakage problems as the engine must operate at high pressure, from 5 to 20 MPa, to maximise the power output [5]. Another problem of these power plants is the relatively short lifetime, while to make the system economically feasible a life cycle of about 20 years is required. It is then necessary to consider the replacement of components to increase the lifetime of the system.

An alternative to Stirling engines for solar dish applications are micro gas turbines (MGTs). MGTs are usually characterised by a recuperated Brayton Joule cycle. A partial recovery of the exhaust heat is performed using a heat exchanger

called recuperator or regenerator and allows the net cycle efficiency to approach 30%. Figure 5 shows the main components of a MGT.

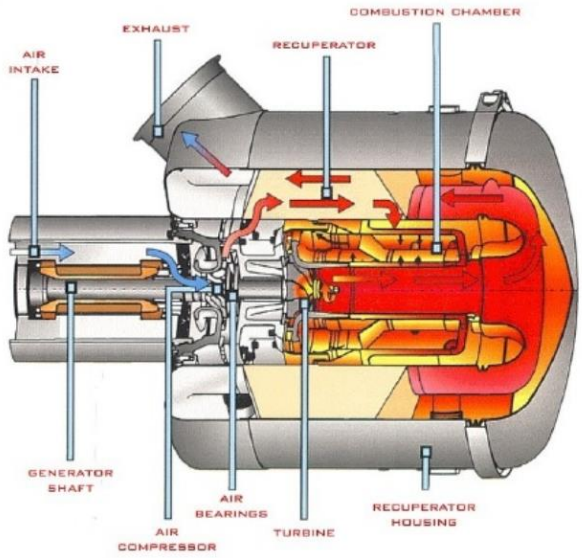

Figure 5: MGT's schematic. Source: CAPSTONE Turbine Corporation.

- *Compressor and turbine:* The heart of the micro turbine is the compressor-turbine package, which is commonly mounted on a single shaft. For applications with a power output lower than 50 kW, the system is usually characterised by a high rotational speed over 100 000 rpm.

- *Recuperator:* Usually is a compact heat exchanger, which can guarantee a heat recovery of the turbine's exhaust gasses, increasing the overall cycle efficiency.

- *Combustion Chamber / Solar Receiver:* For solar Application, usually the combustion chamber is substitute or integrated by a solar receiver, a heat transfer device that can capture the solar energy coming from the dish and transfer it to the cycle working fluid.

- *Generator & Power electronics:* The micro turbine produces electrical power through a high-speed generator usually characterised by permanent magnets arrangement. Given the high rotational speed, power electronics is required to convert the frequency of the generated power and synchronise it with the grid.

A significant complication with the utilisation of solar thermal power as a primary source of energy is the variable supply of solar flux. During the day, the DNI is characterised by a high frequency fluctuation caused mainly by the weather change and the earth rotation. Moreover, during the year the variation of the seasons causes a change in the incidence angle of the sunrays and then a low frequency fluctuation of DNI. Hybrid solar micro gas turbines (MGTs) has the potential to overcome this issue. Hybrid operation, where the solar energy is integrated with a fuel back-up, allows the system to meet the demand during day and night.

Another opportunity to increase the plant operations and its dispatchability is thermal storage. The receiver maximum operating temperature imposes a strict limit on the maximum amount of solar energy that can be transferred and may result in a high amount of wasted solar energy. Thermal storage systems can absorb the excess thermal power increasing the annual solar share of the plant. In 2016, the global thermal energy storage market was valued at USD 3.3 billion and it is predicted to grow to USD 6.2 billion a CAGR at 11% from 2017 to 2023 [6].

Current dish CSP systems do not include thermal storage, this is due to the technological issue that the storage system must be incorporated into the receiver. For this reason, there is a serious limitation to the dimensions which results in a short storage time. Nevertheless, nowadays thermal energy storage systems are necessary for the majority of new CSP plants to achieve a competitive LCOE and its integration could be a necessary step for dish system to achieve attractiveness.

1.1. Project Scope & Objectives

The main aim of this thesis is to study the technical and economic feasibility of incorporated hybridisation and thermal storage in a micro gas turbine dish CSP plant. This will include the development of a fundamental understanding on the

impact of the main cycle parameters onto the plant's performances and cost. The study will also aim to find the optimum plant arrangement considering different plant layouts, economic aspects, technical limitations and its environmental impact.

The final aim of this study is to quantify, through economic and performance parameters, the advantages and disadvantages of integrated thermal storage and/or hybridisation. Moreover, the study will identify possible strategies for performance improvements and cost reduction, distinguishing the influence and contribution of each component on the performances and cost of the pant. Particular attention will be paid to the plant dispatchment and the influence of integrated thermal storage or hybridisation. The goal is to individuate the most suitable control strategy in each operating condition.

1.2. Thesis Structure

Firstly, a techno-economic model suitable for plant optimisation will be presented. The model is based on one dimensional design and off-design performance analysis of each component of the plant. Each component's model was validated against experimental and integrated with a cost function based on the actual size and performance of each constituent of the plant.

Following, different plant layouts will be analysed and optimised to find a trade-off between cost and performances of the plant. Each chapter is dedicated to a single plant layout, the study will analyse pure solar system, hybrid system and integrated thermal storage system from the economic and thermodynamic point of view. This research will also consider technical limitations, emissions and the dispatchability of the plant. Techno-economic optimisations will be performed on each plant layout using machine learning and genetic algorithms.

2. Literature Review

Solar energy is the most abundant form of renewable energy available on earth. Till the last decades, the energy gathered from the sun was mainly converted in electrical power using photovoltaics plants (PV). CSP technology saw a first commercial expansion between 1984 and 1995, but then no further deployment was experienced until 2005. Nevertheless, in this gap period substantial research, progress and demonstration took place [1].

Concentrated solar power plants have been mainly developed in large scale, as supplement of traditional energy sources. Differently from PV, they can only collect the direct normal irradiation and cannot absorb the part of radiation that has been diffused by clouds, dust or other elements. This makes them particularly suitable to areas with a high fraction of clear sky days, in locations with low smog or dust.

The arrangements that are at this time used commercially are: parabolic trough, central receiver tower, linear Fresnel, Fresnel lenses (for CPV), paraboloid dishes.

2.1. Solar Resource

The solar resource usually quantified using two parameters: the direct normal irradiation and the global horizontal irradiation. Direct normal irradiation (DNI) is the main resource for any CSP system. DNI is usually defined in reference to a

tracking area oriented normal towards the sun [1]. Differently, the global horizontal irradiance (GHI) includes both the direct and the diffuse radiation.

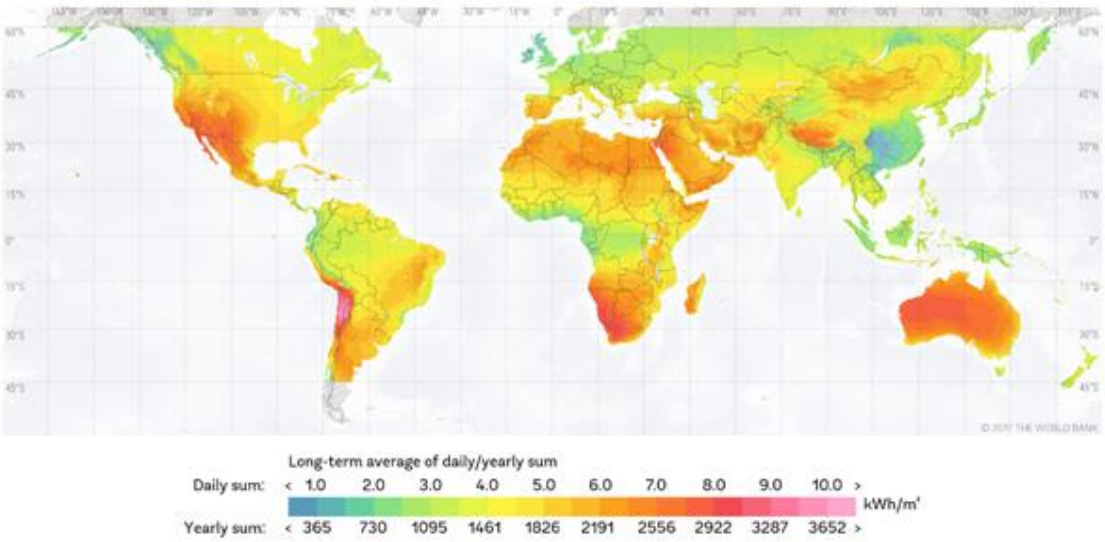

Figure 6. Distribution of the direct normal irradiation across the globe. © 2017 The World Bank, Solar resource data: Solargis.

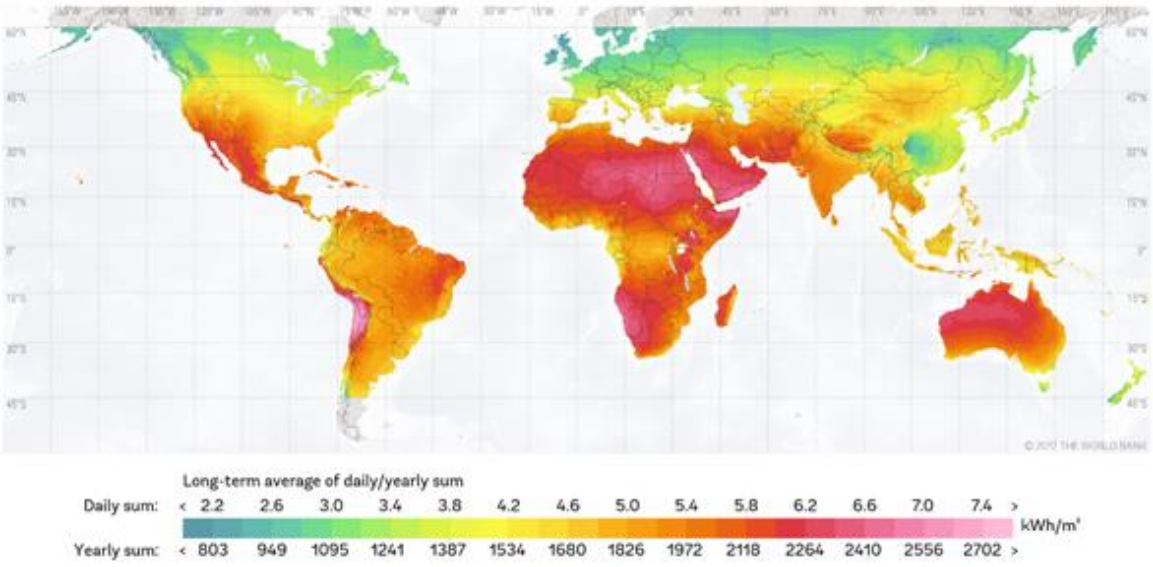

Figure 7. Distribution of the global horizontal irradiation across the globe. © 2017 The World Bank, Solar resource data: Solargis.

Differently from CSP systems, photovoltaic can collect a considerable amount of diffuse irradiance. As consequence of that, GHI is usually the main performance parameter related to the assessment of a PV power plant, while DNI is used for

evaluation of energy yields from CSP and CPV (concentrating PV) plants. As shown by Figure 6 and Figure 7, the distribution across the globe of the direct normal irradiance is less homogeneous compared to GHI, which can guarantee a relatively high irradiance even at high latitudes

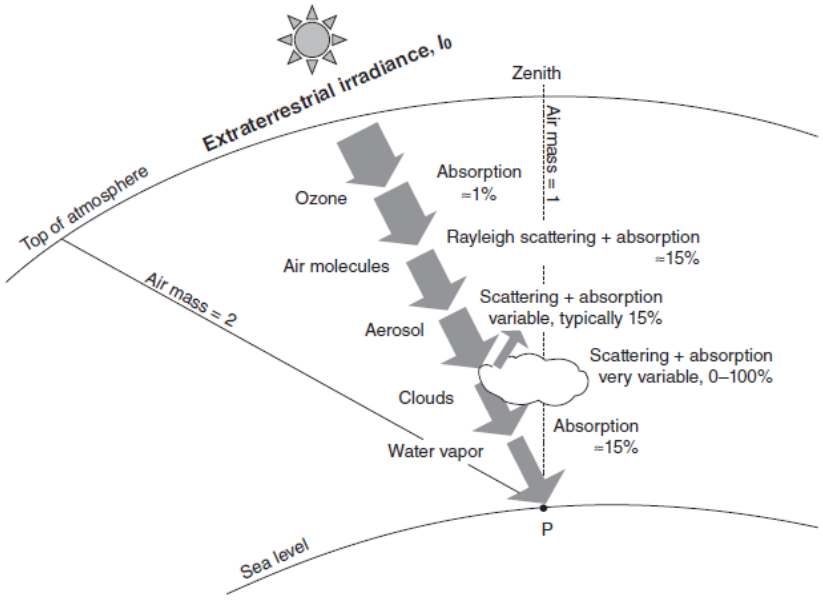

Figure 8. Solar radiation absorbed through the atmosphere. Source: [1].

The extra-terrestrial solar irradiance varies as a result of fluctuations in energy released by the sun and variable distance from the Earth along the year. ISO standards [7] defines the solar constant I_0 as the solar irradiance in the upper atmosphere on a plane normal to the direction of the radiation. This is calculated when the Earth is at its mean distance from the sun (*149,597,871 km*). Its measured average value in the current period is *1366* W/m^2 $\pm$ *0.6* W/m^2 [7]. As shown by Figure 8, across the atmosphere the sun radiation is reduced significantly. The radiation not absorbed or scattered by the atmosphere is the direct normal irradiance (DNI). The diffuse irradiance DHI is the scattered irradiance that reaches the ground and might occur by numerous phenomena. The overall global horizontal irradiance can be consequently defined by equation (1).

$$GHI = DHI + DNI/\cos\,\theta \quad [W/m^2] \tag{1}$$

Where θ is the Zenith angle.

Figure 6a, shows typical average values of the DNI along the day. The sun irradiance is affected by the earth rotation and the DNI results in a bell-shaped function (blue line). Moreover, cloud passages as well as other environmental aspects may reduce significantly the amount of direct radiation causing significant fluctuation in the short period (red line). This is for demonstration purpose only and do necessarily represents an existed DNI variation in any location.

Fluctuation on the long period are instead caused by earth revolution. An example of the hourly average frequencies of DNI, in Rome between 2004 and 2005, is reported in Figure 6b.

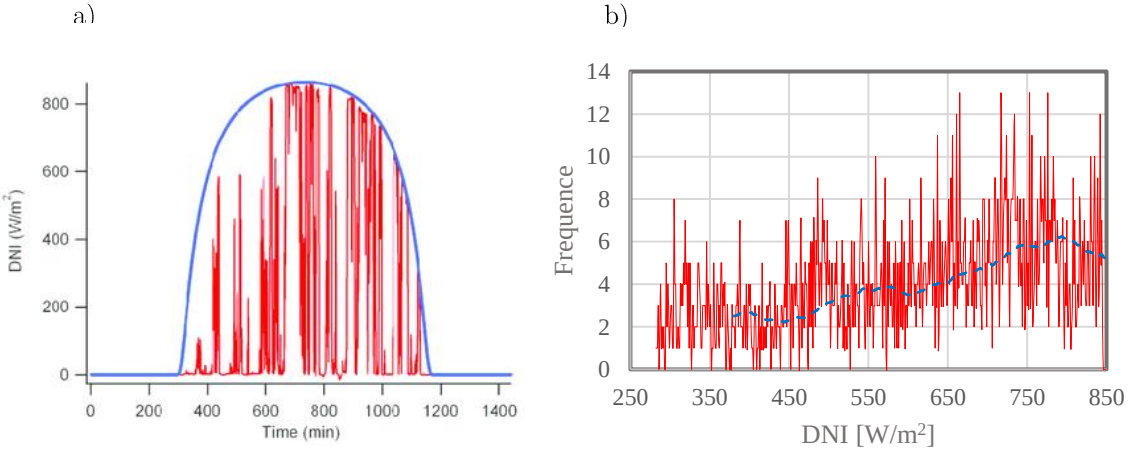

Figure 9. Left: Example of daily variation of DNI. Source [8] Right: Example of annual variation of DNI frequencies. Source: Heloclim, © 2014-2018 MINES ParisTech / Transvalor

2.2. CSP dish

Among all concentrated solar power plants, the least developed but still one of the most promising technology is parabolic dish. Solar dish indeed offers the highest

possible conversion efficiency as they can potentially perfectly track the sun in every position avoiding the cosine effect discussed in the previous section.

As shown by Figure 10 dish CSP systems consist of a (1) parabolic concentrator, which redirect the solar radiation into the solar power conversion unit (2), which consist of a solar receiver and the engine. The engine converts the thermal energy into electricity and usually is integrated with power electronics which is located within the system control unit (3). The system control unit can adjust also the elevation (4) and azimuth (5) tracking systems.

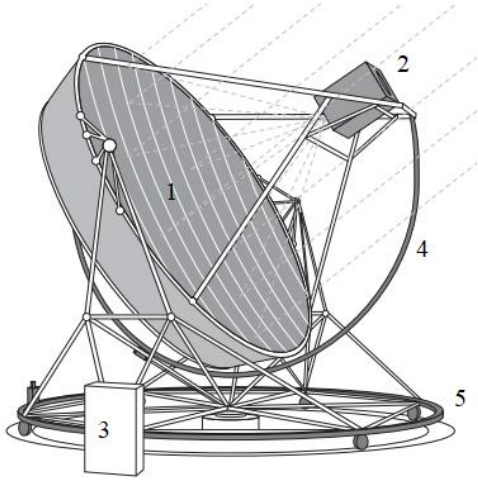

Figure 10. Schematic of solar dish system. Source: [1].

2.2.1. Dish Stirling systems

This system has been mainly developed using Stirling engines. The relatively high efficiency of the power cycle makes the engine particularly appropriate for this application. Nevertheless, some technical matters make this arrangement expensive. One of the biggest concerns related to this equipment is the power cycle working fluid, which for this use are mainly helium or hydrogen, due to their good heat-transfer characteristics [9]. The design of the engine ought to reduce leakages as the engine must operate at high pressure, from 5 to 20 MPa, to maximise the power output. Another problematic of these plants is the fairly short lifetime, while to make

the system competitive in the market a life cycle of approximately 20 years is required [10].

The earliest prototype for commercial purposes adopting Stirling engine was built in the early 1980s. The 25 kW Vanguard system (Figure 11), developed by ADVANCO in Southern California, achieved a maximum solar-to-electric conversion efficiency of 29.4%. The working fluid of the system was hydrogen at a maximum pressure of 20 MPa, the maximum temperature of the cycle was around 700 °C [10].

Figure 11. Vanguard system by ADVANCO. Source: [1].

Figure 12. Membrane dish built in Riyadh, Saudi Arabia. Source: [1]

This successfully prototype was followed by many attempts to develop this technology. In *1984*, two *50 kW* dish Stirling systems were constructed in Riyadh, Saudi Arabia. The dishes were characterised by a dish diameter of *17 m* and was composed by a stretched membrane, shaped by creating a vacuum in the space formed by the dish frame [11]. In the same year McDonnell Douglas Corp. (MDAC),

developed a *25 kW* dish/Stirling system. The dish was composed by curved glass mirror facets of about *10.5 m* diameter and is integrated with United Stirling 4-95 Mark II engine, the same adopted by the Vanguard system and consequently characterised by the same operating conditions: the working gas is hydrogen at a maximum mean working pressure of *20 MPa* and *720 °C*. The plant boosts an efficiency of *29%* to *30%* [1].

The development of the technology in the *80s* has boost the interests of the scientific community and new technologies were made available for the system. In 1991, two innovative Stirling/Dish plant was built by Cummins Power Generation. A *7-kW* system for remote applications and a *25 kW* system for grid-connected power generation (Figure 13). These two systems incorporated advanced technologies into the designs, such as a solar concentrator with a polar-axis drive and polymer, stretched-membrane facets, heat-pipe receivers, and free-piston Stirling engines. Moreover the system adopted a heat-pipe receiver using evaporating sodium as heat carrier fluid.

Figure 13. Cummins Power Generation concentrator. Source: [1].

The development of dish/Stirling system continued also in the 21st century, thanks also to the renewed interest of the scientific community in renewables. Infinia Corporation developed a free-piston, characterised by low-cost, long-life and maintenance free. The company designed together with Schlaich- Bergermann und

Partner in 2006 a *3.2 kW* dish/Stirling power plant. The concentrator is approximately 5 m diameter, the engine working fluid is helium and the entire plant boosts a maximum net solar to electric efficiency of *24%* [12]. In 2009 Australian National University (ANU) in collaboration with Wizard Power and AusIndustry Renewable Energy Development Initiative (REDI) developed the ANU SG4 (Figure 14). The rated net electrical output of the production system is *50 kW*. The dish is characterised by a *25 m* diameter and is integrated with a steam engine. The working gas is air at a maximum mean working pressure of *5 Mbar* and *550°C*.

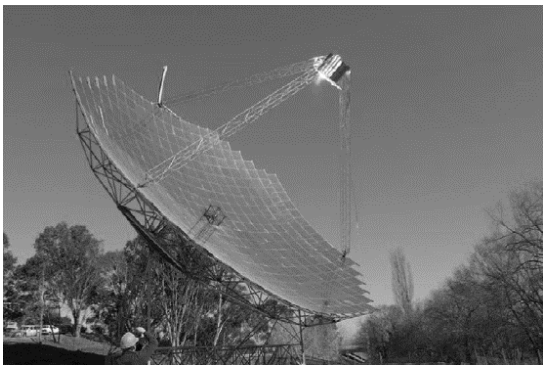

Figure 14. ANU SG4 dish. Source: [13].

Stand-alone systems where the receiver is fixed in the focal point of the dish it's not the only arrangement available for these CSP plants. The use of dishes to provide heat to a central generating plant has also been demonstrated. The first plant with dish array arrangement is a *4.9* MW_{el} system built in California in 1984. As shown in Figure 15, it consisted of 700 stretched-membrane facet mirror dishes. The total accumulating surface was *30'590* m^2. Six hundred of the dishes produced saturated steam at approximately *6 MPa* and the remaining 100 dishes were used to further superheat it to *460 °C [1].*

A more recent attempt is the Maricopa Solar Project, located in Peoria (Arizona, US), inaugurated on January 2010. The plant integrates 60 SunCatcher dishes characterised by *25 KW* power output, *12.5 m* diameter parabolic dish with precision

mirrors that automatically tracks the sun and Stirling engines. The overall power output of the plant is *1.5 MWe*, the Solar-to-Electricity Efficiency (Gross) is *26%* [14].

Figure 15. La Jet plant, California. Source: [1].

Figure 16. Maricopa Solar Project, Arizona. Source: Tessera Solar.

2.2.2. Solar Dish Micro Gas Turbine

A valid alternative to Stirling engines as prime mover are micro gas turbines. Nevertheless, the implementation of a micro gas turbine (MGT) is a substantial innovation in the field of dish technology.

The project OMSoP, started in 2013 and concluded on September 2017, built and demonstrate technical solutions for the use of state-of-the-art concentrated solar power system coupled with a micro-gas turbines to produce electricity. The intended

system is modular and capable of producing electricity in the range of *3 -10 kW*. The system was assembled and tested by ENEA in Casaccia, near Rome.

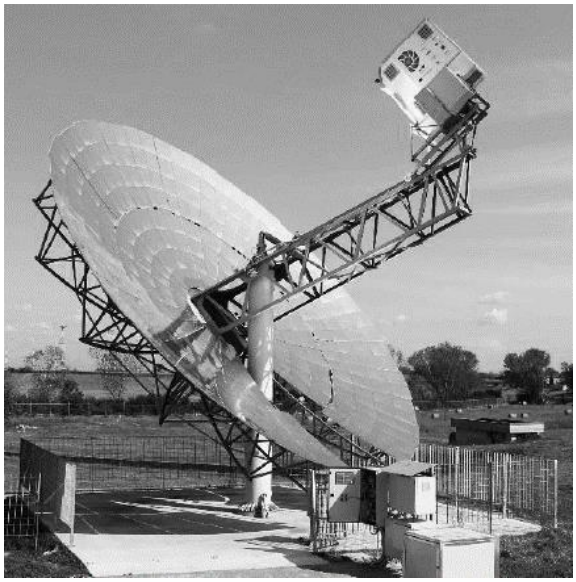

Figure 17. OMSoP solar dish at Casaccia, Rome.

The solGATS project started in 2016, co-founded by Innovate UK and the ministry of science and technology in China. The project aims to develop a dish CSP system for electricity generation powered by a micro gas turbine. The system also aims to advance current technology about solar dish micro gas turbines and integrate it with a thermal storage technology to make it available with minimum needs for backup power. The system was conceptualised to be deployed in standalone mode for off-grid use or stacked in a flexible manner for medium power plants.

2.3. Solar Dish Power Cycles & equipment

2.3.1. Power Cycles and Engines

The thermal energy delivered by the sun can be converted into mechanical power using a central engine. So far, solar dish systems have been powered mainly by

Stirling engines. A Stirling engine for solar application is a machine that works by cyclic compression and expansion of either helium or hydrogen converting the heat to mechanical power. The engine is characterised by a closed thermodynamic cycle.

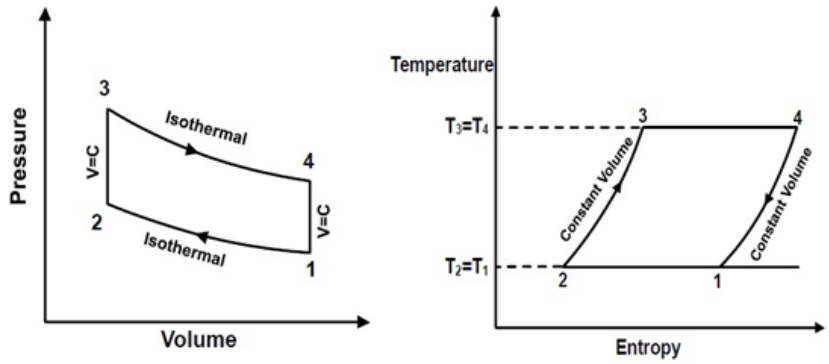

Figure 18. Stirling Cycle power cycle.

As shown by Figure 18 the ideal process is based on a combination of isothermal compression of the cold fluid (1-2), an isochoric heating (2-3), an isothermal expansion (3-4) and finally an isochoric cooling (4-5).

The expanding working gas drives the piston out of the cylinder extracting useful work. When the piston initiates to close, the hot working gas is enforced to pass into the regenerator and consequently to be transferred into the cold section of the engine. In this section the heat is transferred with an isochoric transformation from the working gas to the regenerator. The working gas is subsequently compressed isothermally and transmits exhaust heat to the cold space [1].

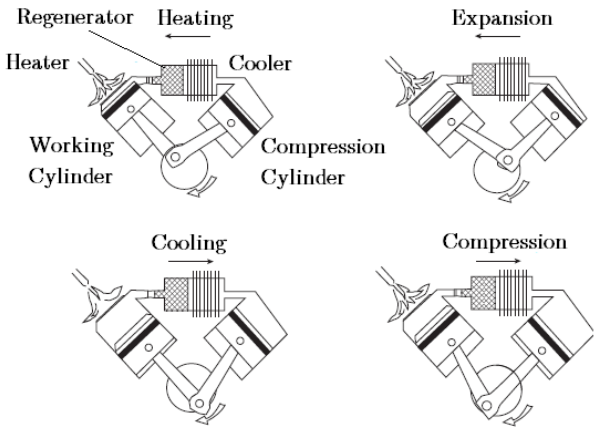

Figure 19. Working principle of Stirling engine. Source: [1]

The mechanical design of the system can include either a single or double-acting cylinder. The main components of a double acting cylinder arrangement include the working and the compressing cylinder, a regenerator and a cooler.

Stirling engines can also be categorized into kinematic and free piston Stirling engines. Kinematic Stirling engines accomplish power transmission adopting a crankshaft mechanism, where the generator is coupled. Free piston Stirling engines lack mechanical connection between the working piston and the displacement device and both pistons move freely. Mechanical inter-linkage is replaced by an interior spring damping system.

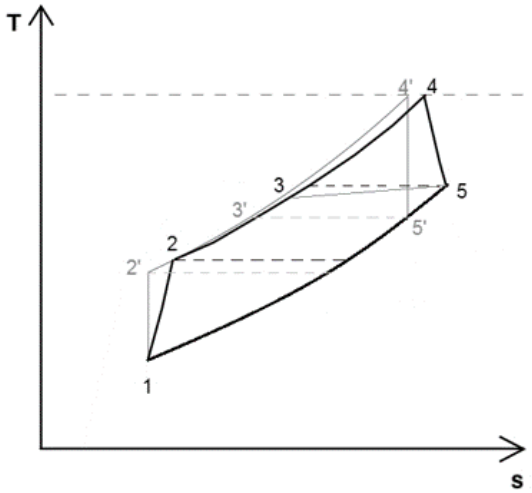

Figure 20. T-s chart of a Brayton-Joule cycle.

An alternative to Stirling cycle is the Brayton-Joule cycle. For solar dish application, small machines are required and relatively low pressure ratios are used. Therefore, it is possible to adopt a recuperative cycle to improve the efficiency by part recovery of the exhaust heat using a recuperator. Figure 20 shows the main thermodynamic transformations characterising a recuperative Brayton-Joule Cycle. The ideal cycle is composed by an isentropic compression (1-2') an isobaric heat recovery (2'-3') and heating (3'-4') and finally an isentropic expansion (4'-5').

The thermodynamic transformations are subject to irreversibility and the constituents are characterised by losses which implies a deviation from the ideal performance of the plant. Moreover, the recuperator is not capable of a full recovery of the exhaust heat and hence characterised by an effectiveness around 85-90 % [15].

Brayton-Joule cycle for dish CSP application is achieved adopting a micro gas turbine (MGT). An MGT is composed mainly by a compressor, a recuperator, a turbine and a high-speed generator.

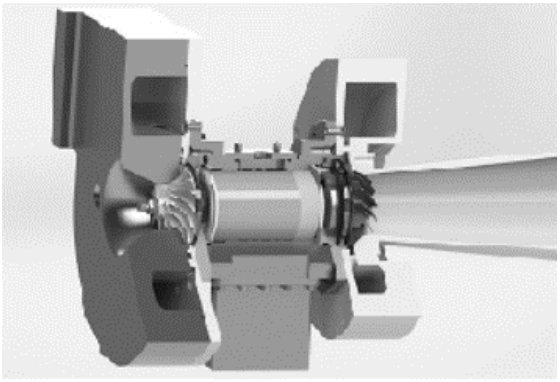

Figure 21. Micro gas turbine breakthrough (Without recuperator). Source: OMSoP.eu

Centrifugal compressors: for MGT application the compressor is a radial machine composed by an impeller, a diffuser, either vaned or vaneless and a volute.

Recuperator: A micro gas turbine is by definition a compact machine. Moreover, for solar dish application, the engine is in the front side of the dish. Consequently, the weight and volume of the MGT must be preserved as low as possible. Compact

heat exchangers are then usually adopted as recuperator. The recuperator is the most expensive component of the MGT and an accurate selection of arrangement and materials is required to achieve a low cost of the device. On the other hand, the heat exchanger must be able to withstand the high temperature of the air and a trade-off between cost and maximum temperature must be found.

Radial turbine: are normally adopted as expanders. They are mainly composed of the impeller, nozzle vanes and the volute [15]. More details about the plant components will be discussed in the next chapter.

2.3.2. Solar Receiver

A solar receiver is a device that can absorb the solar energy and reallocate it to the working fluid. In a Stirling engine, two layouts are mainly adopted. In the first arrangement (Figure 22, a), the directly illuminated tube receiver, adopt small tubes located in the concentrated solar flux. The working fluid, passing through the pipes, is directly heated. The second arrangement (Figure 22, b) adopts a liquid metal, usually sodium, as intermediate heat transfer fluid. The liquid metal is vaporized on the absorber area and condenses on tubes heating the engine's working fluid (Figure 22, b). This second type of receivers are called a heat pipe receiver [1].

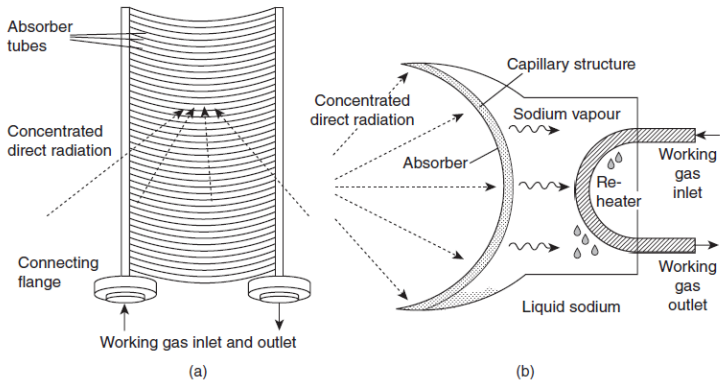

Figure 22. Stirling Engines solar receivers: (a) DIR, (b) Heat pipes receiver. Source: [1]

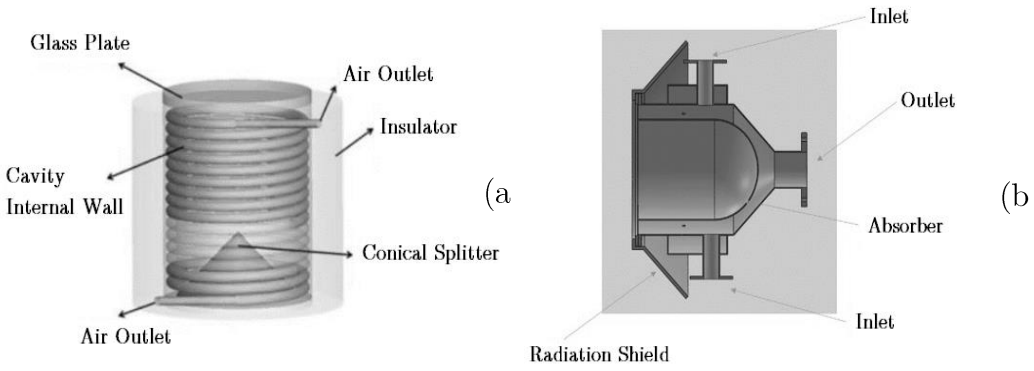

Figure 23. Air Cavity solar receiver: (a) Air Tubes, (b) Volumetric. Source: [15].

For MGT application different layouts can be conceptualized. One arrangement is the Air tube cavity receiver. As shown by Figure 23 (a), an air tube cavity receiver is mainly composed from a cylindrical cavity cover by an insulator to minimise heat losses. At the end of the cavity an optical splitter can be present to redirect incident radiation and in the upper part of the cavity, a quartz glass can be placed to minimise convection losses between the device and the ambient. Nevertheless, this arrangement suffers from non-negligible thermal stresses. The design of the system, the collocation of the pipes and the material selection, should then take into account this aspect.

A valid alternative was already tested by KTH as part of the OMSoP project is the volumetric cavity receiver. In this arrangement, preheated air enters the receiver at the side, is distributed around the circumference of the cavity in an inflow mixing box and then redirected to the outlet [16].

2.4. Hybridisation

Many CSP plants use fuel as a source of backup energy whenever the sun is absent or not enough to guarantee a valid power output. Hybridisation has the potential to increase CSP plants dispatchability obviating the problem of sun

intermittency. Moreover, the higher plant availability will sensibly increase the operating hours and consequently the reliably of the plant in rural areas, where the power output is needed independently from the climatic conditions and during the night. Nevertheless, hybrid dish Stirling concentrating solar power plants are not yet available in the market and few demo plants have been demonstrated.

From 2016 RIPASSO energy is developing a hybrid Stirling-dish system. The system consists of a solar-tracking parabolic mirror dish coupled with a 33 kW Stirling engine. Using a unique hybrid adaption, the heat from the sun is combined with another fuel-based source of heat. Combustion takes place outside the engine with consequent benefits on the life length of pistons, bearings and sealing [17].

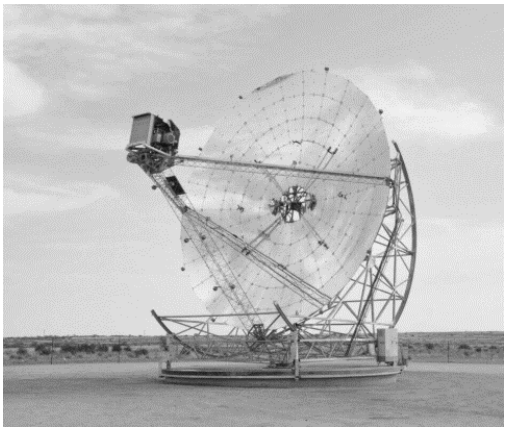

Figure 24. Hybrid dish Stirling system developed by RIPASSO. Source: [17].

Moreno et al. [18] presented tests of a hybrid heat pipe receiver for dish/Stirling application. The receiver has been ground tested (gas only) at different power levels from 18 to $75\ kWt$ and output temperatures up to $750\ ^{\circ}C$. Differently from the RIPSASSO concept, as shown in Figure 25 the combustion takes place inside the engine with consequent benefits for the heat transfer but resulting in a reduced life expectancy of the receiver. Moreover, test conducted by the authors highlights reduced efficiency of the receiver during hybrid operation and observed that at the maximum firing rate the thermal efficiency is of about 68%.

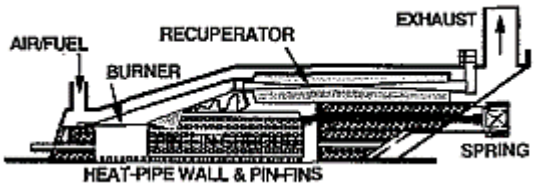

Figure 25. Breakthrough of the Heat pipe hybrid receiver and Stirling engine conceptualised by Moreno. Source: [18].

Another prototype of hybrid heat pipe receiver has been developed by DLR (Figure 26). The system was tested for a total of about *265 h* on the Plataforma Solar power plant, 92 of which were gas-only mode, *117 h* solar-only mode and *56 h* hybrid mode. In gas-only mode maximum power output was *4.1 kW*. System efficiency of *17.7 %* has been achieved adopting a working fluid maximum temperature of *640 °C* and *16.6 %* with a temperature of *600 °C*. In pure solar mode maximum power production was *7.8 kW*, maximum efficiency *16%*. During hybrid operations the highest efficiencies lie between *15* and *16%* [19].

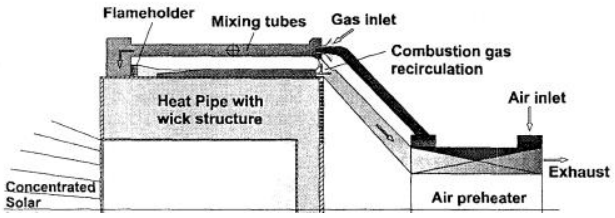

Figure 26. Hybrid heat pipe receiver developed by DLR. Source: [21].

Micro gas turbines seem to be a more attractive option for hybrid operation. The inherent design of the system to incorporate a combustion chamber can easily overcome the technological issue demonstrated by hybrid Stirling systems. So far, no hybrid MGT demo plant has been developed for solar dish application.

Different arrangements are available for MGT's combustors. Tuccillo et al. [20] give a comprehensive view on micro gas turbines combustors, presenting design approaches and the dissimilar geometries. In addition, they also present a numerical study of three classes of combustors (diffusion annular, lean pre-mixed and Rich

Burn-Quick Quench-Lean burn), where the flame stabilization was reached using a swirler.

2.5. Thermal Storage

Another opportunity to extend the capacity of the plant is thermal storage. Thermal energy storage (TES) systems can absorb part of the thermal power coming from the sun to be used during solar fluctuation or low sun irradiance periods. This characteristic gives a significant advantage to concentrated solar power plants over most other renewables systems, ensuring a constant power output and then an easier integration into the grid [15].

There are mainly three types of TES: Sensible heat storage, latent heat storage and thermos-chemical energy storage. In the sensible energy storage systems the stored energy depends on the temperature difference and the thermal energy is stored through sensible heat (2).

$$\Delta Q = m \int_{T_1}^{T_2} C\ T\ dT\ . \qquad (2)$$

Where m is the mass of the storage material and $C(T)$ its specific heat.

Solid and liquid materials have been widely used as storage media, common adopted materials include: water, concrete, iron, rocks and bricks. The most promising storage media for CSP application are molten salts, a mixture of salts with a relatively low freezing temperature (≅220 °C). Molten salts are good candidates because of their high heat capacity, density, thermal stability and low cost. Nonetheless, complexity and cost of CSP systems with integrated molten salts TES increase because of the need of external heating system to prevent salts solidification

during low solar activity periods. Furthermore, the higher is the operating temperature the higher are concerns about stability and corrosion.

Latent heat storage systems are the second type of TES system. These systems are based on the heat absorbed and release during the phase change of the storage media. The biggest benefit of storage concepts adopting phase change material (PCM) is the option to store energy within a narrow temperature range close to the phase change temperature [13].

The third TES system is the thermochemical energy storage. These systems use the energy stored in the enthalpy change of a reversible chemical reaction, is characterised by high energy density compared to the other storage systems with consequent benefits on the compactness. During the charging phase, energy is provided to a chemical compound favouring an endothermic reaction. During the discharge process, the reaction products are recombined exothermically producing heat [15].

Current commercial dish CSP systems do not include thermal storage, this is due to the technological issue that the storage system must be incorporated into the receiver to reduce thermal energy losses in transmission pipes and hence innovative arrangements are required.

Sandia National Laboratories (SNL) worked with the National Renewable Energy Laboratory (NREL) and the University of Connecticut, under the National Laboratory R&D competitive funding opportunity, to demonstrate key thermal energy storage (TES) system components for dish Stirling power generation. In this concept, storage and engine are mounted on the rear of the dish rather than at the focus in order to reduce the cantilever weight of the dish. The storage media is a PCM, for high-density isothermal storage. The proposed approach aims to improve the operability and dispachability of an existing high-temperature dish Stirling [23].

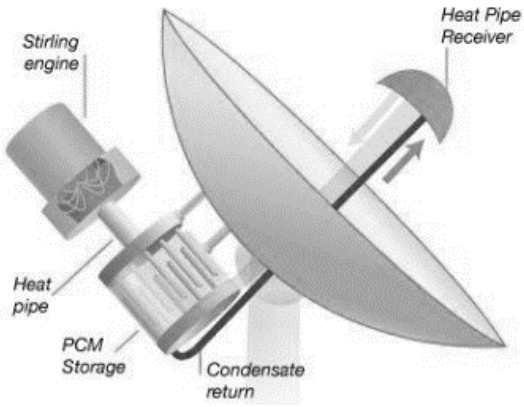

Figure 27. SNL Dish-Stirling with integrated thermal storage.

Australian national university developed and demonstrate a solar driven closed-loop thermochemical energy storage system using ammonia. The demo system has shown that ammonia dissociation is suitable for solar application. The ammonia synthesis heat recovery reactors are capable of stable, predictable operation with heat recovery at temperatures suitable for high-quality superheated steam production [25]. The study conducted by ANU demonstrate that, considering a 30 MPa case study, an exegetic efficiency of the heat recovery process is possible at design condition, with an overall solar to electricity conversion efficiency of about 20% [26].

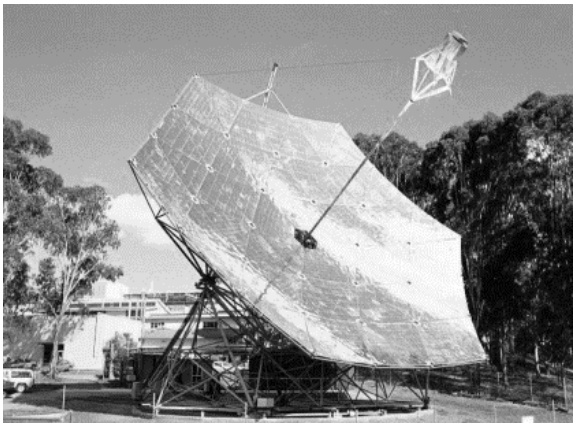

Figure 28. ANU ammonia synthesis system. Source: [25].

2.6. Modelling Solar Dish MGT Power Plant

CSP systems are generally designed and analysed based on the nominal design point. However, given the intermittence of the solar radiation, they operate for most of the time in off-design conditions. Modelling plant's components is then a key aspect for an accurate thermo-economic assessment of the plant.

Mazzoni et al. [28] developed a simulation tool for a pure solar dish – micro gas turbine applications. The set-up of the CSP plant simulator is built on a modular arrangement at components level as presented by Cerri [30]. A library of suitable component models for the plant was realised. The simulator has been adopted to perform steady state simulations for predicting the performance under variable direct normal irradiation.

The biggest advantage of the modular approach is the prospect to generate any possible plant layout and integrate new components. This characteristic creates the possibility to include the desired number of compression and expansion stages and the option to integrate any number of heat exchangers for intercooled recuperative cycles. Moreover, modularity of the tool permits an easy integration of new components such as combustion chamber for hybrid operations and reheating cycles or thermal storage units. On the other hand, for optimisation purposes it's important to evaluate different plant designs considering dissimilar main cycle design parameters. To evaluate the correct size of the plant is then necessary to design and evaluate off-design performances of a wide range of possible components assembly solutions. In this situation new components must be designed. In most of the commercial software available on the market for power plant analysis, the user is often provided with a library of components to choose from, resulting in a less or limited flexibility, lower applicability in terms of components selection and poor adaptability to optimisation processes.

Gavagnin et al. [30] presented a paper aimed to find the optimum design and performance of solar micro-turbine powered by dish collectors using an innovative methodology which integrates the design and off-design models of the system, tailored over existing components of the project OMSoP. The design model was run for two different sets of turbine inlet temperatures and recuperator effectiveness (TIT and ε_{rec}): 800 °C- 85% and 900 °C-90%. Different systems were designed for each case, yielding different off-design performance maps that link the net power output of the system to the boundary conditions of the site (ambient temperature and DNI).

Ghavami [31] developed a computational model for pure solar dish-MGT systems. The model combines the cycle analysis of the MGT with component models to perform design point performance simulation, generate component performance maps and perform off-design performance evaluation. The computational model has been coupled with an up to date economic model which was specifically developed through the OMSoP project for dish-MGT systems. The integrated model was coupled to an optimisation tool to find system designs which lead to optimal thermo-economic performance for a 5kWe system. Then the optimisation was extended over the rated power of 5-30kWe to find the power rating which results in the minimum cost of generated electricity by the dish-MGT systems. To generate new performance maps of the components the model adopted the scaling techniques.

2.7. Thermo-economic Assessment of a Solar dish MGT Power Plant

The approach to dish technologies has been mostly technical in the past. More recently, Semprini et al. [22] presented a thermodynamic valuation of a dish-MGT solar power plant with fossil fuel backup. The study concluded that there are

economic and thermodynamic advantages to use the dish-MGT system with integrated hybridisation, although this should be limited to sun hours. Extended operation on fuel only is not recommended as it rises the operational cost and the carbon footprint.

In a further study the authors performed a comprehensive cost analysis covering manufacturing, transportation and installation for a dish and MGT solar power generator, considering pure solar and hybrid operations. The study demonstrates that for the pure solar system the average system purchase equipment cost, considering a production volume of *1000 units/y,* results in 3262 €/kWel for the solar-only configuration and 3302 €/kWel for the hybrid version. Regarding the dependence on MGT size, the minimum specific cost seems to be obtained for an air mass flow rate in the order of 200 g/s even if further, more refined optimisation is still needed to find the true optimal combination of size, technical specifications, layouts and configuration [27]. Ghavami [31] also performed a thermo-economic optimisation of a pure solar MGT. The study highlights minimum levelised cost of energy around 17 c€/kW_h at rated power in the range 20 to 25 kW.

The resulting cost of electricity is not yet competitive with other means of power generation, including other renewable energy technologies such as solar photovoltaic, CSP and wind. As shown in Figure 1, according to IRENA [2] cost of energy of PV is in the range between 5 and *10* $c€/kW_h$, while CSP plants such as central receiver or parabolic through are estimated to be around *10-15* $c€/kW_h$. Higher competitiveness can be achieved with small scale power plant such as Stirling dish systems. Abbas [95] in his paper presents performance analyses for solar Dish Stirling system to electrify rural houses in Algeria. The study estimates LCOE of stand-alone system in the range *15-22* $c€/kW_h$. Affandi [96] studied the feasibility of a 25 kW Stirling dish power plant in Malaysia and estimated a LCOE in a range of 17-38 $c€/kW_h$.

2.8. Conclusions

In this chapter a detailed literature review about CSP dish technology was performed. The chapter highlights that the technology, despite years of development it's still in an early stage and needs further technological progress in order to achieve competitiveness and to be ready for a global scale commercialisation. This is especially true for MGT dish, which development it's still at demonstration level.

The chapter also point out that hybridisation and thermal storage could be the key for a bright future of this technology, increasing the plant dispatchability and reliability. Despite few studies have been performed about thermo-economic analysis and optimisation of the plant, in general, the following gaps are identified in the cited previous works in the topic:

- Low aptitude for optimisation. Most of existing tools and studies are based on existing plants, resulting in reduced capability of the tool to design and evaluate accurately off-design performance of the components.
- Scarce flexibility. Most of existing tools do not allow the possibility to integrate new components and consequently compare dissimilar layouts.
- Few thermo-economic assessments concerning solar dish MGT with integrated hybridisation and no study about integrated thermal storage.
- Lack of thermo-economic optimisations, which considers technical limits, economic aspects and environmental impacts

The aim of this thesis is to investigate the technical and economic feasibility of a stand-alone CSP dish power plant with integrated hybridisation and/or thermal energy storage, seeking to identify for the most performant and economically feasible plant arrangement. The present study will compare different plant layout options and control strategies to find the arrangement that maximises the annual electricity

production, the dispatchability of the plant and the power output, while minimising the levelised cost of energy (LCOE) and emissions.

The specific objectives of this research are:

- To study the technical and economic feasibility of incorporated hybridisation and thermal storage in a micro gas turbine dish CSP plant.
- To develop a fundamental understanding on the impact of the main cycle parameters onto the plant's performances and cost.
- To find optimal plant arrangements taking into consideration economic aspects, technical limitation and environmental impact. Comparing different control strategies, dissimilar plant layout and location and to explore possible technological improvements.

3. Plant Modelling

This chapter presents the methodology adopted in this study to evaluate the performance of the plant under variable DNI. A model for each component of the plant has been developed using a modular approach. As shown by Figure 29, the plant for pure solar operations is composed by: compressor, recuperator, receiver and turbine. The fluid coming inside the compressor is pressurised then is heated firstly inside the recuperator, where a partial recovery of the exhaust occurs, then in the solar receiver where the energy coming from the solar irradiation is transferred to the working fluid. Finally, the fluid is expanded in the turbine to obtain mechanical power, which is converted into electrical power by the high-speed generator and power electronics.

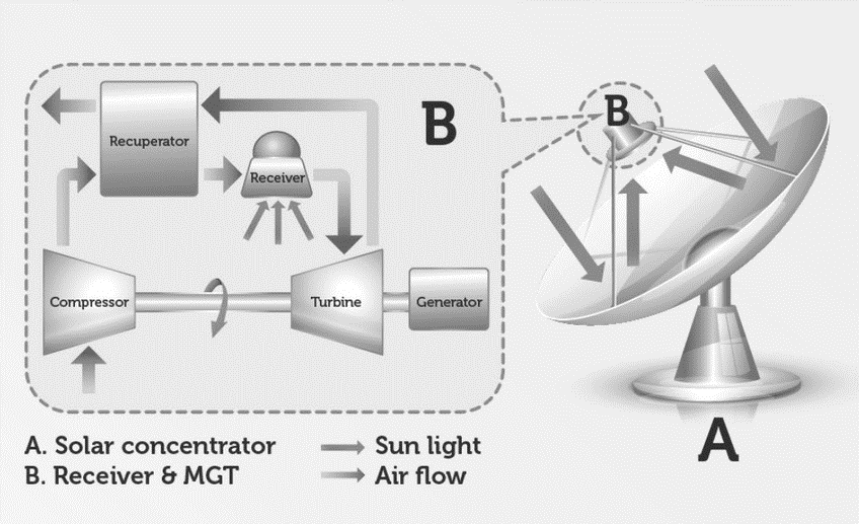

Figure 29. Pure solar system plant scheme. Source: https://omsop.serverdata.net.

In this chapter a model for a pure solar dish-MGT power plant is presented. Further models about supplementary components such as combustion chamber and thermal storage will be presented in Chapter 3 and 4.

3.1. Software Logic

The flowchart of the model is shown in Figure 30 where the generic j-th module, represented by blue boxes, is characterised by two functions (yellow boxes). The first is the 'design function' which calculates the design performance and the geometrical parameters of each component based on the desired set of design input variables. The second is the 'off-design function' which evaluates the performance of the plant at off-design conditions based on the geometrical characteristics, the required set of input variables at off-design conditions (red circles) and the operational strategy. The model has been programmed using the object-oriented language C++.

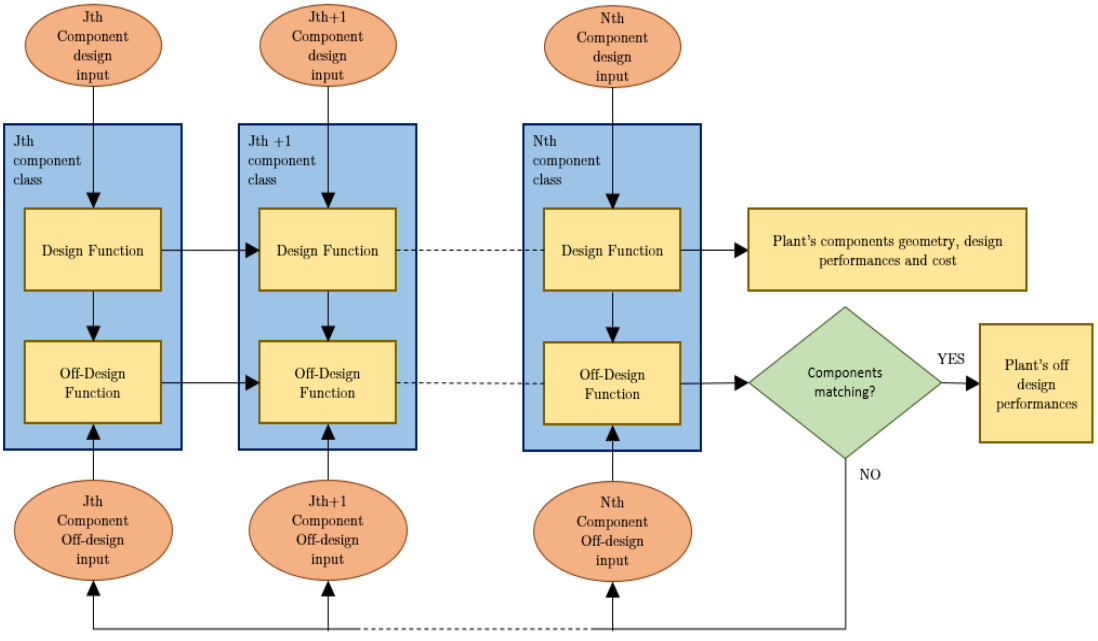

Figure 30. Program logic flow chart

An advantage of the modular approach is the prospect to generate any possible plant layout and integrate new components. This characteristic enable the possibility to include the desired number of compression and expansion stages or integrate any number of heat exchangers for intercooled recuperative cycles. Moreover, modularity of the tool allows the integration of new components such as combustion chamber or thermal storage units.

Once the components are selected, the first step is to design the plant and its main components using design point input parameters. After the design procedure is completed, the off-design performance of the components based on the desired operational strategy. The off-design procedure it's an iterative procedure to find the matching between plant's components. Constraints can be included in the software according to the operational strategy.

3.2. Fluid Properties

Although the fluid is not a component of the plant can be considered as such. A special class for the fluid has been created to obtain the properties of the fluid at a given temperature and pressure. Through this module, each component's module can obtain the properties of the fluid in any working condition. Given the fluid composition, the temperature and the pressure, this module is able to evaluate the thermodynamic properties of the working fluid.

The specific gas constant R is calculated as the ratio between the absolute gas constant and the molecular weight. The specific heat is evaluated using first order polynomial equation (3).

$$C_P = \sum_{k=1}^{n} \mu_k (A_k + B_k T) \tag{3}$$

Where A and B are two coefficients characteristic of the single component k and μ is the mass fraction of the component k. n is the number of constituents of the gas. A and B values for air constituents can be found in [69].

For the purpose of this study only air was considered. The dynamic and kinematic viscosities as well as thermal conductivity are calculated using a second order truncation function (respectively equations (4), (5) and (6)) interpolated from the known properties of the air as a function of the temperature [69]. The effect of pressure is neglected.

$$\mu = \ -8.37 \cdot 10^{-7} \cdot T^2 + 0.0043 \cdot T + 0.634 \ \cdot 10^{-5} \tag{4}$$

$$\nu = \ 5.4 \cdot 10^{-6} \cdot T^2 + 0.007 \cdot T - 1.16 \ \cdot 10^{-5} \tag{5}$$

$$k = \ -1.3 \cdot 10^{-6} \cdot T^2 + 0.007 \cdot T + 0.5 \ \cdot 10^{-2} \tag{6}$$

3.3. Compressor

The compressor module can generate any number of centrifugal compressor objects. The class refers to the fluid module to characterise the fluid thermodynamic properties and it is composed by the Design, Off-design and map generator functions.

3.3.1. Centrifugal Compressor Thermodynamic

Centrifugal compressors consist of four main components: Stationary casing, impeller, stationary diffuser either vaned or vaneless and volute.

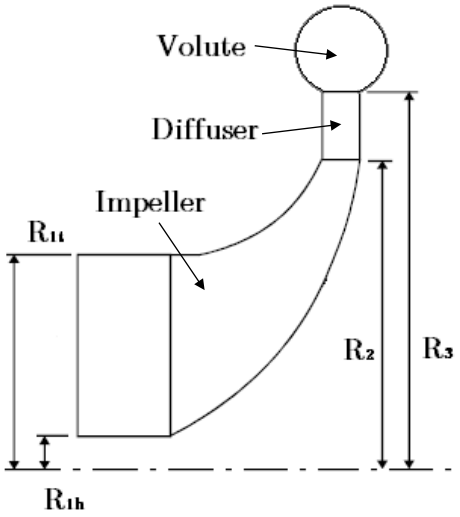

Figure 31. Centrifugal compressor meridional view.

Figure 31 shows the different stations with numbering. The design procedure starts from the inlet, where, applying mass and momentum equations, it is possible to characterise the impeller inlet geometry [33].

$$m = \rho_1 \pi R_t^2 \ 1 - \chi_1^2 \ C_{1a} \tag{7}$$

$$\chi_1 = \frac{R_{1h}}{R_{1t}} \tag{8}$$

Where R is the radius, ρ is the fluid density, C_a is the axial component of the absolute velocity. The subscripts $_1$ refers to inlet station, $_t$ and $_h$ to tip and hub respectively. For a preliminary 1D design procedure, the inlet absolute velocity can be considered completely axial and constant along the blade and the speed triangles can be calculated using equations (9) and (10).

$$U_{1t} = \frac{2\pi n R_{1t}}{60} \tag{9}$$

$$W_{1t} = \sqrt{C_{1a}^2 + U_{1t}^2} \tag{10}$$

In equation (9) and (10) U and W are the tangential and relative velocity.

The rotor is the work transfer device and the outlet design considerations must start with the conservation equations [33].

$$m = \rho_2 2\pi R_2 b_2 C_{2r} \tag{11}$$

$$R_2 = \frac{R_{1t}}{\chi_2} \tag{12}$$

$$W = U_2 C_{2u} = \frac{\overline{C_p}\ T_{02} - T_{01}}{\eta_a} = \frac{\overline{C_p} T_{01}}{\eta_a}\left(\left(\frac{p_{02}}{p_{01}}\right)^{\frac{\gamma-1}{\gamma}} - 1\right) \tag{13}$$

In the previous equations b_2 is the tip width, C_r is the radial component of the absolute velocity, $\overline{C_p}$ is the average specific heat at constant pressure, p_0 is the fluid total pressure, T_0 its total temperature, γ is the specific heats ratio and η_a is the compressor isentropic efficiency. The subscript $_2$ refers to the exit station of the compressor. χ_2, similarly to χ_1, is a non-dimensional parameter defines as the ration between the impeller tip and exit radius.

For this study, a vaneless diffuser has been selected. Compared to vaned diffuser, vaneless diffuser can guarantee a wide range of operating condition with relatively high efficiency. This is particularly important for solar application, as during the day solar fluctuations force the machine to work mainly in off-design conditions. In this situation, the lower efficiency of the machine is compensated by a wider range of operating condition with acceptable efficiency [34].

3.3.2. Compressor Design

Generally, parameters which readily describe the performance of the machine are required in order to assess the compressor design and compare the performance with already existing geometries. A standard approach involves the definition of a set of non-dimensional parameters which can reduce the design variables and facilitate the design.

A parameter which can be defined at preliminary stage in order to find the correct rotational speed is the specific speed, defined by equation (14).

$$N_s = \frac{\omega\sqrt{Q}}{\Delta h_{0s}^{3/4}} \tag{14}$$

Where ω is the angular velocity expressed in $[rad/s]$, Q is the volumetric flow rate expressed in $[m^3/s]$ and Δh_{0s} is the total isentropic enthalpy difference, expressed in $[J/kg]$ and defined by equation (15).

$$\Delta h_{0s} = \overline{C_p} T_{01} \left(\left(\frac{p_{02}}{p_{01}} \right)^{\frac{\gamma-1}{\gamma}} - 1 \right) \tag{15}$$

Solar dish MGT usually operates with a mass flow in the order of magnitude of 10^{-1} kg/s. Moreover, MGT operates with a recuperative cycle, which is characterise by relatively low-pressure ratio (≈3). According to Baines et al. [33], optimum efficiency can be achieved when the specific speed value is comprised between 0.6 and 1.2, which with a mass flow rate of 0.1 kg/s and a pressure ratio of 3, correspond to a rotational speed comprise between 120'000 and 240'000 $[rpm]$. In this study the rotational speed will be kept constant at the value of 130'000 $[rpm]$ as already experience by OMSoP project [36]. A higher rotational speed indeed could result in mechanical stability problems. Thus, this value will be kept constant for design conditions.

Two non-dimensional parameters have already been defined by equation (8) and (12). According to Japikse [39], the hub to tip inlet radius ratio χ_1 is set to structural requirements in the range 0.3 to 0.5. Regarding, χ_2, it's value can be found using an iterative process based on the evaluation of the slip factor. The slip factor equation proposed by Bajie [43] was adopted.

$$\sigma = \left(1 + \frac{6.2}{2 \cdot Z\left(\frac{1+\chi_1}{\chi_2}\right)^{\frac{2}{3}}}\right)^{-1} \tag{16}$$

Compressor design procedure has been performed using a one-dimensional model based on the mass, momentum and energy conservation equations. The procedure requires the knowledge of some basic thermodynamic cycle quantities and non-dimensional parameters. Table 1 report the required input parameters.

Table 1. Compressor Design Procedure Input parameters

Cycle Parameters		**Impeller Geometrical Parameters**	
Mass flow rate	m	Back sweep angle	β_2
Total inlet pressure	T_{01}	Slip Factor	σ
Total inlet pressure	p_{01}	Inlet Tip radius/Inlet Hub radius	χ_1
Pressure Ratio	PR	Inlet Tip radius/outlet radius	χ_2
Rotational speed	n	Blade thickness/tip inlet radius	t_1/R_{1t}
		Blade Thickness/exit radius	t_2/R_2
		Axial Length	L_a

The design procedure is composed by two main parts: the inlet design and the outlet/diffuser design. Figure 32 shows a flow chart of Inlet design procedure.

The procedure starts assuming a value for the axial component of the inlet absolute velocity(C_{1a}), then applying the mass and momentum conservation equations can evaluate the main geometrical parameters that characterised the compressor inlet. A wrong assumption for C_{1a} can lead to supersonic fluid conditions. For this reason, the procedure requires a verification on the blade tip relative Mach number (M_{rt}). The process iterates until a value lower than 0.85 M_{rt} is reached.

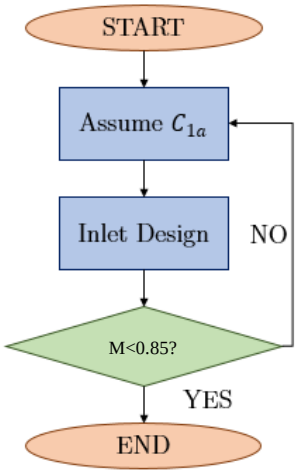

Figure 32.Compressor inlet design flow chart.

Figure 32 describes the outlet design procedure. The procedure starts assuming a first value for the overall compressor efficiency and for the impeller efficiency. The procedure iterate until the convergence is reached, the convergence of the two efficiency values is performed with empirical relations that can be easily found in literature [33]-[37]-[38].

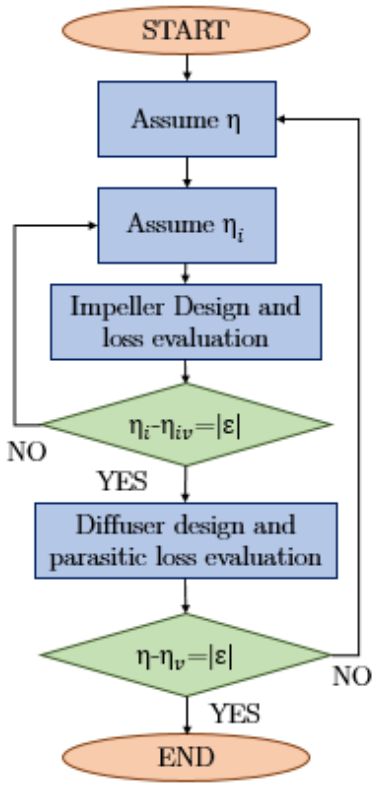

Figure 33. Compressor outlet design flow chart.

In this model, a distinction between external or parasitic losses and internal losses was applied. Internal losses include all the losses that cause a pressure drop across the main channel such as Incidence Losses, blade loading, skin friction, mixing losses, tip clearance losses and vaneless diffuser losses. The external losses are all those losses characterised by an enthalpy loss but not a pressure loss across the main channel. Belong to this category: the disk friction losses, the leakage losses and the recirculation losses.

Incidence Losses: This kinetic energy loss is generated by a different inlet flow incidence angle. This loss is proportional to the square of the tangential component of the inlet relative velocity. Equation (17) shows the equation suggested by Whitfield and Baines [33].

$$\Delta h_{0i} = \frac{W_1^2 * sin^2 \left|\beta_1 - \beta_{i,opt}\right|}{2} \tag{17}$$

Where W_1 is the relative inlet velocity, β_1 is the inlet relative angle and $\beta_{1,\mathrm{opt}}$ is the optimum inlet relative angle, which in this work has been considered equal to the design condition relative angle.

Skin friction losses: This contribute is due to friction between the fluid and the impeller surface. According to Botha and Moolman [38], the contribute of this loss can be calculated using equation (18).

$$\Delta h_{0sf} = 2Cf \left(\frac{L_b}{D_{hb}}\right) W_m^2 \tag{18}$$

$$W_m = \frac{C_{1a} + C_2 + 3W_2 + W_{1t} + 2W_{1h}}{8} \tag{19}$$

$$L_b = \frac{\pi}{8}\left(2R_2 - \frac{R_{1t} + R_{1h}}{2} - b_2 + R_2\right) \frac{2}{\frac{cos\ \beta_{1t}\ + cos\ \beta_{1h}}{2} + cos\ \beta_2} \tag{20}$$

$$D_{hb} = 2R_2 \left(\frac{cos\ \beta_2}{\frac{Z}{\pi} + \frac{2R_2 cos\ \beta_2}{b_2}} + \frac{0.5\left(\frac{R_{1t}}{R_2} + \frac{R_{1h}}{R_2}\right)\frac{\left(cos\ \beta_{1t}\ + cos\ \beta_{1h}\ \right)}{2}}{\frac{Z}{\pi} + \frac{2R_{1t} + 2R_{1h}}{2R_{1t} - 2R_{1h}} * \frac{cos\ \beta_{1t}\ + cos\ \beta_{1h}}{2}} \right) \tag{21}$$

$$Re = \frac{\rho_1 \frac{C_{1a} + C_2}{2} D_{hb}}{\mu} \tag{22}$$

$$C_f = \frac{0.455}{log\ Re^{\ 2.58}} \tag{23}$$

Diffusion and Blade Loading losses: The diffusion and blade loading losses is caused by the growth of the boundary layer along the impeller, Jansen [39] describes the blade loading loss as the momentum loss due to boundary-layer growth, function of a parameter called diffusion factor.

$$D_f = 1 - \frac{W_2}{W_{1t}} + \frac{\left(\frac{K_{Df}\Delta h_{th}}{U_2^2}\right)}{\frac{W_{1t}}{W_2}\left(\frac{z}{\pi}\left(1 - \frac{R_{1t}}{R_2}\right) + \frac{2R_{1t}}{R_2}\right)} \tag{24}$$

$$\Delta h_{bl} = C_{BL} D_f^2 U_2^2 \tag{25}$$

Where $K_{Df} = 0.6$ for splitter blades and 0.75 for normal blades and $C_{BL} = 0.05$.

Mixing Losses: These losses occur at the exit of the impeller. At this location, the growth of the boundary layer results in a two-zone fluid. Using conservation of mass and momentum equations, Johnston and Dean [41] assumed a square-behaviour of the jet-wake relative velocity profile with no variation of relative velocities across the passage depth. In addition, they assume static pressure constant around the impeller rim. With a number of blades $Z > 10$ the mixing loss can be calculated with equation (26).

$$\Delta h_{ml} = \frac{1}{1 + tan\ \alpha_2\ ^2} \left(\frac{1 - \varepsilon_w - b_i}{1 - \varepsilon_w}\right)^2 C_2^2/2 \quad ; \tag{26}$$

In equation (26) ε_w is the fraction of the wake fluid zone, considered equal to 0.35 [41] and b_i is the ratio between the vaneless diffuser inlet width and the impeller exit width.

Tip Clearance Losses: In order to allow free rotation of the impeller, a tip clearance gap is required between the blade and the casing. This causes the fluid to leak from the pressure to the suction side of the impeller. Jansen [41] calculate the tip clearance losses using equation (27).

$$\Delta h_{cl} = 0.6 \cdot \varepsilon_{cl} \frac{C_{2u}}{b_2} \sqrt{\frac{4\pi}{b_2 z} \frac{R_{1t}^2 - R_{1h}^2}{R_2 - R_{1t} \ \left(1 + \frac{\rho_2}{\rho_1}\right)}} C_{2u} C_{1a} \tag{27}$$

In equation (26) ε_{cl} is the clearance gap between the shroud and the impeller tip, considered equal to the *2%* of the blade height [33].

Recirculation Losses: At the blade outlet a part of the fluid leak through the gap between the impeller and the back plate causing a significant loss especially in off design condition. Oh et al. [42] developed equation (28) to consider these losses.

$$\Delta h_{rc} = 8 * 10^{-5} sinh \ 3.5\alpha_2^3 \ D_f^2 U_2^2 \tag{28}$$

In the previous equation α is the absolute flow angle.

Disk Friction Losses: The friction between the rotating disk and the fluid in the surrounding enclosure causes this loss. Oh et al. [42] calculates the disk friction losses using equation

$$\Delta h_{df} = \frac{f_{df} \left(\frac{\rho_1 + \rho_2}{2}\right) * R_2^2 U_2^3}{4m} \tag{29}$$

$$\begin{cases} f_{df} = \dfrac{2.67}{Re_{df}^{0.5}} & if \ Re_{df} < 3 * 10^5 \\ f_{df} = \dfrac{0.062}{Re_{df}^{0.2}} & if \ Re_{df} \geq 3 * 10^5 \end{cases} \tag{30}$$

$$Re_{df} = \frac{U_2 R_2 \rho_2}{\mu} \tag{31}$$

Leakage Loss: Some of the flow leaks through the clearance gaps and labyrinth seals to the lower pressure regions of the compressor. Aungier [43] developed equation (32) to predict this loss contribute.

$$\Delta h_{lk} = \frac{m_{cl} U_{cl} U_2}{2m} \tag{32}$$

$$m_{cl} = \rho_2 z \varepsilon_{cl} L_a U_{cl} \tag{33}$$

$$U_{cl} = 0.816 \sqrt{\frac{2\Delta p_{cl}}{\rho_2}} \tag{34}$$

$$\Delta p_{cl} = \frac{m \; R_2 C_{2u}}{z \dfrac{R_{1t} + R_{1h}}{2} \; \dfrac{b_1 + b_2}{2} \; L_a} \tag{35}$$

Vaneless Diffuser Loss: Caused by the friction between the fluid and the surfaces of the diffuser. Stanitz et al. [44] define the enthalpy loss in the vaneless diffuser using equation (36).

$$\Delta h_{vd} = c_{p2} T_{02} \left(\left(\frac{p_3}{p_{03}} \right)^{\frac{\gamma-1}{\gamma}} - \left(\frac{p_3}{p_{02}} \right)^{\frac{\gamma-1}{\gamma}} \right) \tag{36}$$

Considering all the loss contributes given by these equations it is possible to calculate and then verify within the design procedure the value of the Impeller and the overall efficiencies. The impeller efficiency and the overall efficiency can be calculated using respectively equations (37) and (38).

$$\eta_i = \frac{\Delta h_{0s} - \Delta h_i - \Delta h_{sf} - \Delta h_{bl} - \Delta h_{cl} - \Delta h_{ml}}{\Delta h_{th}} \tag{37}$$

$$\eta = \frac{\Delta h_{0s} - \Delta h_i - \Delta h_{sf} - \Delta h_{bl} - \Delta h_{cl} - \Delta h_{ml} - \Delta h_{vd}}{\Delta h_{th} + \Delta h_{rc} + \Delta h_{lk} + \Delta h_{df}} \tag{38}$$

3.3.3. Compressor Off-design

To evaluate the off-design performances of the compressor, a similar model can be applied. As result of the design procedure, the geometrical parameters have been defined. The software can then evaluate the off-design performances of the plant using the same relationships described so far.

3.3.4. Compressor model validation

The compressor model has been validated against experimental data for three different compressor sizes [38]. Figure 34 shows the main geometrical characteristics of the impeller for these compressors.

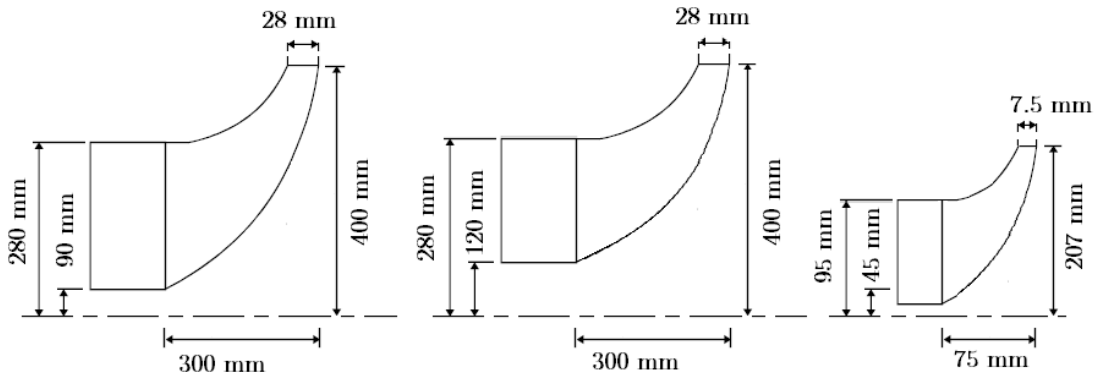

Figure 34. Impeller geometries considered for the validation (not in scale).

The results obtained from the model validation for the maps are given Figure 35, Figure 36 and Figure 37. The comparison with experimental results regarding Eckardt impeller O demonstrates good accuracy for a wide range of operating conditions, showing a maximum relative error of *2.5* % for the efficiency and *3*% for the pressure ratio. Moreover, the curves demonstrate comparable behaviour and the error is located only in short sections of the curves. The same observations are valid for Eckardt impeller A. In this case the model shows a maximum relative error of *4*

% for the efficiency and *4.3* % for the pressure ratio. Despite the higher maximum relative error, the overall average accuracy of the model is higher when compared with the Eckardt impeller O, especially the efficiency. On the other hand, the pressure ratio shows a more accentuated slope of the curve when getting close to the chocking limit. Nevertheless, the accuracy of the model was considered acceptable for the purpose of this study.

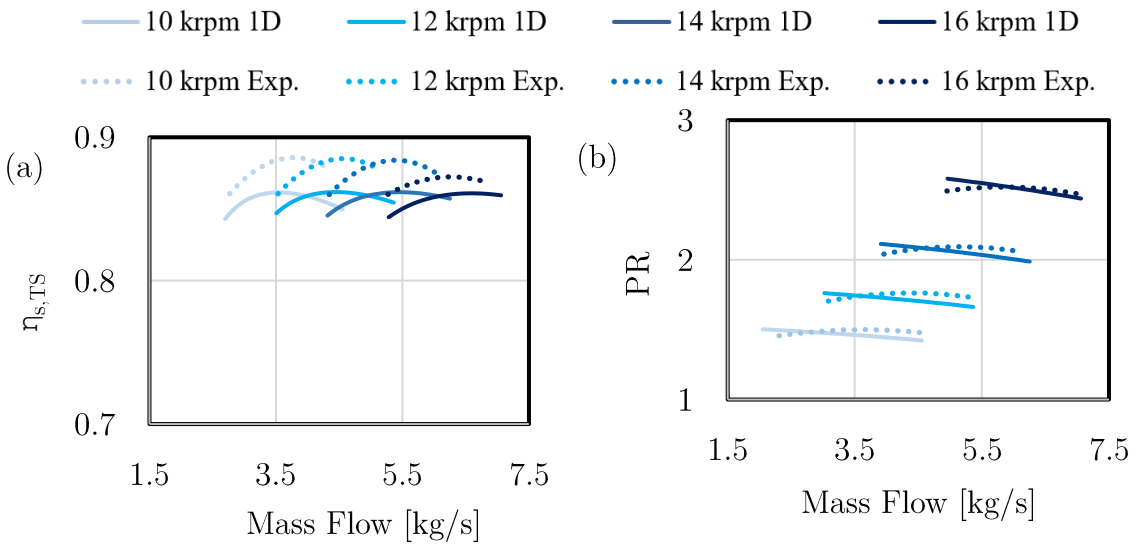

Figure 35. Compressor validation: Characteristic maps for Eckardt impeller O. (a) Total to static isentropic efficiency versus mass flow rate. (b) Pressure ratio versus mass flow rate

For the case of KIMM compressor geometry, the efficiency chart was not available, and the comparison has been performed only with the pressure ratio chart. The comparison shows good agreement with the experimental results when compared to the other two compressor geometries showing a maximum relative error of *1.5* %. This demonstrates the applicability of the present model for small size compressors.

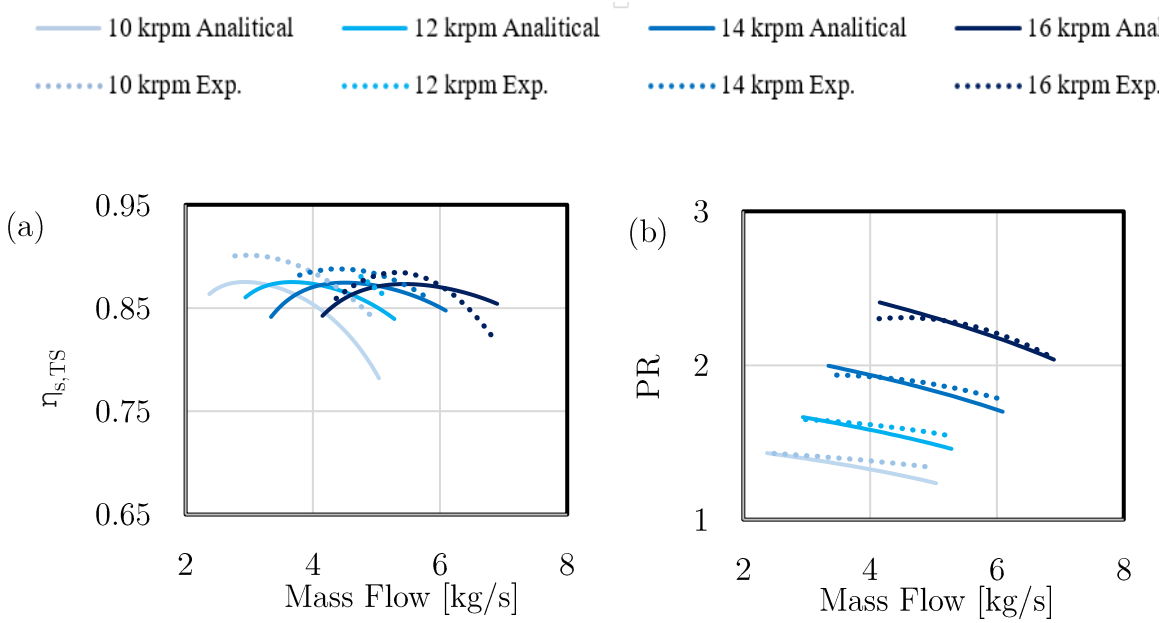

Figure 36. Compressor validation: Characteristic maps for Eckardt impeller A. (a) Total to static isentropic efficiency versus mass flow rate. (b) Pressure ratio versus mass flow rate

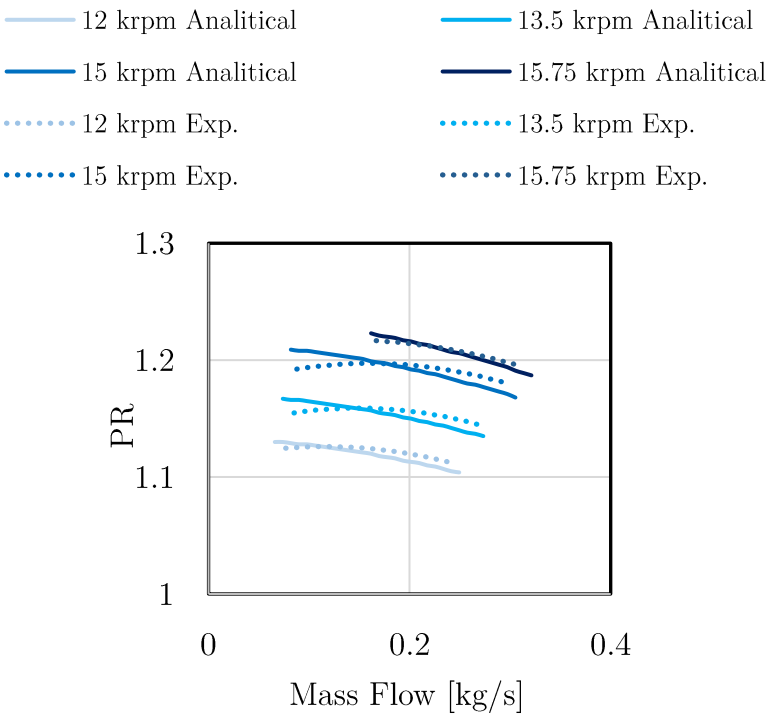

Figure 37. Compressor validation: Characteristic maps for KIMM impeller.

3.4. Recuperator

The recuperator chosen for this study is a cross flow plate-fin heat exchanger with off-set strip fins. This arrangement has one of the highest heat transfer to volume ratio between all the heat exchangers available in the market [45]. Figure 38 shows a schematic of the heat exchanger and the geometric characteristics of the off-set strip fin.

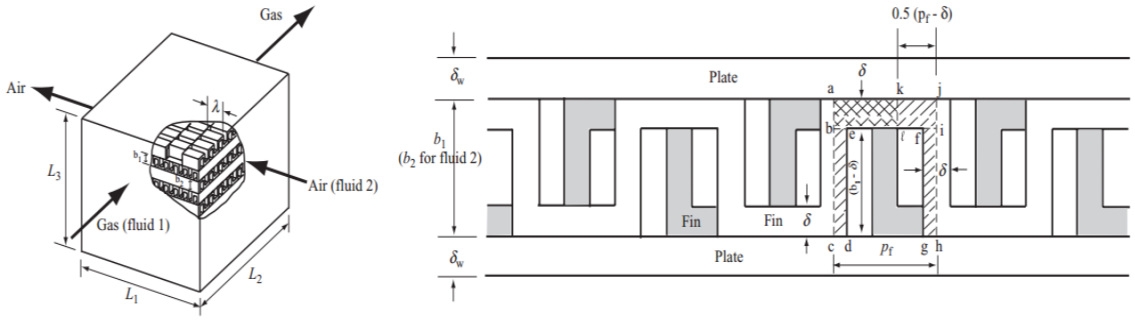

Figure 38. Schematic of a plate-fin heat exchanger with offset strip fin. Source: [45].

3.4.1. Recuperator geometrical characteristics

The core of the recuperator is characterised by a width L_1 for the cold side and L_2 for the hot side. The height of the recuperator core can be calculated using equation (39) as a function on the number of passages on cold (N_P) and hot side ($N_P + 1$).

$$N_P = \frac{L_3 - b_2 - 2\ N_P + 1\ \delta_W}{b_1 + b_2 + 2\delta_W} \tag{39}$$

Where the subscripts $_1$ refer to the hot side and $_2$ to the cold side. δ_W is the plate thickness and b the fin height. For both sides the number of fins can be calculated using equation (40)

$$n_{f1} = \frac{L_1}{p_{f1}}\ N_P \tag{40}$$

The previous equation can be applied also to the hot side 2.

The overall heat transfer surface is divided in two zone: a primary zone and a secondary zone. The total primary area can be calculated as the sum of the total plate surface, the passage side wall surface and the front and back surface minus the fin base surface. The following procedure is presented for the cold side, similar approach can be applied to the hot side.

$$A_{p1} = 2L_1L_2N_P + 2b_1L_2N_P + 2\ b_2 + \delta_W\ L_1\ N_P + 1\ - 2\delta L_2 n_{f1} \tag{41}$$

The fin surfaces and the offset strip edge surface compose the secondary zone. The surface can be calculated using equation (42).

$$A_{f1} = 2\ b_1 - \delta\ L_2 n_{f1} + 2\ b_1 - \delta\ n_{f1}\delta\frac{L_2}{\lambda_1} + (p_{f1} - \delta)\delta\left(\frac{L_2}{\lambda_1} - 1\right) n_{f1} + 2\delta p_{f1} n_{f1} \tag{42}$$

The hydraulic diameter can be calculated using equation (43) as a function of the total surface A_{t1}, sum of the primary and secondary surface, and the free flow cross section, given by equation (44).

$$D_H = \frac{4A_{c1}L_2}{A_{t1}} \tag{43}$$

$$A_{c1} = \ b_1 - \delta\ \left(p_{f1} - \delta\right) n_{f1} \tag{44}$$

3.4.2. Heat transfer and Pressure Losses

To evaluate the overall heat transfer coefficient and pressure losses Manglik and Bergles [47] developed the following model valid for each flow side. In this model, the heat transfer coefficient on each side can be calculated using equation (45) as a function of the Colburn number j, the average specific heat at constant pressure $\overline{C_p}$, the volumetric flow rate G and the Prandtl number Pr.

$$h = \frac{jGC_p}{Pr^{2/3}} \tag{45}$$

The Colburn number is calculated using equation (46).

$$\begin{aligned} j = \ & 0.6522\ Re^{-0.5403} \left(\frac{p_f\ -\ \delta}{b\ -\ \delta}\right)^{-0.1541} \left(\frac{\delta}{\lambda}\right)^{0.1499} \left(\frac{\delta}{p_f\ -\ \delta}\right)^{-0.0678} \\ & \cdot \left[1 + 5.269 \cdot 10^{-5}\ Re^{1.34} \left(\frac{p_f\ -\ \delta}{b\ -\ \delta}\right)^{0.504} \cdot \left(\frac{\delta}{\lambda}\right)^{0.456} \right. \\ & \left. \cdot \left(\frac{\delta}{p_f\ -\ \delta}\right)^{-1.055} \right]^{0.1} \end{aligned} \tag{46}$$

To evaluate the overall heat transfer coefficient the overall surface efficiency η_o and the fin efficiency η_f must be calculated on each side.

$$\eta_o = 1 - \frac{(1-\eta_f)A_f}{A_t} \tag{47}$$

$$\eta_f = \frac{tanh(mL_{f1})}{mL_{f2}} \tag{48}$$

L_{f1} can be calculated in each side using equation (49), the fin parameter m using equation (50).

$$L_f = \frac{b}{2} - \delta \tag{49}$$

$$m = \left(\frac{2h}{k_f \delta}\left(1 + \frac{\delta}{\lambda}\right)\right)^{0.5} \tag{50}$$

In equation (50) k_f is the fin thermal conductivity and λ the fin length.

Finally, the main heat transfer paramer can be calculated using equation (51) as a function of the the wall thermal resistence R_w described by equation (52) and the fin thermal resistance R_o on each side (equation (53)).

$$UA = \frac{1}{(R_w + R_{o1} + R_{o2})} \tag{51}$$

$$R_w = \frac{\delta_W}{k_w A_W} \tag{52}$$

$$R_o = \frac{1}{\eta_o h A_t} \tag{53}$$

The heat transfer can be then characterised using the $\varepsilon - NTU$ method. The effectiveness of the heat exchanger is defined as the ratio between the actual heat transferred Q and the maximum possible heat transfer that can be hypothetically achieved. For a crossflow heat exchanger the effectiveness of the heat exchanger can be calculated using equation (54).

$$\varepsilon = 1 - e^{\left(\frac{1}{\chi} NTU^{0.22}\left(e^{-\chi NTU^{0.78}} - 1\right)\right)} = \frac{Q}{C_{min}\Delta T_{Max}} \tag{54}$$

In equation (54) C_{min} is the minimum heat capacity rate ($C_p m$) among the hot side and cold side fluid. NTU is the number of transfer unit and its defined by equation (55), χ is the ratio between the minim and maximum heat capacity rate C_{min}/C_{max}.

$$NTU = \frac{UA}{C_{min}} \tag{55}$$

According to Manglik and Bergles [47] pressure losses can be calculated using equation (56).

$$\Delta p = \frac{G^2}{2\rho_i}\left(1 - \sigma^2 + K_c \; + 2\left(\frac{\rho_i}{\rho_o} - 1\right) + \frac{4fL}{D_h}\frac{\rho_i}{\rho_m} - \; 1 - \sigma^2 + K_e \; \frac{\rho_i}{\rho_o}\right) \tag{56}$$

Where σ is the porosity of the heat exchanger, ρ_i and ρ_o are respectively the inlet and outlet density calculated using the ideal gas law, while ρ_m is defined by equation (57), f is the friction coefficient defined by equation (58) and K_c and K_e are respectively the contraction and expansion coefficient. According to HoSung Lee [45] these coefficients can be calculated for circular tubes using equations (59) to (61).

$$\frac{1}{\rho_m} = \frac{1}{2}\left(\frac{1}{\rho_i} + \frac{1}{\rho_o}\right) \tag{57}$$

$$f = 9.6243\, Re^{-0.7422} \left(\frac{p_f - \delta}{b - \delta}\right)^{-0.1856} \cdot \left(\frac{\delta}{\lambda}\right)^{0.3053} \cdot \left(\frac{\delta}{p_f - \delta}\right)^{-0.2659} \cdot \left(1 + 7.669 * 10^{-8}\, Re^{4.429} \left(\frac{p_f - \delta}{b - \delta}\right)^{0.92} \cdot \left(\frac{\delta}{\lambda}\right)^{3.767} \cdot \left(\frac{\delta}{p_f - \delta}\right)^{0.236} \right)^{0.1} \tag{58}$$

$$C_c = 4.374 * 10^{-4} e^{6.737\sqrt{\sigma}} + 0.621 \tag{59}$$

$$f_d = \begin{cases} 0.049 Re^{-0.2} & if\ Re \geq 2300 \\ \dfrac{16}{Re} & if\ Re < 2300 \end{cases} \tag{60}$$

$$K_{dc} = \begin{cases} 1.09068\ 4f_d\ + 0.05884 \sqrt{4f_d} + 1 & if\ Re \geq 2300 \\ 1.33 & if\ Re < 2300 \end{cases} \tag{61}$$

The value for circular tubes of the coefficient K_d can be converted to the correspondent coefficient for a squared tube using equation (62) and the contraction and expansion coefficients can be finally calculated using equation (63) and (64).

$$K_d = \begin{cases} 1 + 1.17(K_d - 1) & if\ Re \geq 2300 \\ 1.39 & if\ Re < 2300 \end{cases} \tag{62}$$

$$K_c = \frac{1 - 2C_c + C_c^2(2K_d - 1)}{C_c^2} \tag{63}$$

$$K_e = 1 - 2K_d\sigma + \sigma^2 \tag{64}$$

3.4.3. Design and Off-Design Procedure

In this study, an air-to-air single-phase crossflow heat exchanger design procedure has been implemented using C++ object orientated programming. Offset strip fin has been considered in both hot and cold side; the selected material is Inconel

625 with $k = 18$ $[\frac{W}{mK}]$. Table 2 contains all the input parameters for a complete design assessment.

Table 2. Recuperator Design Input Parameters

Recuperator Design Thermodynamic Input Parameters		Recuperator Design Geometrical Input Parameters	
Mass flow rate hot side	m_1	Fin thickness	δ_W
Mass flow rate cold side	m_2	Plate thickness	δ
Hot side inlet temperature	T_{11}	Fin height	p_f
Cold side inlet temperature	T_{21}	Fin width	b
Hot side outlet pressure	p_{12}	Offset Length	λ
Cold side inlet pressure	p_{21}	Recuperator Height	L_3
Effectiveness	ε	`	

The procedure is straight forward and without iterations. The objective is to identify the value of $L1$ and $L2$ that can guarantee the heat transfer in respects of the design input parameters. As a matter of simplicity, $L1$ is considered equal to $L2$. The same simplification is applied to the fin width, the offset length and the fin height.

Differently from the design procedure, in the Off-design procedure the geometry is completely defined. The output from the off-design function are the effectiveness and the pressure losses.

3.4.4. Recuperator Model Validation

The model for the recuperator has been validated against available experimental data for a range of fin geometries as proposed by Kays and London [48]. The fin geometries and arrangements used for the validation, namely 1/10-27.03 and 1/8-16.00(D), are presented in Figure 39 .

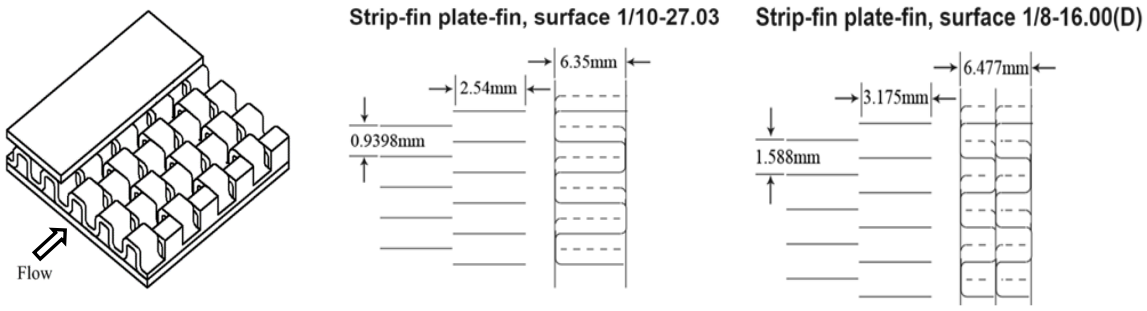

Figure 39. Fin geometries considered for the recuperator model validation.

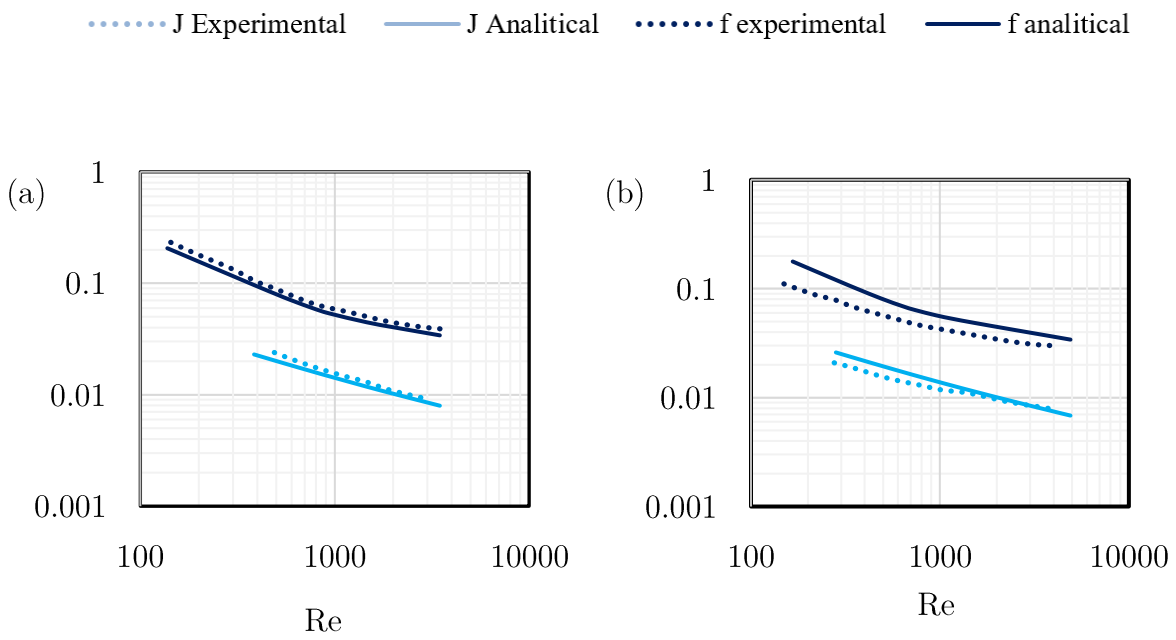

Figure 40. Comparison between experimental and analytical data. Colburn factor (cyan) and friction factor (blue). Fin geometry *1/10-27.03* (a). Fin geometry *1/8-16.00(D)* (b).

Figure 40 shows the modelling results of the Colburn factor (j) and friction factor (f) for both *1/10-27.03* and *1/8-16.00(D)* fin geometries. The modelling for the first geometry presents a maximum relative error of *3* % for both Colburn factor and friction factor. Nevertheless, there is some inaccuracy in the results of the second fin geometry, with a maximum relative error around *18%* for the Colburn number and *6* % for the friction factor. Given the higher accuracy of the model in predicting the

performance of the *1/10-27.03* fin geometry this layout will be adopted by the model for the recuperator design.

3.5. Receiver and Dish Model

The Receiver is one of the key components as it significantly affects plant's performance. The receiver considered in this study is a cylindrical air tube cavity receiver. As shown by Figure 41, the receiver is manly composed by a cylindrical cavity surrounded by an insulator. At the bottom of the cavity, an optical splitter is used to readdress incident sun rays, and at the top of the cavity, a quartz glass is present to minimise heat transfer between the receiver and the ambient.

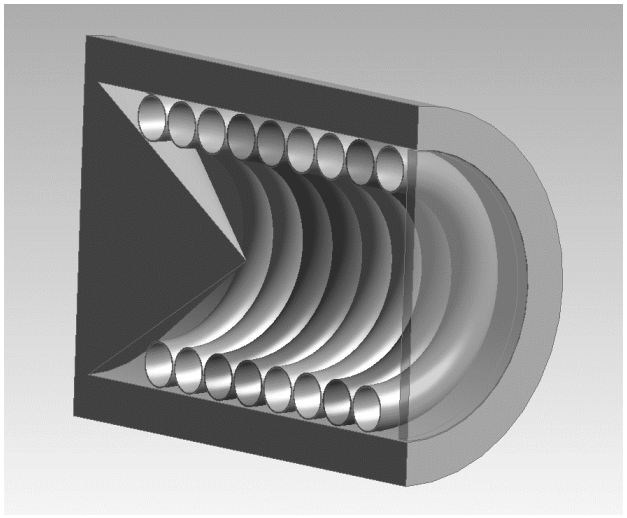

Figure 41. Breakthrough of the adopted cavity receiver.

The performances of an air tube cavity receiver are strongly influenced by the losses. According to Zou [50], this arrangement is characterised by two different types of loss: convection and radiation loss. The presence of the glass reduces the amount of losses due to convective heat transfer with the ambient eliminating the heat transfer inside the cavity. However, the arrangement is still subject to convective losses due to the heat dissipated by the external cavity surface.

$$Q_{conv} = h_{conv} A_{ext} (T_w - T_{amb}) \tag{65}$$

In equation (65) T_{wall} is the receiver wall temperature, T_{amb} is the ambient temperature, A_{ext} is the overall external surface and h_{conv} is the heat transfer coefficient, calculated though the Nusselt number described by equation (66).

$$Nu_{conv} = 0.88\ Gr \left(\frac{T_w}{T_{amb}}\right) cos\ \theta\ ^{2.47} \tag{66}$$

In equation (66) Gr is the Grashoff number. To evaluate this number all fluid properties have been calculated at the film temperature. The film temperature is the arithmetic average between the ambient and the wall temperature. θ is the receiver inclination angle.

The second contribution to losses is due to irradiation phenomena. This dissipated heat can be decomposed in three different components: the re-irradiation, which is characteristic of high temperature materials (Equation (67)), the radiation absorbed by the glass and the radiation reflected by the pipe surface admitting zero transmission (Equation (68)).

$$Q_{rad1} = A_{cav} \varepsilon_p \sigma_b (T_w^4 - T_{amb}^4) \tag{67}$$

$$Q_{rad2} = (1 - \alpha_p) Q_{sun} + \alpha_g Q_{sun} \tag{68}$$

In the previous equations ε_p is the pipe emissivity, σ_b is the Boltzmann constant, α_p and α_g are respectively the pipe and the glass absorptivity. A_{cav} is the internal cavity surface. Q_{sun} is the heat flux at the focal point of the receiver.

To fully characterise the heat transfer inside the receiver, the following equation must be satisfied.

$$\begin{aligned} Q_{abs} = DNI \cdot A_{dish} \cdot \eta_{dish} - Q_{conv} - Q_{rad1} - Q_{rad2} \\ = \ mC_p(T_{gIN} - T_{gOUT}) = h_p A_p \Delta T_{gML} \end{aligned} \tag{69}$$

$$\Delta T_{gML} = \frac{\left((T_w - T_{g,IN}) - (T_w - T_{g,OUT})\right)}{log\left(\frac{T_w - T_{g,IN}}{T_w - T_{g,OUT}}\right)} \tag{70}$$

In the previous equations $T_{g,IN}$ and $T_{g,OUT}$ are the gas inlet and outlet temperature respectively. DNI is the sun direct normal irradiation expressed in $[W/m^2]$, A_{dish} is the parabolic equivalent dish area and η_{dish} is the dish optical efficiency. This efficiency considers the capacity of the dish of readdressing the incident sunrays. Drop in this parameter are usually caused by the surface finishing of the mirror and its capacity to concentrate all the sunrays in the receiver focal spot.

The heat transfer and the pressure losses within the receiver pipe have been evaluated considering the tube as a helically coiled tube. Many relationships to describe the heat transfer characteristics of a helicoidally coiled pipe are available in the literature. The model adopted in this study is the one proposed by Xin and Ebadian [49]. Heat transfer coefficient is calculated using equation (71).

$$h_p = \frac{Nu_p k_g}{D_p} = \frac{k_g}{D_p}\ 0.65 \cdot\ De^{\ 0.5} + 0.76\ \cdot Pr^{0.175} \tag{71}$$

Where λ_f is the fluid thermal conductivity is, Pr is the Prandtl number and De is the Dean number. Dean number, defined by equation (72), is a function of the Reynolds number, the pipe diameter D_p and the cavity diameter D_{cav}.

$$De = Re\ \left(\frac{D_p}{D_{cav}}\right)^{0.5} \tag{72}$$

Pressure losses have been calculated using equation (73) and (74).

$$\Delta p = 32 \cdot f \cdot m^2 \cdot \frac{L_p}{\pi^2 \rho_f D_p^5} \tag{73}$$

$$f = \left(1 + 0.0823 \cdot \left(1 + \frac{D_p}{D_{cav} - \delta_i - \frac{D_p}{2}}\right) \cdot \left(\frac{D_p}{D_{cav} - \delta_i - \frac{D_p}{2}}\right)^{0.53} \cdot Re^{0.25}\right) \cdot \left(\frac{0.079}{Re^{0.25}}\right) \quad (74)$$

3.5.1. Receiver and Dish Design

Figure 42 shows the receiver design procedure. The procedure starts assuming a 1st attempt dish diameter and receiver wall temperature. The procedure then continues with the receiver design and loss evaluation. The actual value of the wall temperature is then calculated in the first loop.

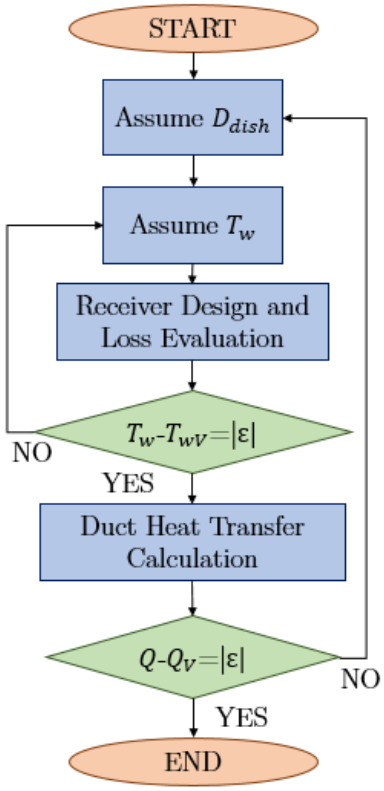

Figure 42. Receiver design flow chart

The next step is to evaluate the heat transferred to the working fluid across the receiver and compute the heat balance described by equation (69). An iteration is

required to find the dish diameter, which can guarantee to absorb the required amount of thermal energy necessary to meet the design requirements.

The required inputs for a complete design of the receiver are reported in Table 3. The outputs of the procedure are the complete geometry, the receiver effectiveness and pressure drop across the pipe.

Table 3. Receiver design input parameters.

Receiver Design Thermodynamic Input Parameters		**Receiver and Dish Design Input Parameters**	
Mass flow rate	m_1	Emissivity	ε
Direct normal irr.	DNI	Pipe thermal conductivity	k
Inlet temperature	$T_{g,IN}$	Inclination angle	θ
Outlet temperature	$T_{g,OUT}$	Cavity diameter	D_{cav}
Inlet pressure	p_1	Dish efficiency	η_{dish}
Ambient temperature	T_{amb}	Pipe thickness`	δ
		Glass absorbance	α_g
		Pipe absorbance	α_p

The off-design procedure is similar to the design. In this case, the geometry is given, and the objective is to calculate the performance of the receiver under variable DNI, air inlet temperature and mass flow rate. The iteration on the dish diameter is substituted by a procedure aimed to find the outlet temperature of the fluid.

3.5.2. Receiver model Validation

The receiver model was validated by comparing the results obtained from the one-dimensional model with experimental results available in literature [51]. The receiver consists of *15-turns* helically coiled tube with inner diameter of *12 mm* and thickness of *1 mm*. The inner diameter and height of the cavity are *140 mm* and *200 mm*, respectively.

Results shown in Figure 43 demonstrate good agreement in the outlet temperature evaluation for a wide range of operating points with a maximum relative error below *2.5 %* which is considered adequate for the purpose of this study.

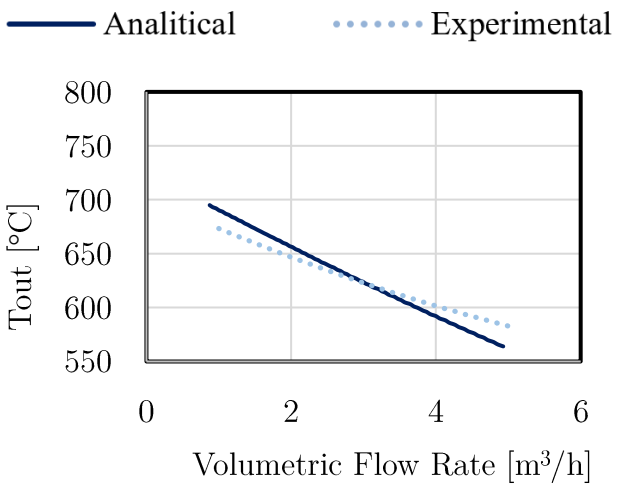

Figure 43. Results from receiver validation.

3.6. Turbine Model

A volute, nozzle vanes, impeller and diffuser mainly compose a radial turbine. Figure 44 shows a schematic cross sectional and frontal view of a typical radial turbine.

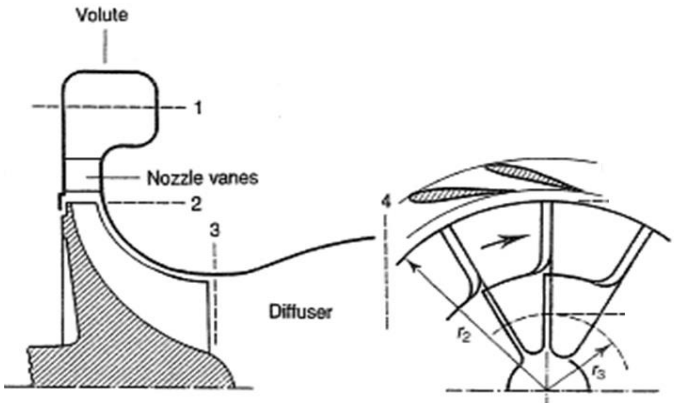

Figure 44. Radial turbine schematic

Similarly to centrifugal compressors, the design of a radial in-flow turbine can be characterised applying the mass, energy and momentum conservation equation at impellers inlet and outlet.

$$m = \rho_2 2\pi R_2^2 b_2 C_{2a} \tag{75}$$

$$S_W = \eta_{TS}\left(1 - \frac{1}{\left(\frac{p_{01}}{p_4}\right)^{\frac{\Upsilon-1}{\Upsilon}}}\right) \tag{76}$$

$$\Delta h_s = S_W * \frac{C_p T_{02}}{\eta_{TS}} \tag{77}$$

$$U_2 = \sqrt{\frac{\eta_{TS}\Delta h_s}{\psi}} = \frac{2\pi R_2 n}{60} \tag{78}$$

In the previous and following equations, symbols are the same adopted in the compressor modelling, subscripts refer to Figure 44.

The design procedure is facilitated by the assumption of a series of non-dimensional parameters: the power input factor ψ , flow coefficient φ and the axial velocity ratio (ξ), described by the following equations.

$$\psi = \frac{\Delta h_0}{U_2^2} \tag{79}$$

$$\varphi = \frac{C_{m3}}{U_2} \tag{80}$$

$$\xi = \frac{C_{m2}}{C_{m3}} \tag{81}$$

In the literature, it is possible to find optimal value for these non-dimensional geometrical parameters [33]-[56]. According to Mustapha, maximum efficiency occurs for flow coefficients in the range 0.2-0.3 and power input factor between about 0.9 and 1. The axial velocity ratio is usually near unity.

Outlet geometric characteristics can be calculated applying continuity, energy and momentum equation at impeller exit.

$$m = \rho_3 \pi R_{3t}^2 (1 - \frac{R_{1h}{}^2}{R_{1t}}) C_{3a} \tag{82}$$

The nozzle guide vanes and scroll design procedure has not been implemented inside the program. The program will only consider losses caused by these two components based on typical values which can be found in literature [56].

3.6.1. Radial In-Flow Turbine Design and Off-Design

The design procedure is an iterative process that aims to find the main geometrical parameters of the turbine. Table 4 describe the design input parameters.

Table 4. Radial In-Flow Turbine Design Input Parameters

Cycle Parameters		Impeller Geometrical Parameters	
Mass flow rate	$\dot{m}$	Power Input Factor	ψ
Total inlet pressure	T_{01}	Flow Coefficient	φ
Total inlet pressure	p_{01}	Axial velocity Ratio	ξ
Pressure Ratio	PR	Outlet tip radius/Outlet Hub radius	χ
Rotational speed	n	Number blades	Z
		Nozzle enthalpy loss	Δh_{nl}
		Axial clearance gap [%]	ε_{clT}
		Radial clearance gap [%]	ε_{clR}

The procedure it's iterative and starts assuming a value for the overall turbine efficiency, then applying the continuity, momentum and energy equations can evaluate the main geometrical parameters that characterised the turbine design. The process verifies the overall efficiency through empirical relationship and iterate until it reaches the convergence. The losses considered in this model are described below.

Incidence loss: the incidence loss is caused by a different in-flow angle from the blade constructive angle. According to Mustapha and Japikse [56] can be expressed as a kinetic energy loss using equation (83).

$$\Delta h_i = \frac{W_2^2 \, sin|\beta_2 - \beta_{2opt}|^2}{2} \tag{83}$$

Passage loss: Includes all the losses occurring in the impeller passage: skin friction, blade loading, mixing losses and losses due to secondary flows. According to Mustapha and Japikse [56] this loss can be calculated using equation (84) to (87).

$$\Delta h_{pl} = 0.11 * \frac{1}{2}\left(\frac{Lh}{Dh}\right)(W_2^2 + W_3^2) \tag{84}$$

$$L_h = \frac{\pi}{4}\left(\left(L_a - \frac{b_2}{2}\right) + R_2 - R_{3t} - \frac{b_3}{2}\right) \tag{85}$$

$$Dh = \frac{1}{2}\left(\left(\frac{4\pi R_2 b_2}{2\pi R_2 - Z b_2}\right) + \left(\frac{2\pi R_{3t}^2 \; 1-\chi^2}{\pi R_{3t}^2 \; 1-\chi \; + Z b_2}\right)\right) \tag{86}$$

$$L_a = 1.5 \; R_{3t} - R_{3h} \tag{87}$$

Where L_h is the hydraulic length, D_h is the hydraulic diameter, L_a is the axial length calculated using equation and is the ratio between the hub and tip inlet radius.

Tip clearance loss: A gap between the impeller and shroud must be included in the design, consequently a leakage from the pressure to suction sides occurs at the tip of the blade. Spraker [57] calculates the clearance loss by modelling the leakage flow and considering a simplify geometry of the shroud with a clear separation between axial and radial components.

$$\Delta h_{cl} = \left(\frac{U_2^3 Z}{8\pi}\right)\left(K_x \varepsilon_x C_x + K_r \varepsilon_r C_r + K_{xr} \sqrt{\varepsilon_x \varepsilon_r C_x C_r}\right) \tag{88}$$

$$\varepsilon_x = b_2 \left(\frac{\varepsilon_{clT}}{100}\right) \tag{89}$$

$$\varepsilon_r = \ R_{3t} - R_{3h} \ \left(\frac{\varepsilon_{clR}}{100}\right) \tag{90}$$

$$C_x = \frac{\left(1 - \left(\frac{R_{3t}}{R_2}\right)\right)}{C_{m2} * b_2} \tag{91}$$

$$C_r = \left(\frac{R_{3t}}{R_2}\right) \left(\frac{L_a - b_2}{C_{m3} R_{3m} \ R_{3t} - R_{3h}}\right) \tag{92}$$

With $Kx = 0.4, Kr = 0.75$ and $Kxr = -0.3$. ε_{clT} and ε_{clR} are the clearance percentage in axial and radial direction respectively.

Windage loss: it's caused by the flow leaked on the back face of the turbine disk. Daily and Nece [58] expressed this loss as a power loss function of the Reynolds number.

$$\Delta h_{wl} = \frac{1}{4} K_f \rho \omega^2 R_2^2 \tag{93}$$

$$\begin{cases} K_f = \dfrac{3.7 \left(\frac{\varepsilon}{R_2}\right)^{0.1}}{Re^{0.5}} & for\ Re < 10^5 \\ K_f = \dfrac{0.102 \left(\frac{\varepsilon}{R_2}\right)^{0.1}}{Re^2} & for\ Re > 10^5 \end{cases} \tag{94}$$

Nozzle and Scroll loss: According to Rodgers [59] all the losses contribute occurring in in the Nozzle and the volute can be summed and expressed by either a total pressure loss or static enthalpy loss using equation (95) and (96).

$$K = \frac{p_{01} - p_{03}}{p_{03} - p_3} \tag{95}$$

$$\xi = \frac{h_2 - h_{2s}}{\frac{1}{2} C_2^2} \tag{96}$$

According to Hiett and Jhonston [60] radial turbines in general shows a value for K within *0.05* and *0.13* for the volute and nozzle combined. Benson [61] obtained values of enthalpy loss ξ between *0.05* and *0.15*.

Considering all the losses discussed so far, using equation (97) it is possible to calculate a more accurate value for the overall turbine efficiency.

$$\eta_{TS} = \frac{\Delta h_s - \sum \Delta h_{loss}}{\Delta h_s} \tag{97}$$

To evaluate the off-design performances of a radial in-flow turbine, a similar model can be applied. As result of the design procedure, the geometrical parameters have been defined and the software can evaluate the off-design performances of the machine using the same relationships described so far.

To completely evaluate the off-design performances a relationship which correlates the mass flow rate to the pressure ratio and the inlet total temperature and pressure is needed. In early part of the 1900s, Stodola observed from experiments that the variation of the mass flow rate with the variation of exit static pressure for a turbine has the shape of an ellipse. According to Stodola [66], under the hypothesis of stationary, one-dimensional, adiabatic and isentropic flow, the mass flow rate provided by a turbine can be evaluated with a "nozzle analogy". Combining mass and energy conservation equations, it is possible to obtain equation (98).

$$m = \frac{p_{0in} A}{\sqrt{R T_{0in}}} * \sqrt{\frac{2k}{k-1}\left(\left(\frac{p_{out}}{p_{0in}}\right)^{\frac{2}{k}} - \left(\frac{p_{out}}{p_{0in}}\right)^{\frac{k+1}{k}}\right)} \tag{98}$$

Where m is mass flow rate, p_{0in} and T_{0in} the total inlet pressure and temperature, p_{out} is the static exit pressure and A the flow area. Many form of equation (98) are available in literature; one of the simplest and most used relationship is the Flügel formula given in equation (99).

$$m \propto \frac{p_{0in}}{\sqrt{T_{0in}}} * \sqrt{\left(\frac{p_{out}}{p_{0in}}\right)^{\frac{m+1}{m}} - 1} \tag{99}$$

$$\frac{m-1}{m} = \frac{k-1}{k}\eta_{pc} \tag{100}$$

With $\eta_P = 0.9$ and $k = 1.3$ the pressure ratio index $m + 1/m$ has a value around *1.8*, thus it is often approximated with *2* for both steam and gas turbines [64]. This is especially true when the turbine efficiency is not known *a priori*.

The Flügel formula and the ellipse law in general have been widely used for steam turbines, especially with large number of stages, demonstrating good accuracy for off-design performance analysis. Nevertheless, this model loses its accuracy when the number of stages is reduced, and then it is not particularly suitable for single stage radial inflow turbines. Moreover, the ellipse law does not consider the dependency on the rotational speed and efficiency [63].

To evaluate the characteristic maps of a radial inflow turbine, a model based on the Flügel formula has been developed. This formula does not consider the dependency on the rotational speed. For this reason, the modification adopted by Wang [62] was considered. The model in this form still doesn't consider the dependency on efficiency. The performance of a radial turbine can vary significantly from its axial counterpart and the approximation on the pressure ratio index may not be true. To remove this approximation, it is necessary to consider the real exponent of the thermodynamic transformation, which takes into account the irreversibility occurring in the turbine.

$$\mu^{off} = \mu * \vartheta * \sqrt{\frac{\left(\frac{p_{\text{out}}^{off}}{p_{\text{in}}^{off}}\right)^{\frac{m^{off}-1}{m^{off}}} - 1}{\left(\frac{p_{\text{out}}}{p_{\text{in}}}\right)^{\frac{m-1}{m}} - 1}} \tag{101}$$

$$\vartheta = \sqrt{1.4 - 0.4\left(\frac{n^{off}}{n}\right)} \tag{102}$$

In equation (101), μ is the corrected flow rate define as $\mu = m\sqrt{T_{01}}/p_{01}$. The superscripts off refers to off-design condition.

3.6.2. Turbine model validation

Usually, in MGT the expander characterised by a small diameter, relative low-pressure ratio, as they work in a recuperative cycle, and relatively high rotational speed. For this reason, the procedure described so far has been validated against experimental data available in literature for a design with the abovementioned characteristics [65]. The tests were conducted with a turbine inlet temperature of *400 K* and atmospheric exit static pressure in the range of rotational speeds *30-60 krpm*. Total to static efficiency were evaluated considering the temperature measurements, Total to Total efficiency was estimated using a model to determine the velocity at the exit. The characteristics maps were evaluated adopting the corrected mass flow rate as defined in equation (103) and considering the reference pressure equal to *101325 Pa* and the reference temperature to *288 K*.

$$\mu = \frac{m\sqrt{\frac{T_{01}}{T_{ref}}}}{\frac{p_{01}}{p_{ref}}} \tag{103}$$

Table 5. Turbine geometrical specifications

Rotor inlet tip diameter	*99.1 mm*
Rotor inlet tip width	*10.2 mm*
Rotor blade number	*11*
Rotor outlet tip diameter	*79.0 mm*
Rotor outlet hub diameter	*30.0 mm*
Rotor outlet blade angle, r.m.s. diameter	50.1^{o}

Table 5 shows the main geometrical characteristics of the radial turbine adopted for the validation of the present model. Results of the validation demonstrate good accuracy of the present one-dimensional model for a wide range of operating points (Figure 45 and Figure 46). The model reproduces quite accurately the behaviour of the turbine, especially near chocking condition, while for a given rotational speed, it seems to lose its precision accuracy moving to lower mass flow rates. Nevertheless, the maximum relative error is relatively low in the investigated range of operating points. This value is exceeded only in few points which are always below 13.1%. The coefficient of determination decreases with the rotational speed and it is always above 0.994.

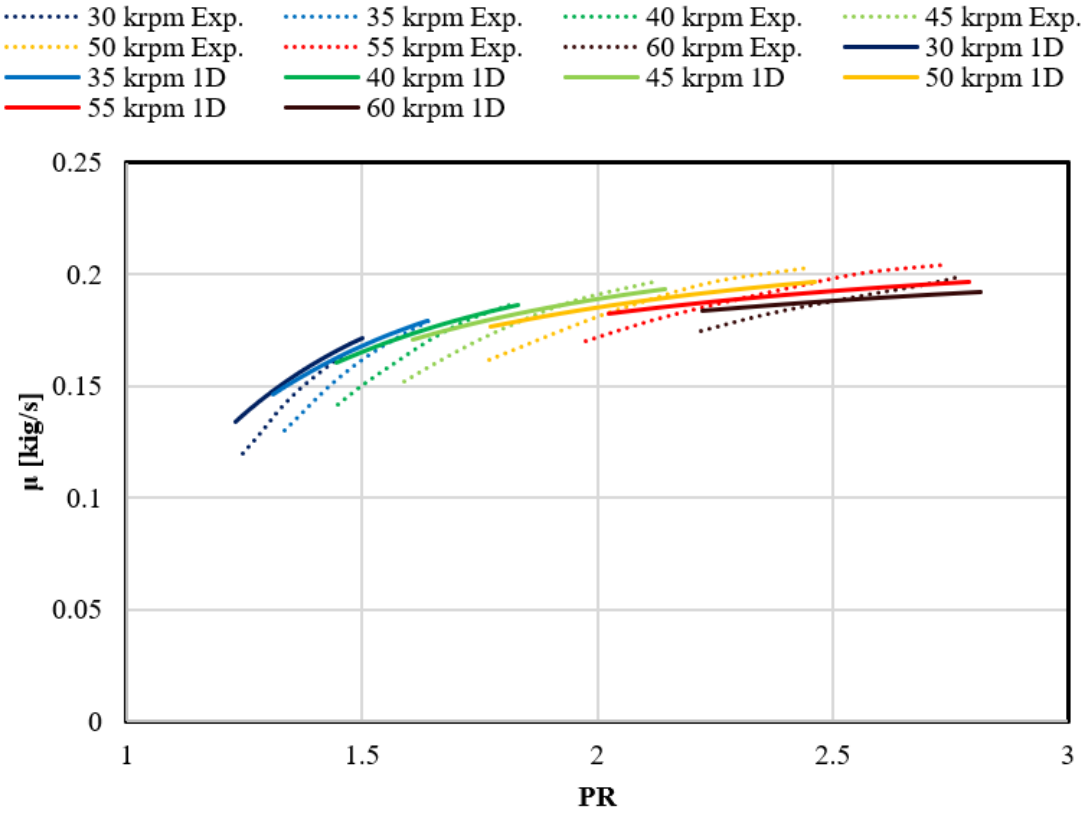

Figure 45. Results of the model validation.

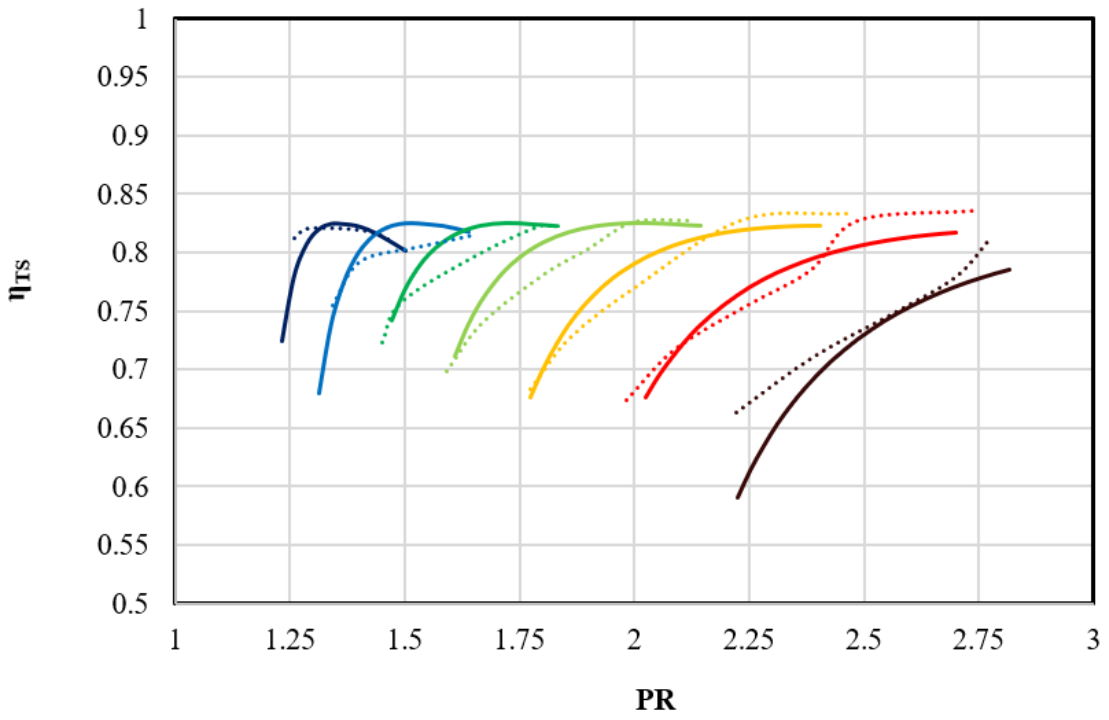

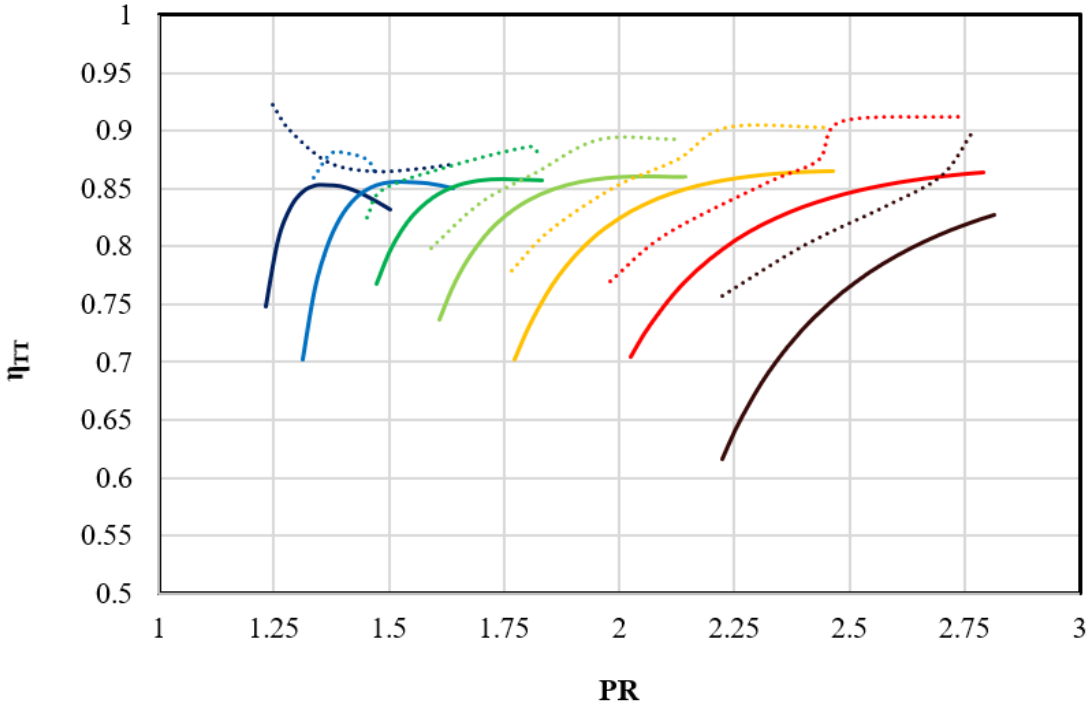

Figure 46. Comparison between analytical and experimental data. (a) Total to Static Isentropic efficiency. (b) Total to Total isentropic efficiency

3.7. Shaft, High Speed Generator and Power Electronics

3.7.1. Rotor dynamics considerations

A challenge is associated with the mutable solar irradiation requiring the MGT to operate at a much broader range than conventional technology. This has a substantial influence on the rotor dynamic design of the shaft-bearing organisation and mass distribution. At least three different mechanical arrangements can be considered for the MGT components (compressor, bearings, turbine and the electricity generator). These are as follows: cantilevered design, generator-in-middle design and coupled shaft design. The main features of each are summarised below:

Cantilevered arrangement: This is the most common arrangement in small-scale micro gas turbines. In this assemblage, the turbine and compressor are hanged from one end of the rotor. The main benefit of this design is that no substantial cooling is required for the high-speed generator (HSG) as incoming air to the compressor can act as cooling subsystem. The main drawback is that this design suffers from rotor dynamic issues.

Coupled shaft arrangement: In this design, two separate shafts are coupled, using flexible joint that does not transmit bending moment; one contains the rotor and the HSG and the other shaft will contain the compressor and turbine impellers. The rotor dynamics of this arrangement is improved compared to the cantilevered design and no excessive cooling is required for the HSG as it sits on a separate shaft and far from the turbine.

Generator-in-middle arrangement: The HSG rotor is located between the compressor and turbine wheels in this design. It provides a simpler mechanical design with improved dynamic stability. Similar to the coupled shaft design, it is possible to move all bending modes out of the extended range of operation required for the solar application. However, a more significant cooling is required for the HSG as it is sitting in the vicinity of the turbine wheel. [35]

A study was undertaken as part of OMSoP project showed that the generator-in-middle design could potentially fit better for the solar-powered MGT [67]. The study has considered different factors such as cost, reliability and losses. It was concluded that generator-in-middle arrangement could be more suitable for solar-only-powered micro gas turbine.

Another feature of the rotor dynamic for MGTs is the choice of bearings. Rolling angular contact ball bearings, oil film bearings, floating ring bearings, magnetic bearings and air/foil bearings are different choices for the MGTs. The ball bearings are the most common type. The technology is established; yet, it requires an oil system. Recent progression in the technological advance of high-speed ball bearing makes this equipment a possible selection for the MGTs. For CSP-based MGTs, some form of damping is mandatory to reduce the vibrations produced by passing through the critical modes. Squeeze film damping (SFD) is a viable alternative to be integrated with this type of bearing. More work in larger engines was done on magnetic bearings; however, their development and application cost for MGTs prevented them from being used despite their advantage of operating oil-free and the intrinsic aptitude to control vibrations. Foil air bearings have made important progress in recent times due to their high reliability and their oil-free operation. However, there is still much work to be done for the smaller machines in the lower power range to make them a feasible option.

In this study no further investigations will be done about the mechanical stability and no model will be developed about the mechanical losses. Constant value for these will be applied during off-design operation.

3.7.2. HSG and Power Electronics

The control strategy of the MGT needs to be adapted to the fact that the thermal input to the system cannot be used as a control parameter. Moreover, controlling the dish position in order to adjust the amount of thermal input power would not be an option due to the much slower dynamic response of the dish movement mechanism than that of the MGT dynamic response that is orders of magnitude apart. A feasible option to control the MGT in such system is by adjusting the power taken (or given) to the HSG. This would result in controlling the TIT, TET and rotational speed.

A different power electronic architecture can be considered for the CSP-based MGT. As mentioned before, the power electronics would be responsible for controlling the MGT alongside its primary function to convert the power to and from the grid; this would happen in the electronic power conversion system (EPCS). At least two different architectures can be considered for the power conversion system: single converter architecture and double converter architecture. All designs involve an active inverter to control the power output, as this is essential for solar-based MGT.

Ghavami [68] evaluate in details the performances of each component of the power electronic system of a solar based MGT. Chart in Figure 47 shows the efficiency of the HSG and power electronics, modelled as a single component, as a function of the rotational speed and power. The chart highlight roughly constant efficiency at any rotational speed for power outputs higher than $2\ kW_{el}$.

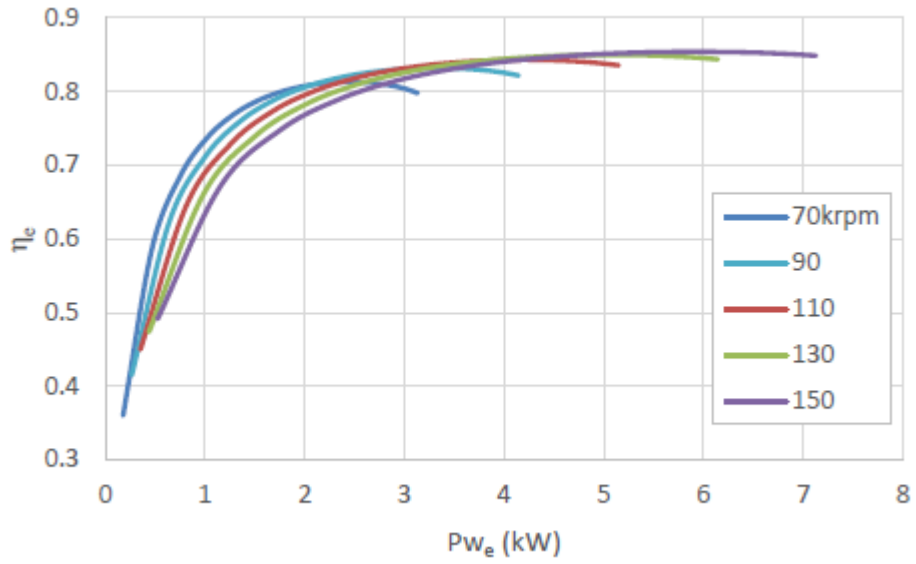

Figure 47. Efficiency of the HSG and power electronics, modelled as a single component, as a function of the rotational speed and power.

This study won't go into details about HSG and power electronics modelling. The overall efficiency of the power electronics system will be considered constant during off-design operations. As such, a minimum output power of the plant will be fixed to 2000 W and points with lower power output were not considered. It should be emphasised that considering any power below this level would neither change the annual produced electricity significantly nor the levelised cost of electricity.

3.8. Economic Model

Unlike large-scale gas turbines, only a few cost evaluation studies are available in literature for micro gas turbines. For this study, the approach used by [52] has been used and the cost functions for the different components are described by the following equations where all the costs are given in Euros.

$$C_{compr.} = 55.8 \cdot ln\ PR_c\ \cdot \left(\frac{m}{0.942 - \eta_{pc}}\right) \tag{104}$$

$$C_{turb.} = 376.1 \cdot ln\ PR_t\ \cdot \left(\frac{m}{0.903 - \eta_{pt}}\right) \tag{105}$$

$$C_{recup.} = 9 f_m \left(625.1 \cdot m \left(\frac{p_{in} \Delta p}{100}\right)^{-0.5} \cdot \left(\frac{\varepsilon}{1-\varepsilon}\right)\right) \tag{106}$$

$$C_{gen.} = 18.7\ P^{0.95} \tag{107}$$

Where PR_c and PR_t are the compressor and turbine pressure ratios, p_{in} the inlet pressure expressed in bar, Δp is the recuperator percentage pressure loss, m the mass flow rate in $[kg/s]$, ε is the recuperator effectiveness and P is the net power output in $[kW]$. The cost of the generator includes also the cost of power electronics and has been evaluated using. The receiver cost function was interpolated from a study conducted by pioneer engineering [55] for a pressurised air solar receiver, adaptable for a solar dish and micro gas turbine system. The study considered direct labour costs, direct material costs and manufacturing costs. Results from this study were interpolated and equation (108) was obtained which expresses the cost of receiver as a function of absorbed heat Q_{Rec} expressed in Watts.

$$C_{rec.} = 0.0304 \cdot Q_{Rec} \tag{108}$$

The dish cost is by far has the biggest contribution to the plant cost and it needs careful consideration for adequate prediction of the cost. In this study, the dish cost was evaluated using a regression model as described by equation (109) based on a study conducted by Gallup [53]. The study evaluated the specific prices of collectors in the range from *67 m²* to *230 m²* for different production volumes. According to Gavagnin et al. [54] the exponent n_{dish} does not vary significantly from unity for a wide range of dish diameters, for this reason a linear dependency of the dish cost from the paraboloid surface was considered.

$$C_{Dish} = 260 * A_{dish}^{n_{dish}} \tag{109}$$

In equation (109) A_{dish} is the dish surface area in $[m^2]$. The overall cost can be then calculated using equation (110).

$$C_{TOT} = C_{MGT} + C_{Receiver} + C_{Dish} + C_{inst} \tag{110}$$

In the previous equation, C_{inst} is the installation cost, which includes the cost of installation and other costs not related directly to components. On the base of the findings of a study conducted by Gavagnin et al. [54] has been approximated as *17%* of the total components' costs.

Using the Chemical Engineering Plant Cost Index (*CEPCI*) each calculated cost was discounted to update the costs at the current year as described in (equation (111)).

$$C_j = \frac{C_{ref} * (CEPCI_j)}{(CEPCI_{ref})} \tag{111}$$

where, C_j is the cost at year j, $\mathrm{CEPCI_j}$ is the Chemical Engineering Plant Cost Index for year, j, C_{ref} is a known cost of the components for a particular year and $CEPCI_{ref}$ is taken for the same reference year. The levelised cost of energy therefore can be calculated using equation (112).

$$LCOE = \frac{\alpha C_{TOT} + C_{O\&M}}{E} \tag{112}$$

$$\alpha = \frac{i * \ 1 + i \ ^n}{1 + i \ ^n - 1} \tag{113}$$

The capital recovery factor α, has been evaluated considering typical values of $i = 0.07$ for the actual interest rate and $n = 25$ *years* for the lifetime of the plant. Operation and maintenance costs have been estimated to be *5%* of the total cost as suggested by Gallup [53].

3.9. Conclusions

In this chapter a thermos-economic model of a solar dish MGT was presented. The model adopts a modular structure to guarantee an easy integration of new components such as combustion chamber or thermal storage units. Each component was modelled using one dimensional approach for design and off design performance evaluation. Every model was validated against experimental data demonstrating acceptable accuracy in the evaluation of the performances of the respective component.

The components presented in this chapter are: centrifugal compressor, off-set strip fin plate heat exchanger, air tube cavity receiver, radial turbine. To each component correspond a module in the software. Modules such as combustion chamber and thermal storage will be discussed in the following chapters. A special module for the fluid was created.

Compressor model demonstrates good accuracy for a wide range of compressor size and particularly suitable for plant optimisation purposes as every component must be re-designed many times. Recuperator model demonstrates higher accuracy with the fin *#1/10-27.03,* for this reason this geometry will be adopted latter. Nevertheless, both demonstrate good accuracy in performance prediction of the heat transfer device. It must be highlight that the accuracy of the model would not change with the size of the recuperator. Given the absence of experimental data in literature, receiver model lack of validation for a wide range of sizes. Nevertheless, the model demonstrates realistic results and was considered suitable for the purpose of this study. A radial turbine model based on Stodola's ellipse was presented. The model is an innovative concept compared to previous studies, which have applied this relationship mainly for steam turbines in isentropic conditions and with constant rotational speed. The model demonstrated higher accuracy compared to existing

models and was considered adapt for the purpose of this study. Nevertheless, for a given rotational speed the accuracy decreases when moving away from choking conditions and there is still ground for improvements. However, this study will demonstrate that this are not working conditions which the turbine will encounter during operations. Finally, the economic model adopted in this study and the component's cost functions were presented. The model is based on existing relationships which can be found in literature based on real components cost database.

4. Pure Solar System

In this chapter a case study of a pure-solar plant powered using a micro gas turbine is presented. The chapter will present firstly the plant design, which requirements are selected based on OMSoP project findings. The selected location is Rome.

Following, off-design performances, operational strategies, cost breakdown and the component's map are analysed and presented. To verify the capability of the software in evaluating the component's matching, the off-design results under variable DNIs are compared with a commercial software: *IPSEpro*.

Subsequently, plant optimisations are performed. Firstly, a plant size optimisation is presented to identify the size of the plant which minimise the levelised cost of energy and maximise the overall energy production, considering only the design mass flow rate of the plant as input parameter. Then, the influence of the design pressure ratio is investigate performing another optimisation of the plant. The optimisation was performed coupling a machine learning algorithm with a genetic algorithm.

4.1. Plant Design

As shown by Figure 48, the plant is comprised of a compressor, a recuperator, a solar receiver, a turbine and a high-speed generator to convert the available mechanical energy to electricity. Preliminary design characteristics have been chosen based on the findings of *OMSoP* project (*Ghavami, 2017*) and a previous work conducted by the authors (*Iaria et al., 2017*). Table 6 reports the preliminary design characteristics of the plant.

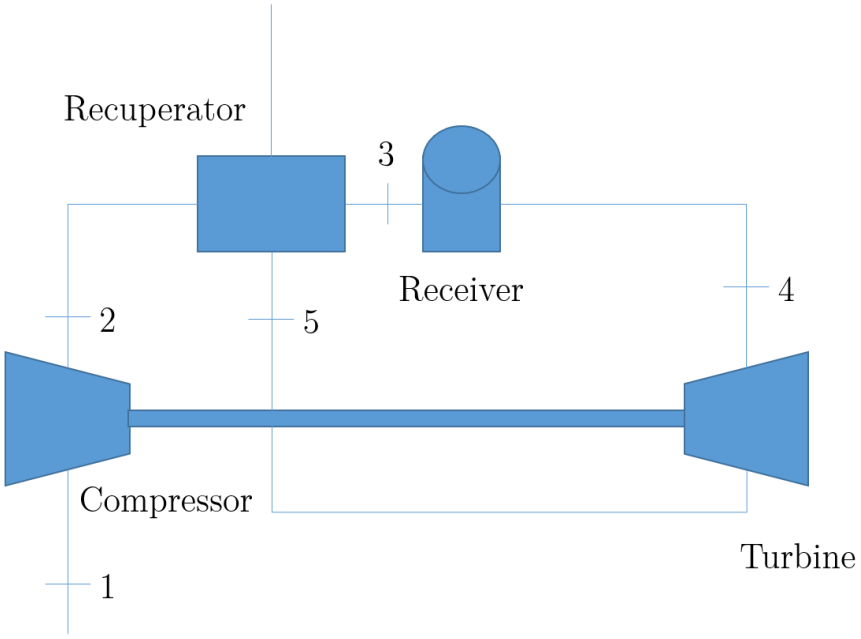

Figure 48. Schematic of a solar microturbine.

Table 6: Main design requirements

Design Point Requirements	
$\dot{m}$ *[kg/s]*	*0.09*
DNI[W/m²]	*800*
n [krpm]	*130*
p_{01}*[kPa]*	*101.3*
T_{01}*[K]*	*298*
TIT [K]	*1073*

In the previous table m is the mass flow rate, n the rotational speed, p_{01} and T_{01} the inlet pressure and temperature respectively and TIT the turbine inlet temperature.

The study has been performed considering data available in literature for solar irradiation in Rome for the period between January *2004* and *2005*. Rome was chosen as it is the construction site of the OMSoP project. *Figure 49* shows the DNI frequencies diagram and the moving average of the DNI for a constant period of *100* W/m^2 for the *DNI*. As can be seen in *Figure 49* the highest moving average frequencies levels, considering a period of 100, are for the *DNI* around the value of *800* W/m^2. For this reason, this value has been chosen as design *DNI* while *DNIs* lower than *300* W/m^2 have not been investigated due to negligible power that can be produced in such solar irradiation level.

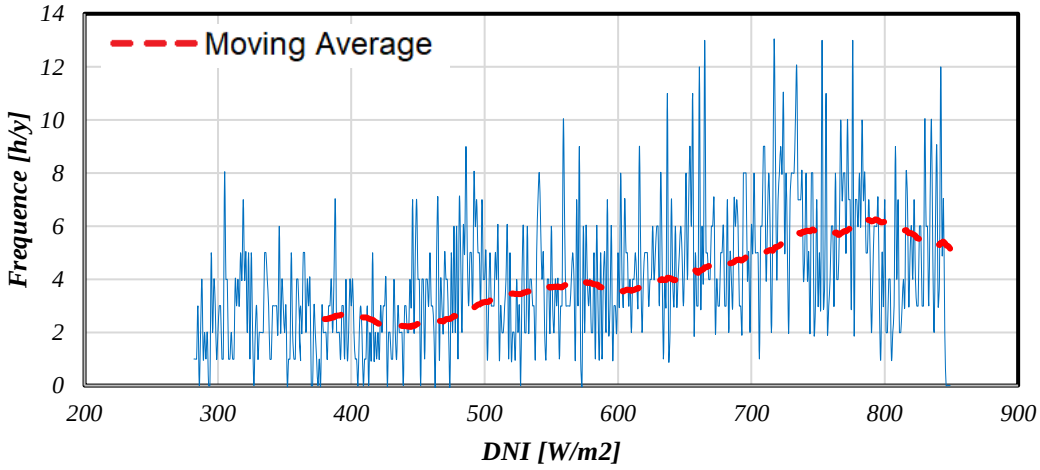

Figure 49. DNI frequencies in Rome for the period between 2004 and 2005 and the moving average of DNI (red line).

4.1.1. Design Results

The results from the design procedure are presented in *Table 7* based on the design requirements of *Table 6* and the chosen design *DNI*. The net power output

has been evaluated considering mechanical and electrical efficiencies of *90%* and *85%* respectively.

Table 7. The design parameters for the 7 kWe plant

Thermodynamic quantities		***Performance parameters***	
$\dot{m}$ *[kg/s]*	*0.09*	P_c *[W]*	*12316.7*
DNI [W/m²]	*800*	P_t *[W]*	*20361.7*
n [krpm]	*130*	*P [W]*	*6878.4*
p_{01} *[kPa]*	*101.3*	η_c	*0.796*
p_{02} *[kPa]*	*304.1*	ε_r	*0.850*
p_{03} *[kPa]*	*305.5*	η_r	*0.759*
p_{04} *[kPa]*	*299.5*	η_t	*0.818*
p_{05} *[kPa]*	*103.9*	η	*0.195*
T_{01} *[K]*	*298.1*		
T_{02} *[K]*	*435.4*		
T_{03} *[K]*	*804.0*		
TIT [K]	*1074.6*		
T_{05} *[K]*	*869.2*		

Using the models discussed previously, each component of the system was designed based on the performance parameters of those components given in *Table 7*. The compressor is composed of an impeller with *12* blades and a vaneless diffuser of *60 mm* radius. The impeller has a tip exit radius of *36 mm* and width of *1.5 mm*; the isentropic efficiency of the compressor is *0.80*. The *1/10-27.03* fin geometry has been adopted for the recuperator and it has an overall heat transfer surface area of about *17* m^2 and a heat transfer to volume ratio around *2900* m^{-1}. Its effectiveness was set to *0.85* and the heat transfer coefficient was evaluated at *163* W/m^2K and *119* W/m^2K in the hot and cold sides respectively. The pressure drop is estimated to be 1% at hot side and 3% at cold side.

Table 8. Detailed results of the components design for the compressor, receiver, dish, recuperator and the turbine

Compressor				Receiver and Dish			
Thermodynamic quantities		Geometry		Thermodynamic quantities		Geometry	
T_{01} [K]	298	R_{1t} [m]	0.0199	T_{out} [K]	1073	D_{cav} [m]	0.19
p_{01} [kPa]	101.3	R_{1h} [m]	0.0092	T_{in} [K]	803.7	L_{rec} [m]	0.336
T_{02} [K]	435.4	R_2 [m]	0.0368	p_{in} [pa]	308.6	L_{pipe}[m]	3.748
p_{02} [kPa]	304.1	b_2 [m]	0.0015	p_{out} [pa]	302.6	D_{pipe} [m]	0.04
p_{03} [kPa]	309.4	Z	12			D_{dish} [m]	8.37
		b_3 [m]	0.0015			N_{Turns}	8
		R_3 [m]	0.1000	Performances			
Performances				η	0.761	Q_{rad2} [W]	4578
η_{sTT}	0.796	η_p	0.834	Q [W]	26780	Q_{rad3} [W]	1761
				Q_{rad1} [W]	2044	Q_{Cond} [W]	58.6

Recuperator				Turbine			
Geometry		Heat Transfer		Thermodynamic Quantities		Geometry	
L_1 [m]	0.303	h_h [W/m^{2}K]	163.2	T_{0in} [K]	1073.6	R_{4t} [m]	0.0286
L_2=L_3 [m]	0.200	h_c [W/m^{2}K]	119.2	P_{0in} [kPa]	298.9	R_{4h} [m]	0.0149
p_f [m]	0.002	J_h	0.028	p_{0out} [kPa]	105.4	R_{4t} [m]	0.0286
δ [mm]	0.102	J_c	0.022	T_{0out} [K]	868.3	R_2 [m]	0.0385
δ_w [mm]	0.500	f_h	0.149			b_2 [m]	0.0044
λ [m]	0.003	f_c	0.106			Z	11
b_c=b_h [m]	0.001	ε	0.85				
Thermodynamic quantities				Performances			
G_h [m^3/s]	5.227	G_c [m^3/s]	5.149	η_{sTT}	0.799	η_p	0.790
T_{hin} [K]	868.5	T_{cin} [K]	436.4				
T_{hout} [K]	527.6	T_{cout} [K]	803.7				
p_{hin} [kPa]	105.4	p_{cin} [kPa]	309.5				
p_{hout} [kPa]	101.3	p_{cout} [kPa]	308.6				

The receiver is characterised by a cavity diameter of *19 cm* and length of *33.6 cm*. The overall length of the pipe, which has a diameter of *4 cm*, is *3.748 m* and is formed of a helical coiled pipe with *8* turns. The efficiency of the receiver is *0.76* while the overall pressure loss is around *3%*. Based on the receiver performance, the

dish aperture diameter required to produce the desired electrical power of 7 kWe is *8.37 m*, assuming dish optical efficiency of *0.8*. The turbine impeller, with isentropic efficiency of *0.799*, consists of 11 blades with an inlet radius of *38.5 mm*, exit hub radius of *14.9 mm* and exit tip radius of *28.6 mm*. Detailed results of the components design and off-design performances for the compressor, receiver, dish, recuperator and the turbine are reported in Table 8.

4.1.2. Components Maps

The characteristic maps of the components have been generated based on the models provided in section 3.3. Figure 50 shows the compressor maps which were obtained considering an inlet pressure of *101.3 kPa* and inlet temperature of *289 K*.

$$\mu = \frac{m\sqrt{\frac{T_{0,in}}{289\ K}}}{\frac{p_{0,in}}{101325\ pa}} \tag{114}$$

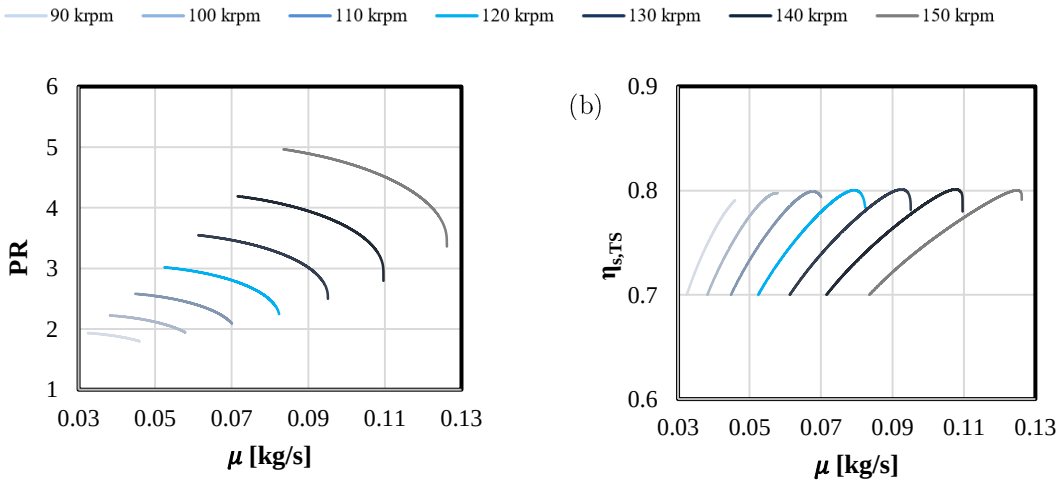

Figure 50 . Compressor characteristic maps. (a) Pressure ratio as a function of the corrected flow rate for different rotational speed. (a) Total to static isentropic efficiency as a function of the corrected flow rate for different rotational speed

Each rotational speed line is limited by the chocking limit for high mass flow rates and minimum efficiency of *0.7* for low mass flow rates which was considered as surge limit in any rotational speed. The charts report the efficiency (b) and the pressure ratio (a) as a function of the compressor corrected mass flow rate, where the corrected mass flow rate is defined by *Equation* (114).

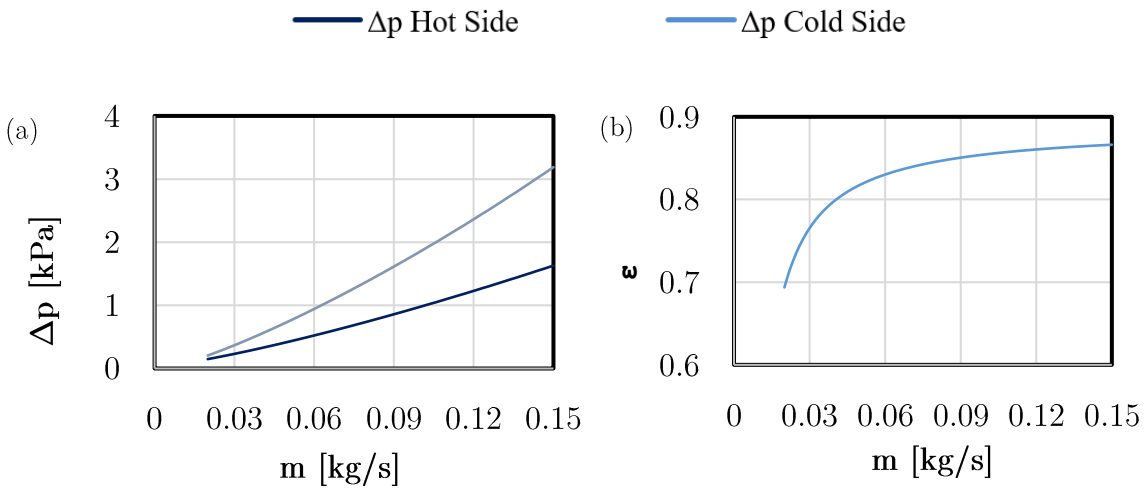

Figure 51. (a) Pressure drop across the recuperator as a function of the mass flow rate for both cold and hot side. (b) Recuperator effectiveness as function of the mass flow rate.

The receiver maps have been generated by varying the *DNI* under variable mass flow rate at a given inlet temperature (Figure 51). The proposed one-dimensional model was used to calculate the outlet temperature, the receiver efficiency and the pressure drop. The results suggest that the efficiency of the receiver is proportional to the mass flow rate, but the *DNI* has the most influence on the efficiency and the maximum achievable efficiency is dictated by its value. The calculations have been performed for ambient temperature of *298 K*, inlet temperature of *800 K* and inlet pressure of *308600 Pa*.

Figure 523 shows the turbine maps obtained for different rotational speeds, in the same operating range of speed of the compressor and similar to the compressor maps, each speed line is limited by the efficiency drop.

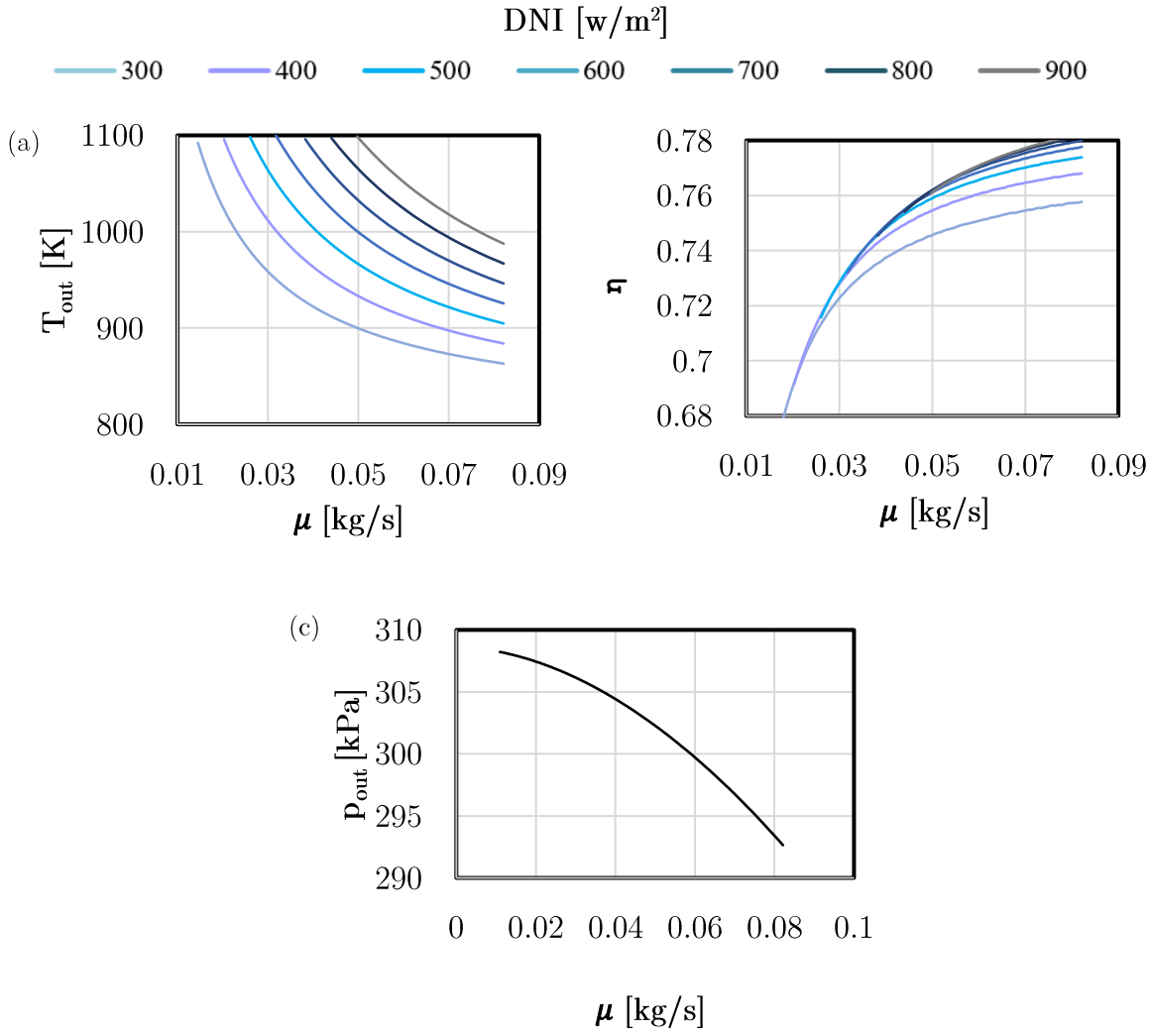

Figure 52. Receiver characteristic maps: variation of outlet temperature (a), efficiency (b) and outlet pressure (c) with air corrected mass flow rate

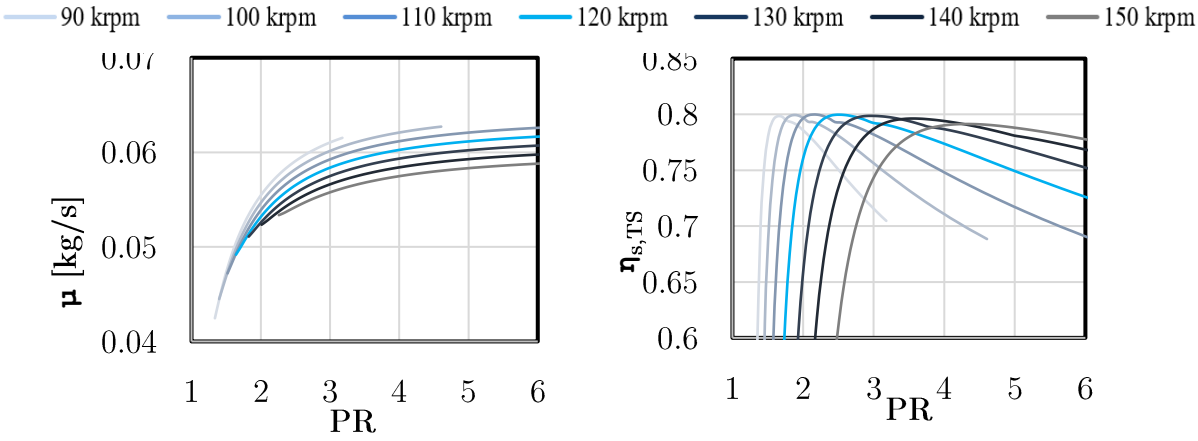

Figure 53. Turbine Characteristic maps: corrected mass flow rate and efficiency for different rotational speeds

4.1.3. IPSEpro simulation set-up

This section was developed in cooperation with Stavanger University and in particular with Prof. M. Hassadi and Dr. H. Nipkey. The micro gas turbine was modelled and simulated using a commercial software named *IPSEpro.* Characteristics maps for the turbomachinery and recuperator have been generated using the models of components as discussed in the preceding sections and are implemented in *IPSEpro* for off-design calculations. In the commercial software the inputs are rotational speed, *DNI* and ambient conditions, i.e. air relative humidity, ambient air pressure and ambient air temperature. The *TIT* is considered as constraint with maximum allowable limit of *1073±1 K*. The model outputs are pressure, temperature and mass flow rate at downstream and upstream of the components, by which performance indicators such as power and electrical efficiency are calculated.

4.2. Off-Design results

For typical pure-solar applications, the MGT operates with a constant *TIT*, at the highest allowable level, to maximise the overall efficiency of the plant. It should be noted that here, the *TIT* has been limited due to material limitation of the receiver rather than turbine material limitations. In case of OMSoP plant this limit was estimated at *1073 K*. To achieve a constant *TIT*, it is necessary to operate at variable mass flow rate and consequently variable rotational speed. For lower *DNIs* it wouldn't be possible to achieve the highest allowable *TIT*, which means the MGT will operate at low efficiency. Moreover, the power output for these operating points is relatively low as well as their occurrence frequency as shown in Figure 49. As such, a minimum output power of the plant was fixed to *2000 W* and points with lower power output are not considered. It should be emphasised that considering any power

below this level wouldn't change significantly the annual produced electricity nor the levelised cost of energy.

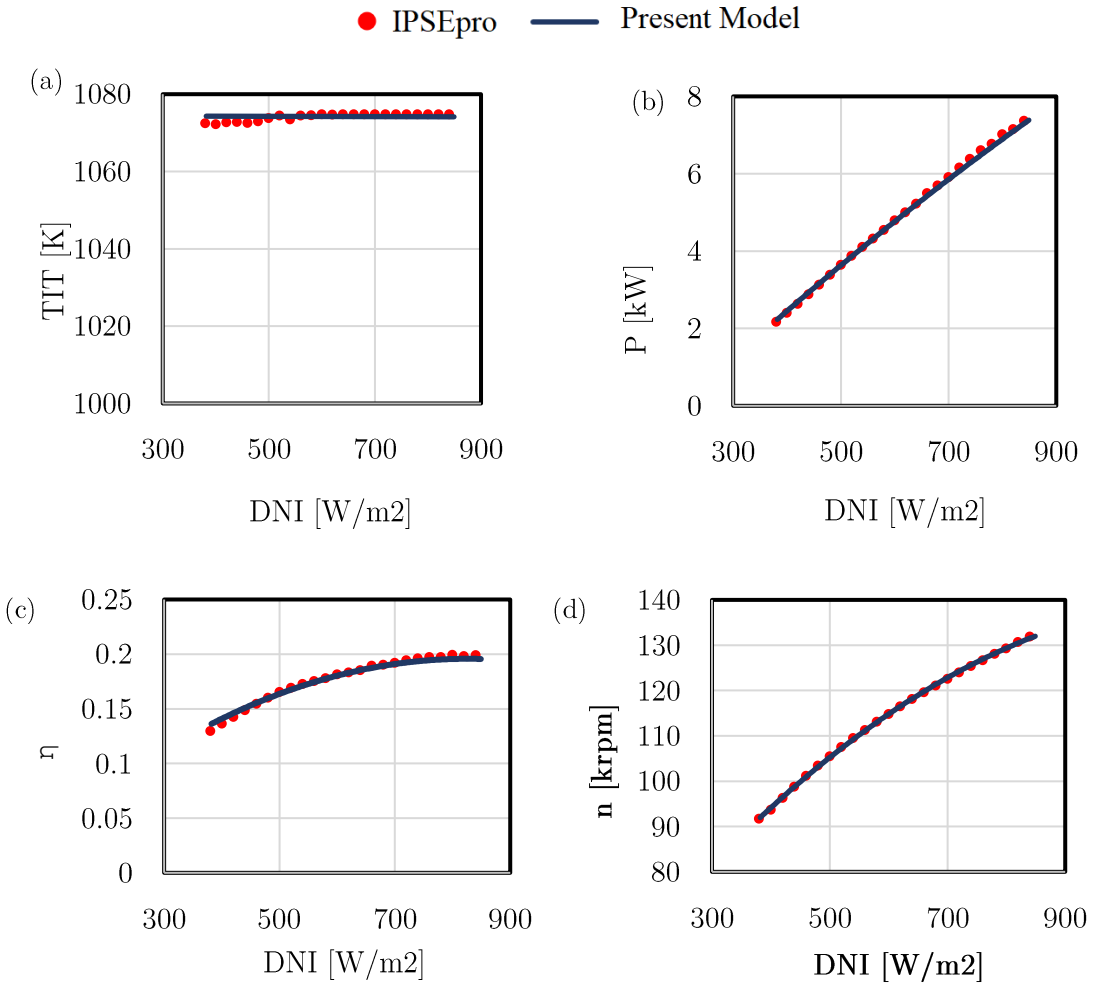

Figure 54. Plant Off-Design Performance charts: variation of TIT (a), output power (b), efficiency (c) and rotational speed (d) with DNI.

The results of the present model have been compared with the results from *IPSEpro* tool where the same components characteristic maps and operational strategy were considered. This comparison was aimed to verify the components matching procedure adopted for the present model. The results in *Figure 54* demonstrate good accuracy for the whole range of operation. The discrepancy in the results is due to the setup in *IPSEpro* where the *TIT* is limited not to a single value, 1073K in this case, but to a range with a minimum tolerance of *1K*. Thus, while the

desirable *TIT* is set to 1073 K in the present model this parameter was set to *1073±1 K* in *IPSEpro* model.

4.2.1. Operational strategies

Different control strategies can be conceptualised. In this study two different control strategy will be presented.

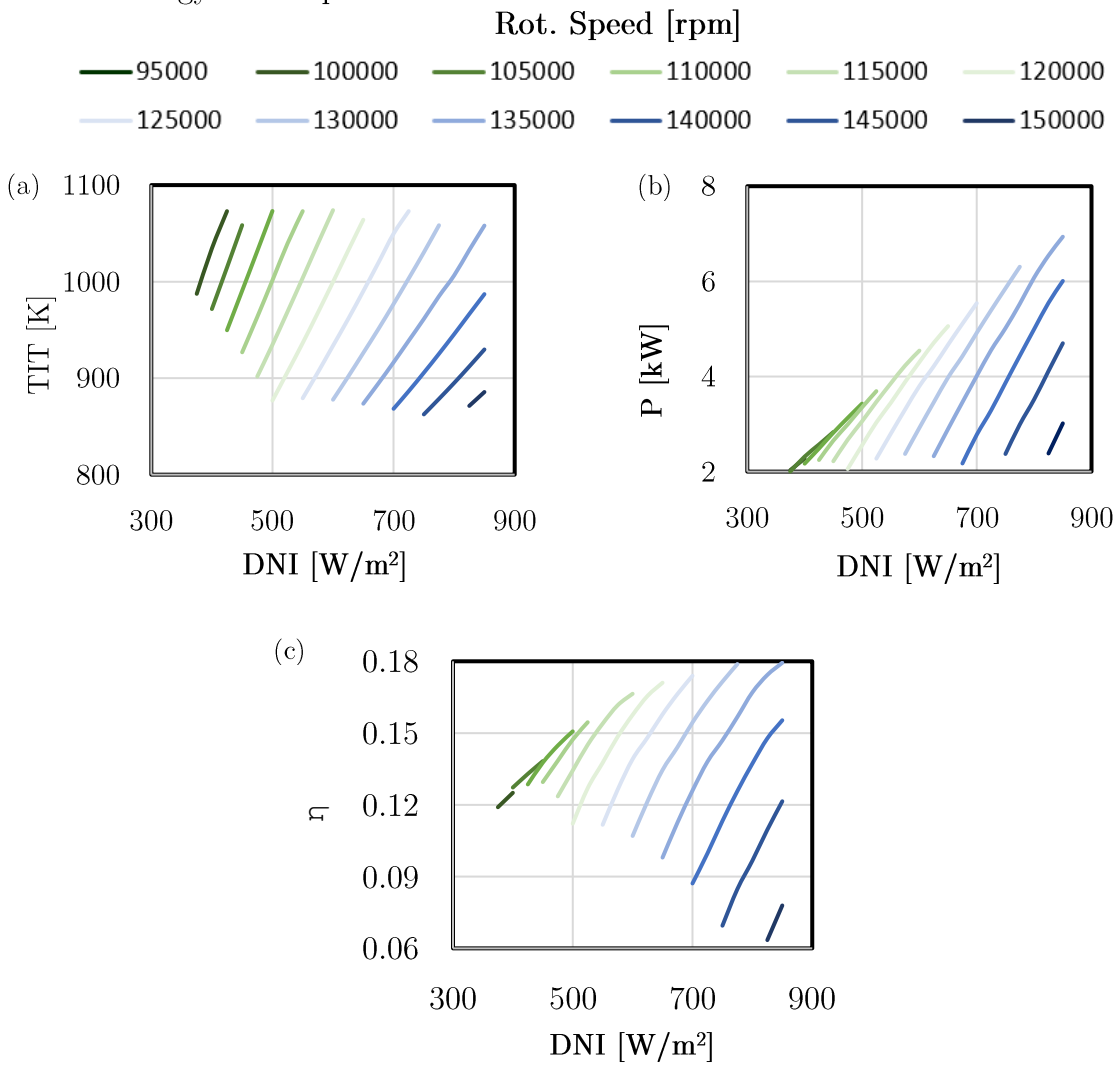

Figure 55. Control Maps of the plant. Variation of TIT (a), Power output (b) and efficiency (c) with DNI.

The first control strategy presented in the previous section adopt constant TIT to maximise the power output at any DNI with regards to the technological limits of

the plant. This control strategy can be adopted when the plant is integrated within a grid where potentially the plant is free to produce its maximum power. The second control strategy is characterised by constant power output where the plant needs to supply the demand of power generation or downstream productions such as desalinised water, fuel et. As shown by Figure 55 constant TIT can be achieved in most of the operating DNIs for a wide range of TITs. The situation is different for the power output, which range depends upon the selected value. Figure 55 shows the operating maps of the plant under variable DNI and rotational speed. The domain of feasible points it's limited by technological limits such as the maximum temperature of the receiver (*1073 K*), the component's matching and the minimum power output. The last limit was set based on the considerations already discussed in Chapter 1 about the HSG and the power electronics.

4.2.2. Cost Analysis

The annual electricity generation and the levelised cost of electricity have been

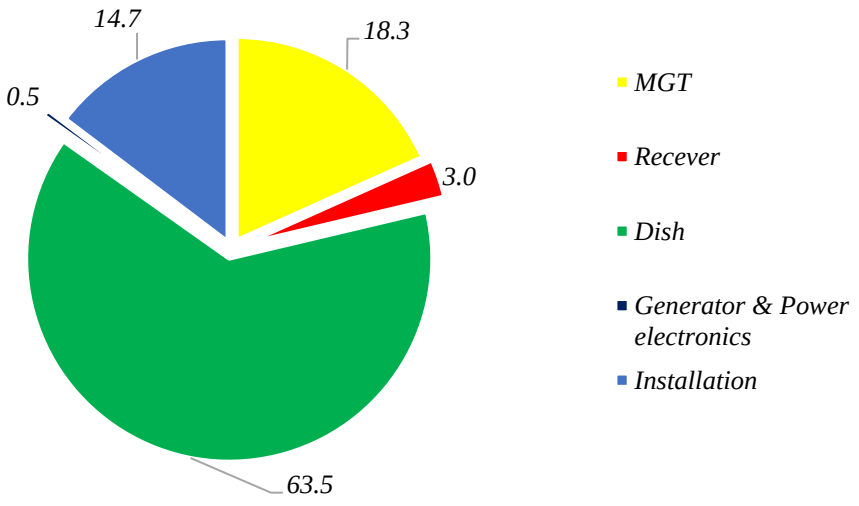

Figure 56. Cost breakdown of the plant

calculated using the components' characteristics maps and the plant overall performance parameters. The analysis has been carried out considering the *DNI*

frequencies in Figure 49 based on hourly average values of Rome in the period between *2004 and 2005*. For each DNIs the performance of the plant were evaluated and the overall energy produced by the plant was estimated to be *10 682 kWh*. Figure 56 shows the breakdown of the overall energy produced along the year by each *DNI* level and not surprisingly, the electricity is mostly produced during the high sun irradiance period in the range between *650* and *850* W/m^2.

The cost functions described previously have been used to estimate the cost of the plant and cost of producing electricity. Figure 56 shows the plant cost breakdown for different components of the plant. The capital cost has been estimated to be *27 051 €*, the specific cost of the plant, defined as the ratio between the cost of components and output power in design condition, has been estimated to be around *3980* $€/kW_{el}$. As can be seen in Figure 56, the costliest component is the dish with *63.5%* of the overall cost while the MGT represent *18.3 %* of the overall cost. Results from the LCOE analysis demonstrate a levelised cost of energy of *22.81 c€/kWh* considering a life cycle of the plant of 25 years. These results are comparable with those obtained by Gavagnin [54] considering 0.1 kg/s as design mass flow rate and *500 unit/year* production rate. In his study Gavagnin estimates a specific cost of the plant around 3700 *€/kWel* with a cost breakdown that consider MGT as 17 % of the overall cost, the dish as *62 %* and a receiver *4 %*. This gives confidence to the model which will be then used in the next section for optimisation purposes.

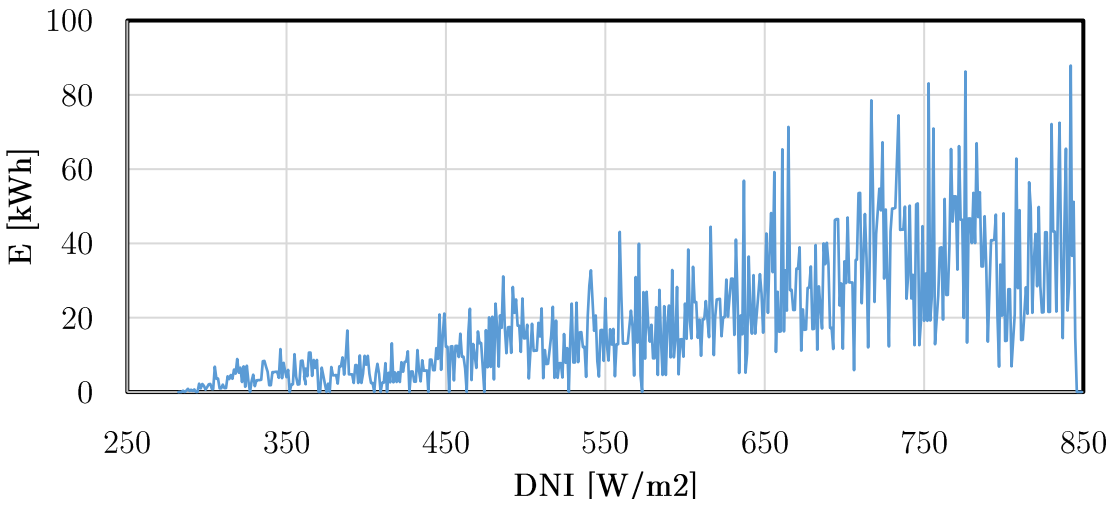

Figure 57. Annual energy produced at each DNI level

4.3. Plant Optimisation

In this section two different optimisation are presented. The first optimisation considers as input parameter only the design mass flow rate. The size of the plant is directly proportional to the design mass flow rate, for this reason this study will be named plant size optimisation. The second part of this section is dedicated to study the joint variation of the design pressure ratio and mass flow rate. Both optimisations aims to find the plant design parameters which minimise the levelised cost of energy and maximise the annual energy production.

4.3.1. Plant Size Optimisation

The analysis discussed above was repeated for different plant design parameters to optimise the plant size in order to achieve minimum *LCOE* while maximise the annual electrical production. Rome was selected as location site, characterised by *DNI* levels and frequencies already shown in *Figure 49*. For each given DNI an off-design performance analyses were carried out considering constant *TIT* as operational

strategy. The overall energy produced along the year was then calculated together with the levelised cost of energy. As discussed previously, the most expensive component of the plant is the dish and its size is directly proportional to the mass flow rate for a given *TIT*. On the other hand, the design mass flow rate is the main parameter influencing the power output of the plant and subsequently the annual electricity generation. For this reason, the mass flow rate was chosen as the optimisation variable, while pressure ratio and *TIT* were kept constant and equal to *3* and *1073 K* respectively. The design space of the optimisation variable is limited to the values *0.07-0.16 kg/s*. These limits have been evaluated to keep the compressor efficiency as high as possible by limiting the compressor specific speed to its optimum value. At both ends of this range, the compressor efficiency drops significantly.

As shown in Figure 58, results of the optimisation demonstrate a minimum *LCOE* of *21.53 [c€/kWh]* for a design point mass flow rate of about *0.11 kg/s*. This correspond to an overall cost of the plant around *32 600 €*, with a dish diameter of 9.4 m and an annual electricity production of *13 700 [kWh]*. As expected the annual energy production increases with the mass flow rate as has been shown in Figure 58.

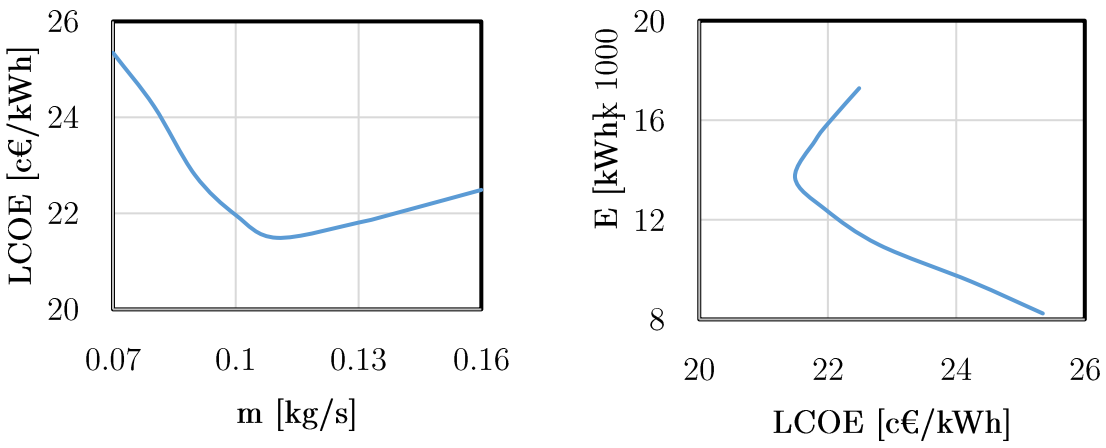

Figure 58. Plant size optimisation results. Left: Levelised cost of energy as function of the mass flow rate in design condition. Right: Energy produced along the year as function of the LCOE (pressure ratio = 3)

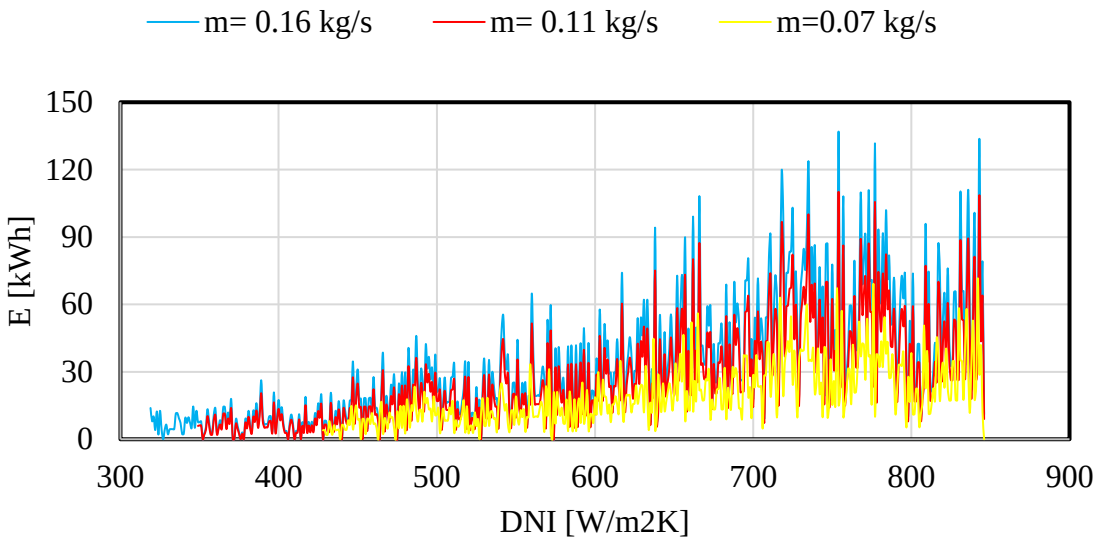

Figure 59. Specific annual power output for each DNI considering three different design mass flow rates.

As shown by Figure 59 *t*he range of *DNIs*, which the plant produces more than *2 kWe*, is getting wider with increase of the mass flow rate. Nevertheless, the dish size and consequently the overall cost is proportional to the mass flow rate; the right trade-off between annual energy production and levelised cost of energy should be decided based on specific power demand for each application. Figure 59 highlights that for the whole range of mass flow rate still most of the annual energy produced occurs in the range within *650* and *850 [W/m²K].*

4.3.2. Plant Design Optimisation

In this section a multi-objective optimisation of the plant is presented. A flow chart of the optimisation technique is shown in Figure 60. The technique is called response surface optimisation and generates an approximated function that can be used for optimisation purposes. Starting from the initial plant design performances, the first step is to select the variables (or parameters) influencing the optimisation process, the input and output parameters.

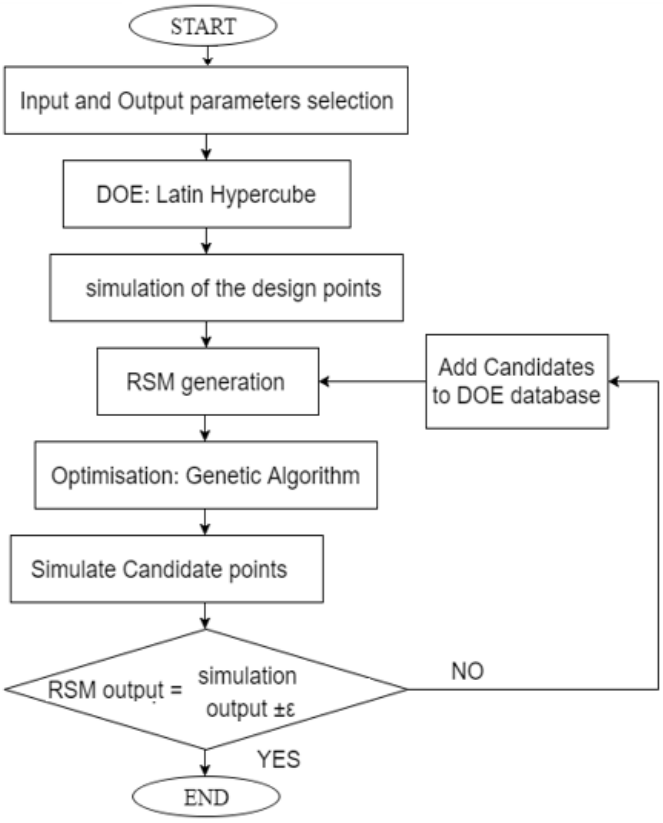

Figure 60. Flow chart of the optimisation technique.

Input parameters are needed to fully characterise the problem from the design point of view, but it should be taken into consideration that the complexity of an optimisation problem increases exponentially with the number of parameters. The output variables, resulting from the solution of plant simulations, are functions of the input parameters. These parameters give information about the problem and are the variables to be optimised.

A significant number of training points are needed to build the surface. To achieve the maximum accuracy with the minimum number of samples a DOE technique was used to generate the training database. Simulations output were used to evaluate the output variables for each point of the database.

The *DOE* technique used in this work is called *Latin Hypercube DOE*. Latin Hypercube uses a statistical approach to generate random training points (or

samples) for each parameter. The design space of each variable M is subdivided into N intervals of the same length, generating a matrix. The samples are chosen in these intervals, in such a way that each row and each column of the matrix are not selected twice. Different techniques are available to select the training points in the matrix, in this paper an orthogonal sampling scheme was used and all the samples were chosen simultaneously subdividing the intervals N into N sub-volumes. The selection process was performed by choosing the same amount of training points randomly from each of the sub-volumes.

The DOE was then coupled to an *RSM* to approximate the behaviour of the system in the design space. Among all the available techniques, the technique adopted in this study is the *Standard full second order polynomial*; a regression technique which determines the relationship between the input and the output parameters with a second order polynomial trend line.

The advantage of using a DOE with a RSM technique is that it is easy to apply an optimisation algorithm on it. The drawback is that it is still an approximation, and its accuracy depends on the number of training points used to generate the surface. To overcome this issue an iterative approach was applied:

1. Apply a DOE+RSM technique.
2. Run a response-surface-based optimisation.
3. Simulate the optimisation candidate points.
4. Add the new samples to the DOE database.
5. Update the RSM and repeat until the accuracy of the surface meet the requirements.

Once the response surface is built, its goodness must be evaluated through statistical quantities. During the optimisation and in particular during the response surface

building, for each output parameter the following statistical quantities will be calculated in order to estimate the goodness of the response surface:

Coefficient of Determination (R^2): In statistics, the coefficient of determination, denoted R^2, is a ratio that indicates how well data fit a statistical model or in our case is the statistical measure of how well the regression line approximates the real data point and give some information about the goodness of fit of a model. The best value is *1*.

$$R^2 = \frac{\sum_{i=1}^{N}\left(Y_i - \widehat{Y}_i\right)^2}{\sum_{i=1}^{N}(Y_i - \bar{Y}_i)^2} \tag{1}$$

Root Mean Square Error: The RMSE represents the standard deviation of the differences between predicted values and observed values. The best value is *0*.

$$RMSE = \sqrt{\frac{1}{N}\sum_{i=1}^{N}\left(Y_i - \widehat{Y}_i\right)^2} \tag{2}$$

Where:

N= Number of samples.

Y_i= Predicted value of the output parameter at the *i*-th point

$\widehat{Y}_i$= Actual value of the output parameter at the *i*-th point

$\bar{Y}_i$= Arithmetic mean of the values of the output parameter.

σ_y = Standard deviation of the values

The selected optimisation variables in this study are two: The mass flow rate and the pressure ratio at design condition. The design space of the optimisation is

constrained by the compressor: for a given rotational speed the variation of pressure ratio and mass flow rates lead to a variation of the isentropic enthalpy difference and consequently the specific speed. This lead to reduced design efficiency of the compressor. For this reason the considered range is limited as shown by Table 6.

Table 9. Design space of the optimisation

	PR	$\dot{m}$ [kg/s]
Lower bound	2.7	0.07
Upper bound	3.6	0.16

The output parameters of the optimisation are the total energy produced along the year (E_{TOT}), the overall cost (C), the levelised cost of energy ($LCOE$) and the maximum power output (P_{MAX}).

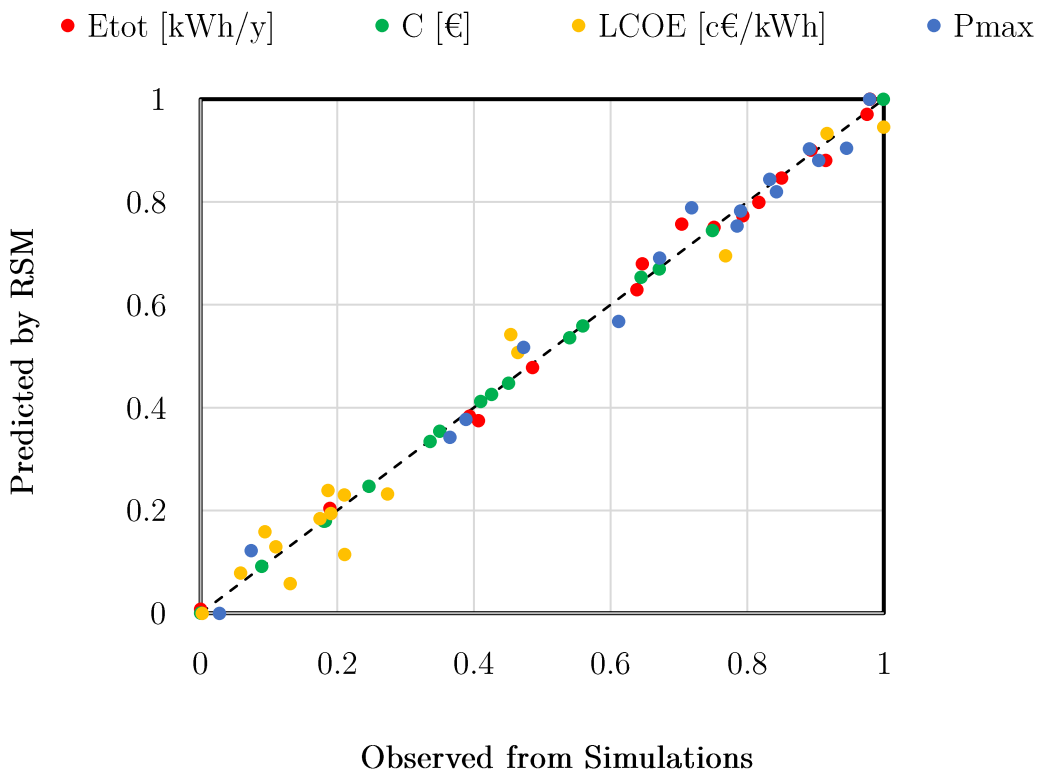

Figure 61. Goodness of fit of the response surfaces.

Figure 61 shows the goodness of fit of the optimisation. The chart compares the normalised value, of any output parameter, predicted by the response surface and the value observed from the design point. An accurate response surface must guarantee a distribution nearby the x-y axis bisector line. As shown by Figure 61 the output parameters predicted by the surface are fairly distributed along the bisector of the x-y axis. Moreover, as shown by Table 10, statistical analysis also confirmed the accuracy of the response surface in predicting the output parameter values. For any output parameter, the coefficient of determination is above 0.97 and the root mean square error is always two order of magnitude lower than the absolute value.

Figure 62 shows an example of the generated response surfaces. As highlight by the charts the levelised cost of energy presents a minimum in the range of pressure ratios between 3.1-3.4 and mass flow rates 0.09-0.12. On the other hand, the annual energy production presents its maximum value in the range of pressure ratios 3.2-3.6 and mass flow rates 0.12-0.16. This situation highlights the necessity of a multi-objective optimisation of the plant design parameters. The aim of the optimisation is to maximise the annual energy production while minimise the levelised cost of energy.

Table 10. Statistical analysis of the response surface

`	E_{TOT} [kWh/y]	C [€]	LCOE [c€/kWh]	P_{MAX} [W]
R^2	0.994	0.999	0.971	0.987
RMSE	164.8	78.6	0.34	140.34

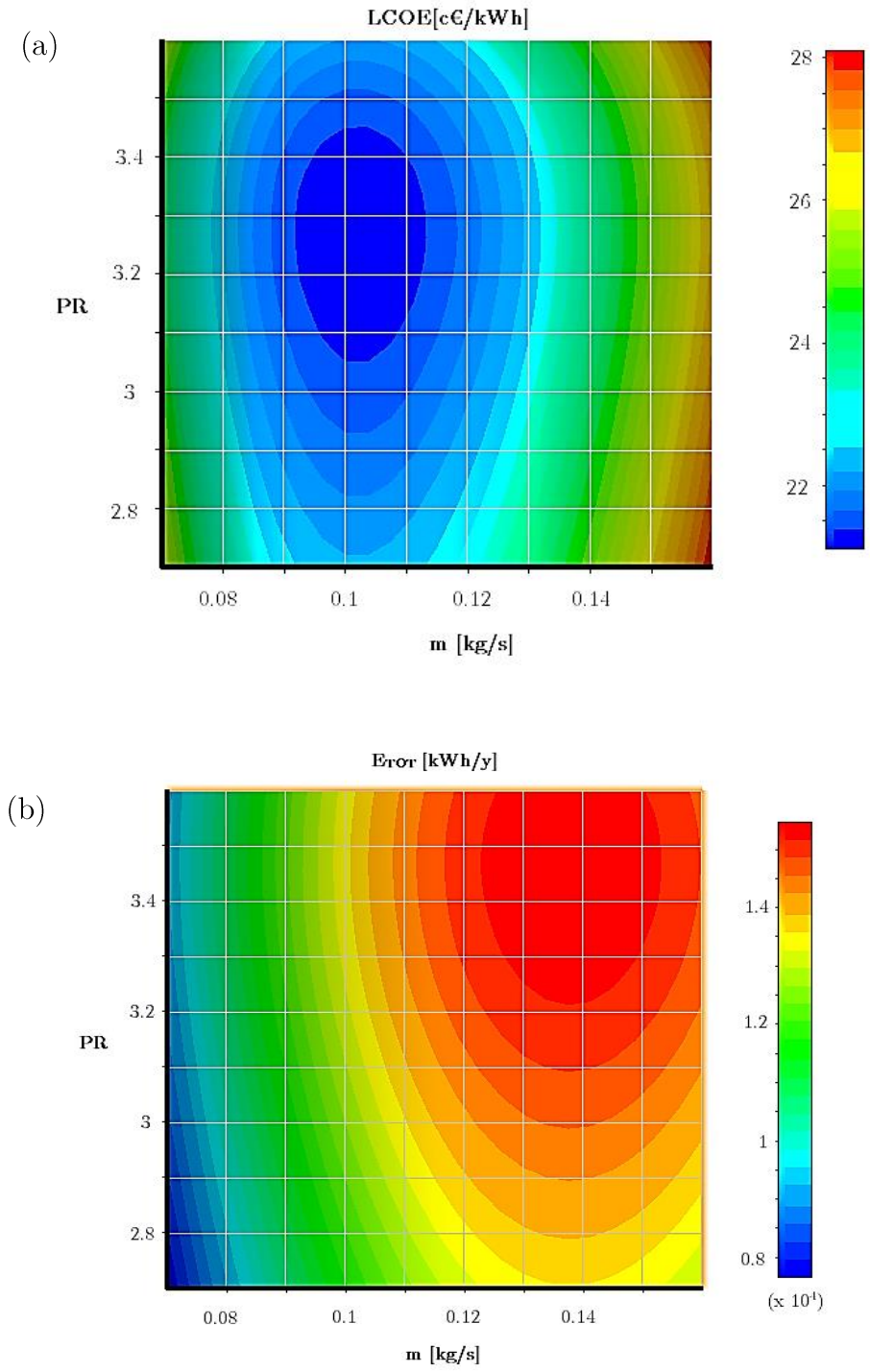

Figure 62. Response Surface: (a) LCOE as function of design PR and mass flow rate. (b) Annual energy generated as function of design PR and mass flow rate.

The optimisation algorithm used in this work is a Multi-Objective Genetic Algorithm (*MOGA*) considering as convergence criteria a convergence stability percentage of 0.2 % and a maximum allowable Pareto percentage of 95 %. The first

represent the stability of the population in the current generation, the second is the ratio between the number of points on the Pareto front and the number of samples.

Convergence was achieved after 7 iterations with an overall number of generated points of $7*10^4$. Figure 63 shows the history of the generated points for the two optimisation variables. The charts highlight that convergence was achieved. As outcome of the optimisation a Pareto front was generated (Figure 64) and 5 candidate optimum points were selected and analysed.

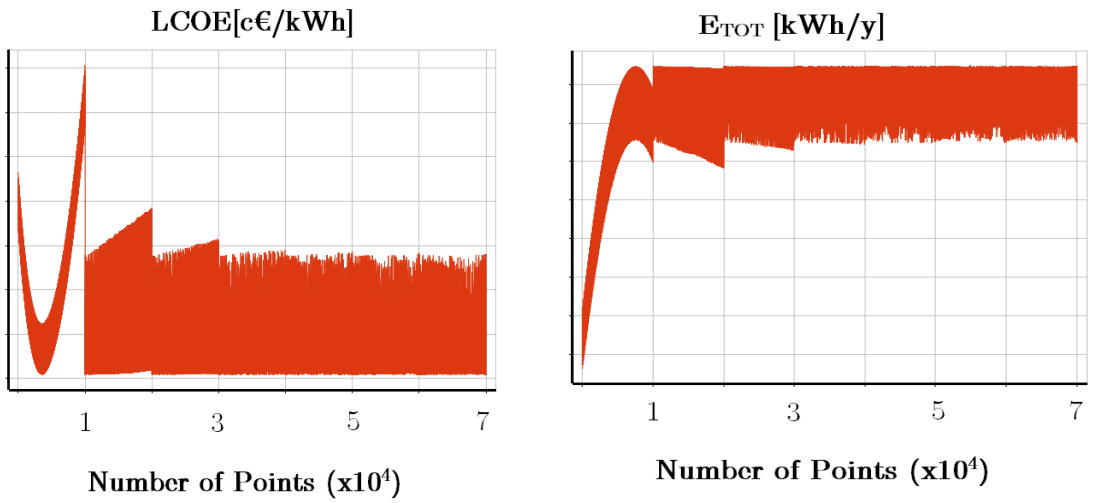

Figure 63. History of the optimisation variables

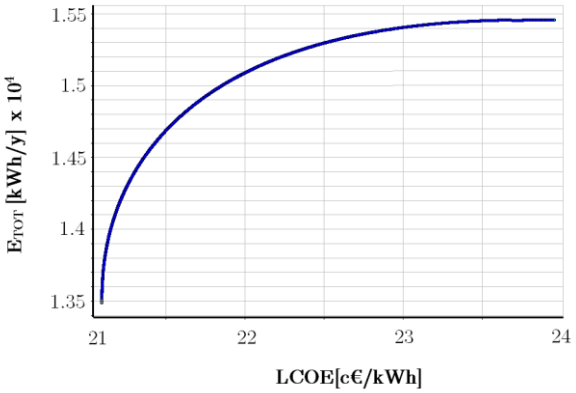

Figure 64. Pareto front of the optimisation.

Table 11. Candidate points in output from the optimisation.

	m [kg/s]	PR	E_{TOT} [kW/y]	C [€]	LCOE[c€/kWh]	P_{MAX}[W]
Candidate 1	0.12	3.34	14712	35492	21.52	9441
Candidate 2	0.12	3.35	14801	35834	21.61	9485
Candidate 3	0.12	3.37	14952	36460	21.79	9562
Candidate 4	0.12	3.35	14956	36475	21.79	9574
Candidate 5	0.12	3.36	14957	36478	21.79	9573

Candidates' analysis highlights that optimum performance and cost can be achieved with a mass flow rate of 0.12 kg/s and a pressure ratio oscillating between 3.34 and 3.37.

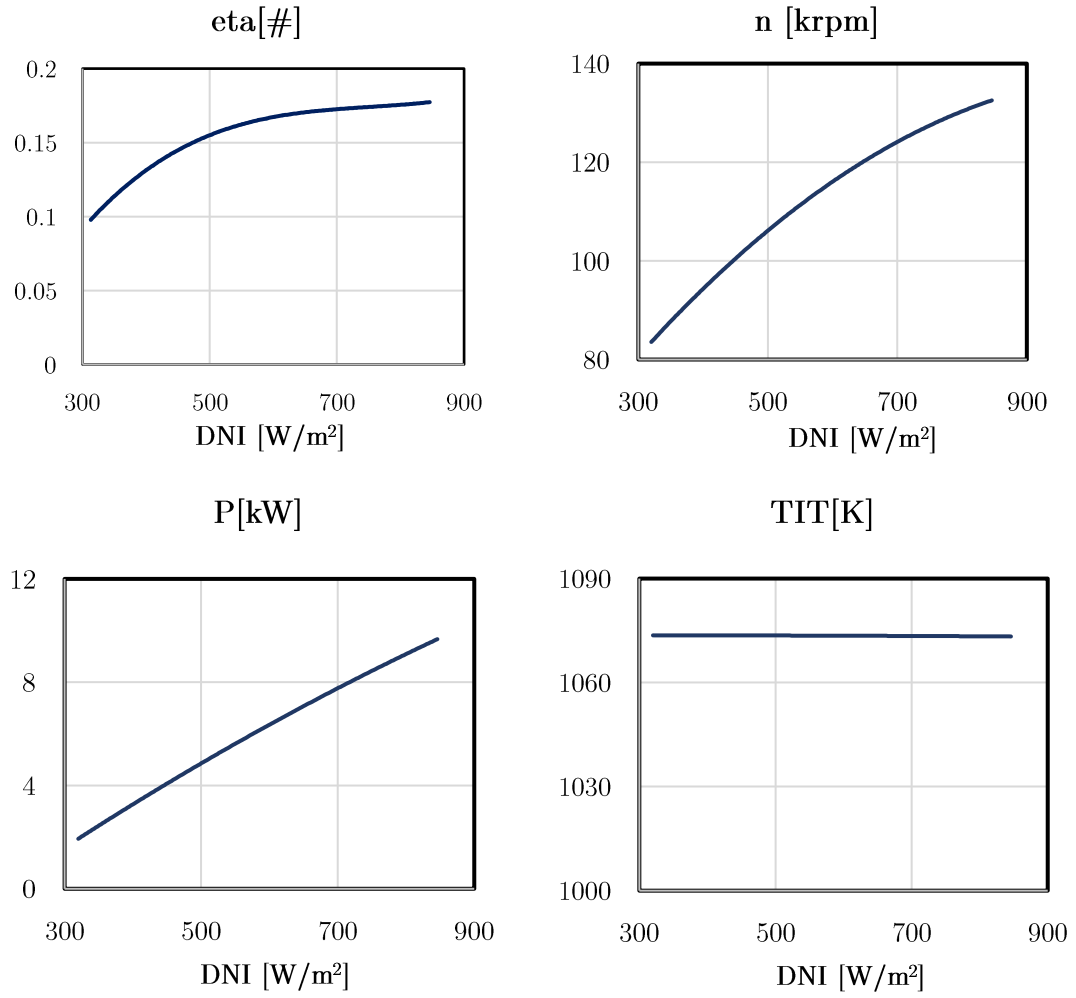

Figure 65. Plant Off-Design Performance charts: variation of TIT, output power, efficiency and rotational speed with DNI.

Off-design performance of the candidate #1 was analysed. As shown by Figure 65, plant's operations are characterised by a maximum power output of about 9.5 kW, while minimum power was fixed to be 2 kW as already discussed in Chapter 1. The maximum efficiency of the plant is 0.185, it drops down to 0.1 during low sun irradiation periods. TIT is fixed to *1073 K* as required by the operational strategy. Rotational speed varies in the range *85 krpm - 135 krpm*. The specific cost of the plant is *3760 [€/kW]*.

4.4. Plant Parametric Analysis

In this section a parametric analysis of the plant is presented. Starting from the multi-objective optimisation candidate point the techno-economical performances of the plant were analysed considering dissimilar recuperator effectiveness and *TIT* at different locations characterised by different *DNI* levels. The locations considered in this study are Rome, Seville and Azalim (Israel).

Results from the parametric analysis demonstrate that minimum LCOE can be achieved with a recuperator effectiveness around 0.8~0.85. Lower recuperator effectiveness causes the efficiency of the plant to drop, while higher effectiveness increases the cost of the component with consequent augmented cost of investment and *LCOE*. On the other hand, as shown by Figure 67 the overall energy produced along the year increases with the recuperator effectiveness. Regarding the *TIT*, increasing the turbine inlet temperature decreases significantly the *LCOE* with major influence also on the overall energy produced along the year. Increasing the *TIT* has also a major influence on the optimum recuperator effectiveness. Its optimum value indeed is shifted on the right side of the chart towards higher values. Increasing the

TIT plays also a major role in the overall energy production along the year, significantly increasing its value at any location and recuperator effectiveness.

Figure 67 shows the energy produced along the year versus the levelised cost of energy. The chart highlights a significantly reduction of the levelised cost of energy when the TIT is increased. The overall energy produced along the year displays the same behaviour. The curves have been constructed considering variable recuperator effectiveness.

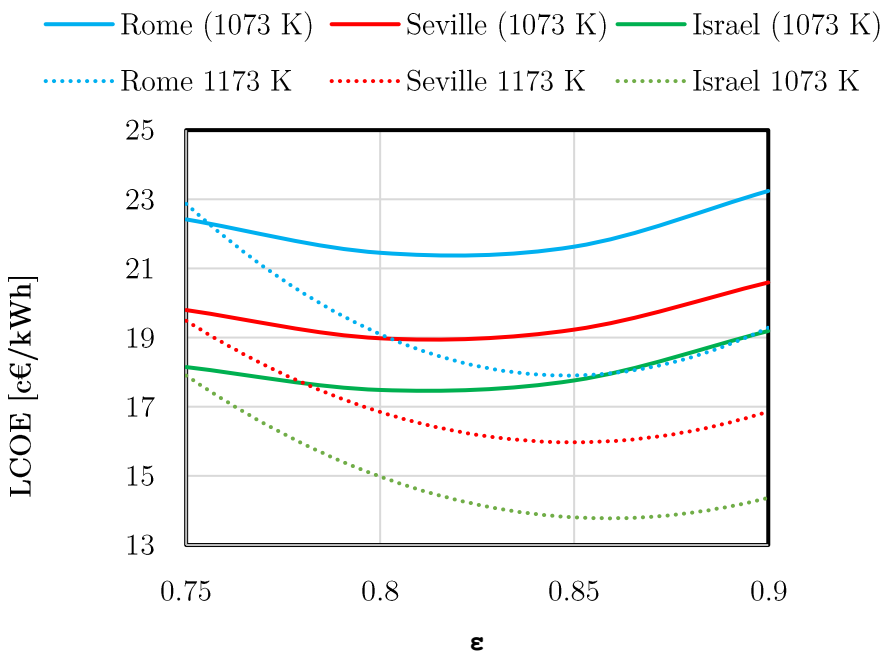

Figure 66. Results of the parametric analysis, LCOE versus recuperator effectiveness for different locations and TITs.

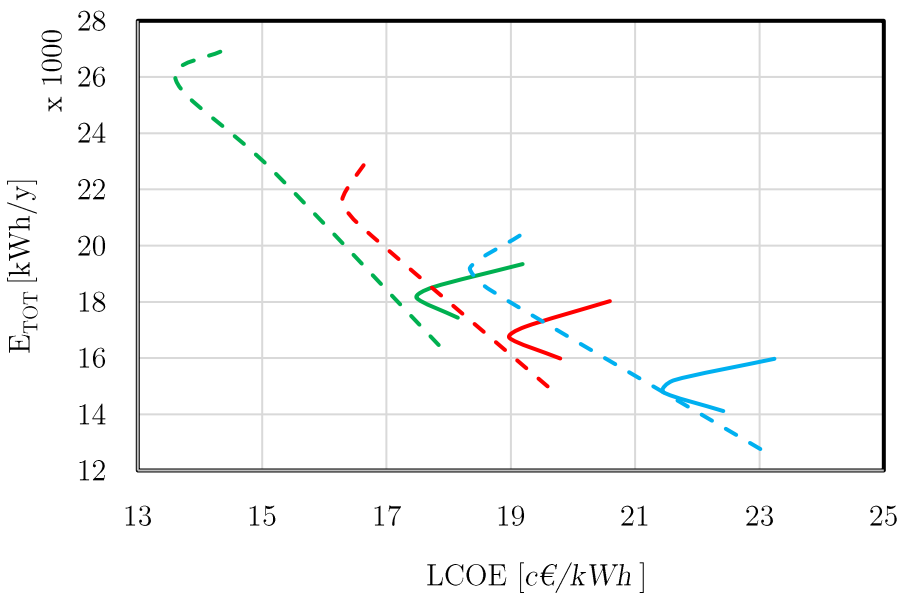

Figure 67. Total annual energy produced versus levelised cost of energy. Comparison between different locations and TITs.

4.5. Conclusions

In this chapter a thermo-economic assessment of a pure solar microturbine was presented. In the first part of the chapter, a *7kW* microturbine case study was analysed. Plants' design and off-design performances were examined by the tool described in Chapter 1 and compared with the results in output from a commercial software named *ipsePRO 7*.

The chapter continues with a plant size optimisation, a single objective optimisation carried out to verify the applicability of the present model for optimisation purpose. The study was aimed to identify the mass flow rate of the plant which minimise the levelised cost of energy. Results from the optimisation demonstrate minimum *LCOE* at mass flow rate of about *0.11 kg/s*. This correspond to an overall cost of the plant around *32 600 €*, with a dish diameter of *9.4 m* and an annual electricity production of *13 700 [kWh]*.

Following, a multi-objective optimisation of the plant was performed. The optimisation technique adopted in this study is called "Response surface optimisation". These techniques actually a combination of different techniques aimed to generate a regression function which correlates input and output parameters. This regression functions can be then easily coupled with an optimisation algorithm. The algorithm adopted in this study is a genetic algorithm.

Statistical analysis was performed on the regression surfaces to verify the accuracy of the model. Results from statistical analysis demonstrated, for any output parameter, coefficient of determination above 0.97 and root mean square error always two order of magnitude lower than the considered absolute value. The response surfaces generated indicate that the levelised cost of energy presents a minimum in the range of pressure ratios between 3.1-3.4 and mass flow rates 0.09-0.12 kg/s, while the annual energy generated presents its maximum value in the range of pressure ratios 3.2-3.6 and mass flow rates 0.12-0.16 kg/s. The optimisation was then aimed to find the optimum trade-off between these two parameters.

As outcome of the optimisation a Pareto front was generated and five candidate points belonging to this curve were selected. One of these candidates was analysed during off -design operations and a parametric study was performed on it. Results from parametric analysis demonstrate minimum LCOE with a recuperator effectiveness around 0.8~0.85 and TIT at its maximum value. The parametric study also confirmed that the location has major influence and the levelised cost of energy can drop as low as 13 $c€/kWh$ in high sun irradiance locations such as Azalim.

LCOE analysis demonstrate levelised cost of energy comparable with other concentrated solar technologies already analysed in section 2.7. Especially when compared with similar size power plants such as dish Stirling.

5. Hybrid System

In this chapter a techno-economic analysis for a solar hybrid dish is performed. Firstly, a model for design and off-design performance evaluation of a can combustor is presented, then a techno-economic analysis of the plant is performed to evaluate the performance of the plant under variable DNIs and estimate the levelised cost of energy.

Two different operational strategy are presented in this study: constant power output and constant receiver outlet temperature. In both cases, a multi-objective optimisation is carried out to find the design parameters which maximise the annual energy output and minimise the levelised cost of energy. Environmental aspects such as CO_2 and NO_X emission are also considered.

5.1. Combustion Chamber Model

Typically for MGT applications several combustor arrangements are adopted [73]. A first option is an annular reverse flow combustor (Figure 68 (a)), this arrangement can guarantee the maximum compactness of the MGT as the inlet and outlet of the combustor are very close to each other. Another layout widely adopted is the can combustor as shown in Figure 68 (b). This arrangement is characterised by high performances and reduced emissions. Moreover, studies conducted by Cameretti demonstrated the applicability of this arrangement for

MILD (Moderate and Intense Low-oxygen Dilution) combustion regime adopting fuels such as methane or biofuel [20]. MILD combustion represents a promising technology to further reduce the emissions of those systems. This arrangement will be adopted in this study.

(a)

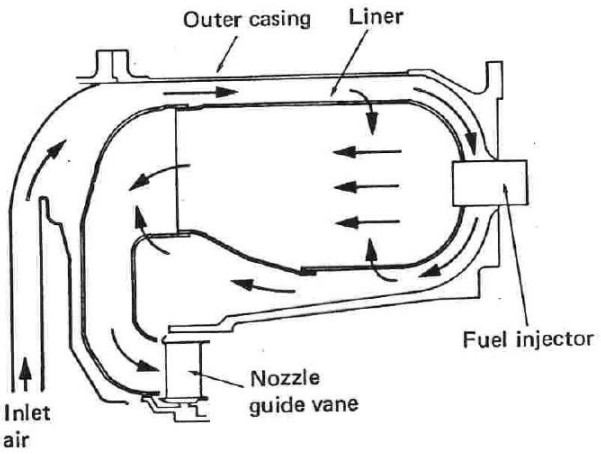

(b)

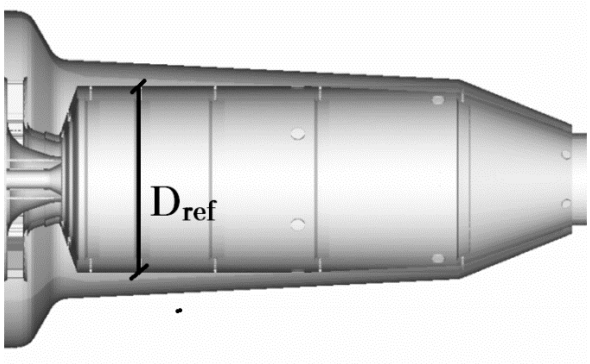

Figure 68. (a) Breakthrough of a reverse flow combustor. (b) Breakthrough of a can combustor. Source: [73].

5.1.1.1. Combustion Chamber Design and Off-design

To evaluate the performances of a can combustor for MGT application a model was developed. The model evaluates design and off-design performance of the combustor considering variable mass flow rate and fuel flow rate. Moreover, functions to estimate its cost, CO_2 and NO_X emissions are integrated. According to Lefevbre [70], pressure losses along the liner can be calculated using equation (115).

$$\frac{\Delta p}{p_{in}} = \frac{\Delta p}{q_{ref}} \frac{R}{2} \left(\frac{m_{in} T_{in}^{0.5}}{A_{ref} p_{in}} \right)^2 \tag{115}$$

Where p_{in} is the inlet pressure, T_{in} the inlet temperature and A_{ref} is a reference area of the can combustor. $\frac{\Delta p}{q_{ref}}$ is called pressure-loss factor and usually is characterised by a value in a range between 20 and 37. The design procedure aims to evaluate the combustor reference area and then the reference diameter of the combustor when the pressure loss is fixed as 4% of the inlet pressure.

Applying the energy conservation equation and assuming a combustor efficiency (Typically 0.96/0.98) it is possible to calculate the air to fuel ratio for a given turbine inlet temperature.

$$\alpha = \frac{H_i \eta_b - C_{pexh} TIT}{C_{pexh} TIT - C_{pair} T_{in}} \tag{116}$$

Where $C_{p,exh}$ and $C_{p,air}$ are respectively the exhaust gas and inlet air specific heat capacity and H_i is the fuel high calorific value. The specific Heat of the exhaust gas was evaluated as weighted average of the elements which constitute the exhaust gas. Air excess in respect of the stoichiometric air to fuel ratio was considered.

$$\begin{aligned} CH_4 + \ 1 + e \ 2O_2 + \ 1 + e \ 7.52N_2 \\ \rightarrow CO_2 + 2H_2O + \ 1 + e \ 7.52N_2 + 2eO_2 \end{aligned} \tag{117}$$

$$e = \frac{\alpha}{\alpha_{st}} - 1 \tag{118}$$

Where α_{st} is the stoichiometric air to fuel ratio. The stoichiometric air to fuel ratio for natural gas is 16.

For off-design calculation the geometry of the combustor is given and then the pressure losses can be easily evaluated using equation (115). However, to complete the off-design procedure is necessary to evaluate the efficiency of the burner. According to Kurzke [71] combustion efficiency in off-design conditions can be

calculated as a function of the burner loading coefficient Ω, described by equation (119).

$$\Omega = \frac{m}{P_{in}^{1.8} V e^{\frac{T_{in}}{300[K]}}} \tag{119}$$

Where V is the volume of the combustion chamber. The efficiency can be calculated using equation (120).

$$log\big(1 - \eta_b\big) = a + b\ log\Big(\frac{\Omega}{\Omega_{ds}}\Big) \tag{120}$$

Where the suffix $_{ds}$ indicates the design condition and the constant a is a function of the design point efficiency as shown by equation (121).

$$a = log(1 - \eta_{b,ds}) \tag{121}$$

Thus, it is possible to describe the burner part load efficiency, with a single constant: the burner part load constant b, which usually has a value around 1.6.

5.1.1.2. Combustion Chamber Cost

The cost of the combustor was calculated adopting the approach suggested by Galanti [52]. The cost function is described by equation (122).

$$C_{CC} = 36.1 \cdot \frac{m_{f,ds}}{\frac{\Delta p_{ds}}{p_{in,ds}} - 0.01} \tag{122}$$

Where $m_{f,ds}$ is the fuel flow rate in design conditions and $\frac{\Delta p_{ds}}{p_{in,ds}}$ are the pressure losses evaluated as percentage of the inlet pressure, both in design condition.

In this study natural gas was considered as fuel. Fuel cost was evaluated based on the European average prize for the industry sector. According to Eurostat [72], the average cost of natural gas in 2017 in Europe was estimated to be 32 c€/kWh.

5.1.1.3. Emissions

CO_2 emissions can be calculated considering the stoichiometry of the combustion reaction, already described in equation (117). The nitrogen oxides emissions have calculated using equation (123), adopting the approach suggested by Kurzke [71].

$$NO_X = 32 \left(\frac{p_{in}}{2.965 \cdot 10^6}\right)^{0.4} e^{\left(\frac{T_{in}-826}{194}\right)+0.118} \cdot \frac{m}{1000} \tag{123}$$

5.2. Plant Design and Off-Design Performances

Differently from the pure solar system, they hybrid system has one more control parameter at disposition: The fuel flow rate. Controlling the fuel flow rate, it is possible to split the heat demand among the receiver and the combustion chamber, potentially admitting a higher TIT without violating the limitation related to the receiver maximum temperature. Nevertheless, technological issues connected to flame stability inside the combustor must be taken into consideration. Moreover, ignition and shut down of the burner cause harmful transient operations, the combustor should always be operating providing a minimum heat to the system in accordance with its flame stability limits.

Flame stability inside a can combustor cannot be easily modelled and the study of this phenomenon it's not within the main objective of this research. Nevertheless, to consider this limitation a minimum temperature variation inside the combustor was set to be 50 K in any working condition of the plant.

Table 12 reports the main design parameters of the plant. For this first case study, the TIT was kept at the value 1073 K and the receiver outlet temperature

was fixed to be 1023 K. In accordance with what was already done in chapter 2, design mass flow rate, pressure ratio and rotational speed were set to be *0.09* kg/s, *3* and *130* krpm respectively.

Table 12: Main design requirements

Design Point Requirements			
$\dot{m}$ *[kg/s]*	*0.09*	*PR*	*3*
DNI[W/m²]	*800*	T_{01}*[K]*	*298*
n [krpm]	*130*	T_{04} *[K]*	*1023*
p_{01}*[kPa]*	*101.3*	*TIT [K]*	*1073*

Table 13. The design parameters for the 7 kWe plant

Thermodynamic quantities		*Performance parameters*	
$\dot{m}$ *[kg/s]*	*0.09*	P_c *[W]*	*11631*
DNI [W/m²]	*800*	P_t *[W]*	*19492*
n [krpm]	*130*	*P [W]*	*6720*
p_{01} *[kPa]*	*101.3*	η_c	*0.796*
p_{02} *[kPa]*	*304*	ε_r	*0.850*
p_{03} *[kPa]*	*302.6*	η_r	*0.759*
p_{04} *[kPa]*	*296.8*	η_t	*0.818*
p_{04} *[kPa]*	*290.8*	η_{cc}	*0.96*
p_{05} *[kPa]*	*105.6*	η	*0.189*
T_{01} *[K]*	*298.1*		
T_{02} *[K]*	*428.4*		
T_{03} *[K]*	*809.7*		
T_{04} *[K]*	*1023*		
TIT [K]	*1073*		
T_{06} *[K]*	*874.2*		

The study was performed considering Rome as location. Solar data available in literature for the period between January *2004* and *2005* was considered. The results from the design procedure are presented in Table 13, the design of the plant was performed in accordance with the design requirements of Table 12 and the chosen design *DNI*. The net power output has been evaluated considering mechanical and electrical efficiencies of *90%* and *85%* respectively.

To evaluate off-design performances is necessary to define an operational strategy. As already mentioned before, two different operational strategies are considered in this study, constant power output and constant receiver outlet temperature. In this section of the chapter only the first will be considered. Both will be analysed with further details later in this chapter.Off-design performances of the plant have been evaluated under variable DNI. Figure 69 shows the main cycle performance parameters. As already mentioned previously, the power is set to be constant at all operating conditions. To achieve this operational strategy rotational speed and fuel flow rate must change in harmony with DNI to guarantee the objective power output. The Rotational speed is characterised by a small variation caused by the variation of the fuel flow rate which modify the overall turbine inlet mass flow rate. The fuel flow rate decrease linearly, as increasing DNI level necessarily leads to a lower heat demand required from the combustor to achieve the objective TIT. This aspect has also consequences on the efficiency and the emissions. As shown by Figure 69 (b), the maximum efficiency of the plant, which is almost 0.22, is achieved during low sun irradiation periods. As the DNI increases the efficiency drop down to 0.185. This behaviour can be justified by the fact that the combustor has a higher efficiency compared to the solar receiver. Lower fuel flow rate obviously leads also to reduced CO_2 emissions. This is not necessarily true for the NO_X, which value depends on the combustor inlet temperature and pressure. The curve representing the NO_X emissions

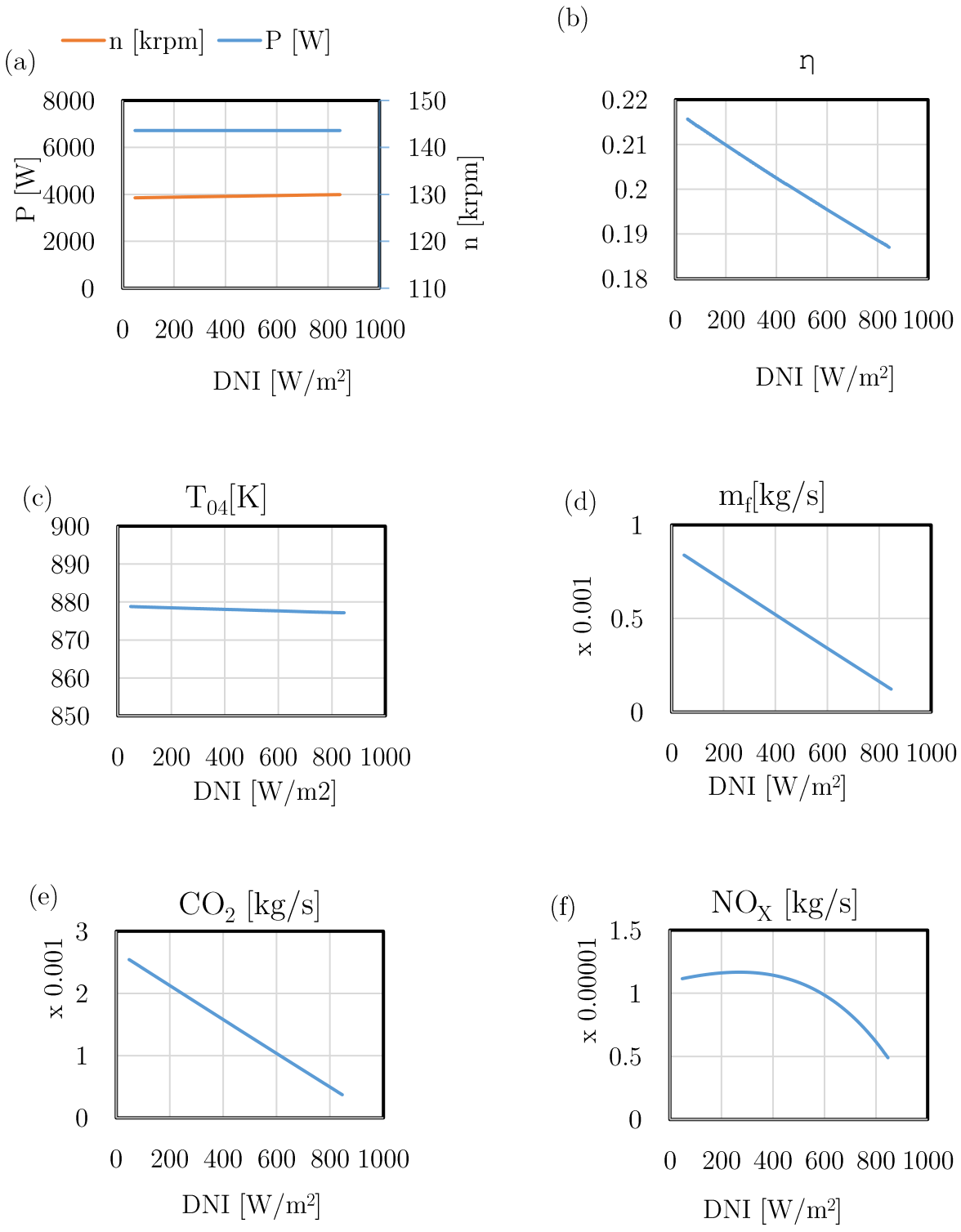

Figure 69. Plant performances during hybrid operation with constant power output and TIT. (a) Rotational speed and power output as a function of DNI. (b) Cycle efficiency as a function of DNI. (c) Receiver outlet temperature as a function of DNI. (d) Fuel flow rate as a function of DNI. (e) CO_2 emissions as a function of DNI. (f) NO_X emissions as a function of DNI.

as a function of the DNI has quadratic shape presenting a maximum when the DNI is around 300 W/m²K.

Differently from the TIT, the receiver outlet temperature T_{05} vary as consequence of the variation of the rotational speed.

5.2.1. Cost Analysis

The annual electricity generation and the levelised cost of electricity have been calculated using the plant overall performance parameters. The analysis has been carried out considering the DNI frequencies based on hourly average values of Rome in the period between 2004 and 2005. For each DNIs the performances of the plant were evaluated, and the overall energy produced by the plant was estimated to be 2.28*10⁴ kWh. Figure 70 shows the breakdown of the overall energy produced along the year by each DNI level. As expected and differently from the pure solar system the energy produced is evenly distributed for each DNI. The power output is indeed constant, and the overall amount of energy produced along the year for each DNI depend only on the frequency of the same. The lower DNI limit was set based on minimum receiver efficiency requirements of 10%.

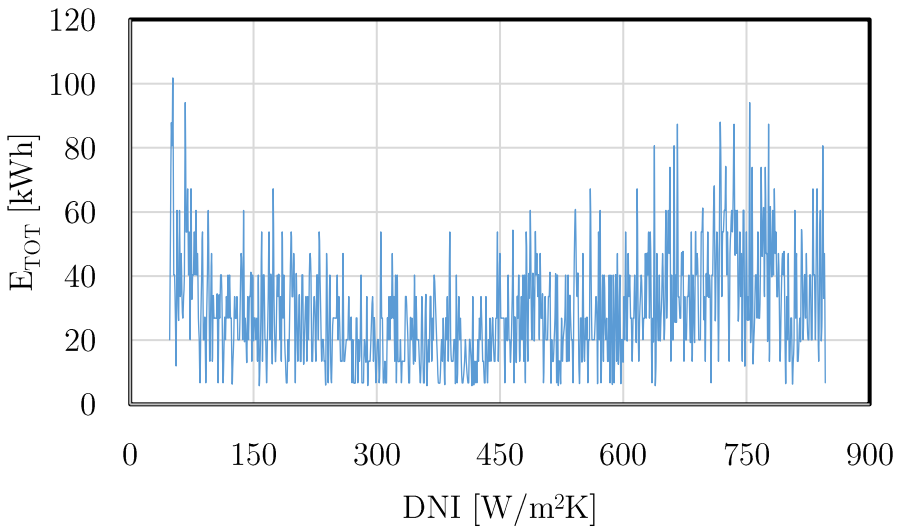

Figure 70. Overall energy produced along the year for each DNI.

The cost functions described in section 3.8 have been integrated with the combustor cost function and used to estimate the cost of the plant and cost of producing electricity. Figure 71 shows the plant cost breakdown for different components of the plant. The capital cost has been estimated to be *20610 €* and consequently the specific cost of the plant, defined as the ratio between the cost of components and output power in design condition, has been estimated to be around *3660 €/kWel*. As can be seen in Figure 8, the most expensive component is still the dish with *58%* of the overall cost while the MGT represent *24 %* of the overall cost. Results from the LCOE analysis demonstrate a levelised cost of energy of *32.5 c€/kWh* considering a life cycle of the plant of 25 years. The reduced cost of the dish can be justified by the fact that the heat demand is divided among the receiver and the combustor, resulting in a lower dish size. Despite this capital cost reduction, the LCOE results increased compared to the pure solar system as the fuel cost along the year (*9405 €*) has a higher weight on levelised cost of energy than the discounted capital cost.

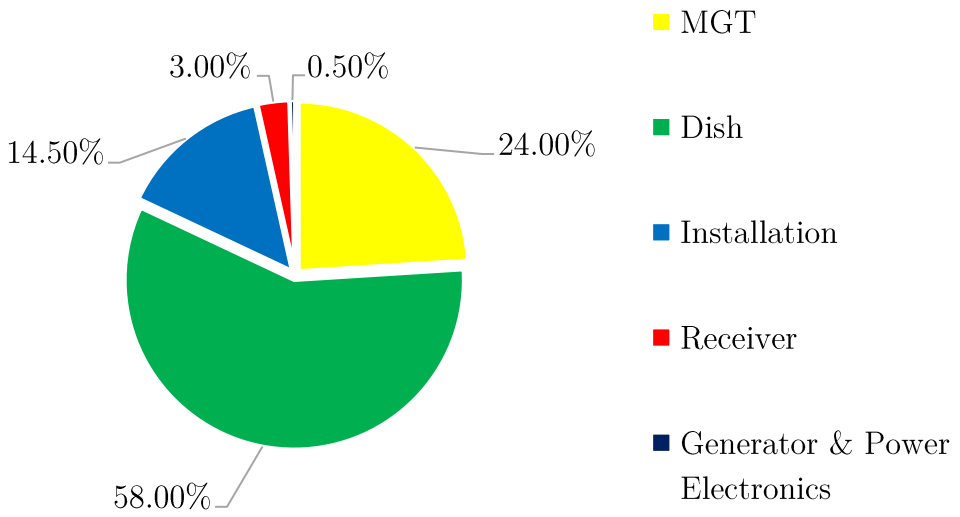

Figure 71. Cost breakthrough of the hybrid plant.

5.3. Plant Operational Strategies

The combustion chamber introduces one new control parameter for the system. Controlling the fuel flow rate, it is possible to adjust the turbine inlet temperature to the desired value. Nevertheless, turbine and/or the recuperator maximum operating temperature is constrained by the material limitations. Once the TIT is fixed, different operational strategies can be conceptualised. In this study two different operational strategy will be presented: constant power output and constant receiver outlet temperature. Both strategies presented in this section adopt constant TIT to maximise the power output at any DNI with regards to the technological limits of the plant. Moreover, combustor flame stability was considered constraining the minimum temperature rise inside the burner at 50 K.

As shown by Figure 72, constant power output can be achieved in most of the operating DNIs for power outputs higher than 6 kW. For lower values of output power, when the DNI increases the receiver outlet temperature is constrained by the minimum combustor inlet temperature. The receiver outlet temperature can be also kept constant for temperature higher than 900 K.

72 shows that more operational strategies can be conceptualise, i.e. constant efficiency and constant rotational speed. Nevertheless, it must be highlight that both operational strategies won't differ significantly from the already discussed constant power output. The selection of the most suitable operational strategy must be found by the controller.

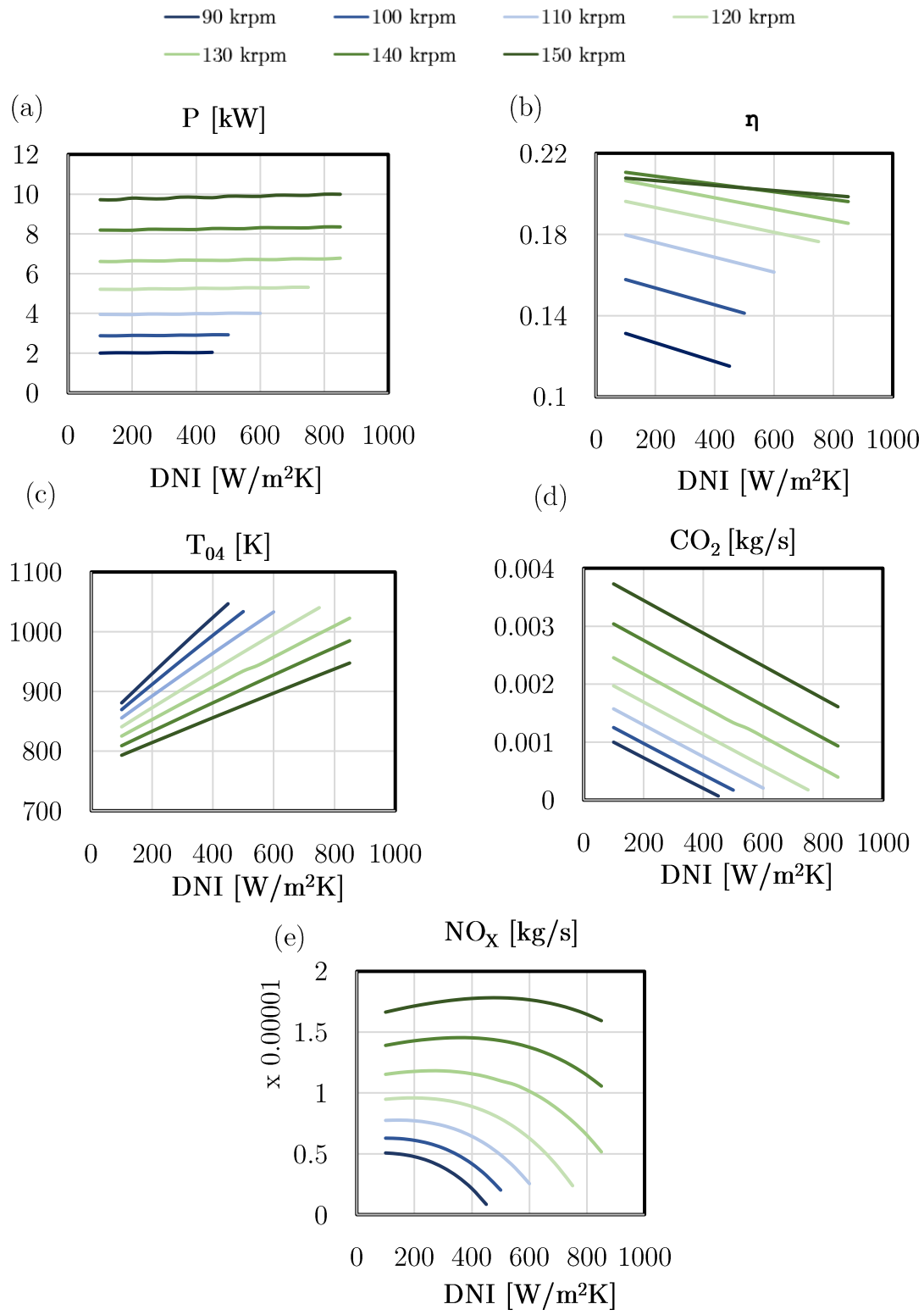

Figure 72. Performance parameters of the plant under variable DNI and rotational speed. (a) Power output as a function of DNI. (b) Cycle efficiency as a function of DNI. (c) Receiver outlet temperature as a function of DNI. (d) CO2 emissions as a function of DNI. (e) NOX emissions as a function of DNI.

5.3.1. Optimum operational strategy

This section was developed in cooperation with Stavanger University and in particular with Prof. M. Hassadi and Dr. H. Nipkey.

The DNI is not the only parameter affecting the performance of the plant which vary along the day. During the day, each operating condition is characterised by dissimilar DNI, ambient temperature and pressure. In this situation, it is possible to adjust the control parameters of the system, likewise rotational speed and the turbine inlet temperature, and identify different working conditions of the plant characterised by different power output and fuel cost. Generally, increasing the power output leads inevitably to a higher fuel consumption and consequently a higher operational cost. The problem is then multi-objective as the right trade-off between fuel cost and power output must be found.

In this section, a case study is presented to verify the applicability of the model for operations optimization. A neural network has been developed and coupled with a genetic algorithm to find the set of control parameters which maximize the power output and minimize the cost of fuel for a given DNI, T_{01} and p_{01}. Solar and meteorological data from Rome on 2th April 2005 were used. The optimization algorithm was run in each operating condition to find the rotational speed and the TIT that maximize the power output and minimize the fuel cost. A time step of 15 mins was adopted.

Given the higher number of input parameter, a multi-layer perceptron (MLP) network with one hidden layer was built up and trained. High number of input parameters results in high number of design points. Compared to full 2nd order polynomial, artificial neural networks can ensure higher accuracy in the prediction of the output parameter. Figure 73 shows a typical MLP structure with one hidden layer.

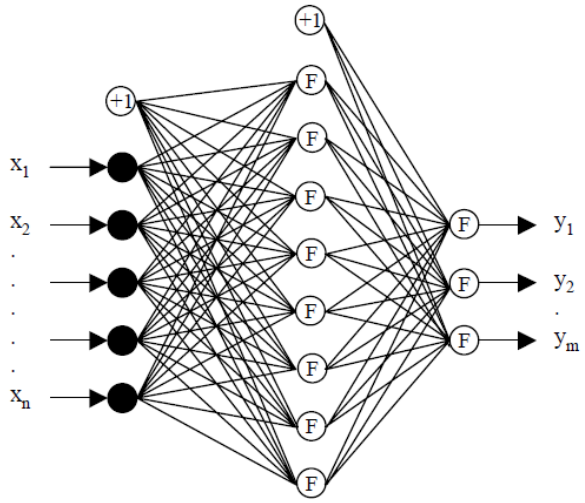

Figure 73. Schematic of a MLP network [74]

The inputs denoted by x are multiplied by weights, which represent the strengths of connections connecting input units to neurons in the hidden layer. The weighted inputs are then summed and transformed while passing through the hidden neurons. The outputs of hidden neurons are the inputs for the output layer. They are weighted, combined and processed in the hidden layer, where the outputs corresponding to inputs are calculated. The functional representation of a MLP network with n inputs, k hidden neurons and m outputs can be defined using equation (124).

$$y_m = g\left(\sum_{j=0}^{k} w_{mj}^{2}\varphi\left(\sum_{i=0}^{n} w_{ji}x_i\right)\right) \tag{124}$$

w_{ji} is a weight connecting input i to the hidden unit j, and w_{j0} is the bias for the hidden unit j, corresponding to the fixed input x_0 equals 1. Similarly, wmj2 denotes a weight, connecting hidden unit j to the output unit m, and wm02 is the bias for the output unit m, corresponding to the fixed input equals 1. $\varphi(.)$ and g(.) represent the transfer function of the hidden and output neurons respectively.

The training procedure of MLPs was performed in two phases. Firstly, errors are evaluated in the output layer and weights between the output and the hidden layer (w_{mj}) are calibrated. Secondly, the resulting error is propagated in a backward path

through the network, and weights among hidden layer and the input layer (w_{ji}) are updated. This process is repeated until the error between the predicted outputs and desired values is converged to an acceptable low level. This algorithm is known as back-propagation [74].

To ensure that the *ANN* can provide reliable predictions, the data used for training of the *ANN* should cover a wide range of operational conditions. This was enabled thanks to the in-house simulation tool, which underwent an extensive simulation runs at various turbine inlet temperatures (*TITs*), rotational speed as well as ambient conditions represented by compressor inlet temperature and pressure. For each set compressor inlet pressure and temperature, a wide-ranging dataset was calculated as a function of *DNI*, *TIT* and rotational speed to simulate the part load operation. Gathered data were screened and thereby inconsistent data caused by simulation errors were filtered from the data set. Finally, *184 761* samples remained for the *ANN* modelling.

The structure of the *ANN* model is shown in the Figure 74. As explained above, the data representing various operational condition of the plant was obtained from the simulation tool by varying *TIT*, ambient conditions, *DNI* and rotational. These parameters were therefore considered as input.

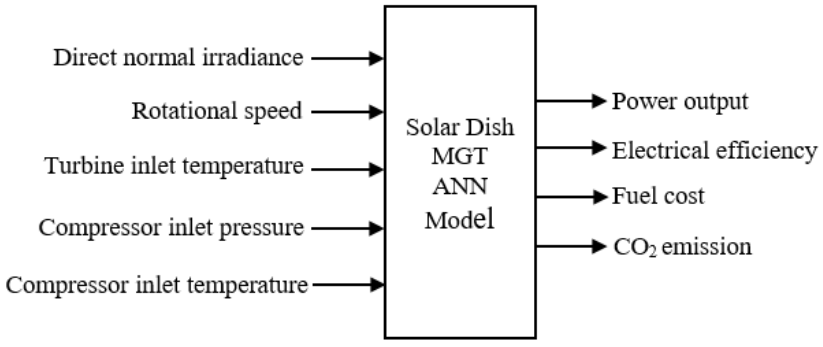

Figure 74. ANN model structure.

The range of input parameters is shown in Table 14. The outputs are the power output, electrical efficiency, fuel costs as well as the CO2 emissions, which are desired parameters for system monitoring and optimization purposes.

Table 14: Range of input parameters

Inputs	**DNI (W/m²)**	**Speed (krpm)**	**TIT (K)**	**T_{01} (K)**	**P_{01} (kPa)**
min value	100	90	1073	270	97
Max value	846	150	1150	310	101.6

For training of the MLP network, the commercial software NeuralSolutions was used [10]. The data set including *184,761* samples was randomized and divided into three subsets, namely, the training, cross-validation and testing subsets containing *75%, 10%* and *15%* of the data, respectively. The training subset was used to tune the weights (i.e. w_{ji} and w_{mj}) using the back-propagation algorithm as discussed above. The cross-validation subset was used to avoid over-fitting of the network to the training samples.

Table 15: Training settings

Parameter	**Value**
Network structure	MLP
Number of hidden lavers	1
Training algorithm	Back-propagation
Activation function	tanh
Error function	MSE
Division of data	Train/CV/Test=0.75/0.10/0.15
Number of samples	184,761
Iteration	20000
Early-stopping	100 iterations
Number of weights initialization	3
Hidden neuron range	4-20 with step size of 2

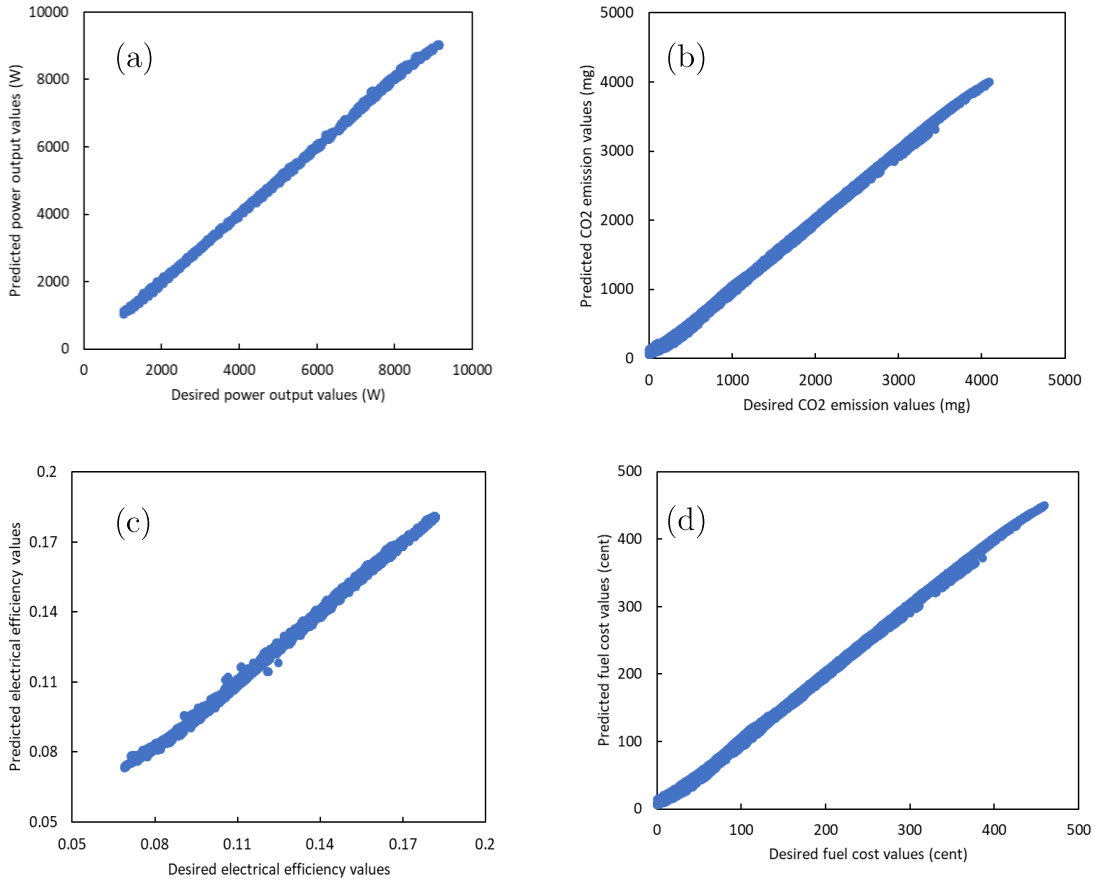

Figure 75. Comparison between the desired and predicted: (a) Power Output. (b) CO_2 emissions. (c) Electrical Efficiency. (d) Fuel Cost.

The prediction accuracy of the best ANN was tested against the testing subset containing unseen *26,941* samples, which had never been used for the training process. Table 16 shows the prediction errors of the output parameters based on absolute errors. Since the scales of output parameters are different, the normalized term (i.e. normalized mean absolute error) was used to ease the comparison between the prediction errors of outputs. As shown by Figure 75 the results show the levels of prediction errors for all output parameters are considerably low and they are approximately the same.

The normalized mean absolute errors (NMAEs) for power output, CO2 emission, electrical efficiency and fuel cost are *0.0035, 0.0036, 0.0038 and 0.0037,* respectively.

This indeed indicates the ability of the developed ANN to predict the output parameters with high and almost the level of accuracy. The accuracy of the ANN is illustrated in Figure 7, where the predictions are compared with desired values for all outputs.

Table 16: Prediction errors of output parameters

Error	P (W)	CO_2 (mg)	η_{el}	Fuel cost (cent)
MAE	30.034	16.294	0.0007	1.8797
NMAE	0.0035	0.0036	0.0038	0.0037
Min Abs Error	0.0032	0.0005	0.0000	0.0000
Max Abs Error	245.85	125.85	0.0072	14.4588

Figure 75 shows that for all outputs, the predicted values obtained from the ANN model well fit the targeted ones calculated by the simulation tool. The quadratic correlation coefficient (R^2) was used to measure the fitness and as can be seen in the figures, there is a strong linear relationship between predictions and targets. The linear coefficient for power, CO2 emission, efficiency and fuel cost is similarly around 0.999, which means that all data points almost lie on straight line.

The validation results show that the ANN model can effectively be used to predict accurately the techno-economic performance of the micro hybrid solar MGT system. Since the ANN does not require an iterative solution process, when the inputs are supplied the outputs are predicted instantly. Therefore, the model can serve as a fast and accurate model for the optimization process to minimize the time and thus the cost required. Furthermore, the developed ANN model can be used as a fast

baseline model for the monitoring application to estimate the expected system performance to detect any degradation. This provides the possibility to monitor the system performance and thus take necessary measures before degradations develop to a major and costly damage. Consequently, the resources and time required for operation of the system can be optimized, and its availability can be improved.

The neural network developed in this study was coupled with a genetic algorithm to verify the applicability of the model for operations optimization aimed to find the set of control parameters which maximize the power output and minimize the cost of fuel for a given DNI, T_{01} and p_{01}. Solar and meteorological data from Rome on 2th April 2005 are used. The optimization algorithm is run in each operating condition to find the rotational speed and the TIT that maximize the power output and minimize the fuel cost.

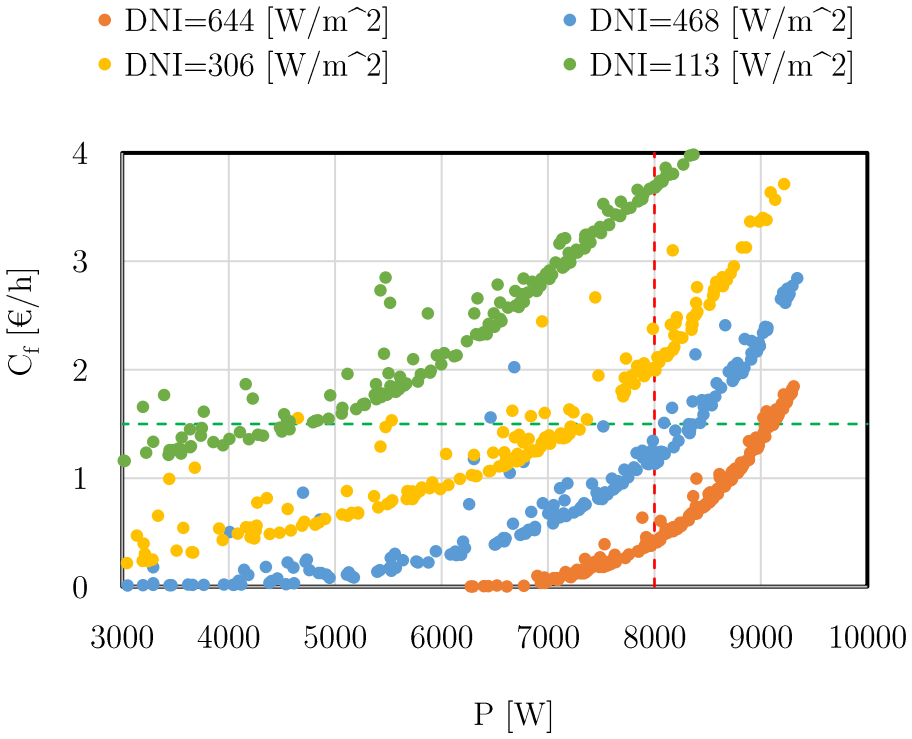

Figure 76. Pareto front of the optimizations at different DNIs.

Figure 76 shows the Pareto front resulting from the optimizations. Four fronts are shown in the chart, each of them characterised by dissimilar DNI, T_{01} and p_{01}.

As expected, when the solar irradiation increases the front move towards higher power outputs and lower fuel cost. Variation of temperature and pressure along the day are not relevant and their influence on the performance of the plant during the day negligible.

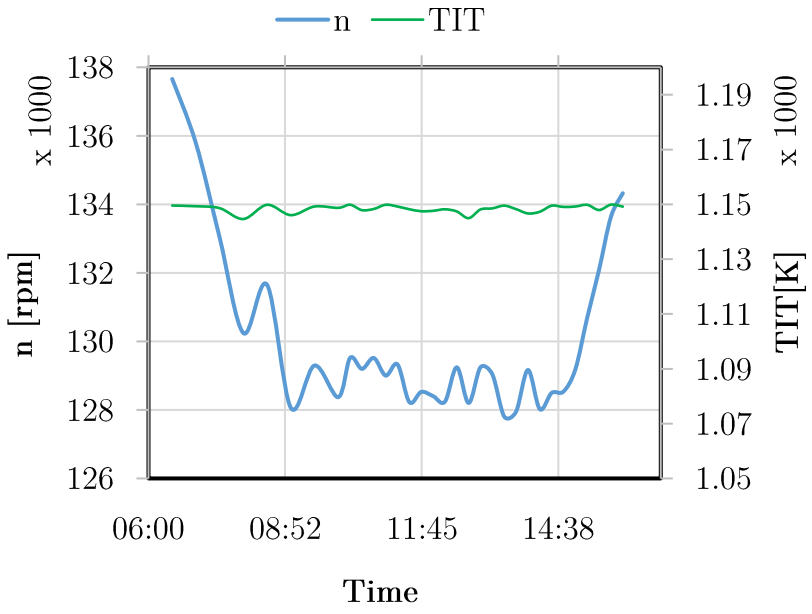

Figure 77. Daily variation of control parameters with constant output power.

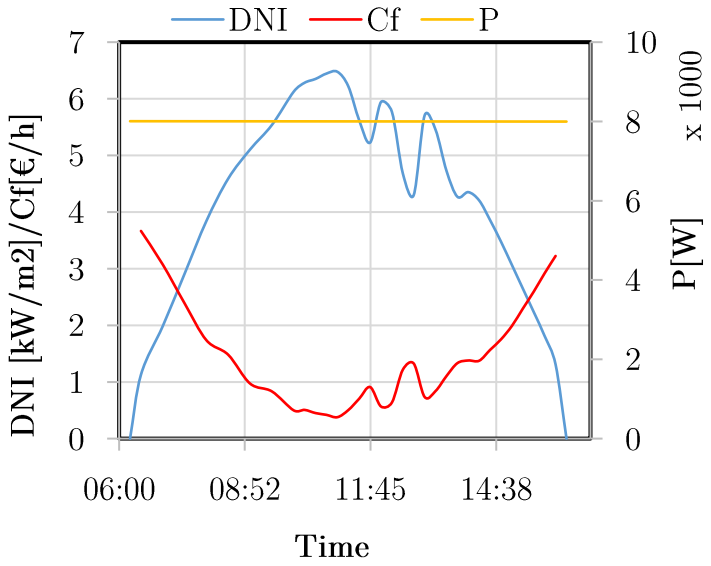

Figure 78. Daily variation of output parameters with constant power output.

As shown in the chart, two operational strategy can be conceptualized: constant power output and constant fuel cost. It must be highlight that for a given TIT, constant fuel cost inevitably leads to constant receiver outlet temperature. Once the operational strategy is set, the optimum point can be defined uniquely for each DNIs value.

Figure 77 and Figure 78 show the daily behaviour of the main parameters influencing the optimization problem when a constant power output operational strategy is assumed. Results of the optimization demonstrates that optimum control parameters have a peculiar behaviour. Optimum TIT is always at its maximum value of *1150 K*, optimum rotational speed is always around the design value of *130 krpm*, slightly increasing at low DNIs up to *138 krpm*.

Figure 78 shows the daily variation of fuel cost and output power. As already mentioned previously, the power output is constant along the day. To meet the power demand the fuel cost must change, following the DNI variation along the day. To low DNIs correspond high fuel consumption and cost, its maximum value during this case study day is around *4 €/h*, its minimum of about *0.5 €/h*.

Figure 79 and Figure 80 show the daily behaviour of the main parameters influencing the optimization problem when a constant fuel cost operational strategy is assumed. Results of the optimization demonstrates that the operational strategy does not affect the optimum TIT, which is always at its maximum value of *1150 K*. On the other hand, optimum rotational speed varies significantly from a minimum value of about *100 krpm* at low DNIs to a maximum value around *145 krpm* at high level of solar irradiation.

Figure 79 shows the daily variation of fuel cost and output power. In this situation the fuel cost is kept constant, to meet this strategy, output power must change and follow the variation of the DNI along the day. The power in output from

the plant is minimum in the morning and the late afternoon when the solar irradiation is low, and maximum around midday when the solar irradiation reaches its highest values. Minimum power output is around *5 kW* and the maximum around *9 kW*.

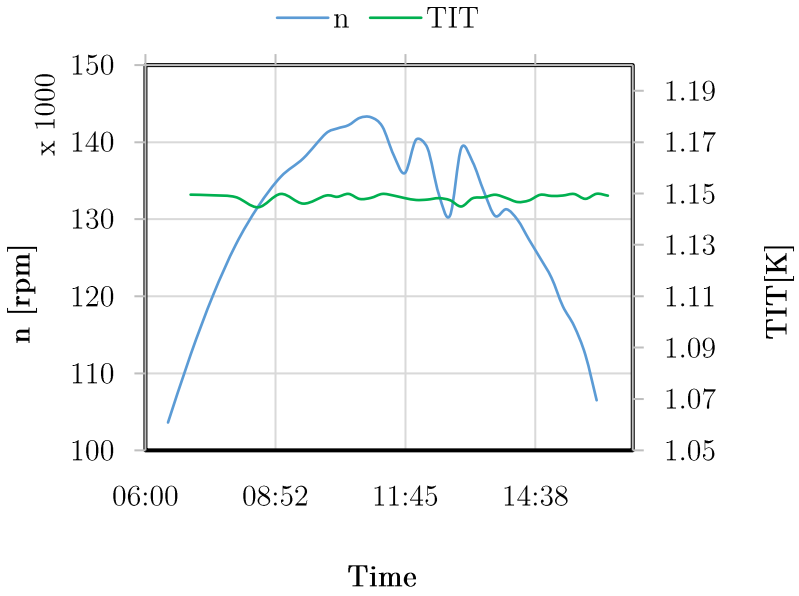

Figure 79. Daily variation of control parameters with constant fuel cost.

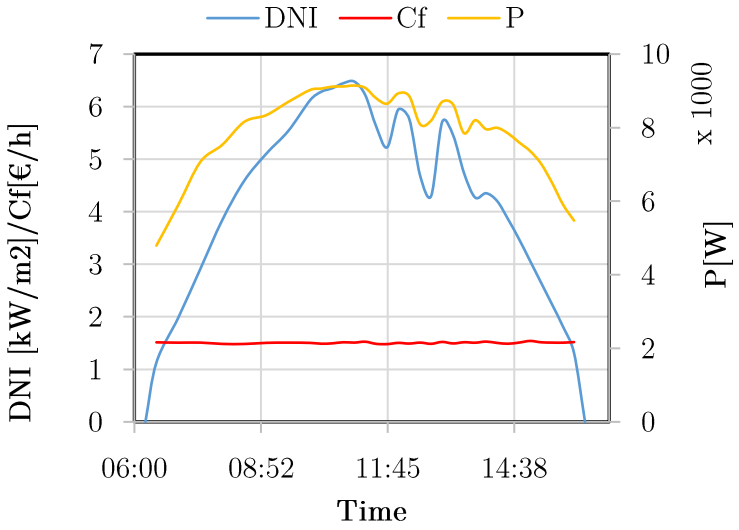

Figure 80. Daily variation of output parameters with constant fuel cost.

It must be highlight that for a given TIT, constant fuel cost roughly corresponds to a constant receiver outlet temperature (T_{REC}). The fuel cost it's a parameter which

cannot be adjusted by the controller, on the other hand the receiver outlet temperature can be monitored during operations and it's more interesting from the cycle design point of view as operating with constant receiver outlet temperature correspond to constant air to fuel ratio, a parameter directly related to the efficiency. For this reason, in the following sections this operational strategy will be referred as constant receiver outlet temperature.

5.4. Plant Optimisation: T_{rec}=cost

In this section a plant multi-objective, thermo-economic optimisation is presented considering constant receiver outlet temperature as operational strategy. To perform the optimisation, annual performances of the plant have been evaluated adopting the same methodology already discussed in the previous section for off-design performance evaluation. In this case, receiver outlet temperature was fixed to be at its maximum value of 1073 K in accordance with receiver material limitations. TIT value is also set to be constant in any operating condition to the value 1173 K. TIT value has major influence on the recuperator inlet temperature, the higher is the TIT the higher is the temperature that the recuperator must withstand. Moreover, increasing the turbine inlet temperature results in increased fuel consumptions and operational cost. The input parameters of the optimisation are reported in Table 17.

Table 17. Design space of the optimisation

	PR	$\dot{m}$ [kg/s]
Lower bound	2.6	0.07
Upper bound	3.5	0.15

The design space of the optimisation is constrained by the compressor: for a given rotational speed the variation of pressure ratio and mass flow rates lead to a

variation of the isentropic enthalpy difference and consequently the specific speed. This led to reduced design efficiency of the compressor. The considered range is limited as shown by Table 17, this ranges were reduced furthermore compared to section 4.3.2 as design convergence issued have been encountered for cases in the upper limit of the design space.

Figure 61 shows the goodness of fit of the optimisation. The chart compares the normalised value, of any output parameter, predicted by the response surface and the value observed from the design points. As shown by Figure 81 the output parameters predicted by the surface are fairly distributed along the bisector of the x-y axis. Moreover, as shown by Table 18, statistical analysis also confirmed the accuracy of the response surface in predicting the output parameter values. For any output parameter, the coefficient of determination is above 0.97 and the root mean square error is always two order of magnitude lower than the absolute value.

Table 18. Statistical analysis of the response surface

`	E_{TOT} [kWh/y]	C [€]	LCOE[c€/kWh]	CO_2 [kg/y]	NO_X [kg/y]
R^2	0.996	0.999	0.986	0.999	0.999
RMSE	155.3	91.7	0.26	1.18	0.008

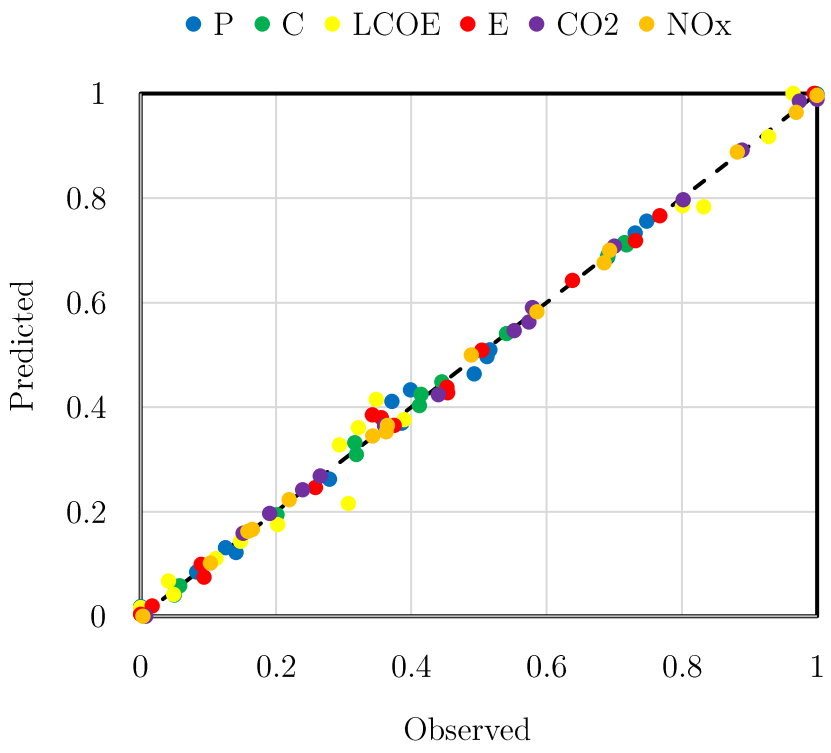

Figure 81. Goodness of fit of the response surface.

Figure 82, Figure 83, Figure 84 and Figure 85 present the obtained response surfaces. The charts highlight that minimum LCOE can be achieved for the highest-pressure ratio of the design space. For this reason, compared to what has been done for the pure solar system, a wider range was considered. This situation highlights the necessity to explore a wider range of pressure ratios increasing the design rotational speed. Nevertheless, a higher design rotational speed could lead to mechanical instabilities and rotor dynamics issues. For this reason, the range was not further extended.

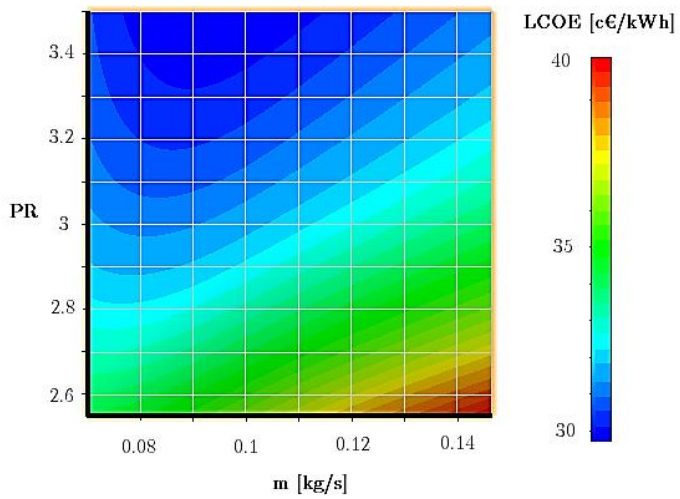

Figure 82. Response surface: LCOE as a function of the design mass flow rate and pressure ratio

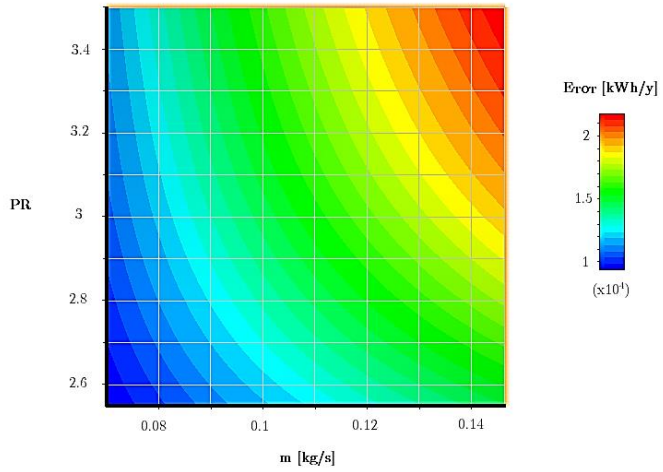

Figure 83. Response surface: Total annual energy produced along the year as a function of the design pressure ratio and mass flow rate.

Figure 83 shows the overall annual electricity production as a function of the design mass flow rate and pressure ratio. As expected, the higher are the design pressure ratio and mass flow rate the higher is the annual yield of the plant. A multi-objective optimisation is then necessary to find the right trade-off between levelised cost of energy and annual electricity production.

Figure 84 shows the CO_2 emissions response surface. The carbon dioxide produced by the plant is proportional to the mass flow rate and the pressure ratio.

Also in this case a trade-off between levelised cost of energy and emissions can be found. As shown by Figure 85 NO_X emission demonstrates linear proportionality to the design mass flow rate. The situation changes under variable pressure ratio as the NO_x emissions assumes a quadratic behaviour.

The optimisation algorithm used in this work is a Multi-Objective Genetic Algorithm (MOGA) considering as convergence criteria a convergence stability percentage of *0.2 %* and a maximum allowable Pareto percentage of *95 %*.

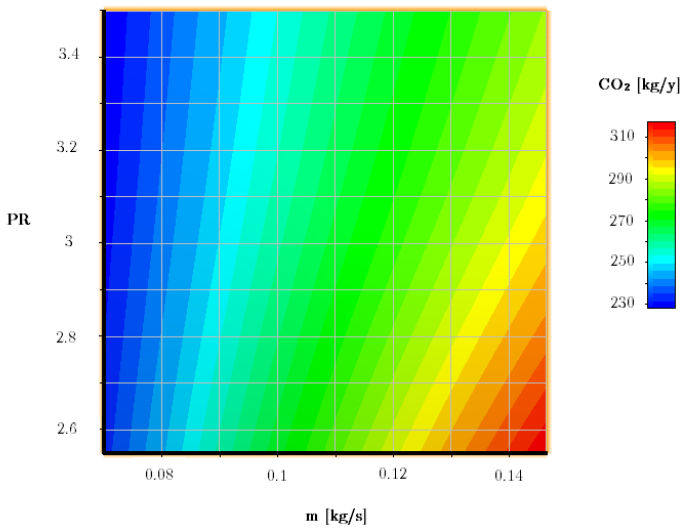

Figure 84. Response surface: Annual CO_2 emission as a function of the design pressure ratio and mass flow rate

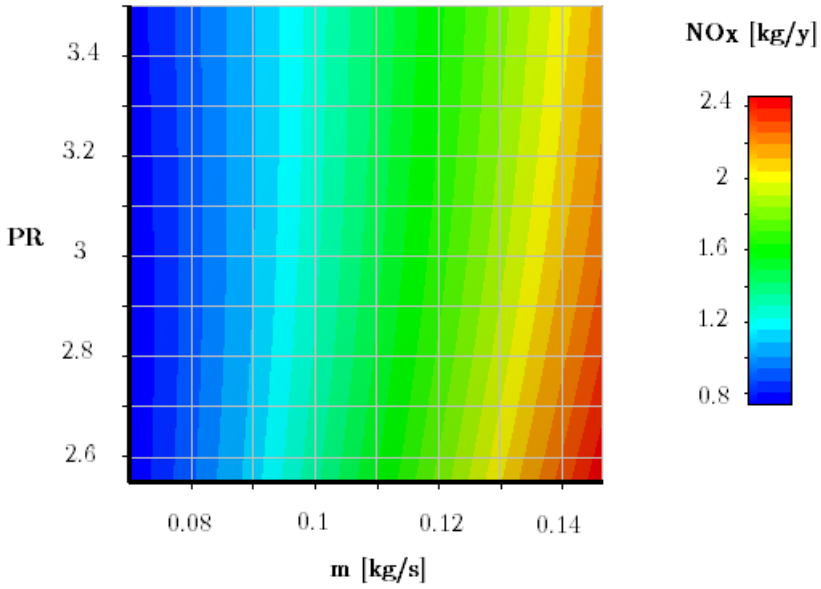

Figure 85. Response surface: Annual NO_X emission as a function of the design pressure ratio and mass flow rate

Convergence was achieved after 12 iterations with an overall number of generated points of *12*10⁴*. Figure 86 shows the history of the generated points for the two optimisation variables. The charts highlight that convergence was achieved. As outcome of the optimisation a Pareto front was generated (Figure 87) and 3 candidate optimum points were selected and analysed.

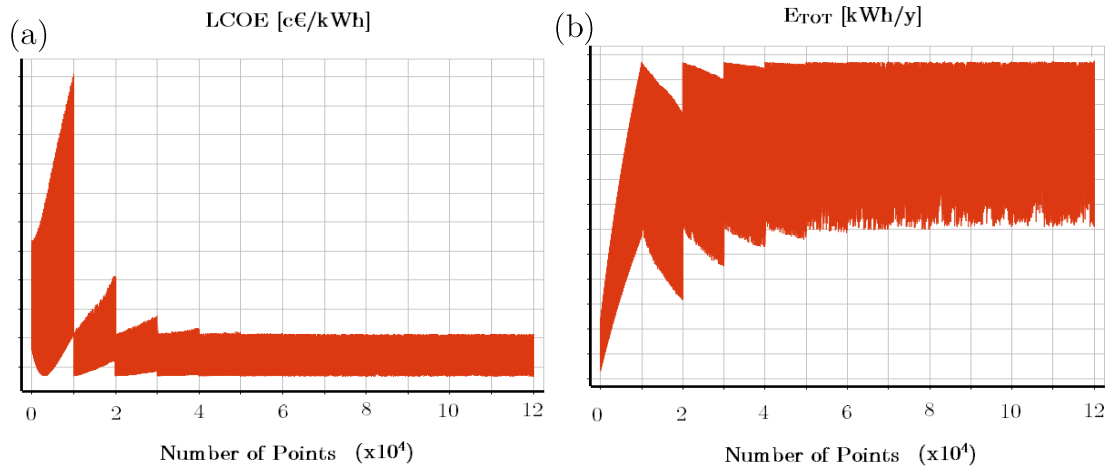

Figure 86. History of the output parameters convergence. (a) LCOE. (b) E_{TOT}.

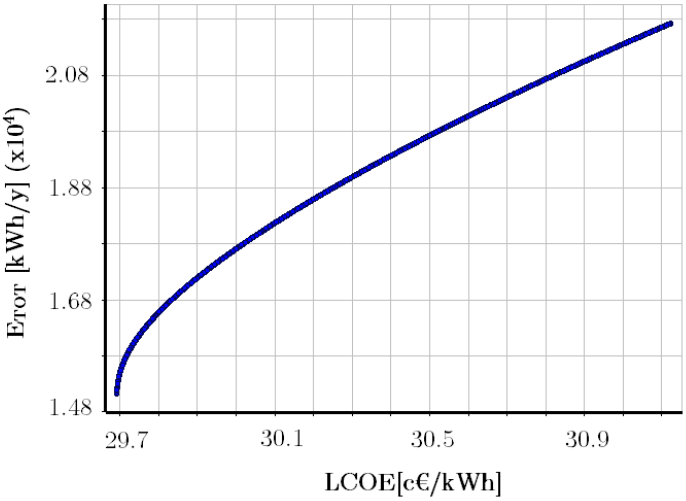

Figure 87. Pareto front of the optimisation: E_{TOT} versus LCOE.

Candidates' analysis highlights that optimum performance and cost can be achieved with a mass flow rate of *0.14 kg/s* and a pressure ratio always at its maximum value *3.5*.

Table 19. Candidate points in output from the optimisation.

	m [kg/s]	P R	P [W]	C [€]	LCOE [c€/kWh]	E [kW/y]	CO2 [kg/y]	NOx [kg/y]
Candidate 1	0.147	3.5	12556	34764	31.12	21724	340.9	2.14
Candidate 2	0.141	3.5	12255	33882	30.94	21159	333.9	2.03
Candidate 3	0.136	3.5	11946	32989	30.75	20579	326.9	1.92

Off-design performance of the *candidate #1* was analysed. As shown by Figure 65, plant's operation are characterised by a maximum power output of about *9.5 kW*, while minimum power was fixed to be *2 kW* as already discussed in Chapter 1. The maximum efficiency of the plant is *0.185*, it drops down to 0.1 during low sun irradiation periods. TIT is fixed to *1073 K* as required by the operational strategy. Rotational speed varies in the range *85 krpm - 135 krpm*. The levelised cost of energy

as predicted by the response surface and verified by the code is *31.12 [c€/kWh]*, the specific cos of the plant is *2 770 [€/kW]*,

5.5. Plant Optimisation: P=cost

In this section a plant multi-objective, thermos-economic optimisation is presented considering constant power output as operational strategy. To perform the optimisation, annual performances of the plant have been evaluated adopting the same methodology already discussed in section 5.2 for off-design performance evaluation. The input parameters of the optimisation are reported in Table 20. For this optimisation the design power output was selected as input parameter. The design space of the optimisation was increased from the previous optimisation.

Table 20. Design space of the optimisation

	PR	P [W]
Lower bound	2.6	4000
Upper bound	3.7	11000

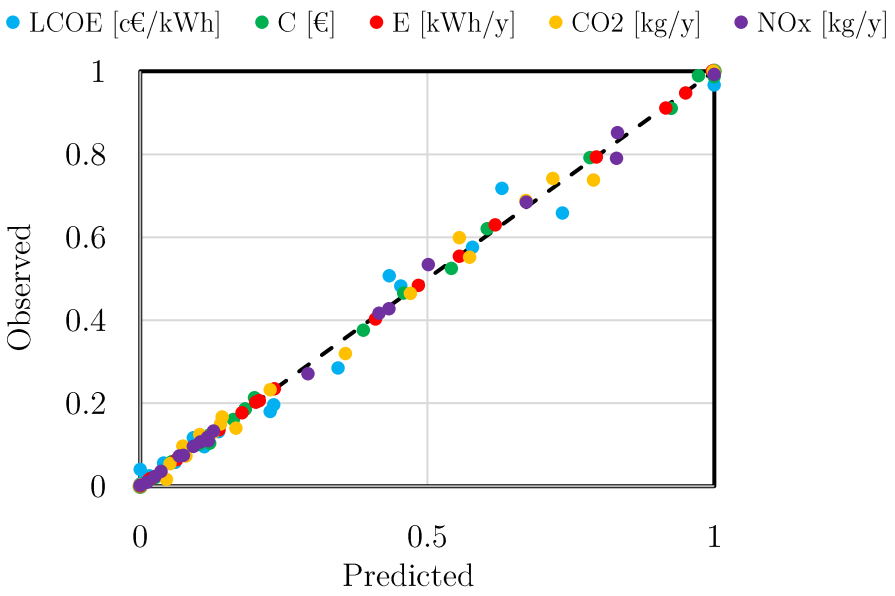

Figure 88. Goodness of fit of the response surface for each output parameter.

Table 21. Statistical analysis of the response surface

`	E_{TOT} [kWh/y]	C [€]	LCOE [c€/kWh]	CO_2 [kg/y]	NOx [kg/y]
R^2	0.999	0.999	0.98	0.993	0.999
RMSE	98.5	294	0.38	6.5	0.002

Figure 88 shows the goodness of fit of the optimisation. As shown by Figure 88 the output parameters predicted by the surface are fairly distributed along the bisector of the x-y axis. Moreover, as shown by Table 21 statistical analysis also confirmed the accuracy of the response surface in predicting the output parameter values. For any output parameter, the coefficient of determination is above *0.98* and the root mean square error is always at least two order of magnitude lower than the absolute value.

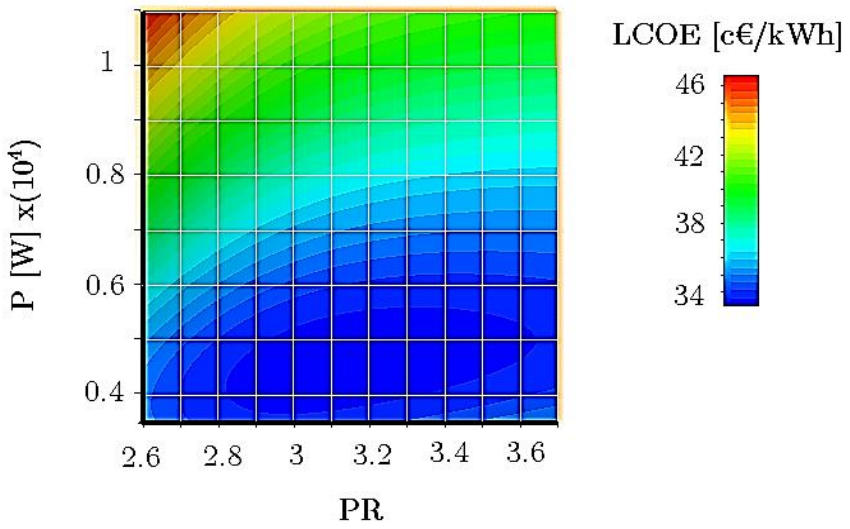

Figure 89. Response surface of the optimisation: LCOE as a function of power output and pressure ratio.

Figure 89, Figure 90 and Figure 91 presents the obtained response surfaces. The charts highlight that minimum LCOE is *34 c€/kWh* and can be achieved for a pressure ratio in the range *3- 3.3* and a power output of about *5 kW*. For a given power output, the levelised cost of energy decreases with the pressure ratio and then performances of turbomachinery decay together with the efficiency of the plant leading to an increased LCOE.

Figure 90 shows the overall annual yield of the plant as a function of the pressure ratio and the power output. As expected, this output parameter is proportional to the power output and the pressure ratio. The maximum annual energy can be produced with a power output of *11 kW* and can be as high as *3.89*10⁴ kWh/y*.

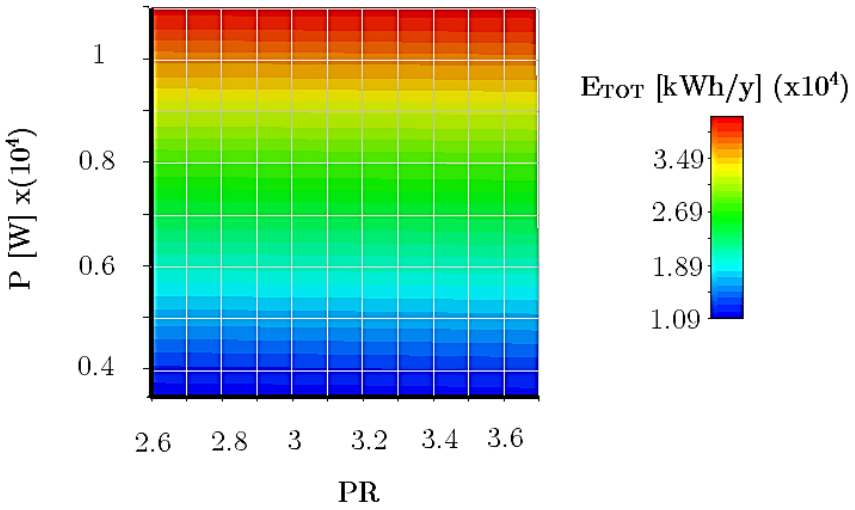

Figure 90. Response surface of the optimisation: E_{TOT} as a function of design power output and pressure ratio.

Figure 91 shows the carbon dioxide emission response surface. CO_2 emission increases proportionally to the power output as for low pressure ratio a higher fuel consumption is expected to achieve high power outputs. Same behaviour can be observed for NO_X, the emissions are proportional to the power output and in the order of magnitude of 1 to *12 kg/y*. The amount of nitrogen oxides emitted by the plant is relatively low and its response surface is not reported in this study.

It must be highlight that the top left corner of each response surface, which correspond to high power outputs and low pressure ratios, should not be considered as representative of the real behaviour of the plant. Although, the response surface can interpolate with acceptable accuracy the input data. When the pressure ratio is below 2.8 the plant cannot achieve power outputs higher than *9 kW*. In that region, no point was included in the DOE and the surfaces were extrapolated by the algorithm. This is particularly evident in Figure 91 where the extrapolated region of the domain is shaded.

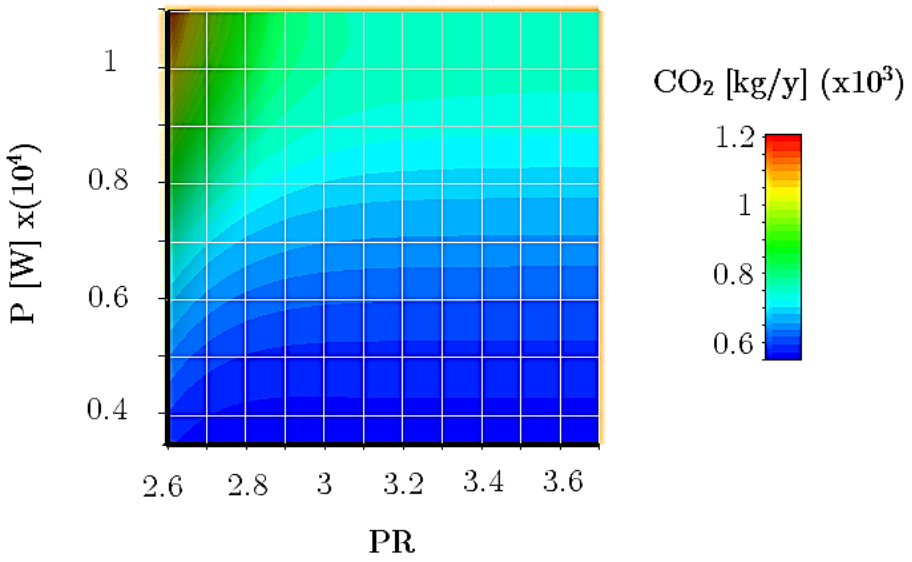

Figure 91. Response surface of the optimisation: annual CO_2 emissions as function of the design power output and pressure ratio.

The optimisation algorithm used in this work is a Multi-Objective Genetic Algorithm (MOGA) considering as convergence criteria a convergence stability percentage of *0.2 %* and a maximum allowable Pareto percentage of *95 %*.

Convergence was achieved after 6 iterations with an overall number of generated points of $6*10^4$. As outcome of the optimisation a Pareto front was generated (Figure 92) and 3 candidate optimum points were selected and analysed. As can be highlight by the front, the range where no objective is better the other cover the entire design space. The history of the convergence is then not representative of the convergence as a wide range of LCOE and E_{TOT} was investigated in each iteration. These charts are consequently not presented.

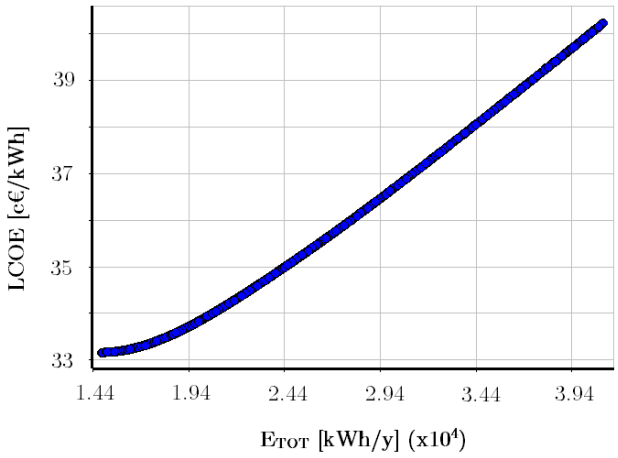

Figure 92. Pareto front of the optimisation LCOE vs E_{TOT}.

Off-design performance of the candidate #3 was analysed. As shown by Figure 65, plant's operations are characterised by a constant power output of about *9.7 kW*. The maximum efficiency of the plant is almost *0.2*, achieved during low sun irradiation periods. As the DNI increases, the efficiency drops down to *0.175*. The design efficiency of the plant is reduced if compared with the case presented in section 5.2. The decreasing behaviour of the efficiency when the DNI increases can be justified by the fact that the combustor has a higher efficiency compared to the solar receiver. When the DNI is low, most of the heat needed to achieve the objective power is given by the combustor, resulting in higher efficiency.

This aspect influences also the CO_2 emission which decreases when the DNI increases. T_{05} slightly decreases while TIT is fixed to *1073 K* as required by the operational strategy. Rotational speed varies in the range *85 krpm - 135 krpm.*

Table 22. Candidates from the optimisation.

	PR	P [kW]	LCOE [c€/kWh]	E [kWh/y]
Candidate Point 1	3.7	10991	40.21	41003
Candidate Point 2	3.7	10340	39.28	38142
Candidate Point 3	3.7	9692	38.36	35341

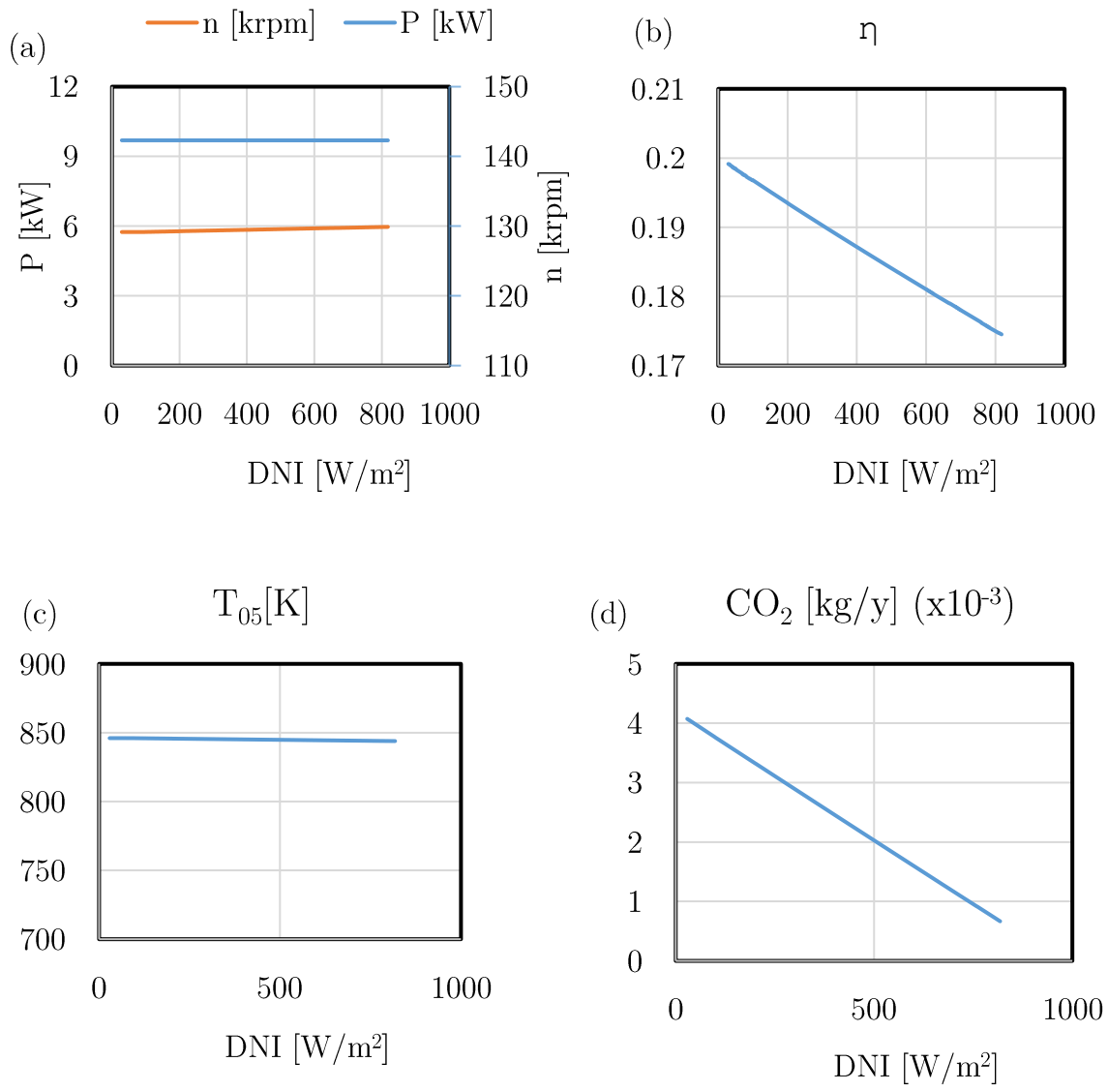

Figure 93. Performance parameters of the candidate point under variable DNI.

5.6. Parametric analysis

In this section a parametric analysis of the plant is presented. Constant receiver outlet temperature was assumed as operational strategy. Starting from the candidate point presented in the previous section, the techno-economical performances of the plant were analysed considering dissimilar recuperator effectiveness and TIT at

different locations, characterised by different DNI levels. As already done for the pure solar system the selected locations are Rome, Seville and Azalim.

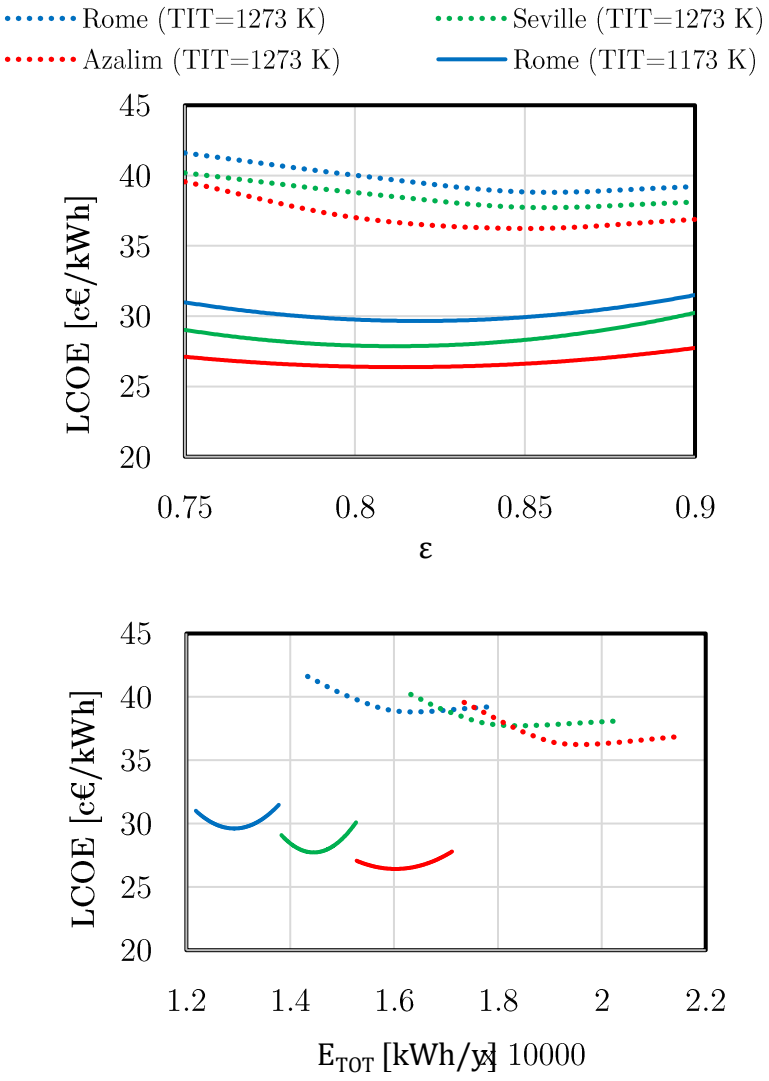

Figure 94. Results of the parametric analysis, LCOE versus recuperator effectiveness for different locations and TITs. Total annual energy produced versus levelised cost of energy. Comparison between different locations and TITs.

Results from the parametric analysis demonstrate that minimum LCOE can be achieved with a recuperator effectiveness around *0.8~0.85*. A lower recuperator effectiveness would cause the efficiency of the plant to drop, while higher effectiveness increases the cost of the component with consequent augmented cost of investment

and LCOE. On the other hand, as shown by Figure 21 the overall energy produced along the year increases with the recuperator effectiveness.

Increasing the *TIT* plays also a major role in the overall energy produced along the year. The higher is the *TIT*, the higher is the E_{TOT} at any location and any recuperator effectiveness. Nevertheless, for a given receiver outlet temperature, increasing the *TIT* increases the *LCOE* as more fuel is required by the system to achieve the objective *TIT*. Increasing the *TIT* has also a major influence on the optimum recuperator effectiveness. Its optimum value indeed is shifted on the right side of the chart towards higher values.

5.1. Conclusions

In this chapter a thermo-economic assessment of the MGT dish power plant with integrated hybridisation was presented. In the first part of the chapter, the model adopted in this study to predict the performances of the combustion chamber was presented. Consistently with the analysis performed in Chapter 4 a *7kW* microturbine case study was designed and analysed. Despite the lower capital cost of the plant (*20 600 €)*, the levelised cost of energy of the plant, in respect of the pure solar system, results increased to*33 c€/kW$_h$* as high operating cost are encountered. On the other hand, the energy amount produced along the year is significantly increased from *1.07 to 2.28*10^4 kW$_h$*

The following part of the chapter was dedicated to analysing the control maps of the plant. Differently from the pure solar system, off-design performances of the plant with integrated hybridisation demonstrated wider operating range in term of power output. Moreover. For power outputs higher than *6 kW$_h$* the power can be kept constant at any operating DNI.

The applicability of the model for live performance prediction was also tested. The computational time required by the software presented in this study is not suitable for live performance prediction, to obviate this problem an artificial neural network (*ANN*) has been developed. The network has been trained using the in-house tool developed in this study. The neural network has been trained considering various operational conditions by varying solar irradiation and other ambient conditions namely, the ambient temperature and pressure. The prediction accuracy of the *ANN* model has been tested with respect to data, which were not used during the training. A case study to verify the applicability of the model for operation optimization was then presented. The artificial neural network model was integrated with a genetic algorithm to find the set of control parameters, which maximize the power output and minimize the cost of fuel for a given *DNI* profile, ambient temperature and pressure. Solar and meteorological data for Rome on 2nd April 2005 were used in this case study. Results of the optimization demonstrates that two different operational strategies can be applied: constant power output and constant fuel (fuel cost). The first strategy is characterized by variable fuel cost (*0.5-4 €/h*), constant *TIT* (*1150 K*) and slightly variable rotational speed (*128-138 krpm*), the second one is characterised by variable power output (*5-9 kW*), constant *TIT* (*1150 K*) and highly variable rotational speed (*105-145 krpm*).

The chapter continues with two plant design optimisations distinguished by different operational strategy, constant power output and constant receiver outlet temperature. The second operating strategy is equivalent to constant fuel consumption as the *TIT* was always kept constant. The same optimisation technique adopted in chapter 4 was implemented.

When the receiver outlet temperature is kept constant, the response surfaces generated indicate that the levelised cost of energy presents a minimum in the range of pressure ratios between *3.3- 3.4* and mass flow rates *0.07-0.09 kg/s*, while, as

expected, the annual energy generated presents its maximum value for the highest-pressure ratio and mass flow rate analysed. The optimisation was then aimed to find the optimum trade-off between these two parameters. As outcome of the optimisation a Pareto front was generated and three candidate points belonging to this curve were shown. One of these candidates was analysed during off-design operations and a parametric study was performed on it. Results from parametric analysis demonstrate minimum *LCOE* with a recuperator effectiveness around *0.8~0.85* and *TIT* at its maximum value. The parametric study also confirmed that the location has major influence and the levelised cost of energy can be as low as *26* $c€/kW_h$ in high sun irradiance locations such as Azalim.

A plant optimisation was performed also considering constant power output as operational strategy. The response surfaces generated indicate that the levelised cost of energy presents a minimum in the range of pressure ratios between *2.8-3.6* and mass flow rates *0.04-0.06 kg/s*, while as expected, the annual energy generated presents its maximum value for the highest-pressure ratio and mass flow rate analysed. Candidate points resulting from the optimisation demonstrate almost doubled energy produced along the year when compared to constant receiver outlet operational strategy. Nevertheless, the *LCOE* results increased from *30* to *40* $c€/kW_h$.

LCOE analysis of the hybrid solar dish demonstrate levelised cost of energy comparable with other concentrated solar technologies already analysed in section 2.7. Especially when compared with similar size power plants such as dish Stirling. Despite the LCOE is increased from the pure solar plant, solar dish MGT with integrated hybridisation can guarantee constant power output along the day demonstrating almost doubled energy generation. This characteristic also results in higher reliability and dispatchability of the plant.

6. Integrated Thermal Storage

In comparison to other intermittent forms of renewable energy such as wind or photovoltaics, concentrated solar power technologies have the potential for integration with cost-effective thermal energy storage to increase the dispachability of the plant [79]. This is particularly important for solar dish *CSP* plants with relatively small size (*1-25* kW_{el}) characterised by a low thermal inertia when compared with large scale technologies such as parabolic through or solar tower [80].

Solar dish power plants, especially when operated by micro gas turbines, are also characterised by a relatively high maximum temperature of the working fluid [84]. This characteristic imposes limitation on the selection of the storage system and media. Moreover, one of the most promising applications of these plants is the possibility to work as a stand-alone system in rural areas. The system then needs to be compact and easy to transport making the compactness of the *TES* unit a major requirement [87]. The aim of this chapter is to evaluate the performance of the plant when a thermal storage unit is integrated, in order to estimate the benefits given by its integration in term of energy generated along the day/year and levelised cost of energy.

In the first part of the chapter is presented a methodology to improve the accuracy of a one-dimensional model of a honeycomb TES. The study will be focused in characterising the heat transfer and pressure loss along the storage, to understand

the effect of a laminar developing flow on the charging and discharging processes. Both thermal and hydrodynamic development of the flow boundary layer will be analysed using conjugate heat transfer simulations, with the objective of evaluating the heat transfer coefficient and the friction factor with dissimilar inlet velocity and duct diameter. The results will then be used to develop accurate regression models for both heat transfer and pressure drop coefficients. These functions will be then integrated in the one-dimensional model to improve its prediction accuracy.

The TES model developed in this chapter will be then included in the software already described previously to evaluate the performance of the plant with integrated thermal energy storage. The performance of the plant will be analysed considering two different case studies: 1) The storage is used as back-up during high fluctuation periods to smooth irradiation fluctuation. 2) The storage is used as back-up during the afternoon/evening when the sun irradiance decreases due to the natural earth rotation.

6.1. Thermal energy storage model

This section was developed in cooperation with Zhejiang University and in particular with Prof. X. Gang and X. Zhou.

Ceramic honeycomb structures have been widely used as heat transfer media within sensible energy storage systems. Their high heat transfer surface per unit volume, large heat capacity and good thermal shock resistance can ensure compactness, high performances and high temperatures [81].

Wang et al [92] performed an experimental investigation of a packed-bed honeycomb ceramic for high temperature thermal storage system to be operated by concentrated solar power. The study analysed the heat transfer characteristics of the system and demonstrated that the honeycomb ceramic material can be used as the

thermal storage material for high temperature thermal storage systems. Andreozzi [75] investigated numerically a high temperature thermal storage in a honeycomb solid matrix. The author performed a parametric analysis considering different porosity values and concluded that an optimal porosity value must be evaluated to identify the right trade-off between heat stored and pressure losses.

6.1.1. Modelling Laminar boundary layer

Modelling the performance of a sensible heat thermal energy storage systems involves the solution of a system of two differential equations, one for the solid media and one for the working fluid. Luo et al. [88] proposed a one-dimensional model for a honeycomb ceramic thermal storage and performed a parametric analysis to evaluate the influence of the main geometrical parameters. The model was solved adopting the Euler implicit scheme and was validated with experimental results. Results of the validation demonstrated an outlet temperature difference between simulations and experimental results of about *5-20 %*.

Given the small size of the plant, a *TES* system integrated within a solar dish *CSP* plant is usually characterised by relatively low mass flow rate which inevitably leads to low Reynolds numbers and consequently laminar flow [88]. For laminar flows, in the first portion of the duct, the development of the thermal and hydrodynamic boundary layers has a crucial impact on the heat transfer and pressure drop. The heat transfer coefficient as well as the friction coefficient may vary significantly form the fully developed flow [90].

The boundary layer development problem was addressed for the first time by Graetz [76]. Graetz studied the development of the boundary layer and, under the hypothesis of uniform wall temperature, derived equation to evaluate the Nusselt number in the entry region of a circular duct. The equation was obtained using an analytical solution of the governing equation (125).

$$\frac{\partial^2 T_f}{\partial r^2} + \frac{1}{r}\frac{\partial T_f}{\partial r} = \frac{u}{\alpha}\frac{\partial T_f}{\partial x} - \frac{\partial^2 T_f}{\partial x^2} \tag{125}$$

Where r and x denote the radial and the axial directions respectively, u is the fluid velocity and α is the thermal diffusivity of the fluid. Inlet parabolic fully developed velocity profile as well as negligible conduction in axial direction can be assumed. Under these assumptions, equation (125) can be transformed in its non-dimensional form and solved by the method of separation of variables resulting equation (126).

$$Nu\ x^* = \frac{\sum_{n=1}^{\infty} G_n e^{-2\lambda_n^2 x^*}}{2\sum_{n=1}^{\infty} \frac{G_n}{\lambda_n^2} e^{-2\lambda_n^2 x^*}} \tag{126}$$

$$x^* = \frac{x}{DRePr} \tag{127}$$

Where x^* is defined by equation (127), the constants G_n and eigenvalues λ_n for this infinite series, are given in Table 23.

Table 23. Infinite-series-solution functions for the circular tube; constant surface temperature; thermal-entry length [93].

n	λ_n^2	G_n
0	7.313	0.749
1	44.61	0.544
2	113.9	0.463
3	215.2	0.415
4	348.6	0.383
>4	$4n + 8/3$	$1.01276\ \lambda_n^{-1/3}$

A similar equation can be derived considering constant heat flux as a boundary condition. Moreover, it is possible to derive a solution for any arbitrary surface

temperature distribution by simply discretising the surface temperature into a number of constant-temperature steps and summing, or superposing, the constant-surface temperature, thermal-entry-length solutions for each step [93].

An alternative to the Graetz series solution is the relationship proposed by Léveque [86], reported in equation (128).

$$Nu = \begin{cases} 1.077\ x^{*-1/3} - 0.7 & x^* \leq 0.01 \\ 3.66 + 6.9\ 10^3 x^{*\ -0.488} e^{\ -57.2x^*} & x^* > 0.01 \end{cases} \tag{128}$$

Similar expressions can be derived considering uniform wall heat flux. The Léveque solution for the thermal boundary layer development problem with constant heat flux is reported is equation (129)

$$Nu \begin{cases} 1.302\ x^{*-1/3} - 1 & x^* \leq 5 * 10^{-5} \\ 1.302\ x^{*-1/3} - 0.5 & 5 * 10^{-5} < x^* \leq 10^{-3} \\ 4.37 + 8.7\ 10^3 x^{*\ -0.488} e^{-41x^*} & x^* > 10^{-3} \end{cases} \tag{129}$$

The most realistic approach to analyse the laminar flow development problem considers also the development of the velocity profile along the duct. The hydrodynamic development of the fluid can be considered in equation (125), introducing non-negligible complications in the solution. Churchill and Ozoe [94] derived the relationship in equation (130) to evaluate Nusselt number simultaneously for the thermal and hydrodynamic flow development with constant temperature as boundary condition.

$$Nu = \left(\frac{0.6366 \left(\frac{4x^*}{\pi} \right)^{-\frac{1}{2}}}{\left(1 + \left(\frac{Pr}{0.0468} \right)^{\frac{2}{3}} \right)^{\frac{1}{4}}} \right) \tag{130}$$

Churchill and Ozoe also derived equation (131) for the Nusselt number considering constant heat flux as boundary condition.

$$\frac{Nu}{4.364\left[1+\left(\frac{\pi/4}{29.6x^*}\right)^2\right]^{1/6}} = \left(1+\left(\frac{\frac{\pi/4}{19.04x^*}}{\left[1+\left(\frac{Pr}{0.0207}\right)^{\frac{2}{3}}\right]^{\frac{1}{2}}\left[1+\left(\frac{\pi/4}{29.6x^*}\right)^2\right]^{\frac{1}{3}}}\right)^{\frac{3}{2}}\right)^{1/3} \tag{131}$$

The forced convection within a sensible heat thermal energy storage is a conjugate heat transfer problem and results in neither uniform wall temperature nor uniform heat flux at the boundaries. The problem in this case must be formulated for the entire solid-fluid system rather than using *a priori* boundary conditions, and equation (132) must be solved simultaneously with equation (125).

$$\frac{\partial^2 T_s}{\partial r^2}+\frac{1}{r}\frac{\partial T_s}{\partial r}+\frac{\partial^2 T_s}{\partial x^2}=0 \tag{132}$$

According to Shah and London [94] the local Nusselt number for the conjugate problem falls in between the constant wall temperature boundary condition problem and the constant heat flux boundary condition problem of the conventional convection problem. In this situation Nusselt number is a function not only of the dimensionless length x^* but also a function of the ratio between the wall thickness δ and the duct diameter and a function of the parameter R_W defined by equation (133). The contribution of R_W can be neglected whenever its value falls below the *0.05* [94]. In an air fed honeycomb TES, the wall thickness and the thermal conductivity of the fluid are usually in the order of magnitude of 10^{-2}-10^{-3}. Consequently, a value of the R_W parameter lower than 0.05 can be expected. Thus, the contribution of R_W can be neglected.

$$R_W=\frac{k_f\delta}{k_s D} \tag{133}$$

In equation (133) k_f and k_s are the thermal conductivities of the fluid and the solid respectively.

To achieve a relatively high efficiency, *MGTs* are usually operated by a recuperated Brayton-Joule cycle. This cycle is characterised by a relatively low pressure ratio. Low pressure losses along the thermal energy storage ducts are then a major requirement to improve cycle efficiency. The pressure drop in a developing flow is due to both wall shear forces and fluid acceleration. According to Kays [94], the pressure drop for the hydrodynamic entrance region is not easy to evaluate. This can be either calculated introducing an apparent Fanning friction factor or considering the pressure drop to consist of two components: the loss due to shear stresses based on the fully developed flow, and additional pressure drop as a result of momentum change and kinetic energy loss. The second contribution to the pressure drop, in a dimensionless form, is designated as the incremental pressure drop number $K(x)$ (equation (134)).

$$\frac{\Delta p}{\rho u_m^2/2g} = \ f_{app}\left(\frac{x}{d}\right) = f_{fd}\left(\frac{x}{d}\right) + K(x) \tag{134}$$

Where $K\ x$, the incremental pressure drop, increases monotonically from 0 at $x = 0$ to a constant value in the fully developed region. This coefficient is a function of the Reynolds number and the duct geometry, which can be calculated by solving the complete set of Navier-Stokes equations. In equation 10, Δp is the pressure loss, ρ is the density, $u_m$is the average fluid velocity, x is the axial distance d is the pipe diameter, f_{fd} is the friction factor for the fully developed flow. In general, this coefficient can be approximated as $16/Re$.

6.1.2. Honeycomb TES model

The investigated geometry is shown in Figure 95. Air flows through the honeycomb structure composed of N_T circular ducts heating the surrounding

material. As shown by the figure, each duct is characterised by a diameter d and a length L. Assuming that each tube exchanges heat with the surrounding storage material in an equivalent control area, it is possible to define the equivalent diameter using equation (135).

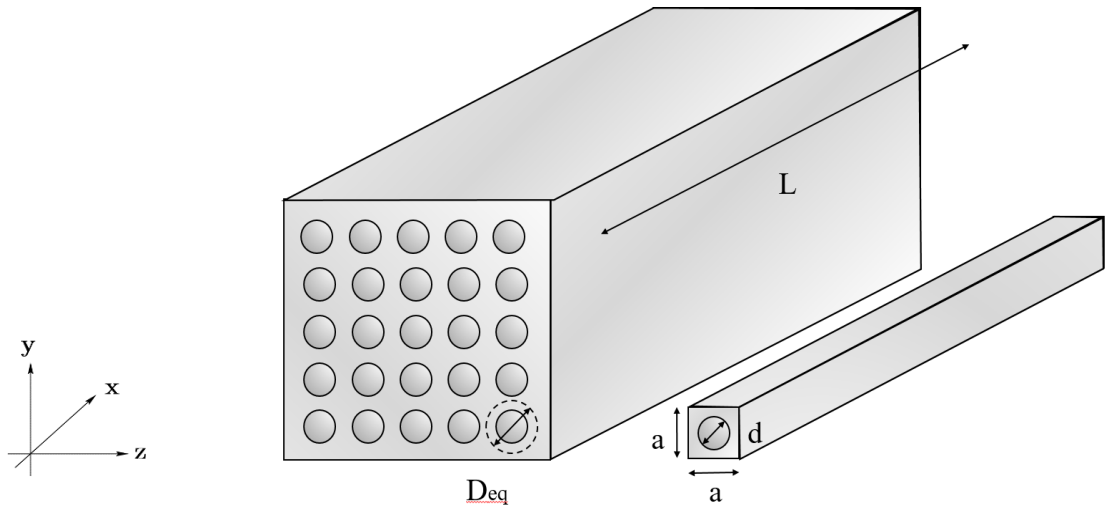

Figure 95. Schematic of the thermal energy storage system

$$D_{eq} = \frac{4a^2}{\pi N_T} \tag{135}$$

Where a is the single storage element side length and N_T is the number of elements in the entire storage unit.

To analyse heat transfer between the fluid and solid materials, the one-dimensional model adopted by Luo [88] was used. The model is based on the following assumption:

- Zero conduction of the material along y and z axis;
- Uniform initial temperature distribution of solid material (T_S).
- Adiabatic external wall of the thermal storage unit.
- The influence of fluid viscosity on its temperature (T_f) is neglected.

- Uniform flow and temperature along y and z axis. The effect of hydrodynamic and thermal development of the boundary layer is considered only from the heat transfer point of view, through the heat transfer coefficient.

The model considers the flow as one dimensional and uses the following governing equations.

For the solid:

$$\rho_S C_S \frac{\partial T_S}{\partial t} - k_S \frac{\partial^2 T_S}{\partial x^2} = hA(T_s - T_f) \tag{136}$$

For the fluid:

$$\rho_f C_{P,f} \left(\frac{\partial T_f}{\partial t} - u \frac{\partial T_f}{\partial x} \right) = hA(T_s - T_f) \tag{137}$$

In the previous equations, ρ_S and ρ_f are the density of the solid material and the fluid respectively, C_S is the solid medium specific heat, $C_{P,f}$ is the specific heat at constant pressure of the working fluid, h is the heat transfer coefficient and A is the heat transfer surface. In the study conducted by Luo, the heat transfer coefficient was evaluated using equation (138), an empirical relationship available in the literature for porous media [77].

$$Nu = \frac{hd}{k_f} = 3.66 + \frac{0.668 RePr \frac{d}{x}}{1 + 0.04 \left(RePr \frac{d}{x} \right)^{\frac{2}{3}}} \tag{138}$$

In equation (138) k_f is the fluid thermal conductivity. This equation demonstrates low variability of the heat transfer coefficient with the axial distance from the inlet not considering the effects of the laminar boundary layer development accurately.

6.1.2.1. Material Selection

The material selection is a crucial aspect in the design of a thermal energy storage system. The storage media should be able to withstand the high temperature of the air and stable enough to avoid deterioration and corrosion. Moreover, to reduce the size and the cost of the TES, a low price per unit volume and a high thermal energy stored per unit volume are required.

To find a suitable material for this application the software CES selector was used. Figure 96 shows the results of the material selection. The ellipses in the chart represent the range of price per unit volume and thermal energy stored per unit volume for any material. These two parameters were selected to identify the right trade-off between volume and price. Each colour in the chart corresponds to a material family: Red correspond to super alloys, yellow to ceramics, black to metals and minerals, cyan to steels and iron and brown to concretes. Silver ellipses are non-feasible materials in term of maximum operating temperature.

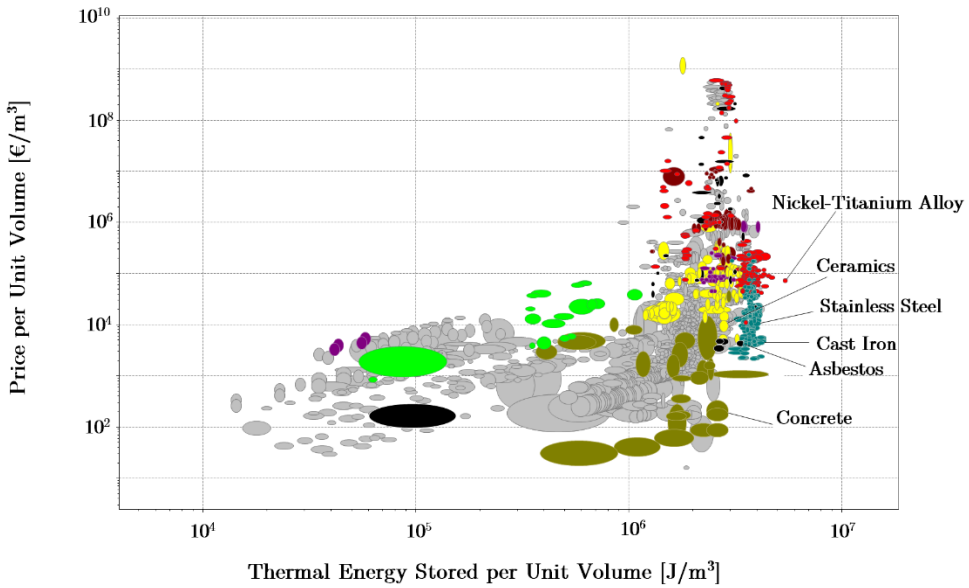

Figure 96. Results of storage media material selection. Source: CES selector software.

The material considered in this study is a ceramic with the properties reported in Table 24.

Table 24. Solid material properties.

ρ_S	C_S	k_S
5000 kg/m³	*1000 kJ/kgK*	*5 W/mK*

Although in this study heat losses are neglected, it is interesting to identify a suitable material to be used as insulator. In this case the parameters of interests are the price per unit volume and the heat flow per unit thickness, both must be minimised. Figure 97 shows the results of the insulator material selection. Concrete and minerals such as vermiculite and basalt are among the suitable materials for this application.

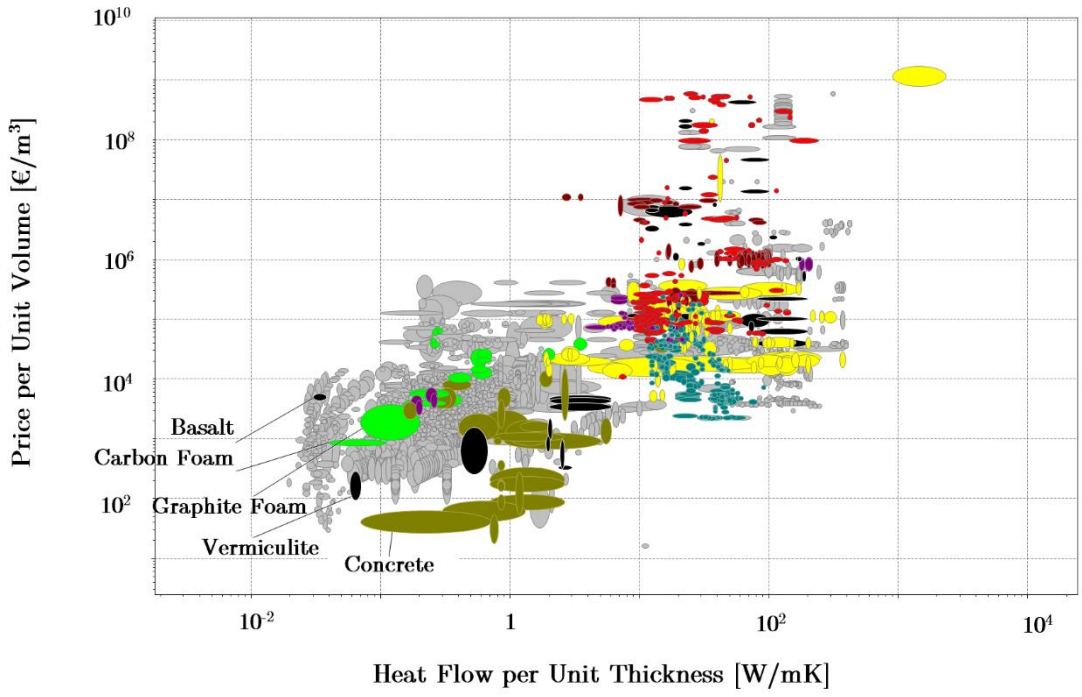

Figure 97. Results of insulator material selection

6.1.3. Heat Transfer coefficient and friction factor

To solve the above mentioned 1D model the knowledge of the heat transfer and pressure loss coefficient are required. These coefficients are strongly influenced by the laminar boundary layer development, the operating conditions (i.e. mass flow rate) and the TES geometry. For these reasons, a function to take into account all these aspects is required.

The heat transfer and pressure loss coefficients were evaluated using a regression model obtained from the results of conjugate heat transfer analysis completed using a commercial software (ANSYS CFX™). According to Bejan [76], in general, for the entry region the Nusselt number can be modelled using the following relationship.

$$Nu = k_1 * \left(\frac{RePr}{\frac{x}{d}} \right)^{k_2} \tag{139}$$

Where k_1 and k_2 are constants, which must be evaluated by the regression model in order to fit computational or experimental results. The value of k_2 is usually around 0.5 and assumed as such. k_1 was chosen to best fit the computational results

A similar approach was adopted for the friction coefficient. As already mentioned, the friction coefficient can be evaluated by separating the contribution of the shear stresses from the kinetic energy loss related to the hydrodynamic development of the fluid. The regression model adopted in this study, reported in equation (140), is based on the model described by Kays [94] in equation (134). The model was modified in this study by inserting two exponents related to the Reynolds number and the ratio x/d to better fit the results.

$$f = \frac{a_1}{Re^{a_2}} + \frac{a_3}{\left(\frac{x}{d}\right)^{a_4}} \tag{140}$$

In equation (140) a_1, a_2, a_3 and a_4 are constants, which will be evaluated by the regression model to fit the computational results. The first term represents the pressure loss due to shear stresses. It is inversely proportional to the Reynolds number and it's prevailing for $x \to \infty$. The second term represents the contribution of the hydrodynamic development and it's prevailing for $x \to 0$.

The numerical solution is obtained over the solid and fluid domains. Mapped mesh with sweeping method was adopted and includes an inflation in the near wall to resolve the heat transfer more accurately (Figure 98). Grid independence study was conducted to find a suitable grid density for the calculations. The computational domain was discretized using five different grid arrangements as shown by Table 25. The heat transfer coefficient was selected for comparison between the different grids. Results from conjugate heat transfer analysis with different grid arrangements demonstrates acceptable variability of *0.3%* passing from $4.5*10^6$ to $5.8*10^6$ nodes. Therefore, the grid arrangement of $4.5*10^6$ for the computational domain has satisfactory grid-independence and is adequate for the resolution of the conjugate heat transfer problem.

Table 25. Mesh Independence study results.

Number of Nodes	Solution Variability
9.7×10^5	
1.8×10^6	8.7 %
3.0×10^6	2.3 %
4.5×10^6	1.8 %
5.8×10^6	0.3 %

The heat Transfer coefficient and pressure drop have been evaluated using equations (141) and (142).

$$h = \frac{q_w}{(T_f - T_w)} \tag{141}$$

$$f = \frac{\tau_w}{\frac{1}{2}\rho u^2} \tag{142}$$

Where q_w is the wall heat flux, T_w is the wall temperature and $\tau_w = \mu\ \partial u/\partial y$ the shear stress. ρ, u and T_f have been calculated as the mass flow averaged value.

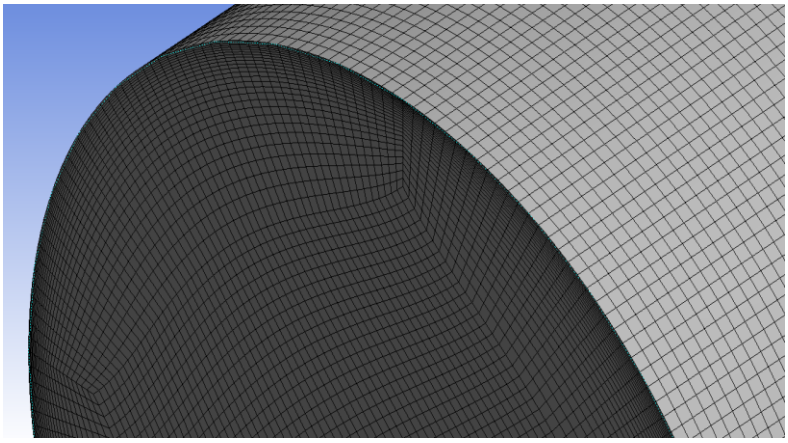

Figure 98. Detail of the fluid domain mesh

To estimate the accuracy of the conjugate heat transfer model in the evaluation of the heat transfer coefficient and friction factor, a comparison with the results obtained using the commercial software TEXSTAN™ was performed. The model was validated for the case of uniform wall temperature. The results were also compared with the Graetz series in equation (126) and the relationship developed by Churchill and Ozoe in equation (130). As already mentioned, the Graetz series assumes of a fully developed velocity profile at the duct inlet. The purpose of this comparison is then to evaluate the influence of the hydrodynamic flow development.

A validation case with a circular duct with constant wall temperature of *310 K* and diameter of *0.07 m* was considered. Air enters the duct with a velocity of *0.225 m/s* uniformly distributed along the radius and a temperature of *300 K*.

Figure 99 shows the results of the validation. Results show that the maximum deviation between the present model and the TEXTAN model for the heat transfer coefficient is always below *4%* and an absolute value of the error in the order of magnitude of 10^{-3}, significantly lower when compared with the Graetz series and the Churchill and Ozoe relationship which presents an absolute value of the deviation of 10^{0} and 10^{-1} respectively. For what concern the friction coefficient, despite the maximum deviation in the first part of the duct is relatively high, the deviation decreases significantly along the duct with an average absolute value around 10^{-3}. For this reason, the accuracy of the model was considered adequate for the purpose of this study.

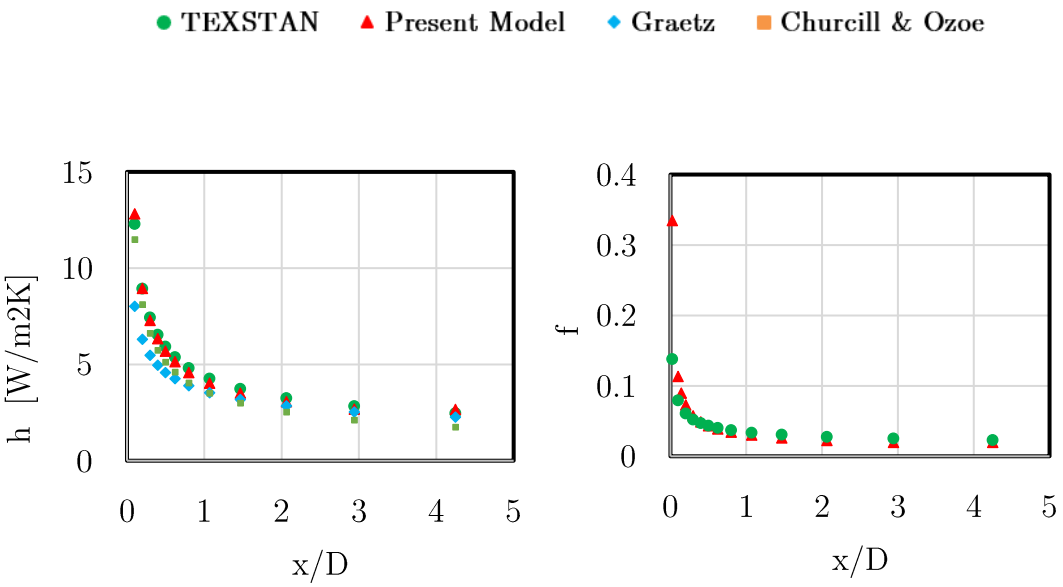

Figure 99. Results of the conjugate transfer model validation: heat transfer coefficient (left). Friction coefficient (right).

The discrepancy in the evaluation of the friction factor between the TEXSTAN code and the present model can be justified by the fact that TEXTAN assumes a quadratic velocity profile as shown in Figure 100 and does not take into account the influence of the velocity overshoot. According to Shah [94], the effects of axial

diffusion of momentum and radial pressure gradient cause the velocity profiles to have peculiar behaviour in the entrance region. Due to this phenomenon the velocity profiles have a local minimum at the tube centreline and symmetrically located maximum on either side near the walls, both experimental and analytical results support the existence of overshoots in the velocity profile. Near the entrance where the fluid particles first meet the wall, viscous friction rapidly decelerates the flow to zero velocity at the wall. The high velocity gradient at the wall results in a higher shear stresses and pressure gradients.

As shown by Figure 100, the present model considers this effect which causes major differences in the development of the velocity profile and consequently in the evaluation of the friction factor. Figure 100 shows the non-dimensional radius as a function of the non-dimensional velocity. r_s is the radius of the duct and v_m the mean velocity.

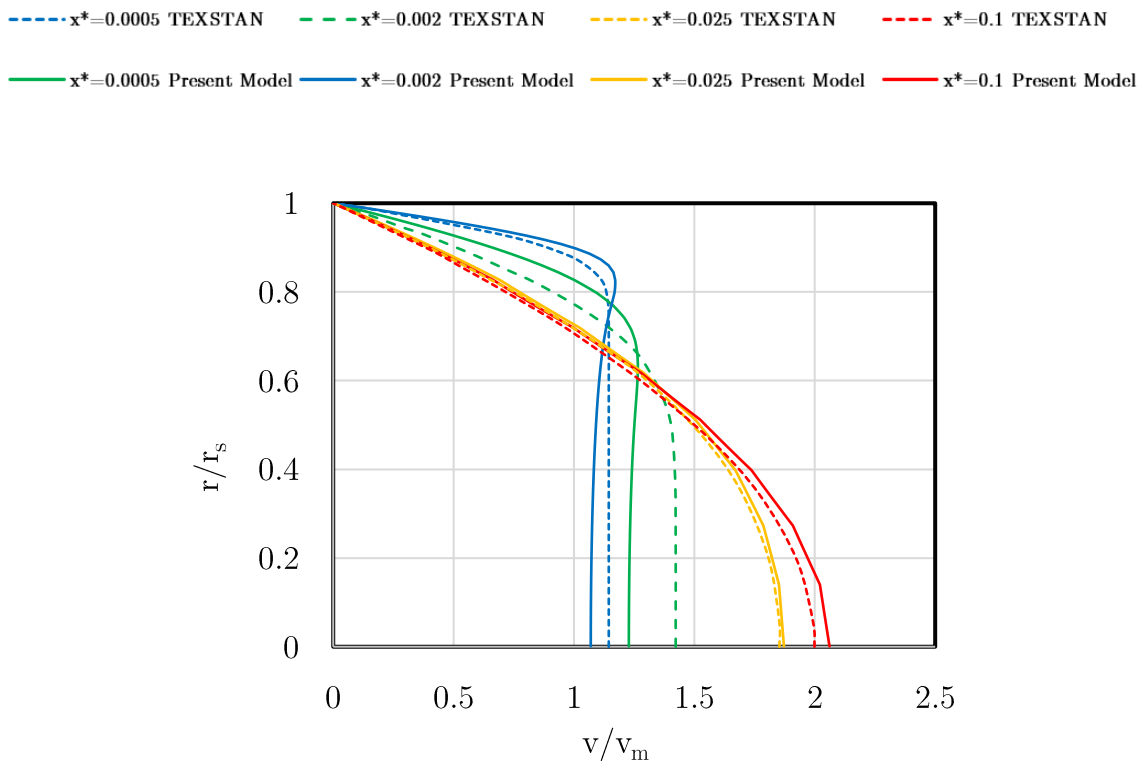

Figure 100. Comparison between TEXTAN and the present model for velocity profiles at different x^*.

6.1.3.1. Conjugate Heat Transfer Results

This section presents results from conjugate heat transfer simulations with the aim of studying the influence of boundary layer development on the velocity, temperature and pressure. Moreover, different duct diameters and mass flow rates were considered and their influence on the flow development was analysed.

Charging and discharging the thermal storage unit are inherently transient problems. Thus, transient simulations considering different diameters of the pipe and inlet velocity of the fluid were carried out. The computational domain is comprised from the solid a domain and the fluid domain. Boundary conditions at the fluid-solid interface are exchanged within the solver using a conservative flux interface model. The wall boundary condition for the momentum equation was set to “no slip”.

Figure 101, 102 and 103 show the results of the conjugate heat transfer analyses. Several simulations were carried out considering dissimilar diameters and mass flow rates. Figure 101 shows the velocity profile at different radii and channel lengths normalised by the inlet velocity. The results highlight that increasing the inlet velocity augments the effect of the velocity overshoot shifting the maximum toward the wall. The same effect can be observed for increasing duct diameter. Moreover, increasing the duct diameter delays the development of the velocity profile along the duct. The same effect can be observed when increasing the inlet velocity.

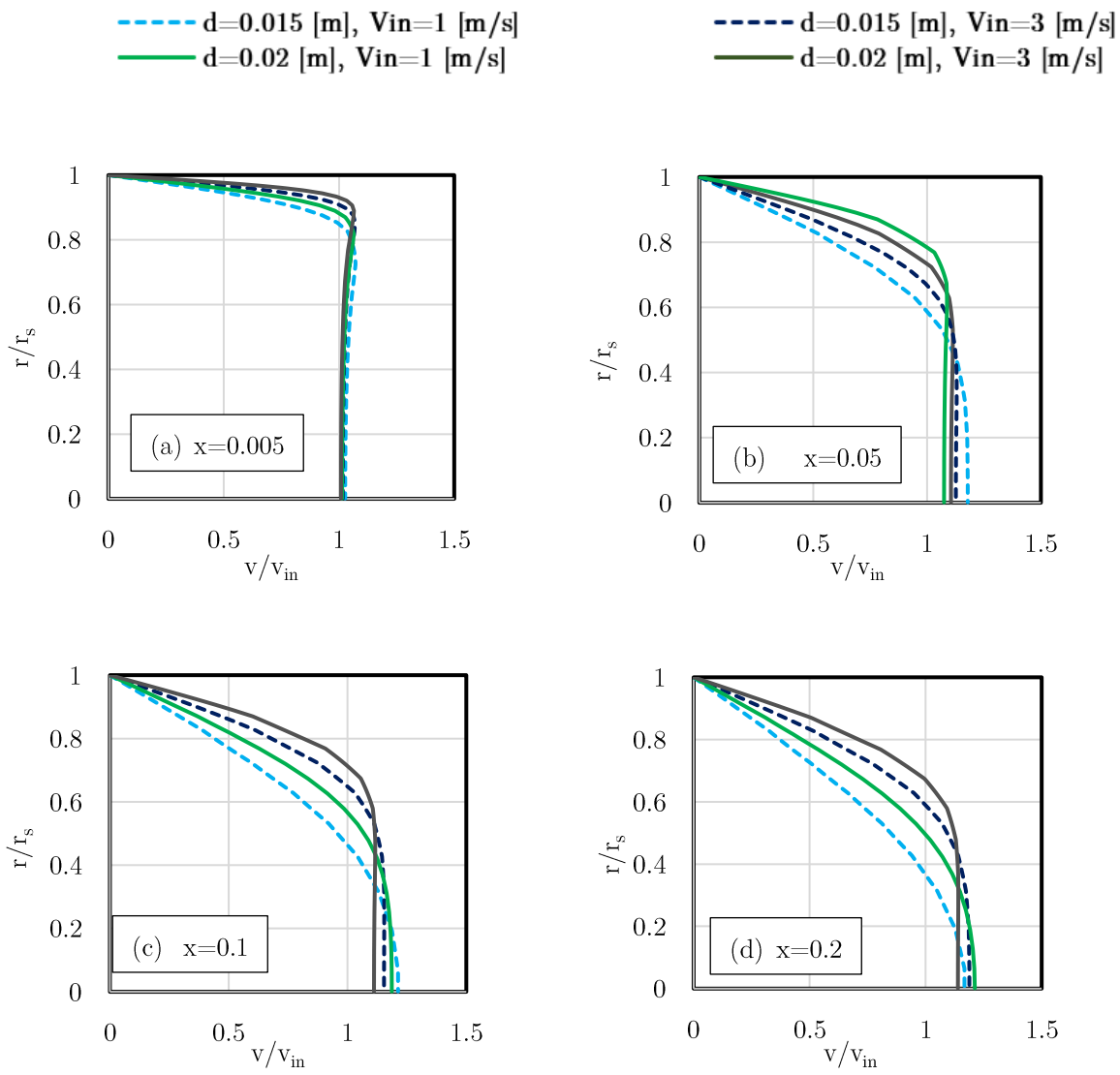

Figure 101. Results of the conjugate heat transfer analysis, velocity profiles at different locations. (a) x=0.005. (b) x= 0.05. (c) x=0.1. (d) x=0.2.

Figure 102 shows the temperature profiles at different radii and channel lengths normalised by the inlet temperature. It can be observed that the thermal boundary layer development involves a larger part of the duct when the inlet velocity is increased. The same effect can be observed with higher duct diameter. Furthermore, increasing the duct diameter delays the thermal development of the flow along the duct; an effect which can be achieved also by increasing the inlet velocity.

Although not shown in the figures, the influence of the equivalent diameter was also analysed demonstrating negligible influence on the thermal boundary layer development. The equivalent diameter also demonstrated small variability of the heat transfer coefficient. Varying its value from *0.02 m* to *0.05 m*, a typical range for this application, demonstrates a maximum variability always below *1%* and an average variability of *0.1%*. Thus, this parameter will not be considered in the following analysis.

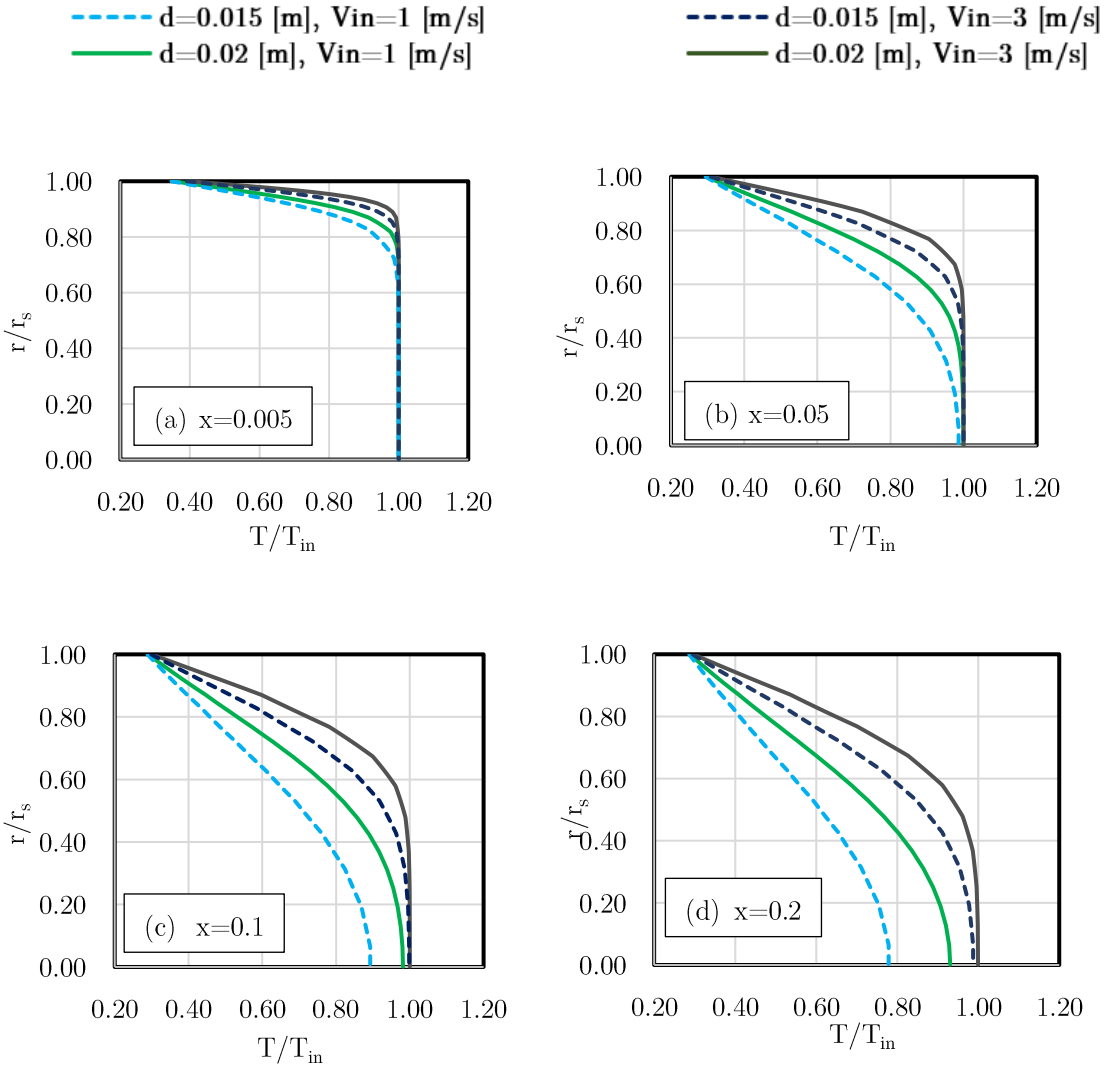

Figure 102. Results of the conjugate heat transfer analysis, temperature profiles at different locations. (a) x=0.005. (b) x= 0.05. (c) x=0.1. (d) x=0.2.

Figure 103 shows the pressure gradient profile at different radii and channel length normalised by the inlet pressure. It is possible to distinguish between two different contributions; the first contribution is due to fluid velocity profile development and it's relevant at the inlet of the duct where the effect of the velocity overshoot can be observed. In this section of the duct the pressure gradient is significantly higher and is characterised by a maximum caused by the velocity overshoot. Increasing the inlet velocity and the duct diameter augment the pressure gradient caused by this effect. From this point of view, the inlet velocity has a major influence by significantly increasing the absolute value of the pressure gradient and the absolute value of the peak caused by the velocity overshoot.

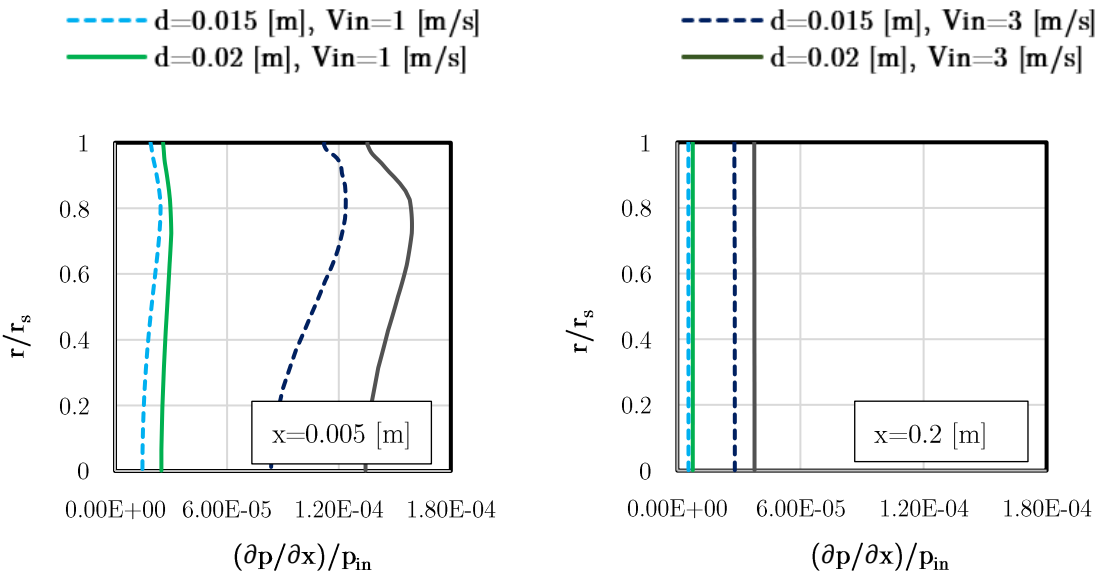

Figure 103. Results of the conjugate heat transfer analysis Pressure profiles at different locations.

The second effect is due to wall shear which occurs at the wall and is prevalent for $x \to \infty$. In this section of the duct the pressure gradient is significantly lower and constant along the radius. When the velocity is increased, the absolute value of the pressure gradient grows but much less if compared with the first section of the duct. For a larger diameter, a higher value of the pressure gradient is observed

which, in this case, is because the velocity profile it's not fully developed as shown in Figure 101.

6.1.3.2. Regression results

Results from conjugate heat transfer analysis described in section 3.1 were used to create a relationship able to describe the behaviour of the heat transfer coefficient and friction factor along the duct under different mass flow rates and duct diameters. The relationships obtained from the regression analyses are reported in equations (144) and (145). The method of the least squares was adopted to calculate the coefficients for the model $f\ x$ so the sum of squares is the smallest possible and equation (140) is satisfied. The analysis starts with the guess and moves towards the minimum of the sum of squares.

$$\min \sum_{i=1}^{n} \left(y_i - f\ x_i\ \right)^2 \tag{143}$$

Where $\boldsymbol{i}$ is the number of the known values y_i obtained from the conjugate heat transfer analyses.

The equations obtained from the regressions were compared with results obtained from conjugate heat transfer analysis.

$$Nu = 0.41 \left(\frac{Pr\ Re}{\frac{x}{d}} \right)^{0.5} + 2.25 \tag{144}$$

$$f = \frac{22.3}{Re^{1.2}} + \frac{0.025}{\left(\frac{x}{d}\right)^{0.64}} \tag{145}$$

The results show that for both Nusselt number and friction factor, the maximum error is very close to the entrance of the duct. This error decreases significantly along the duct and approaches the order of magnitude of 10^{-4} and a relative value of *0.5 %* for each trend line in the fully developed region. This is especially true for the Nusselt number. The friction factor error on the other hand seems to be

dependent on the Reynolds number variation and its accuracy decreases slightly when Reynolds number is increased. Nevertheless, the accuracy of the models was considered adequate for this study.

The results show that for both Nusselt number and friction factor, the maximum error is very close to the entrance of the duct. This error decreases significantly along the duct and approaches the order of magnitude of 10-4 and a relative value of *0.5 %* for each trend line in the fully developed region. This is especially true for the Nusselt number. The friction factor error on the other hand seems to be dependent on the Reynolds number variation and its accuracy decreases slightly when Reynolds number is increased. Nevertheless, the accuracy of the models was considered adequate for this study.

One-dimensional model validation shows a comparison between the results obtained from conjugate heat transfer analysis for Nusselt number and friction coefficient and results obtained from the relationships developed in this study. The regression analysis demonstrates good accuracy. Nusselt number regression shows a maximum relative error around *9%,* an average relative error below *3%* and a coefficient of determination R^2 always above *0.998* in a wide range of diameters and Reynolds numbers. The maximum relative error calculated for the friction factor is around *25%*, while the average relative error is below *9%* and the correlation coefficient is always above *0.995*. Despite a higher relative error, its maximum absolute value is relatively small in the order of magnitude of 10^{-3}. The average value instead falls below the order of magnitude of 10^{-4}.

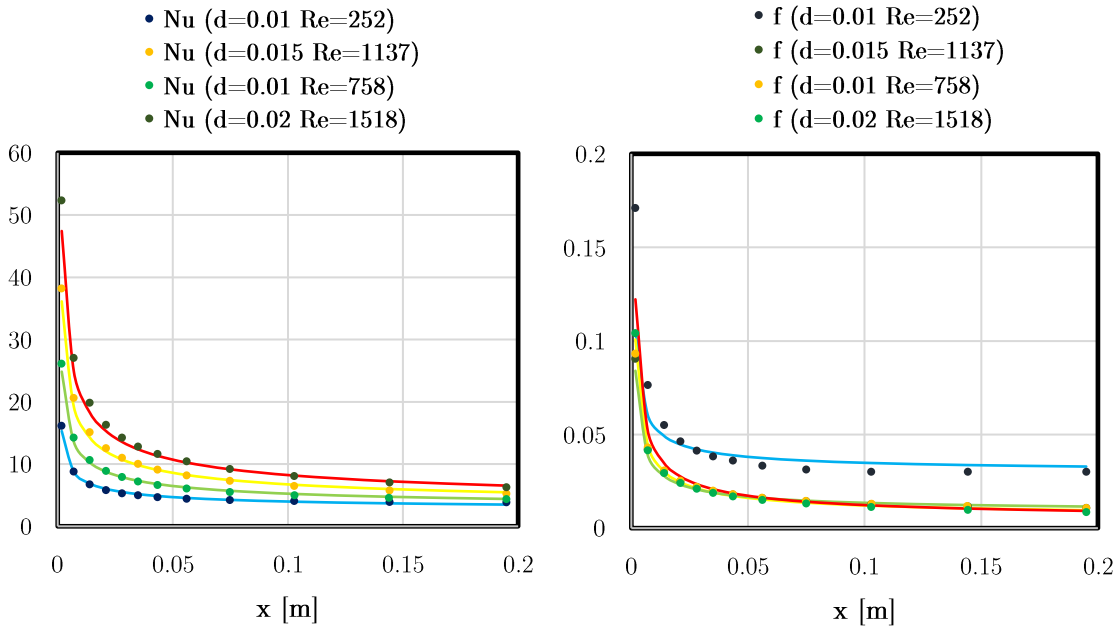

Figure 104. Comparison between conjugate heat transfer analysis (dots) and regression equation (lines) under variable diameter and Reynolds number. Nusselt number (a); Friction factor (b).

The results show that for both Nusselt number and friction factor, the maximum error is very close to the entrance of the duct. This error decreases significantly along the duct and approaches the order of magnitude of 10^{-4} and a relative value of *0.5 %* for each trend line in the fully developed region. This is especially true for the Nusselt number. The friction factor error on the other hand seems to be dependent on the Reynolds number variation and its accuracy decreases slightly when Reynolds number is increased. Nevertheless, the accuracy of the models was considered adequate for this study.

6.1.4. One-dimensional model validation

The equations developed so far were integrated within the one-dimensional model described in section 6.1.2. To demonstrate the accuracy of the model, the charging phase of a single channel characterised by an internal diameter of *0.01* m, equivalent diameter of *0.015* m and 0.2 m length was analysed. Results from the

model were compared with the already validated conjugate heat transfer model in five different sections of the duct. These results were compared for five different Nusselt relationships: the one used by Luo [88] for porous media, the one developed in this study and the Graetz series [76], and the two relationship derived by Churchill and Ozoe for constant temperature boundary condition (T) and constant heat flux (H).

The results of the validation, shown in Figure 105, demonstrate good accuracy of the present model and a maximum relative error below 2%. On the other hand, the Nusselt relationship used by Luo and the Graetz series demonstrate a higher relative error, which can reach 10% for the Graetz series and almost 20% for the Nusselt relationship adopted by Luo. As expected, this discrepancy decreases along the duct as the influence of the developing boundary layer reduces and the Nusselt number gets closer to the fully developed value.

The relationship developed by Churchill and Ozoe for constant heat flux boundary condition (H) [[94]] demonstrate a maximum relative error of about 7% showing good agreement when compared with the Graetz series and the relationship adopted by Luo. Nevertheless, its accuracy is lower than the relationship presented in this study. The second equation developed by Churchill and Ozoe on the other hand show high relative error demonstrating that it is not suitable for this application.

These results are generally in line with what was stated in section 1 and by Shah [94]. The solution of the laminar boundary layer for a conjugate problem falls in between the constant wall heat flux boundary condition and the constant wall temperature boundary condition.

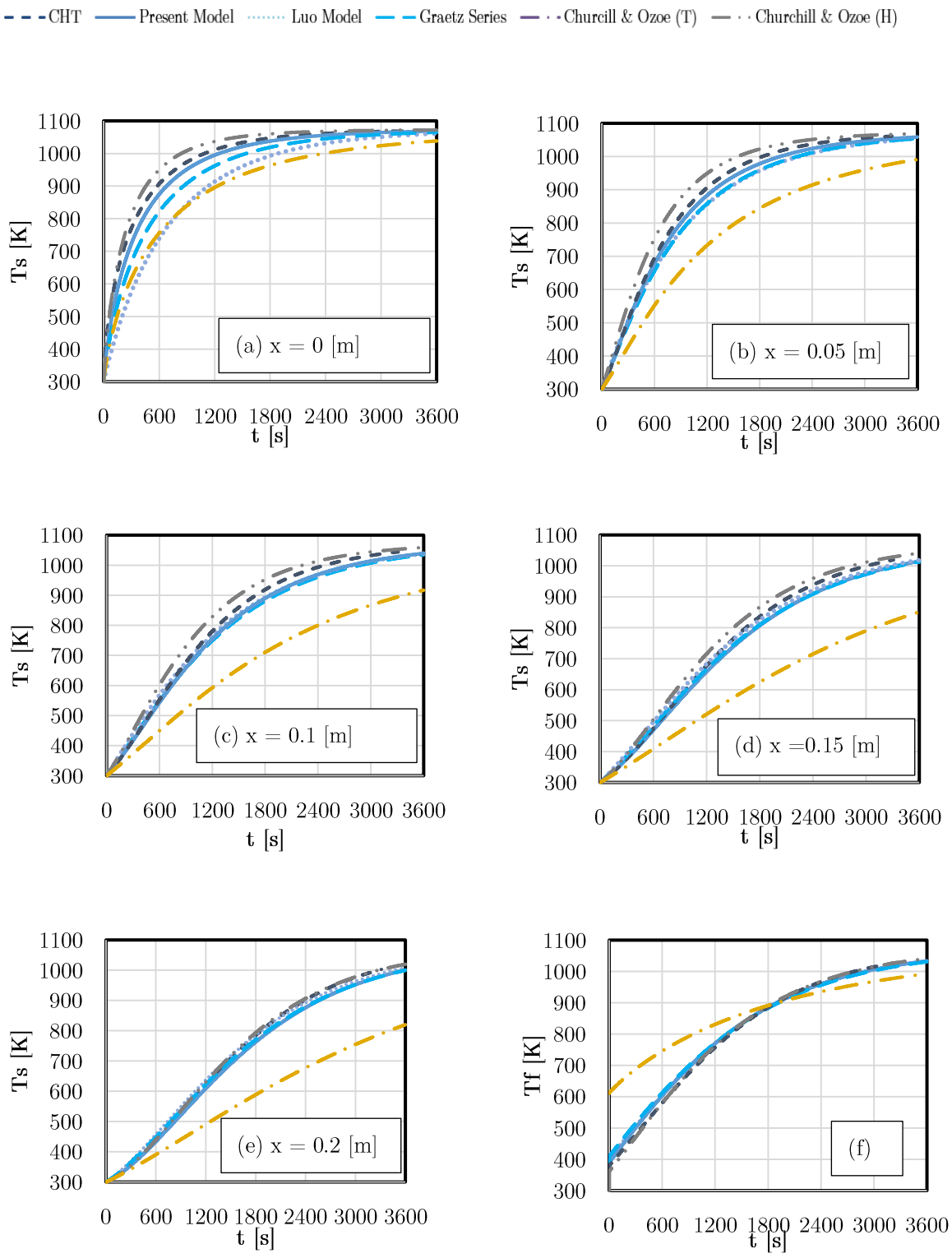

Figure 105. Results of one-dimensional model validation. Comparison between different Nusselt relationships and conjugate heat transfer analysis. Storage temperature at different locations: (a) x=0 m, (b) x=0.05 m, (c) x=0.1 m, (d) x=0.15 m and (e) x=0.2 m. Outlet fluid temperature (f).

As stated in section 6.1.1, the considered Graetz series reflects the behaviour of thermally developing flow with a fully developed velocity profile. Consequently, it can be concluded that the hydrodynamic development has a major influence on the heat transfer within a honeycomb TES system leading to an error which approach *10%* in the first portion of the duct. It can be concluded that the relation proposed by Luo is not suitable for this application. This relationship leads to an error which approaches *20%* in the first portion of the duct and consequently a honeycomb TES should not be modelled as a porous media.

All models demonstrate good accuracy in the prediction of the outlet temperature. Nevertheless, the present model is still the more accurate with a maximum relative error of about *3%* lower when compared with the *4%* and *4.5%* of Graetz series and Luo model respectively and the *3.5%* characterising equation (131).

6.2. Solar Dish MGT with Integrated Thermal Storage.

The integration of a TES unit within a solar dish MGT power plant is not an easy task. Many different layouts can be conceptualised according to the user needs (i.e. Solo electrical power generation or combined heat and power generation), each of them characterised by different advantages and drawbacks.

The arrangement proposed in this study is characterised by the presence of an external closed circuit operating only during the charging phase of the storage. The external circuit includes an air compressor to achieve circulation along the circuit. Moreover, the solar receiver must be redesigned; oversized to accomplish the heat demand of the second circuit and equipped with a pipe dedicated to the TES charging

circuit. The dish as well as the solar receiver must be oversized accordingly to the new heat demand.

During the charging phase the second circuit (blue line) operates to charge the storage unit. The main cycle runs as usual and the fluid in outlet from the receiver is directed to the turbine (orange line). During the discharging phase the second circuit is off-line. The air in outlet from the solar receiver is redirected into the storage and then in the turbine (green line). In this situation, there is no flow in the second circuit and the section of the duct that pass inside the receiver can be subject to a serious overheating. To overcome this problem, a mechanism to exclude from the solar radiation that section of the second circuit could be incorporated inside the solar receiver. The design of this mechanism is referred to future studies.

To realise the second circuit few complications are expected: As the temperature of the storage rise, the outlet temperature of the fluid increases, consequently the compressor should be able to withstand high temperatures. Furthermore, the outlet temperature of the second compressor is necessarily high, and the mass flow rate must be regulated to avoid excessive overheating of the solar receiver. This problem can be overcome integrating a further heat exchanger for downstream production of hot water, using either the closed circuit in Figure 106 or the open circuit in Figure 107. The open circuit could also guarantee to operate the compressor always at its design conditions. Moreover, the pressure ratio of the second compressor is relatively low. This characteristic has serious implication on the design of the compressor, the optimum design could not be a centrifugal machine anymore. For this reason, in this study the design of the second compressor will not be performed in detail as already done previously for other components of the plant. Nevertheless, the power required from its operation will be detracted from the output power of the plant. An isentropic efficiency of 85% was considered.

It is also good to consider that the system must incorporate high temperature valves. This imply complications regarding the control system of the plant as well as further cost.

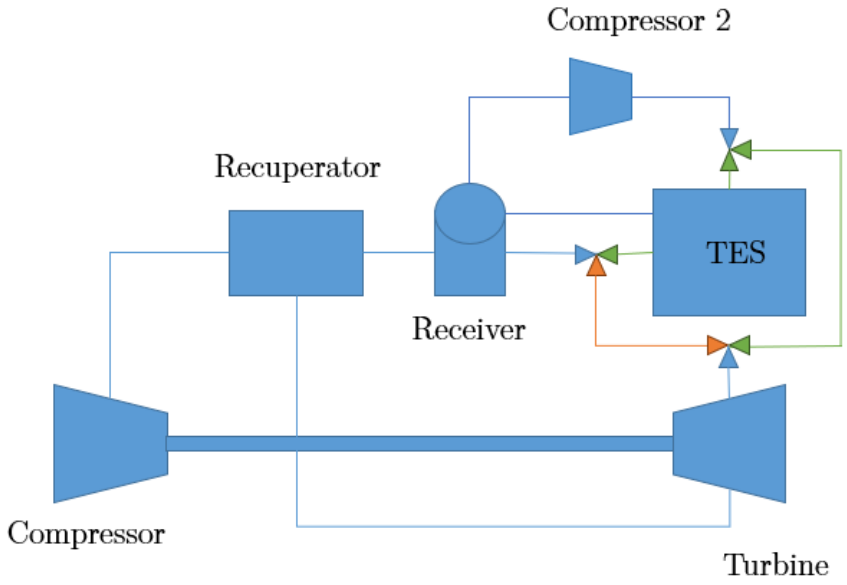

Figure 106. Plant layout with closed circuit.

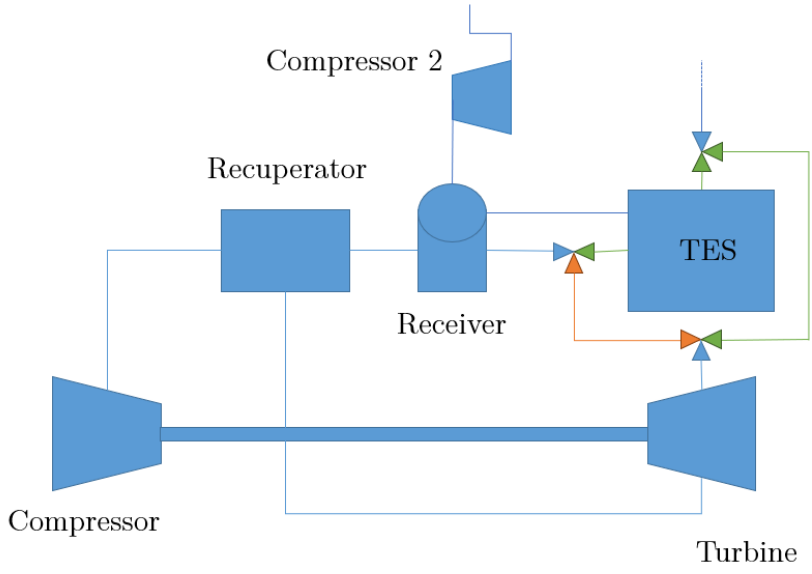

Figure 107. Plant layout with open circuit

6.2.1. Case Studies

The dispatchment of the plant as well as the size of the storage are strongly dependent on the user's demand of electrical power or CHP. Moreover, solar fluctuations along the year and the day have a huge impact on the dispatchment of the plant and the optimum operating strategy could vary day by day or even hour by hour. In this section two different day of July 2005 were chosen as case studies. The first day was chosen to analyse the behaviour of the plant during a day characterised by no solar fluctuations and the typical bell-shaped DNI. The second day is characterised by an irradiation drop in the afternoon and was chosen to highlight the attitude of the plant in smoothing fluctuations. Closed circuit arrangement was adopted. The analysis of the downstream production of heat is referred to future studies.

6.2.1.1. Design of a Thermal Energy Storage System

In the present case studies, a 4-hour storage system is presented. To achieve the target charging/discharging time with the given material and heat transfer fluid, the total heat capacity of the storage media must be higher than the energy transferred by the working fluid [85].

$$V_S \geq \frac{C_{P,f}\ m\ \Delta t}{C_S\ \rho_S} \tag{144}$$

Where V_S is the storage media volume, m is the mass flow rate, $C_{P,f}$ and C_S are the specific heats of the fluid and solid respectively, ρ_S is the storage media density and Δt is the target charging/discharging time.

The overall volume of the system can be calculated using equation (145).

$$V_S = \frac{N_T \pi (D_{eq}^2 - d^2) L}{4} \tag{145}$$

Results shown section 6.1.3.2 demonstrate minimum pressure losses with maximum duct diameter and maximum heat transfer coefficient with the highest Reynolds number possible. For this reason, *Re=1500* was selected as it is the extreme value considered in this research. The diameter instead was considered equal to *0.015 m*. Adopting these values and considering an equivalent diameter of *0.03 m*, the sizing of the storage leads to an overall number of ducts of about 160, an overall length of the storage of about 0.2 m and a total volume of the storage material of *0.38* m^3.

6.2.1.2. Day 1

Figure 108 shows the DNI profile of day 1 and the power output of the plant during pure solar operation with no integrated thermal storage. The plant design was selected based on the findings of section 0. The operational study considered in the calculation of the power output is constant TIT.

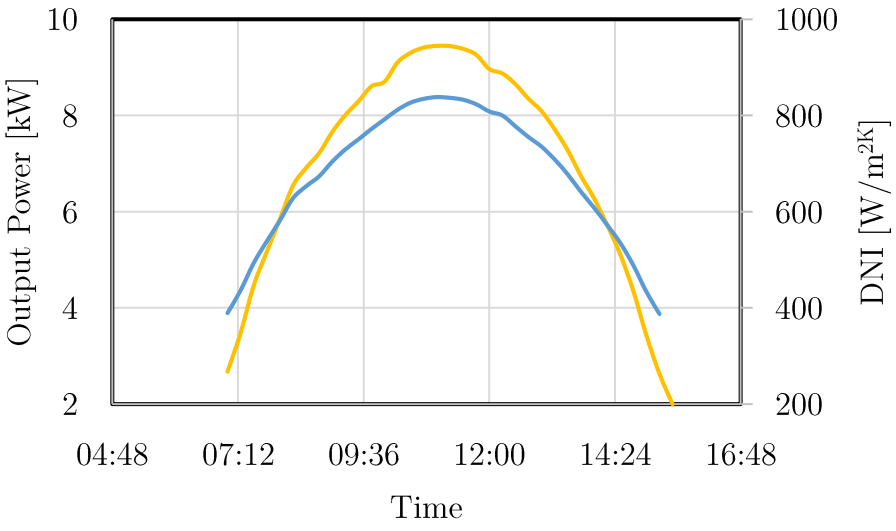

Figure 108. Daily variation of DNI (Blue) and output power (Yellow) during day 1.

During the charging phase the operational strategy is always set to constant TIT, the storage is operated at a starting temperature of *700 K* and a maximum temperature of *1173 K*. Additional electrical power is required to drive the

compressor in the storage circuit. The power required by the compressor #2 is detracted from the overall power output produced by the plant. Moreover, the new arrangement increases the heat demand required from the receiver during the charging phase. This leads inevitably to an increased receiver and dish size. Specifically, the dish diameter is increased from *10.3 m* to *15.4 m* and its cost from *21 600 €* to *26 900€,* calculated accordingly to the new size. The receiver cost is increased from *1 820 €* to *3 030 €,* calculated accordingly to the new heat demand.

The price of the storage media can be calculated through Figure 96. The chart shows that the cost per unit volume of ceramics is around 10^4 €/m^3, while the volume of the storage, calculated in section *6.2.1.1*, is *0.38* m^3. The overall cost of the storage media is then *3 800 €*. This should be augmented considering the cost of the insulator, valves and the other cost related to the second circuit.

The discharging phase starts at 13:00 two operational strategies have been analysed, constant power output and constant TIT. This operational strategy has been analysed just for illustrative purposes as the optimum operational strategy is strongly dependent from the user needs. Nevertheless, Figure 109 shows interesting results from the point of view of the dispatchment of the plant. Operating the plant with constant TIT results in high output power for a short time period extending the operations pf the plant till 15:45. This demonstrates the capability of the plant to meet peak demands for a short period of time. On the other hand, at the end of the day the temperature of the storage results still quite high and a substantial amount of thermal energy remain unutilised. The overall energy produced along the day is equal to *63 523* kW_h increase of about *4.5 %* in respect with the plant operating without thermal storage, which produces *60 773* kW_h.

The strategy with constant power output extends furthermore the operating range of the plant till 16:15. However, as shown by Figure 109 (c) this strategy results in high TIT during operations (up to 1210 K); the turbine design should take into

consideration this aspect. It must be highlight that the operating time range could be extended furthermore operating the plant at a lower power output. The overall energy produced by the plant in this case is *66 336* kW_h. Adopting this strategy, it is possible to use most of the stored thermal energy increasing the daily energy produced by *8.4%*. As shown in Figure 109 (b), also the efficiency is affected during the storage discharging phase. In this situation the efficiency drops due to the higher amount of heat which is provided by the thermal storage. When TIT is kept constant the efficiency drops gradually till no more power can be produced. When power is set to be constant the efficiency drops to 0.11 and stay constant until constant power output can be provided.

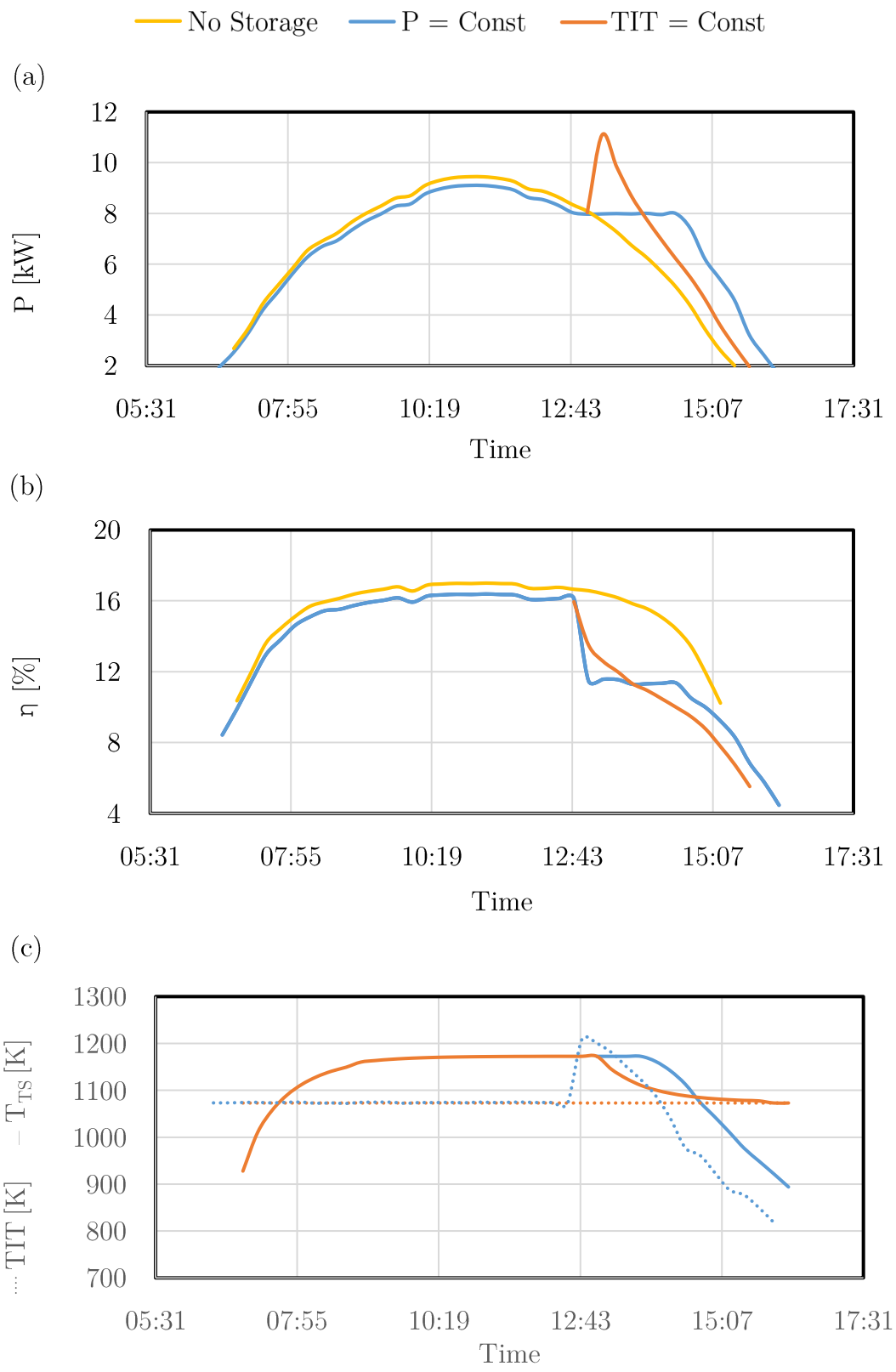

Figure 109. Performances of the plant during Day 1. (a) Power Output. (b) Efficiency. (c) TIT (dashed line) and Storage temperature (Continue line).

6.2.1.1. Day 2

The second day selected as case study is characterised by the DNI in Figure 110 The DNI presents a drop during the afternoon most probably caused by a cloud passage with consequent output power drop which causes the shutdown of the plant between 12:08 and 12:38. This case study aims to demonstrate the capability of the thermal storage to reduce the effects of solar fluctuations. The storage is operated to maintain constant output power.

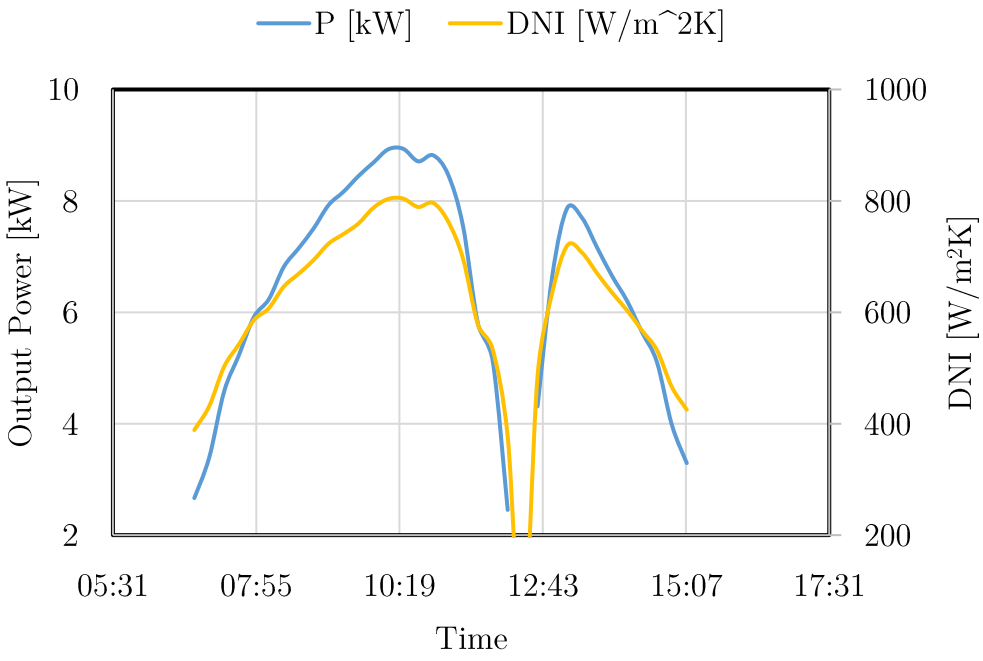

Figure 110. Daily variation of DNI (Blue) and output power (Yellow) during day 2.

Figure 111 presents the performances of the plant when the thermal storage is integrated. The operational strategy applied during the charging phase is constant TIT, during the discharging phase is constant power output. Specifically, in this situation the operations are characterised by two charging and two discharging phases. The daily variation of the solar irradiation is such that a second charging phase can be included during the day. The charts show lower power output of the

plant with integrated TES during the charging phase, when compared with the pure solar system. This is due to the electrical power required by the second compressor.

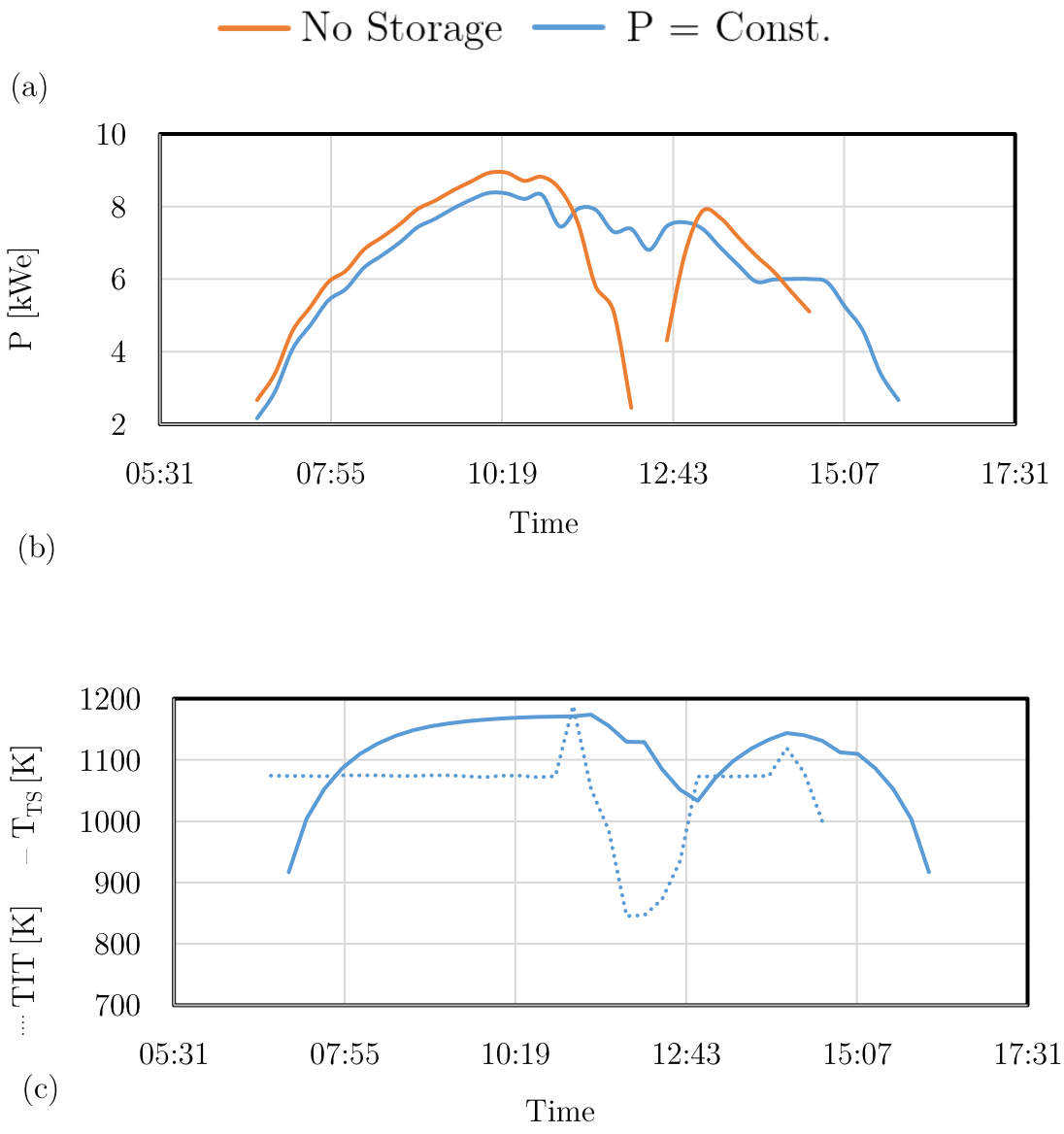

Figure 111. Performances of the plant during day 2. (a) Power Output. (b) Efficiency. (c) TIT (dashed line) and storage temperature (continue line).

During the first discharging phase, the plant is operated to maintain the power output constant to the value $8\ kW_e$. Nevertheless, the irradiation drop is such that the plant cannot produce constant power output. As shown by the chart in Figure

111 (a) the storage can provide enough thermal energy to smooth the solar fluctuation and produces at least *7* kW_e during the low irradiation period. The second discharging phase starts when the plant power output is *6* kW_e. The output is then kept constant or at its maximum value when the solar irradiation and the storage are not able to sustain the heat demand. The overall energy generated by the plant during the day is *61 164* kW_e, increased of *11.7%* in respect with the energy generated by the plant during operations without thermal storage (*54 027* kW_e). The maximum efficiency achieved during the day is around 16%. Moreover, the plant efficiency is generally high during operations and above *15%* for more than *7 h*.

6.2.1.2. Influence of the storage size

In this section the influence of the storage size will be analysed. In the previous sections 6.2.1.2 and 6.2.1.1 the performances of the plant with integrated thermal storage have been analysed considering a 4h storage size. The sizing of the storage has been performed considering steady operating conditions, which are not always encountered along the day. The result storage discharging time is dependent on the daily behaviour of the solar irradiation in the selected location. As shown in Figure 108, in the case study presented in section 6.2.1.2 the resulting discharging time is around *3h.*

For illustrative purpose an *8h* storage was sized and compared with the previous case already analysed in section 6.2.1.2. The storage is characterised by a volume of about 0.76 m^3. Figure 112 shows that an *8h* storage could guarantee only half an hour more than the 4h storage. This is cause by the high heat demand required by the power plant when the DNI is low. The optimum storage size is consequently another variable which should be identified for each specific case. In

this case study, the increased cost of the storage media is not compensated by the augmented power generated along the day

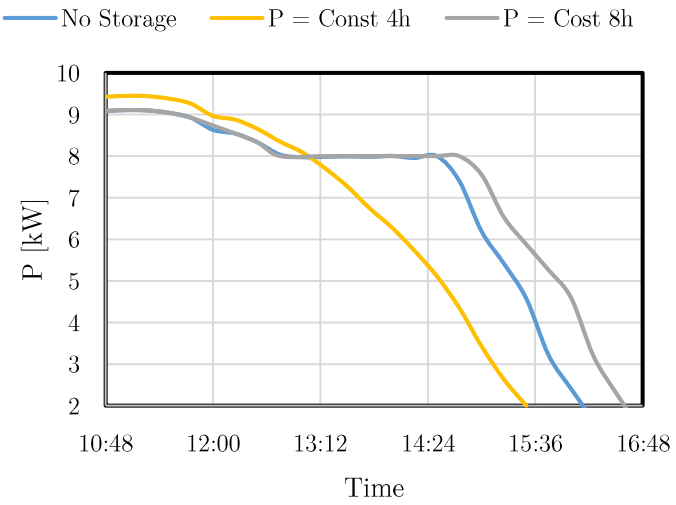

Figure 112. Output power produced along the day. Comparison between no storage, 4h storage and 8h storage.

6.3. Cost and LCOE analysis

Table 26 shows a cost breakdown of the plant with integrated thermal storage. The overall cost of the plant is increased of about *10 000 €* due to the modification arranged to the components of the plant. In this breakdown the cost of the second compressor was considered equal to the first compressor cost and included in this cost item. The cost of the second circuit was included in the storage cost calculated as the storage media cost multiplied by a factor of 1.5. The installation cost was kept to the original value.

As already highlighted in section 6.2 and demonstrated in sections 6.2.1.2 and 6.2.1.1 the optimum operation strategy of the plant cannot be known a priori and can change significantly day by day. In any working conditions encountered along the day the decision variables are 3:

1) The control strategy (i.e. P = 8 kW_h), which is usually given by the user's power demand.

2) The number of charging and discharging phases and their starting time. In the case study analysed in section 6.2.1.1 two charging and discharging phases were adopted, proving benefits in that specific case.

3) The minimum and the maximum storage temperature. Given by the technological limits of the plant.

The resulting annual dispatchment of the plant is strongly dependent on the user needs, the selected location and the frequency of solar fluctuations. For this reason, the annual evaluation of the performance of the plant was not performed. Nevertheless, a preliminary LCOE analysis was performed considering an annual power generation increased by 10% and the new components costs. Results of LCOE preliminary analysis estimate the levelised an annual energy production of *16 735 kW_h* and a levelised cost of energy of about *25 [c€/kW_h]*.

The chart in Figure 113, shows that the dish is still the most expensive component of the plant as it composes the 58% of the overall cost. The storage cost represents almost the 13% of the overall cost, adopting a different storage media, such as concrete, would be possible to diminish the capital cost of the plant and reduce the levelised cost of energy to a value around *22-23 [c€/kW_h]*. Specific cost per unit volume of concrete is assumed from Figure 96.

Table 26. LCOE preliminary analysis.

	Pure Solar	4h Storage
E_{TOT}[kW_h]	15214	16735
Compressors Cost [€]	72	145
Turbine Cost [€]	483	483
Recuperator Cost [€]	5 374	5 374
Receiver Cost [€]	1 133	3 030
Storage Cost [€]	0	5 700
Dish Cost [€]	20 299	26 900
Gen. & Power electronics Cost [€]	157	157
Installation Cost [€]	4 673	4 673
Total Cost [€]	36 524	46 462
LCOE [c€/kW_h]	21.6	25

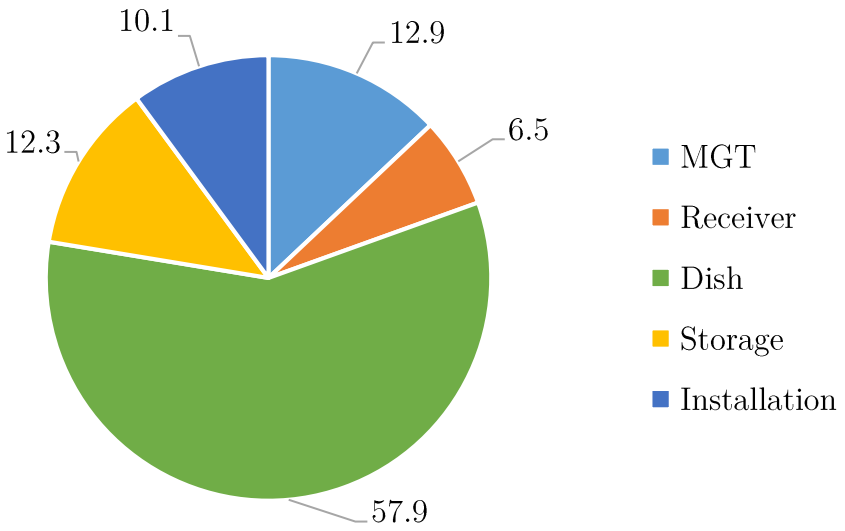

Figure 113. Cost Breakdown of the plant.

6.4. Conclusions

In this chapter a techno-economic study of a solar dish MGT with integrated thermal storage is presented. In the first section of the chapter, a model for a honeycomb thermal energy storage was presented. Conjugate heat transfer analyses, using a commercial software, were performed to develop an accurate regression model

which considers the effect of the laminar flow development at the duct entry on the heat transfer and pressure loss along the storage pipes. The conjugate heat transfer model was validated against data available in literature. Different Nusselt number relationships were then compared to verify the accuracy of the model. The results demonstrated higher accuracy of the present model when compared with the relationship adopted in literature, with a maximum relative error below 2%, significantly more accurate than the Nusselt relationship adopted by Luo and the Graetz series which demonstrate a relative error of about 20% and 10% respectively. As expected, this difference reduces along the duct as the influence of the developing boundary layer reduces and the Nusselt number gets close to the fully developed flow value. Detailed analysis about design of the storage system and storage media material selection were also presented.

In the following sections of the chapter two case studies were presented. A first day characterised by the typical bell-shaped DNI daily behaviour and a second characterised by a significant fluctuation occurring around 13:00. The analysis demonstrated the capability of the thermal storage in extending the operations of the plant. During day 1 operating time of the plant was extended of about *1h* and the energy produced along the day of about *8.5%*. During day 2 results from plant performance analysis demonstrate increased power generation along the day, up to *11%* and significantly reduced effect of the DNI drop occurring during the afternoon. Nevertheless, results from preliminary LCOE analysis estimate increased cost of energy, around *22-25* $c€/kW_h$.

7. Conclusions

The aim of this thesis was to investigate the technical and economic feasibility of a stand-alone CSP dish power plant with integrated hybridisation or thermal storage, looking for the most performant and economically feasible plant arrangement. The present study compared different plant layout options and control strategies to find the arrangement that maximises the annual electricity production, the dispatchability of the plant and the power output, while minimising the levelised cost of energy (LCOE) and emissions.

The specific objectives addressed in this research are:

- Analyse the techno-economical performances of a pure solar dish MGT. The present study demonstrated that solar dish MGT have competitive LCOE in respect with similar size power plants. Its value can be as low as 13 c€/kW_h in location such as Azalim characterised by high solar irradiation.
- *To study the technical and economic feasibility of incorporated hybridisation in a micro gas turbine dish CSP plant:* The study demonstrated no economic advantage in integrating fuel back-up because of higher operational cost due to fuel consumption. Nevertheless, the dispatchability of the plant is significantly increased resulting in doubled energy generation along the year. The addition of a combustion

chamber in the plant also admit the production of constant power output along the day obviating to the problem of solar fluctuations.

- *To individuate optimum design parameter:* Any plant layout investigated in this study was subject to plant design optimisation. The study identified the optimum design parameters of both pure solar system and hybrid power plant. Different operating strategy and dissimilar location were considered. Results from performance analysis demonstrate that the most convenient strategy for the pure solar power plant is constant TIT as constant power output cannot always be achieved during the day. Regarding the hybrid system, the lowest LCOE can be achieved when the receiver outlet temperature is kept constant, although constant power output can guarantee doubled power generation along the year.

- *To study the advantages of integrated thermal storage:* The study demonstrated augmented power generation along the day and demonstrated the capability of the thermal storage in smoothing solar fluctuations. Moreover, the analysis demonstrates increased capability of the plant to meet peak demand of electrical power for a short time. Nevertheless, the increased capital cost of the plant results in higher levelised cost of energy. Despite the higher LCOE, the presence of the storage increases significantly the reliability of the plant and extend considerably the dispatchment time of the plant. This characteristic is a great advantage over other source of renewable power plants.

- *To analyse the influence of each component in the capital cost of the plant:* Results from cost analyst demonstrate that almost 60% of the capital cost of the plant is spent in the dish manufacturing. Decreasing the cost of the dish could be the key to achieve higher competitiveness

in the market. Reducing its cost by 50% would results in a levelised cost of energy reduction estimated around 30% for the pure solar system and 10% for the hybrid system. Regarding the plant with integrated thermal storage, to reduce furthermore the capital cost concrete can be adopted as storage media. This would not significantly affect the size and performances of the storage and is characterised by a specific cost of 10^2 €/m^3, significantly lower than the 10^4 €/m^3 which characterised ceramic materials.

- *To study the performance of each component of the plant and their influence on the overall performances of the plant:* In general, the performances of each component of the plant have been evaluated applying a conservative approach in term of efficiency. Nevertheless, it is possible to draw few conclusions. 1) Results from parametric analysis demonstrate that the optimum recuperator effectiveness lies in the range 0.8-0.85, further effectiveness improvements can be achieved only decreasing the specific cost of the recuperator. 2) The air tube cavity receiver adopted in this study should be replaced with a technology with higher performance. The model adopted in this study estimated a relatively low efficiency in any operating condition, especially during low irradiation periods. The receiver is identified as the component with the lowest efficiency, and consequently the first component to be improved. 3) The optimisation of the turbomachinery could significantly improve the performances of the plant and reduce the levelised cost of energy. In this study the efficiency of the compressor and turbine have always been evaluated in a conservative way and estimated to be around 0.75-0.85 %. An optimised design of these components would increase their efficiency up to 0.85-0.9%.

7.1. Future Researches

These objectives have been achieved analysing the performances of the plant through an in-house tool developed in this study. The tool demonstrated good accuracy in predicting plant components' performances as each model was validated against experimental data available in literature. Nevertheless, further improvements are needed to fully characterise each component of the plant. Specifically, few assumptions have been made during the development of the model and the electrical and mechanical efficiency have been assumed based on previous experiences. Further studies will be aimed to improve the present tool incorporating a model for the high-speed generator and power electronics and the mechanical losses. Moreover, further investigation is necessary regarding the rotodynamic stability of the system. Additional clarifications are also needed regarding the flame stability inside a can combustor, a more accurate model about this is referenced to future studies.

The economic model was also based on few assumptions. Future studies will be aimed to investigate the influence of scale economy and the production volume on the levelised cost of energy of the plant. Moreover, more detailed information should be retrieved about installation cost, transportation cost and other cost not directly related to the main plant components which could be encountered in the specific location. This includes also government incentives sometimes available.

Regarding the integration of a thermal storage, more detailed analyses are required to investigate with increased accuracy the annual performances of the plant and the technical feasibility of the plant layout presented in this study. Moreover, the effect on the plant performances and cost of parameters such as the storage size, storage material and storage dispatchment needs further investigations.

7.2. Dissemination of the research

As outcome of the present research the following papers have been published:

- Iaria D., M. Kader, Al Zaili J. and Sayma A. (2017). **Multi-objective optimisation of a centrifugal compressor for a micro gas turbine operated by concentrated solar power**. Global Power and Propulsion society forum, Zurich, January 2017, GPPF-2017-33.
- Iaria D., Al Zaili J. and Sayma A. (2017). **Reducing Levelised Cost of Energy and Environmental Impact of a Hybrid Microturbine-based Concentrated Solar Power Plant**. Global Power and Propulsion Society forum, Shanghai, November 2017, GPPF 2017-61.
- Iaria D., Al Zaili J. and Sayma A. (2018). **Solar Dish Micro Gas Turbine Technology for Distributed Power Generation. In book: Sustainable Energy Technology and Policies**. Springler 2018. (Book Chapter).
- Iaria D., Quiang Z., Xiao G. and Sayma A. **Development and Validation of a model for performance analysis of a honeycomb thermal energy storage for solar dish application**. Davide Iaria (Pending publication in cooperation with Zhejiang University, China).
- Iaria D., Al Zaili J., Nipkey H., Assadi M. and Sayma A. **Development and Validation of a Techno-Economic Model for Design Optimisation and Off-Design Performance Evaluation of a Pure Solar Microturbine**. Energies 2018, 11(11), 3199 (Publication in cooperation with Stavanger University, Norway).
- Nipkey H., Iaria D., Al Zaili J., Sayma A and Assadi M.(2019). **Application of Artificial Neural Networks for Monitoring and Optimum Operation Prediction of Solar Hybrid MGT System**. Proceedings of ASME Turbo Expo 2019. GT2019-91180 (Publication in cooperation with Stavanger University, Norway).

References

[1] K. Lovegrove, W. Stein (2012). Concentrating Solar Power Technology. Woodhead Publishing 2012.

[2] IRENA (2018). Renewable Power Generation Costs in 2017. International Renewable Energy Agency, Abu Dhabi.

[3] Markets and Markets (2016). Concentrating Solar Power Market by Technology (Parabolic Trough, Power Tower, Linear Fresnel & Dish/Engine system), Components (Solar field, Power Block, and Thermal Storage), End-User (Utilities, EOR & Others), and Region - Global Forecast to 2021.

[4] A. Mueller, M. Orosz, A. Kumar, R. Kamal, H. F. Hemond and Y. Goswami (2016). Evolution and feasibility of decentralized concentrating solar thermal power systems for modern energy access in rural areas. MRS Energy & Sustainability 2016.

[5] V. Pundhir and M. Gupta (2014). Solar Stirling plant, International Journal of Conceptions on Electrical and Electronics Engineering Vol. 2, April 2014.

[6] Market&Market (2017). Thermal Energy Storage Market By Technology (Sensible, Latent, and TCS), Storage Material (Water, Molten Salts and PCM), Application (Power Generation, District Heating & Cooling and Process Heating & Cooling), End-User and Region- Global Forecast to 2022.

[7] ISO 21348:2007

[8] C. M. Fernández-Peruchena, M. J Blanco, Ana Bernardos (2014). Generation of Series of High Frequency DNI Years Consistent with Annual and Monthly Long-term Averages using Measured DNI Data. Energy Procedia 49:2321–2329, June 2014.

[9] V. Pundhir and M. Gupta, Solar stirling plant, International Journal of Conceptions on Electrical and Electronics Engineering Vol. 2, April 2014.

[10] Stine, W.B. Diver, A compendium of solar dish/Stirling technology, R.B, 1994.

[11] T. Mancini, P. Hellet, B. Buttler, B. Osborne, W. Schiel, V. Goldber, R. Buck, R. Diver, C. Andraka and J. Moreno (2003). Dish-Stirling Systems: An Overview of Development and Status. Journal of Solar Energy Engineering MAY 2003, Vol. 125/135.

[12] L. G. Pheng, R. Affandi, M. Ruddin A. Ghani, C. K. Gan, Z. Jano, T. Sutikno (2014). A Review of Parabolic Dish-Stirling Engine System Based on Concentrating Solar Power. TELKOMNIKA, Vol.12, No.4, December 2014, pp. 1142~1152.

[13] K. Lovegrove, G. Burgess, J. Pye (2011). A new 500 m2 paraboloidal dish solar concentrator. Solar Energy 85 (2011) 620–626.

[14] University of Seville (2015). OMSoP project delverable D3.2 reporton potential markets for small scale solar-dish microturbines. Jan 2015.

[15] D. Iaria, J. Al-Zaili and A. I. Sayma. Solar dish micro gas turbine technology for distributed power generation. In: De S., Bandyopadhyay S., Assadi M., Mukherjee D. (eds) Sustainable Energy Technology and Policies. Green Energy and Technology. Springer, Singapore.

[16] Aichmayer L., Garrido J., Wang W., Laumert B. (2018).Experimental evaluation of a novel solar receiver for a micro gasturbine based solar dish system in the KTH high-flux solar simulator. Energy 159 (2018) 184-195.

[17] RIPASSO Energy (2016). A hybrid solution with concentrated solar power (CSP) and fuel for baseload mining operations. Technical Report 2016.

[18] J. Moreno and S. Rawlinson (2002). Dish/stirling hybrid-heat-pipe receiver design and test results, IECEC, (20147):556–564, 2002.

[19] D. Laing, H. Thaler, L. Lundström, W. Reinalter, T. Keck, O. Brost (1999). Development of Advanced Hybrid Heat Pipe Receivers in Dish/Stirling Systems for Decentralised Power Production. Final Publishable Report, 01. January 1996 to 30. June 1999.

[20] Cameretti, Maria & Plazzesi, R & Reale, Fabrizio & Tuccillo, Raffaele. (2009). CFD analysis of the flameless combustion in a micro-gas turbine. Proceedings of the ASME Turbo Expo. 4. 275-285. 10.1115/GT2009-59750..

[21] D. Laing and M. Reusch (1997). Hybrid Sodium Heat Pipe Receivers for Dish Stirling Systems. IECEC-97 Proceedings of the Thirty-Second Intersociety Energy Conversion Engineering Conference (Cat. No.97CH6203), 1997.

[22] S. Semprini, D. Sanchez, A. De Pascale, Performance analysis of a micro gas turbine and solar dish integrated system under different solar-only and hybrid operating conditions, Solar Energy 132 (2016) 279–293.

[23] I. Dincer and M. A. Rosen (2011).Thermal Energy Storage: Systems and Applications, Second Edition. © 2011 John Wiley & Sons, Ltd. ISBN: 978-0-470-74706-3.

[24] C. E. Andraka (2013). Dish Stirling Advanced Latent Storage Feasibility. Proceedings of the SolarPACES 2013 International Conference.

[25] K. Lovegrove, A. Luzzi, I. Soldiani, H. Kreetz, Developing ammonia based thermochemical energy storage for dish power plants.

[26] K. Lovegrove, A. Luzzi, M. McCann and O. Freitag (1999). Exergy Analysis of Ammonia-Based Solar Thermochemical Power System. Solar Energy Vol. 66, No. 2, pp. 103–115, 1999.

[27] G. Gavagnin, D. Sánchez, G.S. Martínez, J. M. Rodríguez, A. Muñoz (2017).Cost analysis of solar thermal power generators based on parabolic dish and micro gas turbine: Manufacturing, transportation and installation. Applied Energy 194 (2017) 108–122.

[28] Mazzoni S., Cerri G., Chennaoui L. (2018). A simulation tool for concentrated solar power based on micro gas turbine engines. Energy

Conversion and Management. Volume 174, 15 October 2018, Pages 844-854.

[29] Cerri G. A simultaneous solution method based on modular approach for power plant analyses and optimized designs and operations. ASME 96-GT-302 1996:1–13.

[30] Gavagnin G., Rech S., Sánchez D., Lazzaretto A. (2018). Optimum design and performance of a solar dish microturbine using tailored component characteristics. Applied Energy 231 (2018) 660–676.

[31] Ghavami, M. (2017). Cycle analysis and optimisation of micro gas turbines for concentrated solar power. Ph.D thesis. City, University of London.

[32] Sánchez D, Bortkiewicz A, Rodrfguez JM, Martfnez GS, Gavagnin G, Sánchez T. A methodology to identify potential markets for small-scale solar thermal power generators. Appl Energy 2016;169:287–300.

[33] Whitfield, Baines, Design of radial turbomachines, 1952.

[34] D. Iaria; M. Kader; J. Alzaili; A. Sayma , Multi-Objective Optimisation of a Centrifugal Compressor for a Micro Gas Turbine Operated by Concentrated Solar Power, GPPF conference 2017.

[35] Iaria D., Al Zaili J. and Sayma A. (2018). Solar Dish Micro Gas Turbine Technology for Distributed Power Generation. In book: Sustainable Energy Technology and Policies. Springler 2018.

[36] Lanchi M., Montecchi M., Crescenzi T., Mele D., Miliozzi A., Mazzei D., Misceo M., Falchetta M., Mancini R. (2015). Investigation into the coupling of Micro Gas Turbines with CSP technology: OMSoP project. Energy Procedia 69 (2015) 1317 – 1326.

[37] H.W. Oh, E.S. Yoon, M.K. Chung, An Optimum Set of Loss Models for Performance Prediction of Centrifugal Compressors, Proceedings of the institution of mechanical engineer, 1997.

[38] B. W. Botha, A. Moolman, Determtning the Impact gf the Diffirent Losses on Cenffigal Compressor Design, R & D Journal 2005.

[39] D. Japikse. Centrifugal compressors design and performances. Wilder, Vt.: Concepts ETI, 1996.

[40] W. Jansen, A method for calculating the flow in a centrifugal impeller when entropy gradients arepresent, Institution of Mechanical Engineers, Royal Society Conference on Internal Aerodynamics (Turbomachinery), 1967.

[41] R.C. Dean, Y. Senoo, Rotating wakes in vaneless diffusers, Journal of Basic Engineering, 1960.

[42] H.W. Oh, Yoon, M.K. Chung, An optimum set of loss models for the performance prediction of centrifugal compressors, Proceedings of the Institution Mechanical Engineers. Journal of Power and Energy, 1997.

[43] Aungier Ronald H, Centrifugal compressors: a strategy for aerodynamic design and analysis, 2000.

[44] J. D. Stanitz, One-dimensional compressible flow in vaneless diffusers of radial- and mixed-flow centrifugal compressors, including effects of friction, heat transfer and area change, National Advisory Committee for Aeronautics, 1952.

[45] HoSung Lee, Thermal design: heat sinks, thermoelectrics, heat pipes, compact heat exchangers, and solar cells, 2010.

[46] Yujie Yang, Yanzhong Li, General prediction of the thermal hydraulic performance for plate-fin heat exchanger with offset strip fins, International journal of heat and mass transfer 2014.

[47] R.M. Manglik, A. Bergles, Heat Transfer and Pressure Drop Correlation for Rectangular Offset Strip Fin Compact Heat Exchangers, Transaction of the ASME 1995.

[48] W.M. Kays, A.L. London, Compact Heat Exchangers, 1998.

[49] Xin R. C., Ebadian M. A. (1997). The effects of Prandtl numbers on local and average convective heat transfer characteristics in helical pipes, J. Heat Transfer 119 (1997) 467–473.

[50] Zou C., Zhang Y., Falcoz Q., Neveu P., Zhang C., Shu W. and Huang S. (2017). Design and Optimization of a High- Temperature Cavity Receiver for a Solar Energy Cascade Utilization System. Renewable Energy 103 (2017) 478-489.

[51] Gang X., Yan L., Ni M. Wang C., Luo Z. Chen K. (2014). Experimental Study of an Air Tube-Cavity Solar Receiver. Energy Procedia 61 496 – 499.

[52] Galanti L. and Massardo A. (2011). Micro Gas Turbine Thermodynamic and Economic Analysis up to 500 kWe size. Applied Energy 88 (2011) 4795–4802.

[53] Gallup D.R. (1994). A Solarized Brayton Engine based on turbocharger technology and the DLR receiver. Intersociety Energy Conversion Engineering Conference, (pp. 1719-1729). Monterey.

[54] Gavagnin, G., Sánchez, D., Martínez, G.S., Rodríguez, J.M. and Muñoz, A., 2017. Cost analysis of solar thermal power generators based on parabolic dish and micro gas turbine: Manufacturing, transportation and installation. Applied energy, 194, pp.108-122.

[55] Pioneer Engineering (1981) Cost analysis of an air Brayton receiver for a solar thermal electric power system in selected annual production volumes, prepared by Pioneer Engineering and Manufacturing Company for the Jet Propulsion Laboratory in 1981.

[56] H. Mustafa, D. Japikse, N. C. Baines and M. Zelesky, Axial and Radial Turbines, USA: Concepts NREC, 2003.

[57] WA Spraker, Clearance and Reynolds number effects on the efficiency of radial flow compressors, 1991.

[58] Daily JW, Nece, Chamber dimension effects on induced flow and frictional resistance of enclosed disks, Journal of Basic Engineering 82:217–232; 1960.

[59] C. Rodgers and R. Geiser, Performance of a high efficiency radial/axial turbine, Journal of turbomachinery, vol.109, April 1987, 151-154;

[60] G. F. Hiett and l. H. Johnston, Experiments Concerning the Aerodynamic Performance In-Ward Flow Radial Turbine, Institution of Mechanical engineer 1964.

[61] R.S. Benson, A Review of Methods for Assessing Loss Coefficients in Radial Gas Turbines, 1970.

[62] Wang W., Cai R. and Zhang N., General Characteristics of Single Shaft Microturbine Set at Variable Speed Operation and its Optimization, Applied Thermal Engineering, vol. 24, p. 1851–1863, 2004.

[63] Cooke D. H. (1983). Modeling of Off-Design Multistage Turbine Pressures By Stodola Ellipse. Energy inc. Pepse User's Group Meeting 1983.

[64] Dixon S. L. (1966). Fluid Mechanics and Thermodynamics of Turbomachinery. El Sevier- Butterworth 1966.

[65] Spence S. T. W., Artt D. W. (1997). Experimental Performance Evaluation of a 99.0 mm Radial Inflow Nozzled Turbine with Different Stator Throat Areas. Proceeding of the Istitution of Mechanical Engineers, Vol 211, Part A.

[66] Stodola A. (1905). Steam Turbines.

[67] Arroyo, A., McLorn, M., Fabian, M. & Sayma, A., 2016. Rotor-Dynamics of Different Shaft Configurations for a 6 kW Micro Gas Turbine for Concentrated Solar Power. Seoul, American Society of Mechanical Engineers.

[68] Ghavami, M. (2017). Cycle analysis and optimisation of micro gas turbines for concentrated solar power, Ph.d. thesis, City, University of London.

[69] Caputo C. (1997). Collana di Macchine, seconda edizione. Zanichelli 1997.

[70] A. H. Lefevbre, Gas Turbine Combustion: Alternative Fuels and emissions, 2010;

[71] GasTurb 12: Design and Off-Design Performance of Gas Turbines by Joachim Kurzke.

[72] https://ec.europa.eu/eurostat/statistics-explained/index.php/Natural_gas_price_statistics.

[73] R. Tuccillo, M. G. Cameretti (2012). Combustion and Combustor for MGT applications. In Micro Gas Turbines (pp. 5-1 – 5-56). Educational Notes RTO-EN-AVT-131, Paper 5. Neuilly-sur-Seine, France: RTO.

[74] Mesbahi, E., et al. A unique correction technique for evaporative gas turbine (EvGT) parameters. in ASME Turbo Expo 2001: Power for Land, Sea, and Air. 2001. American Society of Mechanical Engineers.

[75] Andreozzi, A., Buonomo, B., Manca, O. and Tamburrino, S. (2014). Thermal energy storages analysis for high temperature in air solar systems. Appl Therm Eng 2014; 71:130-41.

[76] Bejan, A. (2013), Convection Heat Transfer, Fourth Edition. © 2013 John Wiley & Sons, Inc. Published 2013, John Wiley & Sons Inc.

[77] G. Dai, Heat Transfer, second ed., Higher Education Press, China, 1998.

[78] Denholm, P. Ela, E., Kirby, B., Milligan M. (2010). The Role of Energy Storage with Renewable Electricity Generation. Technical Report NREL/TP-6A2-47187 January 2010.

[79] Blanco, M., Santigosa, L. R. (2017). Advances in Concentrating Solar Thermal Research and Technology. A volume in Woodhead Publishing Series in Energy 2017, Pages 213–246.

[80] Concentrating Solar Power Technology Principles, Developments and Applications A volume in Woodhead Publishing Series in Energy 2012, Pages 284–322.

[81] Srikanth, O., Sagar, Khivsara, D., Aswathi, R., Madhusoodana C. D., Rathindra, N. D., Srinivasan V. and Dutta, P.. Numerical and Experimental Evaluation of Ceramic Honeycombs for Thermal Energy Storage. Trans. Ind. Ceram. Soc., vol. 76, no. 2, pp. 102-107 (2017). © 2017 Indian Ceramic Society.

[82] Iaria, D., Kader, M., Al Zaili, J. and Sayma, A. (2017). Multi-objective optimisation of a centrifugal compressor for a micro gas turbine operated by concentrated solar power. Global Power and Propulsion society forum, Zurich, January 2017, GPPF-2017-33.

[83] Iaria, D., Al Zaili, J. and Sayma, A. (2017). Reducing Levelised Cost of Energy and Environmental Impact of a Hybrid Microturbine-based Concentrated Solar Power Plant. Global Power and Propuslion Society forum, Shanghai, November 2017, GPPF 2017-61.

[84] Iaria, D., Al Zaili, J. and Sayma, A. (2018). Solar Dish Micro Gas Turbine Technology for Distributed Power Generation. In book: Sustainable Energy Technology and Policies. Springler 2018.

[85] Li, P., Chan, C. L. (2017). Thermal energy storage analyses and designs. 2017 Elsevier Inc.

[86] Leveque, A.. Les lois de la transmission de chaleur par convection, Ann. Mines Mem. Ser., Vols. 12, 13, 1928, pp. 201–299, 305–362, 381–415.

[87] Lovegrove, K. and Stein, W. (2012). Concentrating Solar Power Technology. Woodhead Publishing 19th October 2012.

[88] Luo, Z., Wang, C., Xiao, G., Ni, M., Cen, K. (2014). Simulation and experimental study on honeycomb-ceramic thermal energy storage for solar thermal systems. Applied Thermal Engineering 73 (2014) 622-628.

[89] Mirmanto, M. (2013). Developing Flow Pressure Drop and Friction Factor of Water in Copper Microchannels. Journal of Mechanics Engineering and Automation 3 (2013) 641-649.

[90] Shah, R. K., London, A. L. (1971). Laminar Flow Forced Convection Heat Transfer and Flow Friction in Straight and Curved Ducts- A Summary of Analytical Solution. Technical Report #75. Department of Mechanical Engineering, Stanford University, Stanford, California.

[91] Zhang, Y., Faghri, A. (1996). Semi-analytical solution of thermal energy storage system with conjugate laminar forced convection. lnt. ,L Heat Mass Transfer. Vol. 39, No. 4, pp. 717- 724, 1996 Copyright © 1995 Elsevier Science Ltd.

[92] Wang, Y., Bai, F. W., Wang, Z. F., Kiriki, H., Han M. X., Kubo S. (2014). Experimental research of the heat transfer characteristics using a packed-bed of honeycomb ceramic for high temperature thermal storage system. International Conference on Concentrating Solar Power and Chemical Energy Systems, SolarPACES 2014. Energy Procedia 69 (2015) 1059 – 1067.

[93] Kays, W. M and Crawford, M. E (1966). Convective Heat and Mass Transfer. McGraw-Hill Series in Mechanical Engineering (1966).

[94] Shah, R. K., London, A. L. (2014). Laminar Flow Forced Convection in Ducts: A Source Book for Compact Heat Exchanger Analytical Data. Academic Press, 28 giu 2014.

[95] Abbas M. and Said N. (2009).Techno economic evaluation of solar Dish Stirling system for stand alone electricity generation in Algeria. Journal of Engineering and Applied Sciences. January 2009.

[96] Affandi R., Zamali O., Ghani M. R. and Kim G. C. (2018). Feasibility of 25kw parabolic dish - sterling engine based concentrating solar power

under Malaysia environment. International Journal of Engineering & Technology, 7 (4) (2018) 3874-3878.